Progress in Volcanology

Edited by Angelo Paone and Sung-Hyo Yun

Progress in Volcanology

Edited by Angelo Paone and Sung-Hyo Yun

IntechOpen

Supporting open minds since 2005

We are IntechOpen,
the world's leading publisher of Open Access books
Built by scientists, for scientists

5,800+
Open access books available

143,000+
International authors and editors

180M+
Downloads

156
Countries delivered to

Our authors are among the
Top 1%
most cited scientists

12.2%
Contributors from top 500 universities

CLARIVATE ANALYTICS
BOOK CITATION INDEX
INDEXED

WEB OF SCIENCE™

Selection of our books indexed in the Book Citation Index (BKCI)
in Web of Science Core Collection™

Interested in publishing with us?
Contact book.department@intechopen.com

Numbers displayed above are based on latest data collected.
For more information visit www.intechopen.com

Meet the editors

Angelo Paone received his BS and MS at the Università degli Studi di Napoli Federico II, Italy. He completed an isotopic specialization course at the United States Geological Survey (USGS), Virginia, USA, and obtained his Ph.D. at USGS and the University of Naples Federico II, Italy. He completed a short post-doc at the American Museum of Natural History, New York, USA; a Marie Curie Fellowship (individual postdoc) at Bristol University, England; and an Italian postdoc at the University of Naples Federico II. Since 2008 he has been a science teacher at Italian College Liceo Ettore Majorana Pozzuoli and a research professor at Pusan National University (PNU), South Korea.

Dr. Sung-Hyo Yun is a professor in the Department of Earth Science Education, Pusan National University (PNU), South Korea. He obtained his BSc at the College of Education, PNU, in 1980, and his MEd from the Graduate School, PNU, in 1982. Dr. Yun received his Ph.D. in Geology and Volcanology from the Graduate School, PNU, in 1987. Dr. Yun was the president of the Petrological Society of Korea and the Korean Society of Volcanic Hazards Mitigation.

Contents

Preface

Every volcano is considered a peculiar system governed by the law of chaos. The older an active volcano is, the more difficult it is to forecast its behaviour. The only way to characterize a volcano is to collect as much data about it as possible. All physical and chemical data must be collected in order to understand how a volcano works. In a case where a volcano has been deeply studied and much of its behaviour is known (i.e., Somma-Vesuvius volcanic complex), there are several isotope techniques, together with petrology and geophysical data, that can help us to understand when a volcano may erupt. This prediction can only be made when a volcano is well known from the volcanic stratigraphy, volcanological (eruptive mechanism, volume, and other physical parameters), petrographic, petrological, and geochemical points of view (i.e., fumaroles studies of temperature, volatile content, isotopes). Volcanic seismology is a branch of geophysics that considers tremors and volcanic earthquakes to forecast volcanic eruptions. A Synthetic Aperture Radar (SAR)-based survey of volcanic deformation must be taken into serious consideration. This book is a collection of studies on volcanoes all over the world.

Section 1: "Introduction"

This section contains one chapter that summarizes the main concept of Volcanology with an overview that will help to understand other chapters presented in the book.

Section 2: "Applied Volcanology"

In Chapter 2, Borgia et al. present a geothermal study of the power plants of Mount Amiata in Italy. The authors evaluate the lava mound's impact on freshwater aquifers, seismicity, and air. They state that geothermal tools used at Mount Amiata would increase the amount of reinjection, increasing the risk of induced seismicity, and conclude that the use of deep borehole heat exchangers could perhaps be the only viable solution to the current geothermal energy environmental impacts.

In Chapter 3, Iqbal et al. conduct a study in West Lampung, Sumatra, Indonesia, where tropical volcanic residual soils are formed from weathering of volcanic breccias in hydrothermal alteration areas with a thickness of up to 20 m. The volcanic residual soil was studied from a clay mineralogical approach and will be suitable for agriculture purposes, building foundations, and earth construction.

In Chapter 4, Paripurno Eko Teguh introduces a contingency plan that was carried out for the seven highest villages in Sleman Regency, Yogyakarta Special Region, as areas prone to an eruption of Merapi Volcano. This participatory and child-friendly contingency plan is a model for an emergency response to volcanic eruptions during the COVID-19 pandemic. This document may be adapted for other comparable natural disaster contingency plans. This plan will be easy to implement once it is completed with the Operational Plan document.

Section 3: "Volcanic Sedimentology, Geochemistry and Petrology"

In Chapter 5, Ayalew et al. report field observation, textural description, and mineral chemistry for rhyolitic obsidian lavas from previously under-described effusive Badi volcano, central Afar within the Ethiopian rift. The scarcity of explosive products is explained by the fact that the Badi rhyolite domes and flows resulted from initially volatile-poor silicic magma. The Badi lavas flowed outward due to their high magma temperature and peralkaline affinity with increased fluidity.

In Chapter 6, Lagos and Combina state that during the Miocene, in the distal sectors of the Bermejo Basin, a complex relationship developed between a floodplain and contemporary volcanic activity. Seven stages of sedimentation are established to interpret this relationship. The volcanism that generated these deposits is probably associated with the migration to the east of the Miocene volcanic arc of the Cordillera de Los Andes.

In Chapter 7, Bernard and Alexander present a hydrogeochemistry study where the chemical element sources of the Pidong Crater Lake (Panyam Volcanic Province, Nigeria) are derived mainly from water-rock interaction processes. The lake water is mainly $Mg–HCO_3$ water type. The lake water type is meteoric in origin and is relatively young with an age of 230 ± 30 years before the present. Pidong Crater Lake colour change activities are characterized by a decrease in pH. Increases in PCO_2 are attributed to intermittent degassing of CO_2 gases from fumarole activities from mantle sources.

In Chapter 8, Kumar and Sharma report on the field, petrographical, and geochemical observations of the volcano-plutonic rocks of the Nakora Ring Complex (NRC) from the Neoproterozoic, Malani Igneous Suite (MIS) (Northwestern Peninsular India). The research proposes that the Neoproterozoic magmatism at NRC was controlled by rift-related mechanisms and produced from a crustal source where the heat was supplied by a mantle plume.

Finally, in Chapter 9, Mohammadiha Homayoon presents a petrologic jumble on the origin of anorthosites, which are useful for providing information about the earth's history and evolution. Studying anorthosites yields good information about the conditions of igneous rock formation.

Angelo Paone and Sung-Hyo Yun
Pusan National University,
Busan, Republic of Korea

Section 1

Introduction

Chapter 1

Introduction to the Volcanology

Angelo Paone and Sung-Hyo Yun

Abstract

The main volcanological concept is shown and expressed so that any volcano can be understood easily. Volcanic products are listed and explained in plain language from lava flow to various pyroclastic products. The volcanic products have been explained schematically and their textural, field relationships characteristics are highlighted. The origin of magma within the interior of the Earth is also explained and the link between mantle and crust has been shown. The relationship among crust, mantle, and core has been highlighted embracing the source-to-surface model. An updated explanation of the Pyroclastic Density Currents (PDC) has been done to perceive their danger. Some of the most successful Volcanology books have been used. This will help the students, with a passion for Volcanology, to understand the principles of Volcanology.

Keywords: volcanology, lava flow, explosive activity, fall-out, pyroclastic density currents

1. Introduction

The chapter summarizes the main concept in Volcanology with an overview that will help to understand other chapters presented in this Volcanology Book. This chapter has been chosen, in particular, for under-graduate people who want to deepen their knowledge in Volcanology, producing several avenues that can help them to develop their own research interests—from volcanic geology to forecast volcanic eruption [1–13]. Some concepts about the constitution of the Earth must be described to better understand the volcanology base. We know that the Earth, broadly speaking, is stratified with a temperature around 6000°C at its center, as at the surface of the sun. The stratification gives some cloud on the production and genesis of the magma. The issue is very much complex but worth to investigate for the sake of clarity about magma generation. The Earth is stratified not only for temperature but also for density, minerals, and physics state as liquid versus solid. In fact, it is the fluid zone of the Earth (asthenosphere versus outer core), the areas much advocated for partial melting: The asthenosphere is the denser, weaker layer beneath the lithospheric mantle. It lies between about 100 and 410 km beneath the earth's surface. The temperature and pressure of the asthenosphere are so high that rocks soften and partly melt, becoming semi-molten. Earth's outer core is a liquid layer about 2400 km thick and composed of mostly iron and nickel that lies above the earth's solid inner core and below its mantle. Its outer boundary lies 2890 km beneath Earth's surface. Unlike the inner (or solid) core, the outer core is liquid (**Figure 1**). Hence, the Earth is made of several layers—(a) crust, mantle, inner and outer core. (b) Lithosphere, asthenosphere, mesosphere to core (**Figure 2**). The asthenosphere must be the most productive melt layer within the mantle structure.
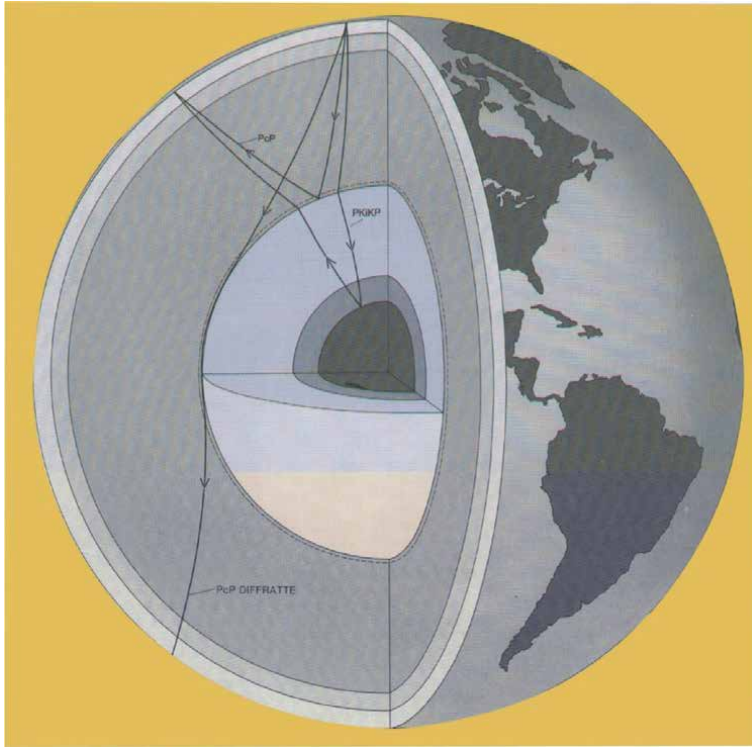
Figure 1.
Earth with a window inside the planet (author's collection).
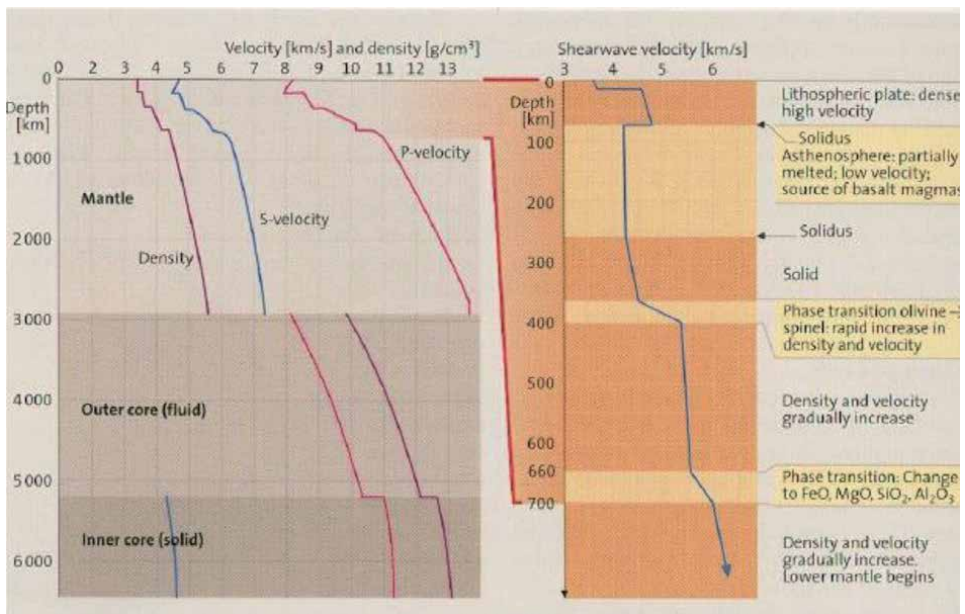
Figure 2.
Plot of the P and S wave velocity, and density versus depth from the surface to the core. Upper mantle with a profile of S wave velocity (V_s) and the seismic discontinuity (redrawn after Schmincke [14]).

2. Mantle structure

The section of crust and upper mantle with a profile of the S wave velocity (V_s, **Figure 2**) recognizes some physical characteristics that help to understand the dynamic of magma in the mantle. Probably, much of the magma that reaches the crust is produced in the asthenosphere, although deeper mantle origin can be envisaged from tomography data (410 and 660 km). Although, it is not clear if some magma can be produced in the outer core and/or in the lower mantle. Helffrich and Wood [15] affirm that seismological images of the Earth's mantle reveal three distinct changes in velocity structure, at depths of 410, 660, and 2700 km. The first two as said are best explained by mineral phase transformations (**Figure 2**), whereas the third D″ layer (2700 km) probably reacts due to change in chemical composition and thermal structure. In addition, tomographic images of cold slabs in the lower mantle, and the occurrence of small-scale heterogeneities in the lower mantle all indicate that subducted material penetrates the deep mantle, implying whole-mantle convection. In contrast, geochemical analyses of the basaltic products of mantle melting are frequently used to infer that mantle convection is layered, with the deeper mantle largely isolated from the upper mantle. The geochemical, seismological, and heat-flow data are all consistent with whole-mantle
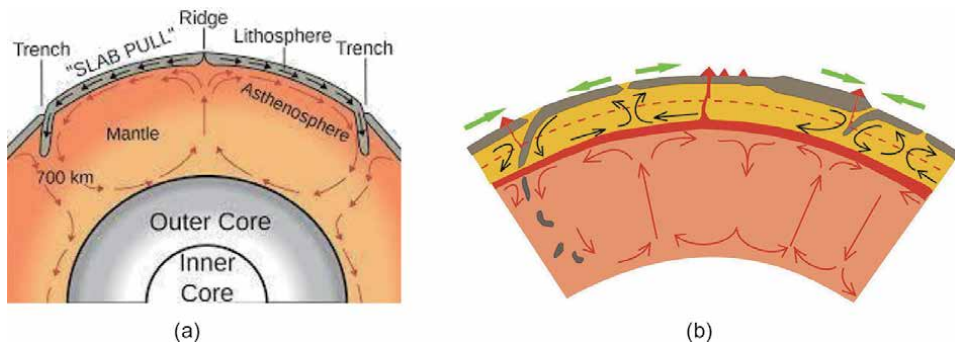
Figure 3.
(a): Earth slide highlighting the convective cycle on all the mantle (author's collection). (b): Earth slide highlighting the mantle with 2 convective cycles—Upper mantle and lower mantle (author's collection).
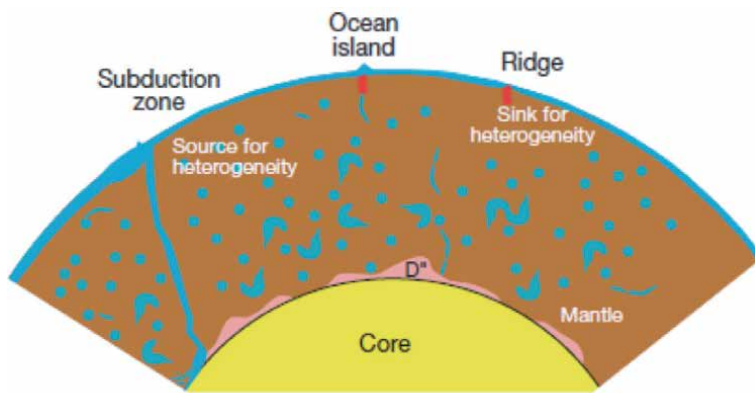
Figure 4.
Mantle slice with a characteristic chemical and physical heterogeneity (modified from Helffrich and Wood [15]). The blue blob is residual slabs and/or metasomatized mantle. The pink blobs are identified with the D layer.

convection provided that the observed heterogeneities are remnants of recycled oceanic and continental, respectively, of mantle volume (**Figure 3**). The convective cells are the engine of the plate tectonic for whole-mantle versus upper-mantle cells (**Figure 3**). **Figure 4** is the best guess for a model of mantle recently published [16, 17].

3. The crust

The Earth is divided into at least 12 main plates of the oceanic or continental type, delimited by distension and compression margins and in some cases by transform faults (**Figure 5**, [18]). **Figure 6** shows the distribution of active volcanism in diverse geodynamic settings (subduction, rift, and hotspot). Crustal end-members are of fundamental importance to understanding the magma evolution on the earth's surface, especially for the continental crust. Lately, we have enjoyed the model of Steve Sparks and collaborator (deep and hot intrusion zone [20–22]). The model clarifies how the volcanic rocks were originated either from metasomatized mantle source with the classical signature and/or by crustal contamination. A detailed explanation of trace elements and isotopes of volcanic systems come anyway, can be in their hand [23]. The continental crust of Wedepohl [19] (**Figure 6**) still can be taken as the best example to use and to perceive the Conrad and Moho discontinuities as the region where the basaltic magma intrudes, stagnate, and evolve through the surface. The bulk continental crust of Wedepohl [19] has a tonalitic composition with distinctly higher concentrations of incompatible elements. A dioritic bulk crust was suggested by Taylor and Mclennan [24] in contrast to Wedepohl [19]. If we make a section from New Zealand to South America (i.e., Chile), we can observe five types of tectonic margin—(a) subduction, oceanic-oceanic plates, (b) hotspot, (c) oceanic rift, (d) subduction oceanic-continental plates, (e) continental rift (**Figure 7**, [18]; a, b, c, d, e are partial melting zone with the production of basaltic magmas). Although other lithotypes are also present, we can surely say that partial melting could be the Holy Grail of Igneous Petrology.
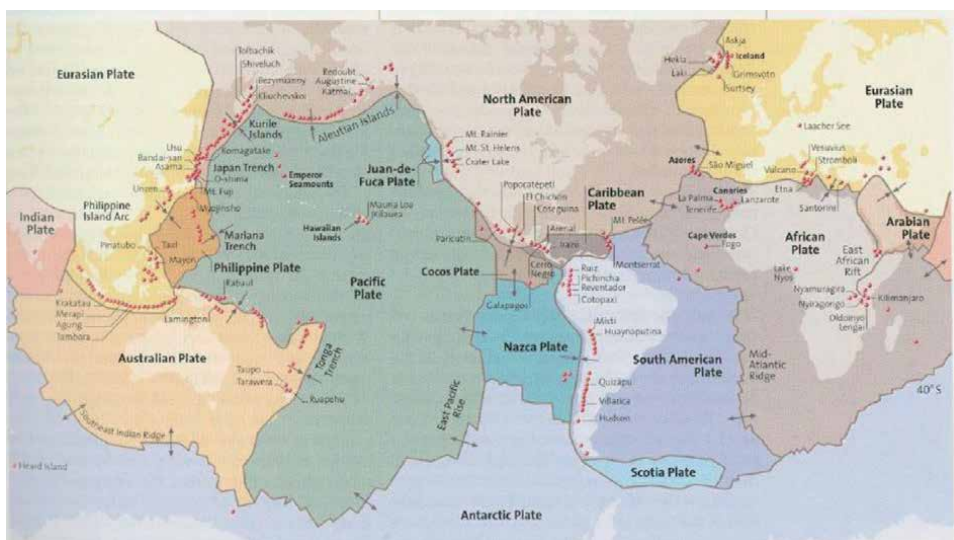
Figure 5.
Plate tectonic with larger and smaller plates and with the location of all the volcanic activity (modified from Schmincke [14]).
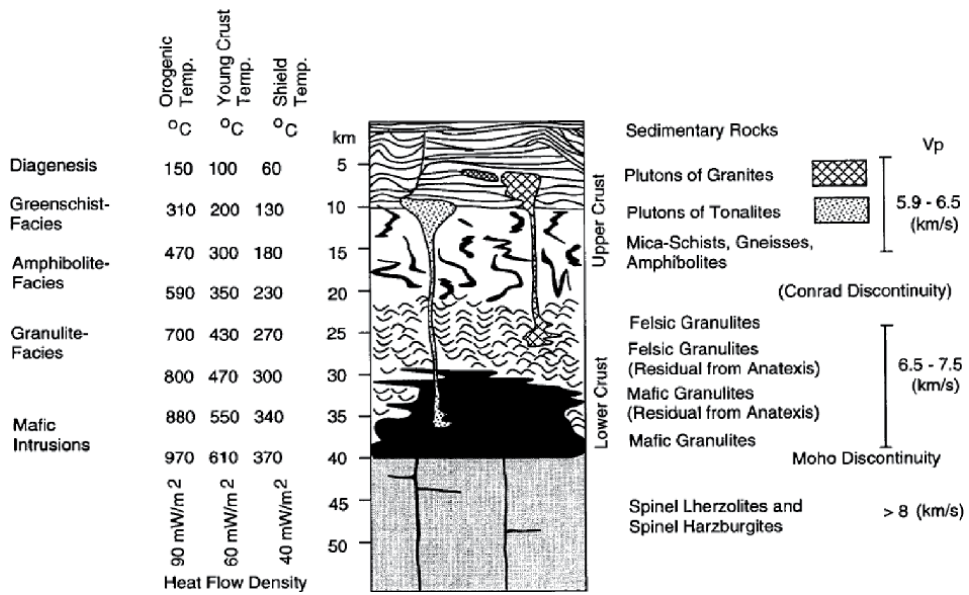
Figure 6.
Crust section (modified from Wedepohl [19]).
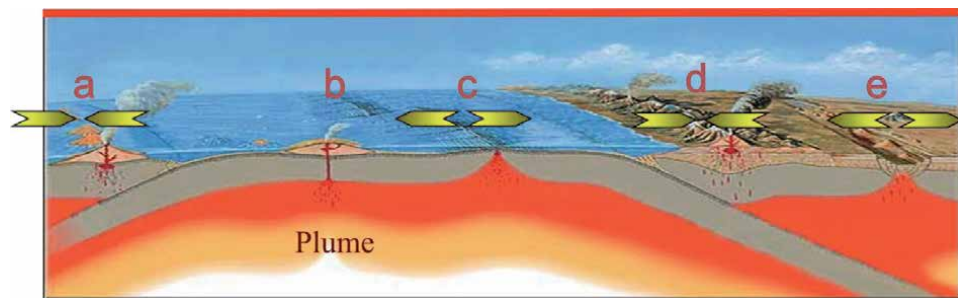
Figure 7.
Plate tectonic section from New Zealand to Chile. Modified from Bosellini [18].

4. Partial melting into the asthenosphere

The rise of the S wave velocity through the lower mantle suggests that little is the melting of the mantle, anyhow, little compared to the asthenosphere. Also, because of the variation of temperature, the pressure and water content are little, and however, not as happens in the asthenosphere. On the contrary, the S wave velocity decrease in the asthenosphere from 70 to 250 km. The velocity still keeps lower numbers until 410 km, as is seen in **Figure 3**. Hence, the magma can be produced, as well in the upper mesosphere, till 410 km. In this part of the mantle (from 70 to 410 km), the rocks are partly melted (**Figure 8**). So, partial melting is the most important process acting in the upper mantle for the production of magma [14]. In other words, the lower mantle could melt when it participates in the convective cycles. Partial melting can be advocated each time there is granular compaction that will cause the production of a magmatic liquid that buoyantly rises through the crust till erupting (**Figure 8**). The rise of magma can have a basalt or broadly much-evolved composition (rhyolitic) depending on how much interaction with the crust will have. However, basalts are compositions that help to model the geochemical
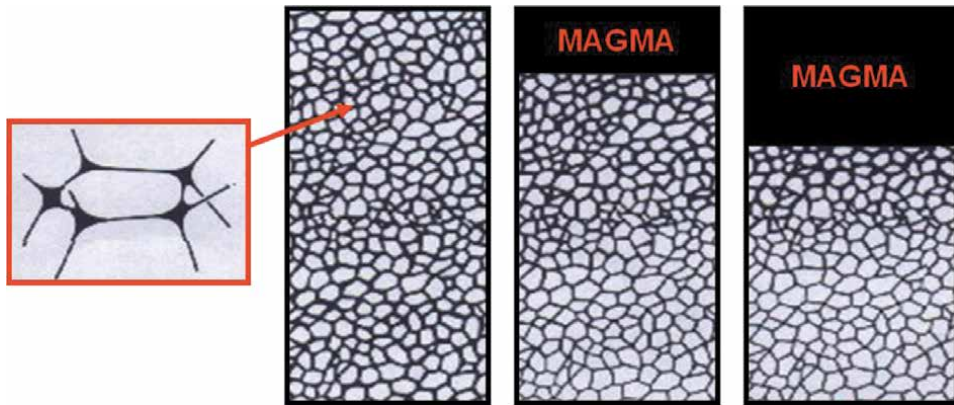
Figure 8.
Partial melting scheme. Magma is formed by the compaction of grains. The liquid is present between grains and is formed squeezing such material and so the magma aggregate and buoyantly rise through channels to the surface (author's collection).
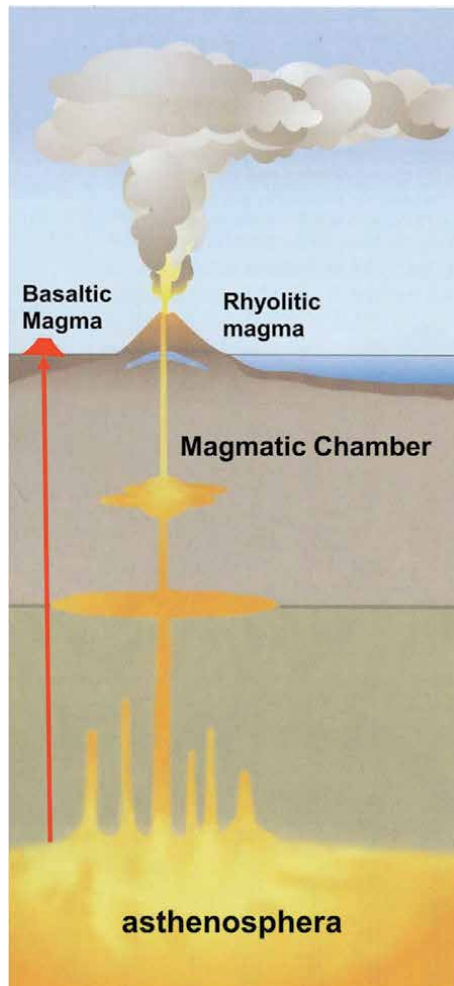
Figure 9.
Rise of basaltic and rhyolitic magma through the crust. Modified from Schmincke [14].
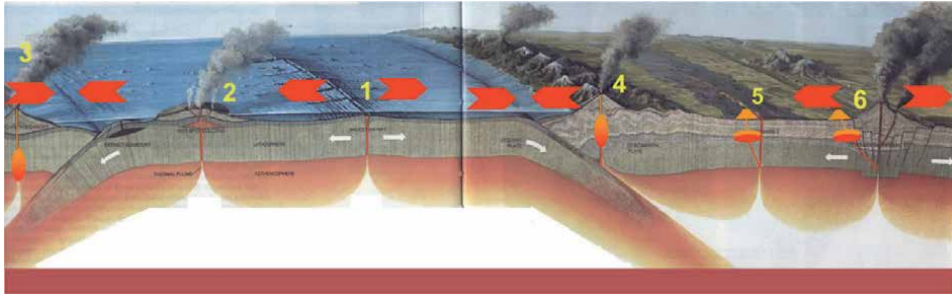
Figure 10.
Diverse magma for the diverse tectonic environment—A simple petrographic outline (modified from Bosellini 17).

processes in the rock origins, so are very important. On the other hand, rocks with an evolved composition help to decipher the processes that occur in the crust—partial melting versus crystal fractionation, assimilation, and other minor processes, such as mixing and/or mingling (**Figure 9**) [25–28].

5. Chemical and mineralogical characteristic of diverse magma in diverse tectonic environment

The Petrographic Classification of magma erupting in diverse tectonic regimes (**Figure 10**)—(1) Distention environment of thin oceanic crust (≈10 km) with the formation of basaltic magmas (e.g., Island and Atlantic rift). (2) Tectonic regime of hot-spot into an internal oceanic plate with the production of basaltic magma (e.g., Hawaii Island and Emperor submerged chain). (3–4) Compressive environment (subduction regime) with insular and continental arcs with the production of rocks with an evolved composition (felsic, andesitic, and rhyodacitic) (e.g., Japan, New Zealand, Chile, and Alaska). (5) Volcanic activity within a continental plate as a hot-spot with the formation of less-evolved and evolved composition, such as basaltic, andesitic, and rhyodacitic (e.g., Etna volcano). (6) Distention environment within a continental crust with the formation of basaltic, andesitic, and rhyodacitic (e.g., Africa rift valley).

6. Effusive magma versus intrusive magma with the corresponding volcanic forms

Two types of volcanism are caused by the magma rise through the mantle and the thick crust (**Tables 1** and **2**; [4]): Intrusive versus Extrusive volcanism (**Table 2**). Volatile content is essential for the behavior of the magma that has shaped the Earth's volcanism and volcanic structures [29]. The subcategories of

Magma			
	Basalt	**Andesite**	**Rhyodacite**
SiO$_2$	<50%	55–60%	>60%
Viscosity	Low	High	High
Volatile content	Low	High	High

Table 1.
Magma composition.

Magma			
Intrusive volcanism		Extrusive volcanism	
Plutonic	Sub-volcanic	Effusive	Explosive

Table 2.
Type of intrusive/effusive volcanism.

these two styles of volcanism are plutonic, sub-volcanic, effusive, and explosive (**Table 2**):

a. *Plutonic intrusive volcanism*: Batholith and Plutons are large intrusive bodies, of granite composition, which originate from partial melting of the crust. They generally have a length of over 2000 km and a maximum width equal to about 1/10 of the length. They are found in areas of the earth's crust where rocks have been folded and dislocated to form mountain ranges (orogenic crust), causing the partial melting process of the deepest crustal part of the folded zone. In practice, they constitute the nucleus of the most impressive mountain ranges, such as the Andes (South America): [Achala Batholith, Argentina, Antioquia Batholith, Colombia, Guanambi Batholith, Bahia, Brazil, Parguaza rapakivi granite Batholith, Venezuela and Colombia, Cerro Aspero Batholith, Argentina, Coastal Batholith of Peru, Colangüil Batholith, Argentina, Cordillera Blanca Batholith, Peru, Vicuña Mackenna Batholith, Chile, Elqui-Limarí Batholith, Chile and Argentina, Futrono-Riñihue Batholith, Chile, Coastal Batholith of central Chile, Panguipulli Batholith, Chile, Patagonian Batholith, Chile and Argentina, North Patagonian Batholith, South Patagonian Batholith] and Europe: The Alps: Adamello Batholith. (**Figure 11A**) (taken from https://en.wikipedia.org/wiki/Batholith). Lopoliths: They are intrusive bodies of smaller dimensions than the batholiths of gabbroic composition and originate from the intratelluric crystallization of basaltic magmas of mantle origin that are localized at the base of the crust (**Figure 11B**).
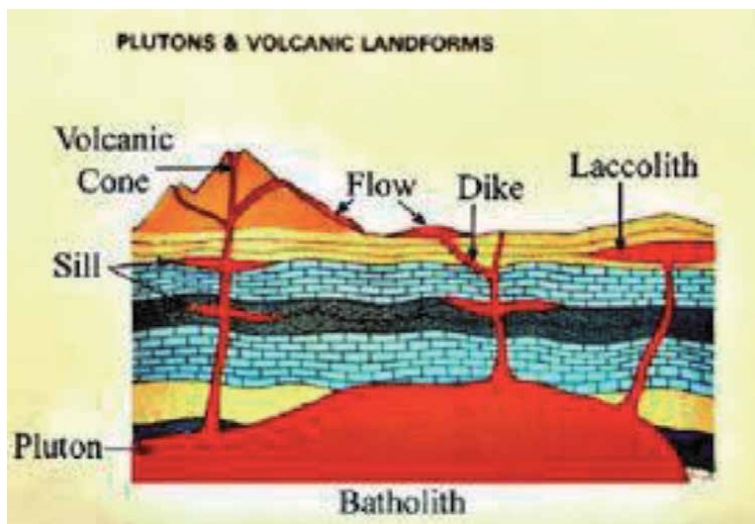
Figure 11.
Scheme of relationship from plutons and Lopolith (author's collections).

b. *Sub-volcanic volcanism*: Dyke Structure: In the upper crust, from the granitic batholithic bodies you can have magmatic ascents that cool down in conduits of various sizes, giving rise to various types of morphologies of sub-volcanic intrusive bodies that take the name of laccoliths, sills, and dikes. **Figure 12** shows a dyke common at the Island of Ponza [30].

c. *Effusive volcanism*: The low viscous basaltic magma due to its low silica and water content escapes from a superficial magma chamber located in the thin oceanic crust and from a deep fracture with a direct ascent from the mantle on the continental crust (**Figure 13**). The great lava effusions form the basaltic plateau in a distention environment, such as oceanic and continental

Figure 12.
Dyke at Ponza Island (Italy) [30].
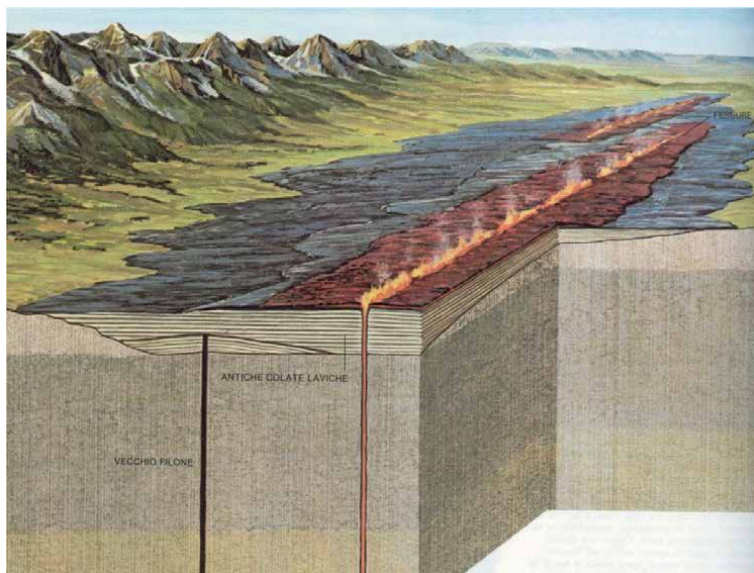
Figure 13.
Lava flow plateau (author's collection).

rifts (**Figure 13**). The most important manifestations of effusive volcanism are lava flows. The mobility of the flow depends on the viscosity of the lava: (1) Basaltic lavas have high temperatures ($\sim$ 1100°C) and less silica (<50%), and therefore, they have a low viscosity. Due to these characteristics, they can flow for tens of kilometers. (2) Andesitic lavas have temperatures of 900–800°C and silica ($\sim$ 57%), and therefore, have a high viscosity, which prevents excessive flow so that the lava tends to break as it flows. (3) The rhyolitic lavas have temperatures of about 700°C and silica >60%. They are so viscous that the lava accumulates at the volcanic mouth giving dome shapes or even spire-like extrusions. The lava flow can be defined in different forms—(1) pahoehoe lava: Characteristic surface form of basaltic lava. It is formed by high temperature and low viscosity. Characteristic form of lava poor in silica (**Figure 14**). (2) AA lava: They are lava morphologies typical of basaltic magmas that give the form of scoria type (**Figure 15**). They are characterized by a lower temperature and a higher viscosity than the basaltic magmas that give the pahoehoe lavas. Flow lava levée: The AA lava and pahoehoe while flowing build levée for fast cooling of the external parts of the flow (**Figure 16**). Lava-tube flow: It can happen that even when the surface of a large basaltic flow has solidified, the inner part continues to flow into a channel below the solid surface of the flow. If the lava flows go out from this channel, an empty space is formed that produces a lava tunnel (**Figure 17**). Block lava flow: A typical form of high viscosity rhyolitic andesitic acid lavas form block lava-like as Paricutin volcano (Mexico) (**Figure 18**). Cooling structures in subareal lava flows: During the final stages of cooling, the inner part of a lava flow contracts in almost hexagonal-shaped columns acquiring a
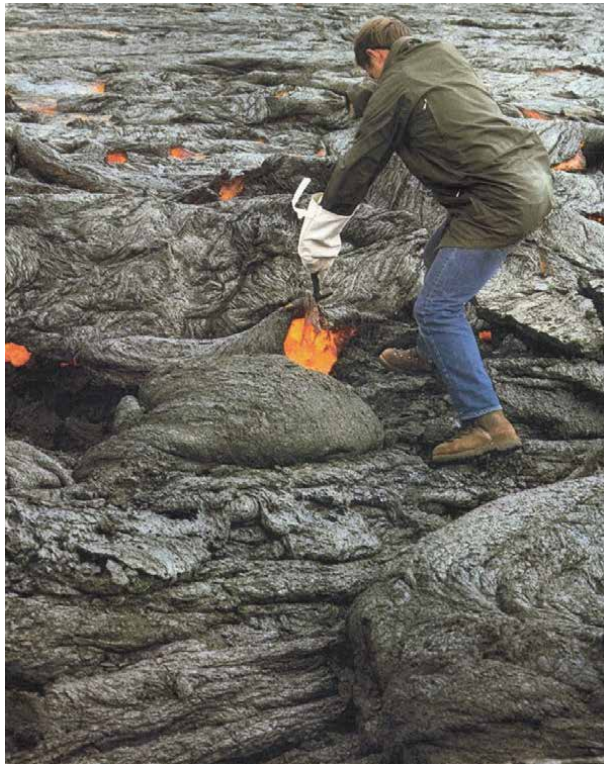
Figure 14.
Pahoehoe lava flow (author's collection).

Figure 15.
Lava flow AA (author's collection). A solidified flow from the last eruption of Vesuvius (1944 AD).

Figure 16.
Lava flow with levee (author's collection). Levee grew during a Hawaiian eruption.

typical columnar crack (**Figure 19**). Submarine lava flows: In underwater basaltic flows, the lava cools much faster, and therefore solidifies and forms a bubble of vitreous lava or cushions that temporarily blocks the advance of the flow. After a while, the internal pressure lava breaks the crust, and a new bubble comes out. The process is repeated several times, forming layers of pillows on top of each other (**Figure 20**).

    d. *Explosive volcanism*: The development of explosive volcanism requires viscous magma with a high content of silica and water. These characteristics are

Figure 17.
Lavatube flow with a growth stalactite melt (unknown volcano).

Figure 18.
Block lava flow. Modified from Schmincke [14].

generally acquired by processes of differentiation of basaltic magmas in the magma chamber or by direct melting of the continental crust by basaltic magmas or by the direct mixing with external water. Headings are from **Table 2**.

Figure 19.
Columnar lava (author's collection).

Figure 20.
Pillow lava formed under the sea (author's collection).

Types of explosive volcanism	
Magmatic volcanism	**Hidromagmatic volcanism**
Volatiles dissolved in magma are those present at the beginning of its formation.	The magma enters in contact with external water and the magma is enriched in water vapor and other volatiles.
In both cases, if products emitted by an explosive plume are affected by a gravitative deposition, falling deposits form. This type of explosive eruption also takes the name of Fall-Out bedded eruptions. In addition, Pyroclastic density currents [31] can also form.	

Table 3.
Types of explosive volcanism.

7. Explosive volcanism

Explosive volcanism can be classified into two types, as shown in **Table 3**. The internal and external eruptive dynamics of the volcano consist of two phases: Phase 1: Exsolution of volatiles from the over-saturated magma, and explosive fragmentation of magma with the conversion of thermal energy in kinetic energy. Phase 2:
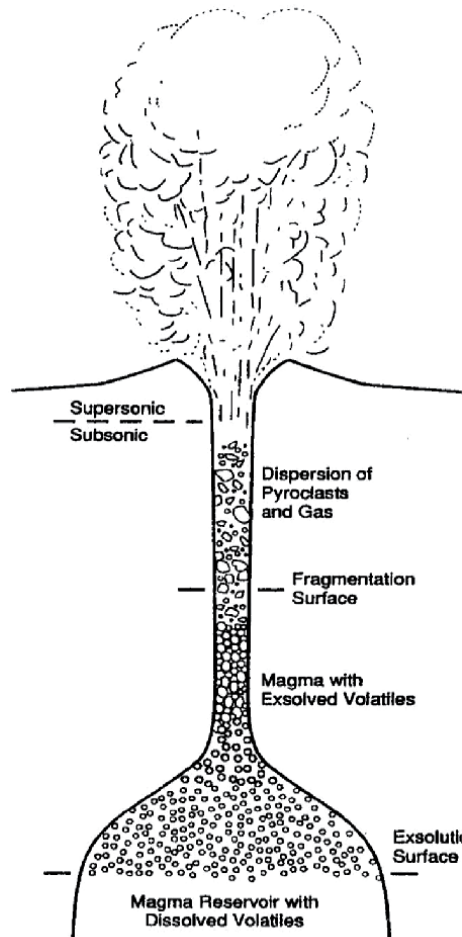
Figure 21.
Draw that show how magma evolves through a pyroclastic material (exsolution and fragmentation). Modified from Cortini and Scandone [25].
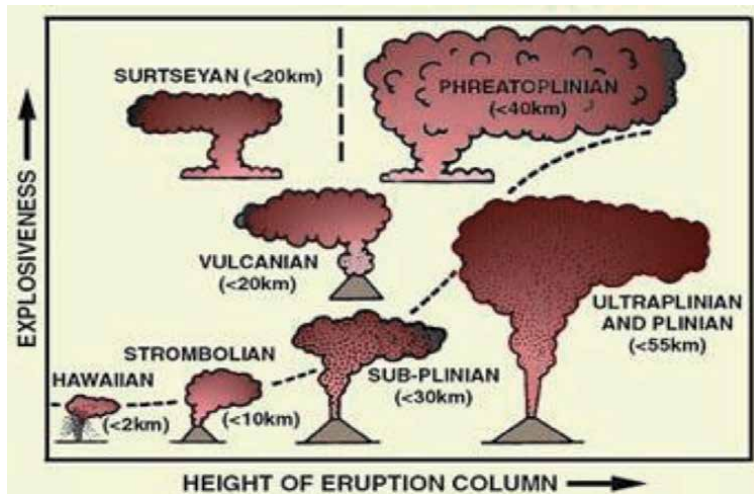
Figure 22.
Diagram of the explosiveness versus the height of the eruptive column. Modified from Cas and Wright [8].

Expulsion of the mixing composed of fragments of solidified magma and gas, and a formation of an eruptive column (**Figure 21**). The two phases are initially connected and determine the explosive style of the eruption. As follow a diagram of the Classification of explosive eruptions with two volcanological parameters (Explosiveness-Height of the pyroclastic column) (**Figure 22**). This diagram explains the differences between various types of volcanic eruptions. Diagram is redrawn after Cas and Wright [8].

8. Magmatic explosive eruptions that produce fall-out bedded deposits caused by Plinian eruption

To explain such deposits, I have schematically subdivided the magmatic explosive eruptions into two phases and sections—how the magma act from inside to outside volcanoes.

Phase 1: The magmatic column rises with a speed of <0.5 m/s.

The volatiles that dissolves form gas bubbles whose upward movement is slow because it is hindered by the viscosity of the magma. The expansion stops when the ratio between gas and magma is about 3:1 causing fragmentation. At the level of fragmentation, the drastic decrease in viscosity causes the sudden increase in speed that passes from subsonic to supersonic (**Figure 23**).

Phase 2: The mixture of gases and particles expelled from the crater forms a Plinian eruptive column in which three zones can be recognized, which are as follows:

a. jet expulsion area with initial acceleration, of height 1–2 km

b. high convective area 25–50 km

c. umbrella area (**Figure 23**)

A typical fall-out bedded deposit is shown in **Figure 24A**. This massive fall-out bedded is a characteristic Plinian deposit of the Somma-Vesuvius volcano. The main
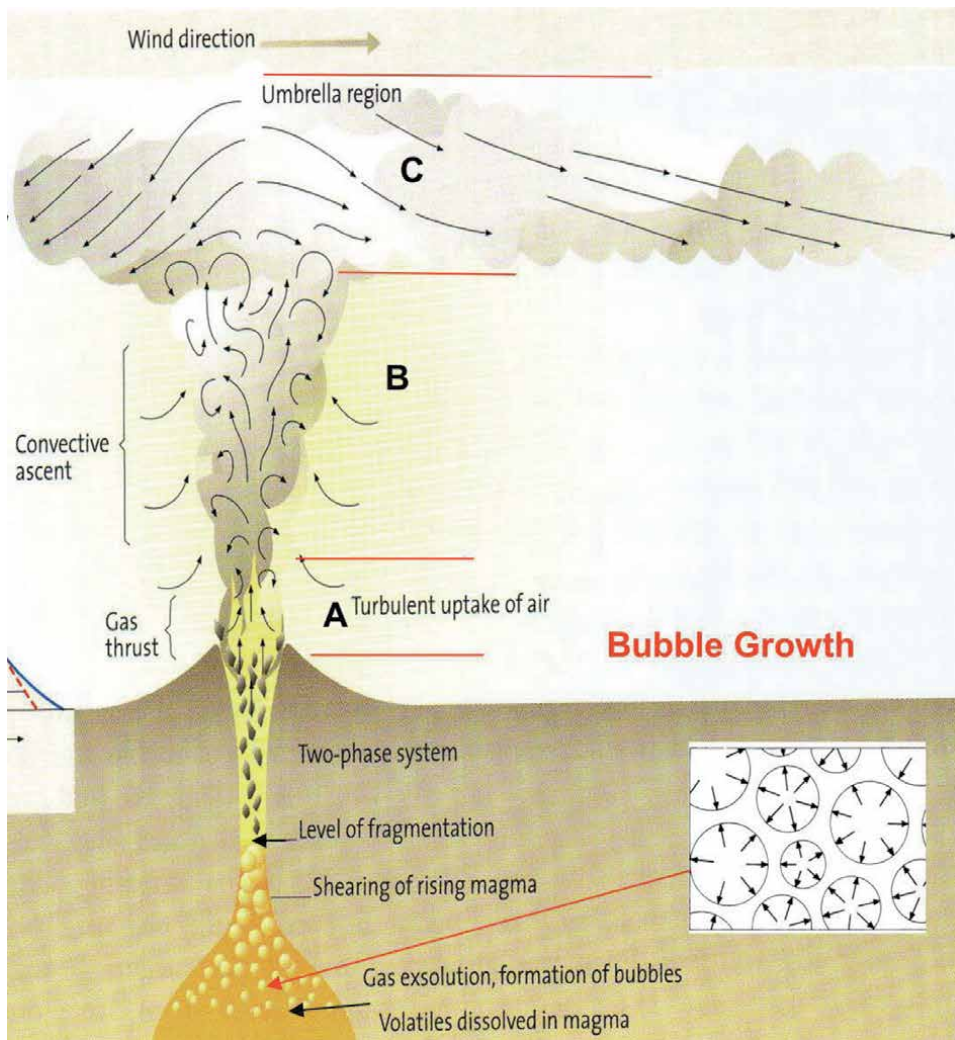
Figure 23.
Eruptive Plinian column from the source up to the surface. Modified from Schmincke [14].

components are pumice, as seen in **Figure 25A** [32]. To compute such deposits is not very easy, the measurements of thickness and pumice size called, respectively, isopach and isopleths can be a difficult task [8]. **Figure 25B** shows a model of isopach calculation seen in three-dimensional space [24]. Each isopach is characteristic on just one thickness that can be followed and extrapolated in the field around a volcano that forms tephra fall-out bedded eruption, many model computations have been published, I just quote some: [33–36]. Generally, Plinian eruptions are characterized by strong volcanic plumes coupled with vertical columns (**Figure 25**), although as shown from **Figure 25** even a strong volcanic plume can have a characteristic bent-over feature like in a weak plume [36].

9. Strombolian eruption

Phase 1: The magmatic column rises at a speed of 0.5–1 m/s. The rising speed of the bubbles is greater than that of the magma so very large bubbles form on the surface. At a depth of about 100 m, the fraction of gaseous bubbles reaches 75%,
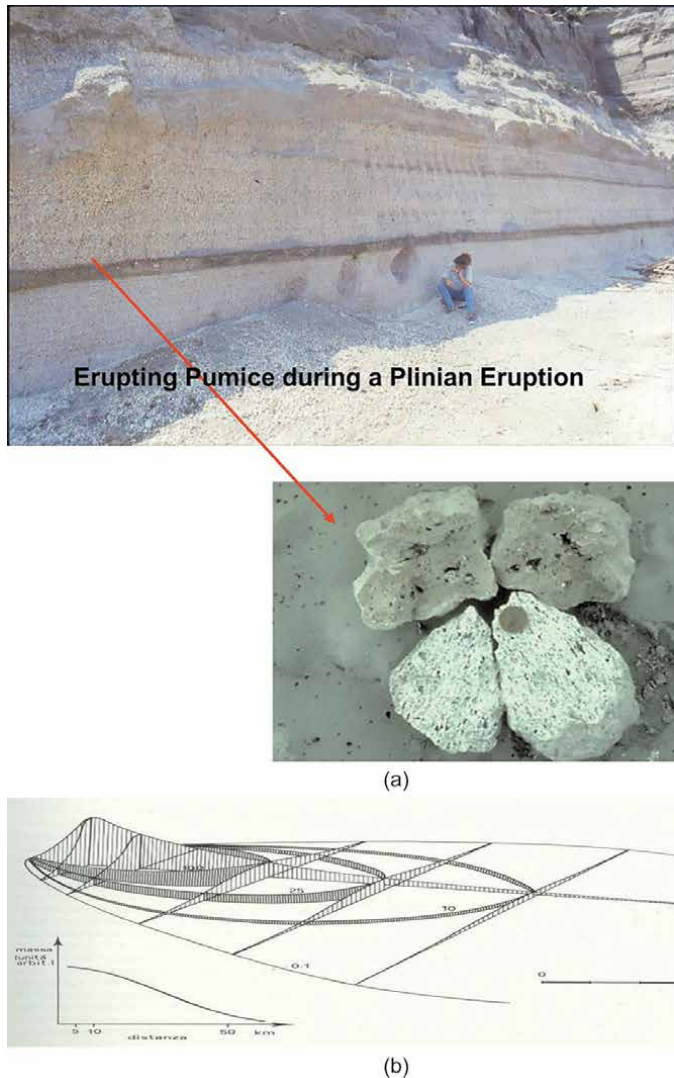
Figure 24.
(a): Fall-out bedded typical with an enlargement of its constituent (pumice) of a Plinian eruption from Somma-Vesuvius volcano (author's collection). (b): A model to visualize the spread of the pyroclastic deposits around a volcano. Modified from Cortini and Scandone [25].

and the magma fragments erupt explosively. The decrease in viscosity produces an increase in speed from subsonic to supersonic (**Figure 26**).

Phase 2: The expulsion of materials occurs through a series of explosions with short time intervals (0.1 sec to 1 h). The exit speed of the mixture of gas and fragmented particles is about 200 m/s.

When the explosions occur in short intervals of time, an eruptive column is formed in which the height of the jet does not exceed 200 m and the convective column reaches heights of 5–10 km (**Figure 26**).

The Strombolian eruption has taken the name from the Stromboli Island part of the Eolian Islands, characterizing such volcanic activity worldwide. The style of the Stromboli eruption has been continuously active in the last 2000 years and it was very important for obsidian trade and as a lighthouse of the Mediterranean Sea. Some examples of Strombolian activity are listed and shown in figures. Eruption column of a Strombolian eruption of Vesuvius, the 1944 AD shown in **Figure 27**.

Figure 25.
Eruptive columns of Plinian eruptions (taken from the web).

Scoria layers deposed during a Strombolian activity of Vesuvius in the medieval period are shown in **Figure 28** [37].

10. Hawaiian eruption

Some eruptions descriptions have been subdivided into phases for the sake of clarity from the inside to outside volcano.

Phase 1: The ascent rate of the bubble-free basaltic magma is >1 m/s. The low viscosity allows the formation of large bubbles that are brought to the surface (**Figure 29**).
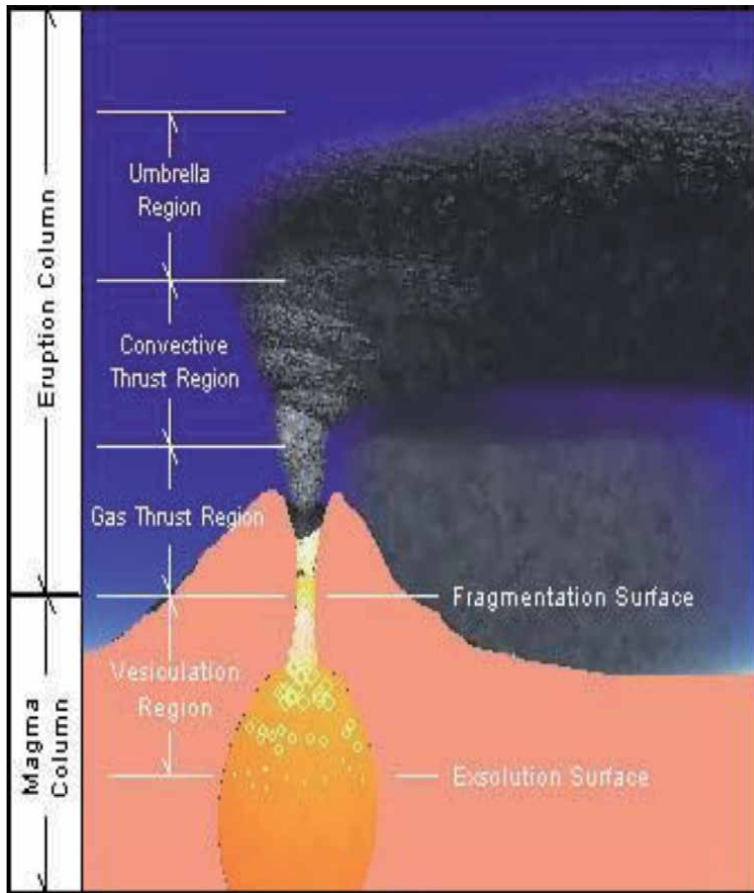
Figure 26.
Strombolian eruption schematically explained (author's collection).

Figure 27.
Paroxysistic phase of the eruption of 1944 AD (author's collection). Photo made from allied force during the second world war.

Phase 2: The expansion of the large bubbles expels fragments of magma outward from the conduit that forms incandescent lava fountains with a speed of 10–20 m/s reaching heights of 200–500 m (**Figure 29**). The lava fountains erupt

Figure 28.
Medieval deposits from a Vesuvius eruption, a sort of Strombolian activity (author's collection).

Figure 29.
Hawaian eruption (taken from the web).

high-temperature scoriae that falling still hot remobilize lava flow without roots (spatter fed lava flow). Lava fountains can also form in craters occupied by a lava lake.

11. Explosive eruptions of the hydromagmatic type that produce fall-out bedded deposits Vulcanian eruption

Vulcanian eruptions are direct explosive eruptions rich in magmatic volatile or any water [38].

Phase 1: The magma rich in volatiles interacts with the groundwater causing rapid vaporization and the relative production of water vapor that increases the explosiveness of the eruption.
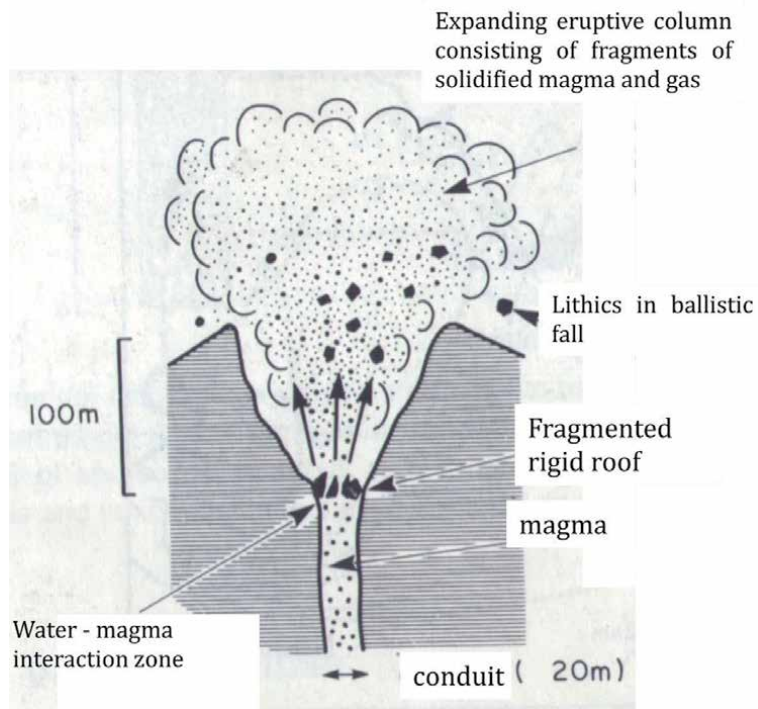
Figure 30.
Volcanian eruption (author's collection).

Figure 31.
Scoria deposit caused by a Volcanian eruptions (modified from Schmincke [14]).

Phase 2: The expulsion of the products is characterized through a number of discrete explosions that follow one another in variable intervals between 10 min and 1 h comparable to cannon shots.

The single explosions produce eruptive columns between 5 and 10 km high (**Figure 30**). A typical example of scoria Vulcanian products is shown in **Figure 31**.
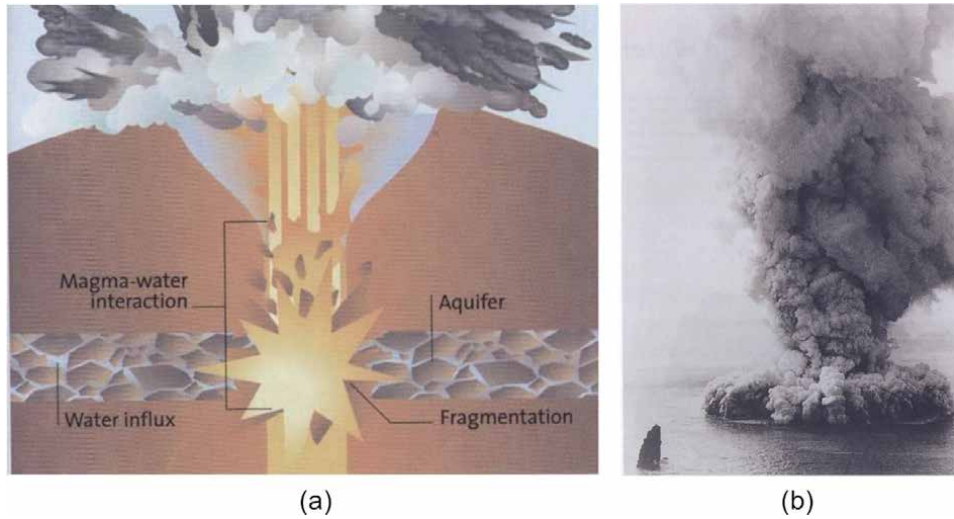
Figure 32.
(a): Phreatoplinian eruption; and (b): Surtseyan eruption (modified from Schmincke [14]).

Figure 33.
Pyroclastic flow (modified from Branney and Kokelaar [31]).

12. Surtseyan and Phreatoplinian eruptions

They are explosive eruptions that produce fall deposits deriving from water-magma interaction processes, but pyroclastic density currents are much more abundant [8] (**Figure 32A** and **B**). As an example, a Surtseyan eruption is an explosive style of a volcanic eruption that takes place in shallow seas or lakes when rapidly rising and fragmenting hot magma interacts explosively with water and with water-steam-tephra. The eruption style is named after an eruption off the southern coast of Iceland in 1963 that caused the emergence of a new volcanic island, Surtsey (**Figure 32B**).
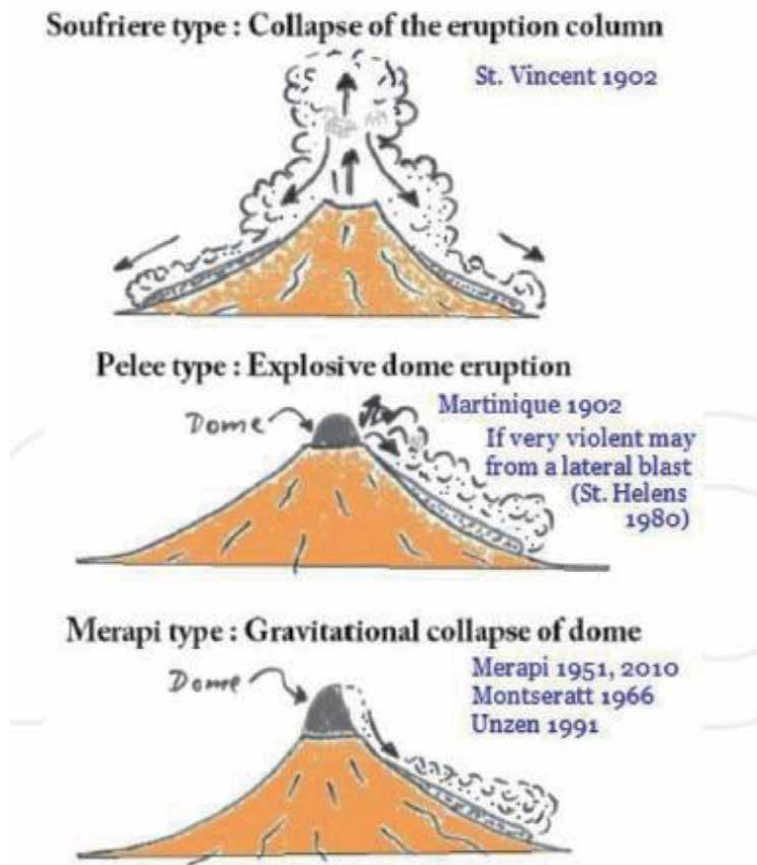
Figure 34.
Origins of pyroclastic density currents. (A): short single-surge current derived by momentary collapse from a Plinian eruption column. (B): sustained current is derived from prolonged pyroclastic fountaining. The height of the jet (gas thrust) that feeds the current may vary and is transitional into (C). (C): A sustained current derived from a prolonged low pyroclastic fountaining explosive eruption. (D): current with a single (or multiple) surges derived from lateral blasts initiated by catastrophic decompression of a magmatic and/or hydrothermal system. (E): single-surge current derived from a collapsing lava dome or flow front. Hot rock avalanches generate turbulent density currents. (F): deposit-derived pyroclastic density current caused by gravitational collapse and avalanching of unstable loose ignimbrite. The current may be a single surge or more sustained where the collapse is retrogressive. Most large-volume ignimbrites derive from current types (B) and (C), which may involve periods of quasi-steady flow. Many may include significant components derived from currents of type (F) from Branney and Kokelaar [31]. For this paper, we chose the following three types: Soufriere, Pelee, and Merapi types (modified from Francis [10]).

13. Explosive eruption form pyroclastic density currents

These eruptions, unlike the previous ones, are characterized by the development of eruptive dynamics with the main component horizontal sliding on the ground. They are divided into—(a) dense pyroclastic currents (pyroclastic flow), (b) diluted pyroclastic currents (base surge).

Both these eruptive types can be found in association with an explosive eruption from fall or develop independently during special types of explosive eruptions. A typical dense pyroclastic current is shown in **Figure 33**. A pyroclastic flow is formed by the collapse of an eruptive column (**Figure 31**). The dense pyroclastic currents can be seen in **Figures 32** and **33**. **Figure 33** also shows the fluidization and turbulence of dense pyroclastic currents. The head of a dense pyroclastic current often is characteristic of an ignimbrite eruption. It can form through a pyroclastic flow formed by the collapse of a volcanic dome (**Figure 34**). Sometimes, it can be easy to find pyroclastic density currents with a massive structure in **Figure 35**.

(a)

(b)
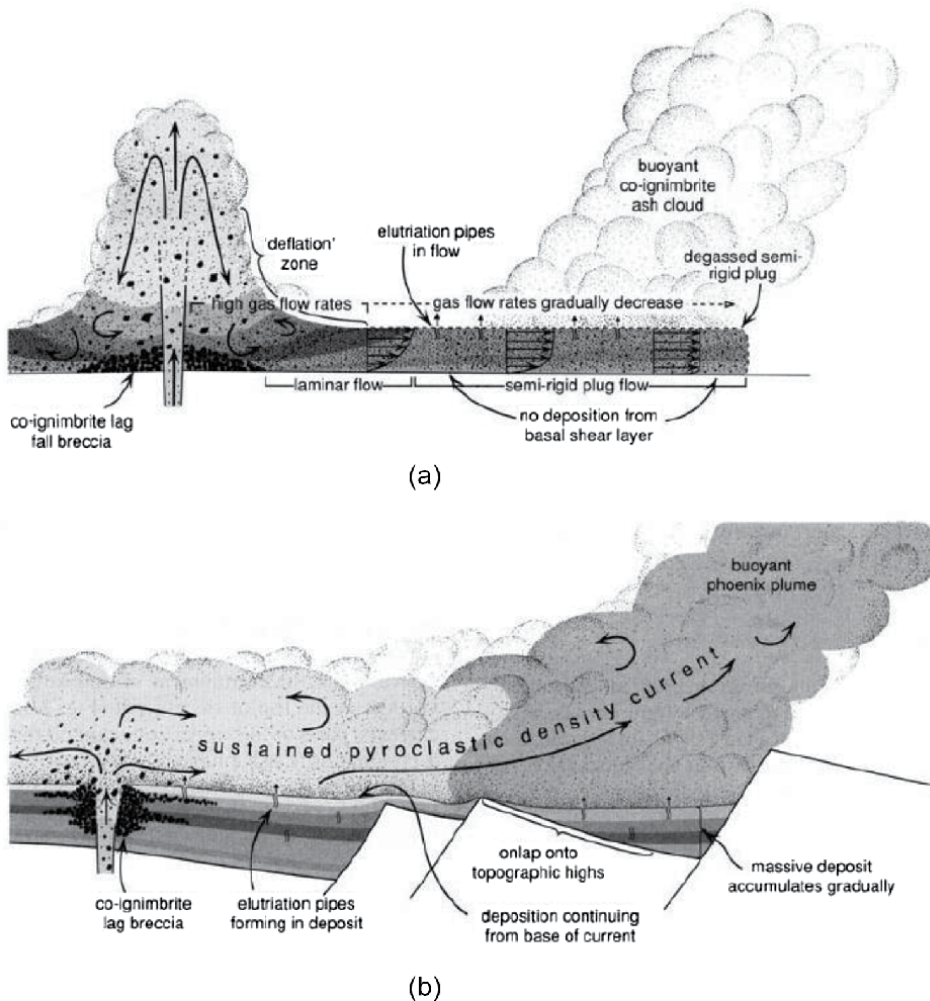
Figure 35.
Shape of typical pyroclastic dense currents. Pyroclastic dense currents with fluidization and turbulence (modified from Branney and Kokelaar [31]).
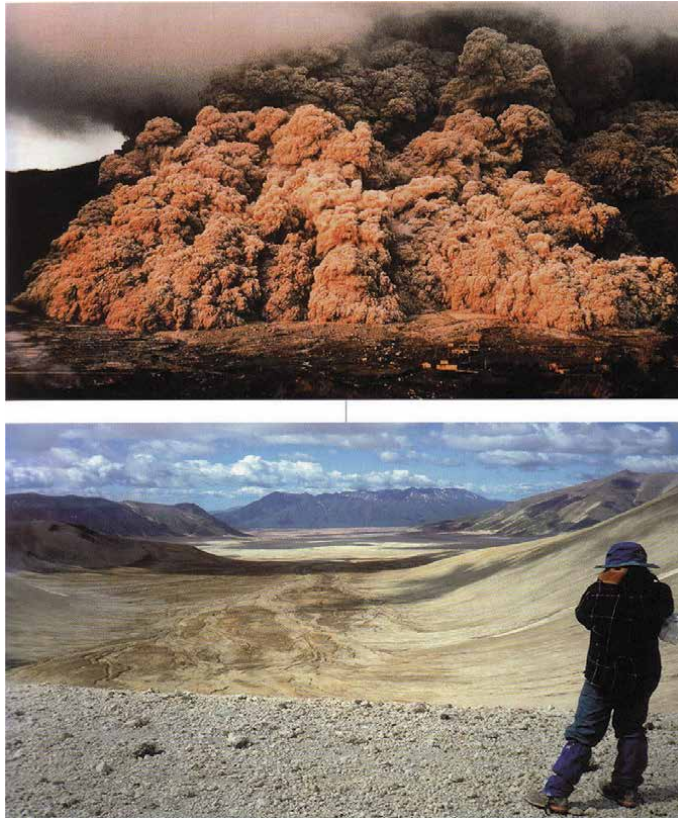
Figure 36.
Head of a pyroclastic dense currents and PDC channeled in a valley. Modified from Schmincke [14].
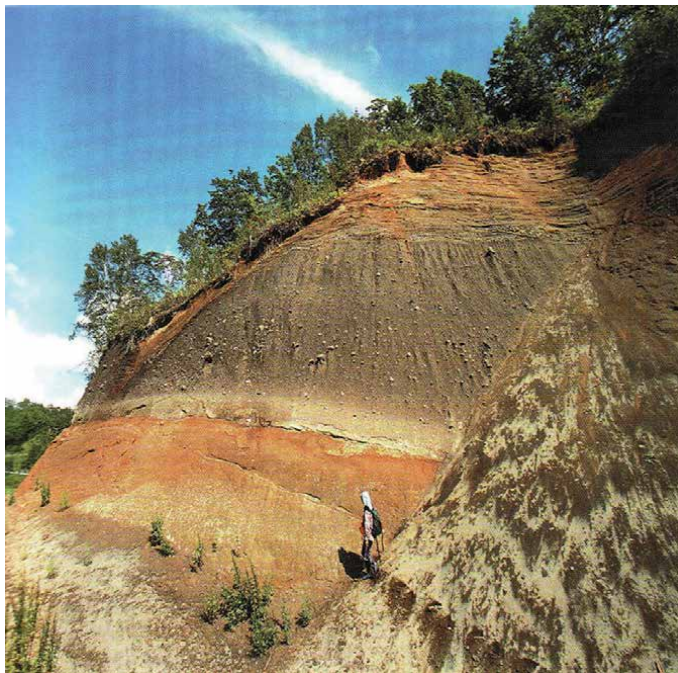
Figure 37.
Pyroclastic flow deposit with massive structure. Modified from Schmincke [14].

14. Diluted pyroclastic currents

Base surge and pyroclastic surge originate from the base of eruptive columns of magmatic and phreatomagmatic eruptions [4, 8–10]. They move radially and are made up of one turbulent cloud of water vapor and ash at high temperatures (**Figures 36** and **37**). For all kinds of volcanic forms, we can look to **Figure 38**
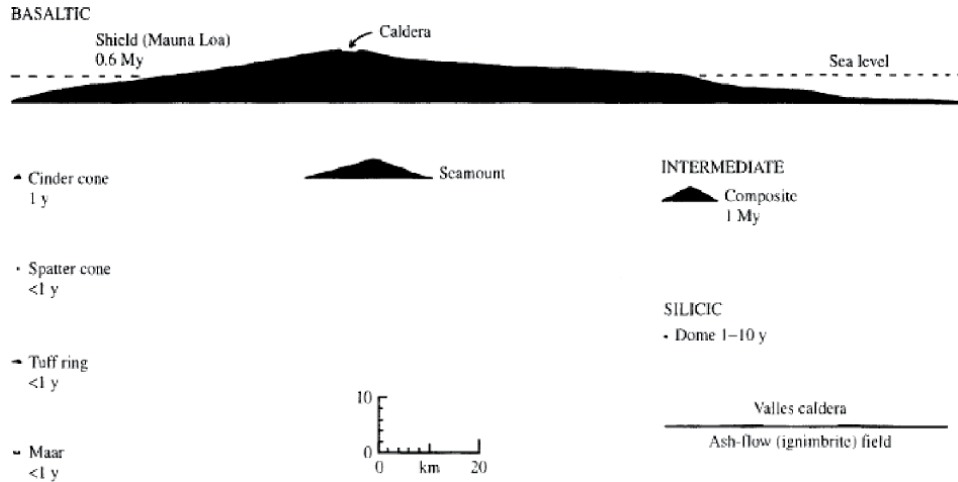
Figure 38.
Morphologies of volcanic structure. Modified from Nemeth and Martin [11].

Figure 39.
Santorini caldera (author's collection).

depending on the size of the eruption and the volume emitted. For large eruptions, often after the volcanic activity, there is a collapse of the roof of the magma chamber that brings to a structure called Caldera. A classic example can be the Santorini Caldera, as shown in **Figure 39**. For a thoughtful explanation of the diverse type of caldera refer to Chris Newhall caldera book [39].

15. Conclusion

This chapter has covered all the basis of Volcanology deepens some aspects where recent information has come out from literature. I believe that young students can understand better the subject and they will be much prepared to face other volcanology research. The work goes very easy to read, and the number of Figures is so high that the aspects much close to the Volcanology theory are easily understood. I have added a rich list of references that will help all the people to deal with them and to improve their knowledge in Volcanology.

Acknowledgements

Author details

Angelo Paone* and Sung-Hyo Yun*
Pusan National University, Busan, South Korea

*Address all correspondence to: angelo.paone1@gmail.com and yunsh@pusan.ac.kr

IntechOpen

References

[1] Nemeth K, Palmer J. Geological mapping of volcanic terrains: Discussion on concepts, facies models, scales, and resolutions from New Zealand perspective. Journal of Volcanology and Geothermal Research. 2019;**385**:27-45. DOI: 10.1016/j.jvolgeores.2018.11.028

[2] Martí J, Groppelli G, da Silveira AB. Volcanic stratigraphy: A review. Journal of Volcanology and Geothermal Research. 2018;**357**:68-91. DOI: 10.1016/j.jvolgeores.2018.04.006

[3] Sparks RSJ, Bursik MI, Carey SN, Gilbert JS, Glaze LS, Sigurdsson H, et al. Volcanic Plume. Hoboken, NJ: John Wiley & Sons Inc; 1997. p. 547

[4] Sigurdsson H, Houghton B, McNutt SR, Rymer H, Stix J. The Encyclopedia of Volcanoes. Second ed. Amsterdam, Netherlands: Elsevier Inc; 2015. p. 1393. DOI: 10.1016/B978-0-12-385938-9.00032-8

[5] Lopes R. The Volcano Adventure Guide. Cambridge: Cambridge University Press; 2005. p. 363. DOI: 10.1017/CBO9780511535567

[6] Loughlin SC, Sparks S, Brown SK, Jenkins SF, Vye-Brown C. Global Volcanic Hazards and Risk. Cambridge: Cambridge University Press; 2015. p. 410. DOI: 10.1017/CBO9781316276273

[7] Parfitt E, Wilson L. Fundamentals of Physical Volcanology. Hoboken, NJ: Blackwell Publishing Ltd; 2008. p. 256. DOI: 10.1007/s00445-010-0352-0

[8] Cas RAF, Wright JV. Volcanic Succession. Alphen aan den Rijn, Netherlands: Kluwer Academic Publishers; 1987. p. 544. DOI: 10.1007/978-94-009-3167-1

[9] Gilbert JS, Sparks RSJ, editors. The Physics of Explosive Volcanic Eruptions. London: Geological Society; 1998. p. 145

[10] Francis P. Volcanoes: A Planetary Perspective. Vol. 249. Walton Street, New York: Oxford University Press; 1993. p. 443

[11] Nemeth K, Martin U. Pratical Volcanology. Hungary: Geological Institute of Hungary (Magyar Állami Földtani Intézet); 2007. p. 220

[12] Wohletz K, Heiken G. Volcanology and Geothermal Energy. Los Alamos Series in Basic and Applied Sciences. California: The Regents of the University of California; 1992. p. 432

[13] Paone A, Yun S-H. Forecasting Volcanic Eruption. Rijeka: IntechOpen; 2020. p. 104

[14] Schmincke H-U. Volcanism. Berlin: Springer; 2005. p. 333

[15] Helffrich GR, Wood BJ. The Earth's mantle. Nature. 2001;**412**:501-507. DOI: 10.1038/35087500

[16] Meibon A, Anderson DL. The statistical upper mantle assemblage. Earth and Planetary Science Letters. 2003;**217**(1–2):123-139. DOI: 10.1016/S0012-821X(03)00573-9

[17] Davies JH, Brodholt JP, Wood BJ. Chemical reservoirs and convection in the Earth's mantle. Philosophical Transactions of the Royal Society. 2002;**360**(1800):2361-2648. DOI: 10.1098/rsta.2002.1086

[18] Bosellini A. Tettonica delle Placche. Bologna, Italy: Zanichelli; 2014. p. 75

[19] Wedepohl KH. The composition of the continental crust. Geochimica et Cosmochimica Acta. 1995;**59**(7):1217-1232. DOI: 10.1016/0016-7037(95)00038-2

[20] Huppert HE, Sparks RSJ. The generation of granitic magmas by intrusion of basalt into continental crust. Journal of Petrology. 1988;**29**:599-624. DOI: 10.1093/PETROLOGY/29.3.599

[21] Annen C, Sparks RSJ. Effects of repetitive emplacement of basaltic intrusions on thermal evolution and melt generation in the deep crust. Earth and Planetary Science Letters. 2002;**203**:937-955. DOI: 10.1016/S0012-821X(02)00929-9

[22] Annen C, Blundy JD, Sparks RSJ. The genesis of intermediate and silicic magmas in deep crustal hot zones. Journal of Petrology. 2006;**47**:505-539. DOI: 10.1093/petrology/egi084

[23] Miles AJ, Graham CM, Hawkesworth CJ, Gillespie MR, Hinton RW. Evidence for distinct stages of magma history recorded by the compositions of accessory apatite and zircon. Contributions to Mineralogy and Petrology. 2013;**166**:1-19. DOI: 10.1007/s00410-013-0862-9

[24] Taylor SR, Mclennan SM. The Continental Crust: Its Composition and Evolution. Great Britain: Blackwell Scientific Publications; 1985

[25] Cortini M, Scandone R. Introduzione alla Vulcanologia. Napoli: Liguori Editore; 1994. p. 216

[26] Scandone R, Giacomelli L. Vulcanologia. Principi Fisici e Metodi d'Indagine. Napoli: Liguori Editore; 1998. p. 642

[27] Rollinson H. Using Geochemical Data: Evaluation, Presentation, Interpretation. (Longman Geochemistry Series). England: Longman Scientific & Technical Longman Group UK Limited Longman House, Burnt Mill, Harlow Essex. 1993. p. 261. DOI: 10.4324/9781315845548

[28] Rollinson H, Paese V. Using Geochemical Data, Understanding Geological Processes. Cambridge: Cambridge University Press; 2021. p. 358. DOI: 10.1017/9781108777834

[29] Carroll MR, Holloway JR. Volatile in Magmas. Review in Mineralogy. 1994;**30**:517

[30] Paone A. Petrogenesis of trachyte and rhyolite magmas on Ponza Island (Italy) and its relationship to the Campanian magmatism. Journal of Volcanology and Geothermal Research. 2013;**267**:15-29. DOI: 10.1016/j.jvolgeores.2013.09.008

[31] Branney MJ, Kokelaar P. Pyroclastic density currents and the sedimentation of ignimbrites. Geological Society, London, Memoirs. 2002;**27**:152. DOI: 10.1144/GSL.MEM.2003.027

[32] Whitham AG, Sparks RSJ. Pumice. Bulletin of Volcanology. 1986;**48**:209-223. DOI: 10.1007/BF01087675

[33] Pyle DM. The thickness, volume and grainsize of tephra fall deposits. Bulletin of Volcanology. 1989;**51**:1-15. DOI: 10.1007/BF01086757

[34] Fierstein J, Nathenson M. Another look at the calculation of fallout tephra volumes. Bulletin of Volcanology. 1992;**54**:156-167. DOI: 10.1007/BF00278005

[35] Bonadonna C, Houghton BF. Total grain-size distribution and volume of tephra-fall deposits. Bulletin of Volcanology. 2005;**67**:441-456. DOI: 10.1007/s00445-004-0386-2

[36] Bonadonna C, Phillips JC, Houghton BF. Modeling tephra sedimentation from a Ruapehu weak plume eruption. Journal of Geophysical Research. 2005;**110**:B08209. DOI: 10.1029/2004JB003515

[37] Rolandi G, Petrosino P, McGeehin J. The interplinian activity at Somma-

Vesuvius in the last 3500 years. Journal of Volcanology and Geothermal Research. 1998;**82**:19-52. DOI: 10.1016/S0377-0273(97)00056-5

[38] Nemeth K, Kosik K. Review of explosive Hydrovolcanism. Geosciences. 2020;**10**(44):27. DOI: 10.3390/geosciences10020044

[39] Newhall CG, Dzurisin D. Historical Unrest at Large Calderas of the World. Vol. 2. Washington, DC: USGS. USGS professional paper (200) E no.1855; 1988. p. 1108

Section 2

Applied Volcanology

The Geothermal Power Plants of Amiata Volcano, Italy: Impacts on Freshwater Aquifers, Seismicity and Air

Andrea Borgia, Alberto Mazzoldi, Luigi Micheli,
Giovanni Grieco, Massimo Calcara and Carlo Balducci

Abstract

Production of geothermal energy for electricity at Amiata Volcano uses flash-type power plants with cooling towers that evaporate much of the geothermal fluid to the atmosphere to condense the geothermal vapour extracted. Because the flash occurs also within the geothermal reservoir, it causes a significant depressurization within it that, in turns, results in a drop of the water table inside the volcano between 200 and 300 m. The flow rates of natural springs around the volcano have also substantially decreased or ceased since the start of geothermal energy exploitation. Continuous recording of aquifer conditions shows substantial increases in salinity (>20%) and temperature (>2°C) as the water table falls below about 755–750 m asl. In addition to hydrologic impacts, there are also a large numbers of induced earthquakes, among which the M_L 3.9, April 1, 2000 earthquake that generated significant damage in the old villages and rural houses. Relevant impacts on air quality occur when emissions are considered on a per-MW basis. For example, CO_2+CH_4 emissions at Amiata are comparable to those of gas-fired power plants, while the acid-rain potential is about twice that of coal-fired power plants. Also, a significant emission of primary and secondary fine particles is associated with the cooling towers. These particles contain heavy metals and are enriched in sodium, vanadium, zinc, phosphorous, sulphur, tantalum, caesium, thallium, thorium, uranium, and arsenic relative to comparable aerosols collected in Florence and Arezzo. Measurements have shown that mercury emitted at Amiata comprises 42% of the mercury emitted from all Italian industries, while an additional comparable amount is emitted from the other geothermal power plants of Tuscany. We believe that the use of air coolers in place of the evaporative cooling towers, as suggested in 2010 by the local government of Tuscany, could have and can now drastically reduced the environmental impact on freshwater and air. On the opposite side of the coin, air-coolers would increase the amount of reinjection, increasing the risk of induced seismicity. We conclude that the use of deep borehole heat exchangers could perhaps be the only viable solution to the current geothermal energy environmental impacts.

Keywords: geothermal energy, environmental impact, aquifer pollution, induced seismicity, air-quality deterioration

1. Introduction

Geothermal energy is the energy stored as heat within the upper crust of the Earth. Due to magmatism and hydrothermal circulation, rocks at high temperatures, in the 150–350°C range, can be found in specific areas at reasonably shallow depths. Because rocks are poor heat conductors, geothermal heat energy is most commonly extracted by circulating fluids in the pores and fractures of the hot rock using water injection and production (withdrawal) wells.

Geothermal energy is commonly perceived as environmentally friendly in Italy [1–3]. However, at Amiata Volcano in Southern Tuscany (**Figure 1**), geothermal energy exploitation has quantifiable and substantial local and more widespread environmental impacts, which suggest that this form of energy production needs substantial technical improvements before it may be considered eco-friendly.

At Amiata, there are six flash-type 20-MWe power-plants units, three for each of the two geothermal fields of Bagnore and Piancastagnaio (**Figure 1**). Briefly, the produced geothermal vapour (**Figure 2**) is used to spin a turbine to produce electricity. Immediately after, the vapour is condensed within a shower of cold geothermal fluid, and separated into two streams, a liquid brine condensate and a non-condensable gas, that are treated as follow:

1. The liquid brine is sent to the cooling tower where it is sprayed from the top, while 9-m-diameter fans pump air upward from the bottom of the towers (counter-current) thereby evaporating one-half to three-quarters of the geothermal fluid which is exhausted to the atmosphere (cf. [7], p. 2). The remaining cooled geothermal fluid, collected at the bottom of the tower is sent back to the condenser to condense again the vapour and complete the cycle; the excess geothermal fluid is sent to reinjection in the reservoir. The fluid balance in the reservoir is maintained through fresh-water recharge from the superficial freshwater aquifers (cf. [8]).

2. The non-condensable gases are passed through the Abatement of Mercury and Hydrogen Sulphide (AMIS) system to reduce the amount of these two pollutants; the H_2S is mixed with air and via catalytic oxidation is transformed into SO_2, which, in turn, is dissolved into the geothermal fluid and sent to the condenser; the remaining gas stream is sent to the cooling towers to be exhausted to the atmosphere.

Because the geothermal fluid contains also a significant amount of ammonia, to mitigate the emissions, sulphuric acid is added to the geothermal fluids, if the SO_2 produced by the AMIS is insufficient, to convert ammonia into ammonium-sulphate salts. In the case that residual SO_2 is present, soda (Na_2CO_3) is added to the liquid stream. In short, the gaseous pollutants are converted to salts that are solubilised in the liquid stream and for the most part, reinjected into the reservoir. However, because of the substantial evaporation occurring in the cooling towers, an unknown fraction of the geothermal fluid droplets evaporate completely leaving fine particles that, with the fine particles contained in the non-condensable gas-stream [9], are emitted as aerosols to the atmosphere with the air-vapour flow. In addition, the majority of the non-condensable gases and smallest size-fraction of droplets of geothermal fluid are emitted to the atmosphere carried by the upward airflow.

In this paper, we present data and explanation to show how, because of this specific type of geothermal energy exploitation, some significant impacts occur at Amiata as follows: (I) decline in the water table of the volcanic freshwater aquifer
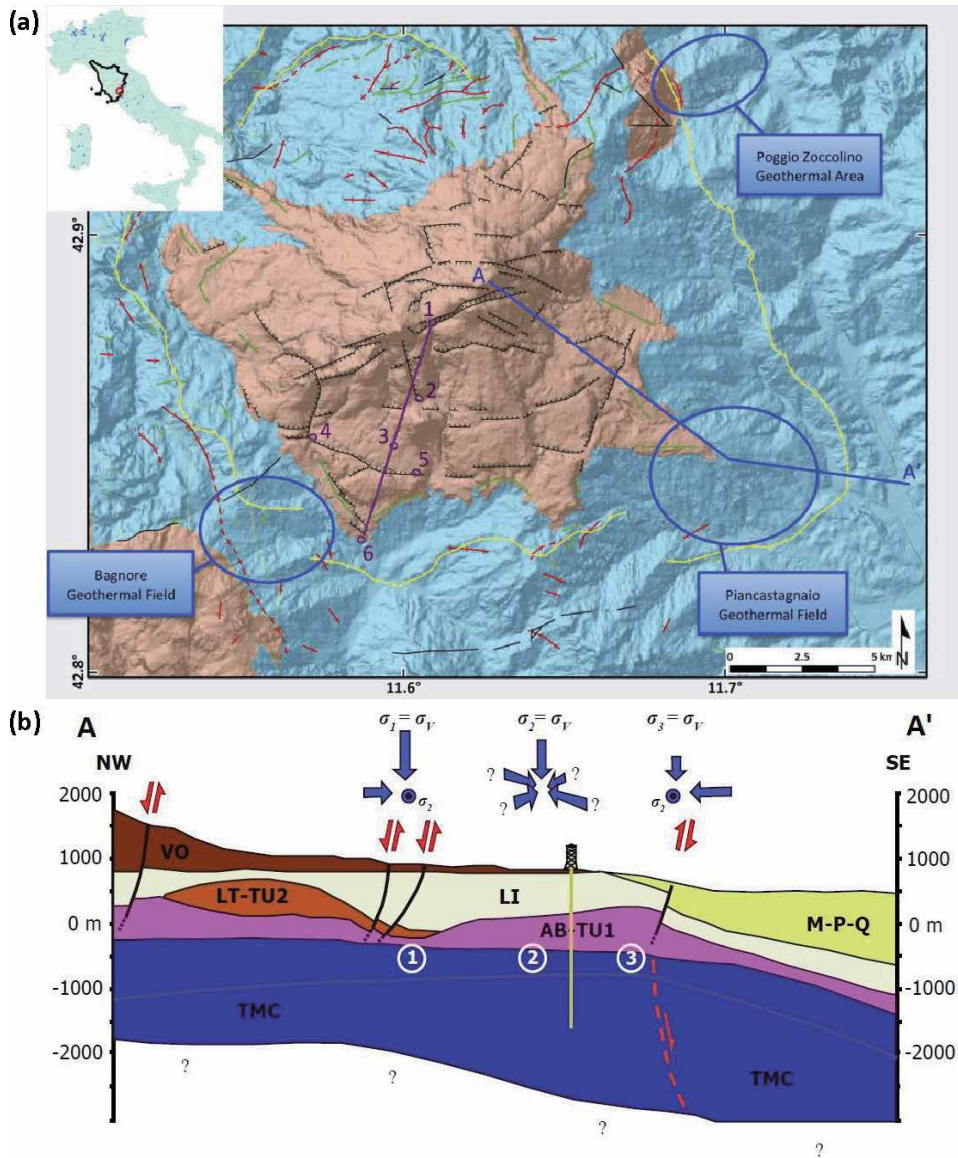
Figure 1.
*(a) Structure of the Amiata volcano area, after Borgia et al. [4]; the three geothermal areas are circled in blue; brown areas = permeable rocks, blue areas = impermeable rocks; black lines = normal faults, yellow lines = basal compressive structures, red lines = anticlines, green lines = synclines. The blue line is the cross-section of (b). Purple line is cross section of **Figure 8**; numbers are piezometers: 1 = Enel inferno, 2 = Lazzaretti, 3 = Enel4, 4 = Enel Castagno, 5 = Enel Valle, 6 = Galleria Nova drainage tunnel. Inset is the location of Amiata volcano in Tuscany (black line), Italy. (b) Cross-section through Amiata volcano and the Piancastagnaio geothermal field (after [4]); section trace is in (a). Note the doming structures of the anhydrites (AB-TU-1) that constitute the superficial geothermal field; TMC is the Tuscan metamorphic complex, VO are volcanic rocks, LT-TU2 are Tuscan units, LI is Ligurian units, M-P-Q are Miocene–Pliocene-Quaternary marine sediments. Numbers 1, 2, and 3 are the locations of local stress fields (indicated on top of the figure) consistent with volcanic spreading, which allow for activation of normal, strike-slip and thrust [5] faults, respectively.*

because of geothermal fluid production and depressurization, (II) increase in induced seismicity mainly because of fluid reinjection, and (III) decrease of air quality because of the atmospheric emissions of gases and aerosols. Other environmental impacts may arise because of overall geothermal-field depressurization, such as subsidence and soil gas emissions, but are not discussed here.
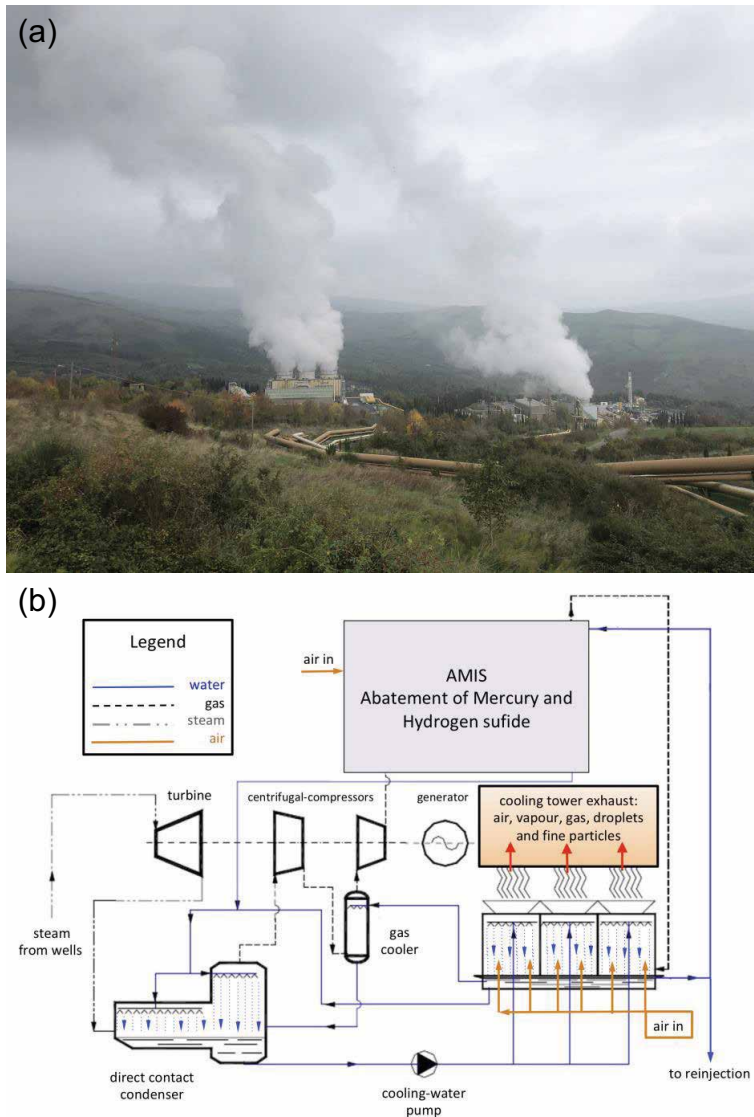
Figure 2.
(a) The PC5 (left-hand side of the photo) and PC4 (right-hand side of the photo) power plants at the Piancastagnaio geothermal field. Note the plumes emitted from the cooling towers and the steam pipes in the foreground. (b) Schematic of a flash geothermal power plant such as those at Amiata volcano (modified from [6]); the cooling towers are composed of three cells exhausting air with vapour, gases, droplets of water and fine particles to the atmosphere. See text for further explanation.

2. Geology

The geology of the Amiata Volcano and the surrounding areas was originally studied by Calamai et al. [8], Ferrari et al. [10], Brogi [11] and references therein. Borgia et al. [4, 12] presented a volcanic spreading model for the volcano-tectonic evolution of Amiata (**Figure 1**), expanding on the idea originally suggested by Ferrari et al. [10] and Garzonio [13], and that relates the deep-seated gravity deformation of the volcanic edifice with the formation of the geothermal fields. More recently, Principe and Vezzoli [14], prefer a three-phases volcano-tectonic-collapse model for the origin of the numerous faults that cut the volcanic edifice of

Amiata, a model originally proposed by Mazzuoli and Pratesi [15] and later by Calamai et al. [8]; these authors, however, fail to recognise the numerous compressive structures and anhydrite and shaley diapirs that are found around the base of the volcano [8, 16–19] and that tectonically balance the collapse and spreading of the volcanic edifice [4]. They also fail to recognise the faulting and grabens in the basement below the volcano [8] that do not correspond to their collapse structures within the volcano but are in good agreement with the volcanic spreading model. Active compressive tectonics away of the eastern base of Amiata Volcano are also shown by recent thrust and strike-slip focal mechanism solutions [20].

Aside from the details of the different interpretations of the volcanotectonic evolution of Amiata, there is a general agreement that a relatively large number of recent and active, normal faults cut the volcanic edifice and its basement at least down to the anhydrites at the base of the Tuscan Formation (in the case of the volcanic spreading model [4]), or to deeper levels above the plutons (in the case of the volcano-tectonic collapse model [14]), or even deeper into the crust (in the case of the regional tectonic model [11]). These faults and the volcanic conduits, in addition to the sandstones of the Ligurian Formations and limestones of the Tuscan Formations, constitute the permeable pathways that connect the shallow freshwater aquifer contained in the volcanic rocks with the regional-scale hydrothermal aquifer [4, 8, 12, 21–23]. This freshwater aquifer is often referred to as the superficial aquifer.

3. Impact on Amiata volcano freshwater aquifer

The Amiata Volcano freshwater aquifer—the name derives probably from Latin "ad meata", which means "at the springs"—is one of the most important sources of potable water in southern Tuscany and Latium serving about 700 thousand people, particularly during the summers, in the provinces of Grosseto, Siena, Arezzo and Viterbo. The richness of this resource is due not only to the freshness and abundance of the water (with productions on the order of 1 m^3/s) but also to the fact that it is located at a relatively high altitude (most springs are between 600 and 900 m asl) in such a way that the aqueducts from Amiata can deliver water to the surrounding country by gravity without the need of pumping.

The first comprehensive study of this aquifer about the development of geothermal power plants is the one by Calamai et al. [8] (**Figure 3a**). In this study, they used all available data from before geothermal exploitation, including an electrical resistivity survey, calibrated with deep boreholes, that had up to 10-km-long survey lines to define the water table in addition to the top of the shaley and sandstone basement (the so-called "impermeable" layer below the volcanic rocks), and the top of the carbonatic rocks (Tuscan Formation) where the geothermal fields are located. It is seen that the water table rises from the lower elevations toward the top of the volcano reaching 1200 m above sea level where at least one spring was known to exist. The maximum gradients of the water table are relatively high at around 10%.

Numerical models of the Amiata Volcano freshwater aquifer have been developed by Delcroix et al. [25] and Caparrini et al. [26]. They find that for adequate permeability of the volcanic rocks and recharge, the water table indicated by Calamai et al. [8] is appropriate.

After the first years of exploitation of the geothermal fields (the first wells were drilled in 1959), the pressure of the geothermal fields was reduced by about 15 bar [21] (**Figure 4**). Around the same time, many fresh-water cold springs had substantially decreased their flow rate or had dried out, without any comparable decrease in rainfall (**Table 1**) [27]. During the same period, several water-drainage
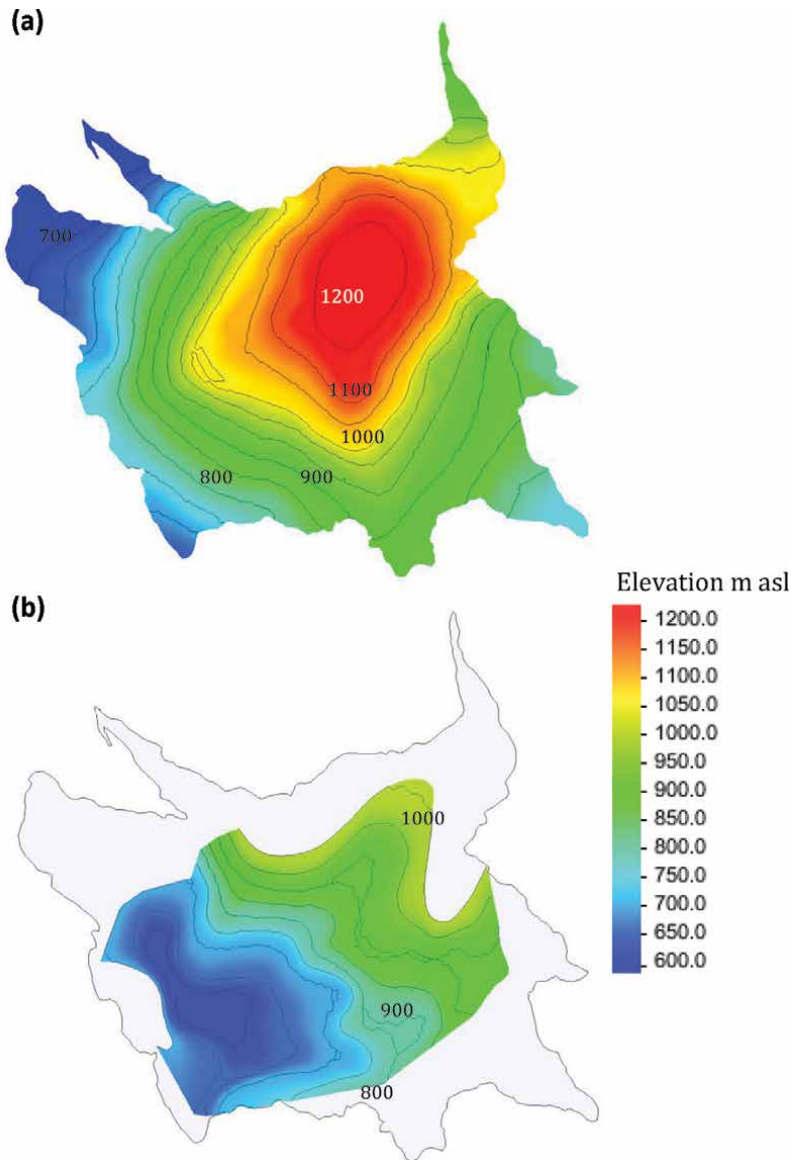
Figure 3.
Piezometric surface of the Amiata volcano freshwater aquifer (a) before geothermal exploitation started in 1959 (redrawn from [8]), and (b) after the beginning of geothermal exploitation (redrawn from [24]). The grey-coloured extent of the drawing is the outcrop of volcanic rocks as in (a). The decrease in elevation of the volcanic water table after the beginning of geothermal exploitation is evident and in the range of 100–300 m. note also in (b) the minimum in the water table that indicates how the water from the superficial aquifer is drained down to the rocks below the volcano, where the hydrothermal system is located.

tunnels had to be constructed to increase the amount of water put into the aqueducts to deliver to the water users. The flow rate of at least one of these drainage tunnels ("Galleria Nova") at the beginning of geothermal production showed an inverse relation with the production of geothermal fluids (**Figure 5**). Namely, as the flow rate of geothermal fluid produced increases, the flow rate of the spring decreases and vice versa.

To study the water table among other things, ENEL carried out an electric resistivity survey [24] to detect changes in the phreatic surfaces of the superficial
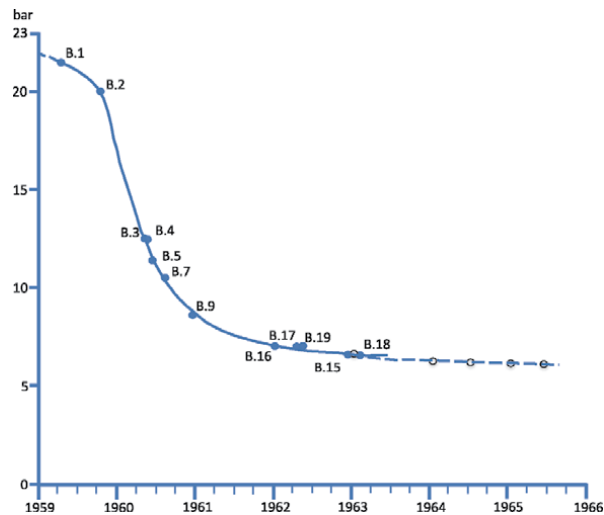
Figure 4.
Decrease in the shut-in pressure of the geothermal wells in the reservoirs after the first years of geothermal exploitation (redrawn from [21]). Note that the initial pressure of the wells changes from about 22 bar in 1959 to about 7 bar in 1964. B.# (closed blue dots) are the names of the various wells first drilled at Bagnore. Open dots are non-producing wells.

Spring ↓ Date →	1940	1950–1951	1960–1964	1970–1972	2001–2002
Acqua d'Alto or Ente	118.00	89.10	97.06	68.00	49.10
Acqua Bona	7.50	7.30	6.00	0.00	0.00
Fontine	13.00	13.00	13.00	1.50	0.00
Vena	31.80	29.30	13.50	6.00	4.00
Total	170.30	138.70	129.56	75.50	53.10

Table 1.
Flow rates in l/s of major springs SW of Amiata volcano that decreased their flowrate or dried out after the beginning of geothermal exploitation (after [27]).

aquifer. This survey (**Figure 3b**) shows a very different water table from the original one (**Figure 3a**) and effectively indicates that the superficial freshwater aquifer was drained through the main faults and the eruptive chimneys that connect the volcano to the geothermal system. It also shows a major minimum in the water table, which the same authors indicate as a potential drainage at depth [24]. This minimum in the water table was later measured also with an electric resistivity survey by the Province of Grosseto [29] and its time-evolution was monitored from August 2003 to April 2006 twice a year using magnetotelluric measurements by the Tuscan Region [30] showing oscillations in the phreatic surface that varied between 700 and 600 m asl.

Delcroix et al. [25] find that fluid production from the geothermal field above 0.5 m³/s can create critical conditions in the superficial freshwater aquifer because many areas of the aquifer could dry out. Also, Caparrini et al. [26] notice a direct correlation between the level of the monitored water table and the pressure below the superficial volcanic aquifer, that is the pressure of the geothermal field.

Additional evidence of the impact of geothermal exploitation on springs comes from the observations of the flow rates at the "Poggetto" hot spring (**Figure 6a**),
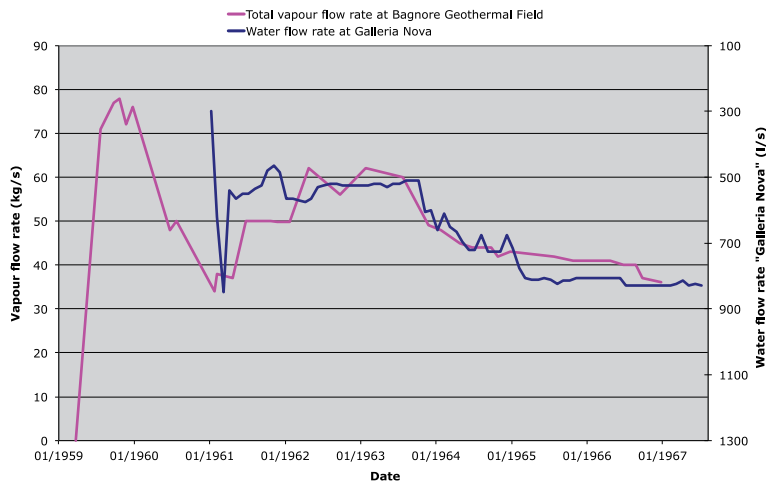
Figure 5.
Correlation between vapour extraction at Bagnore geothermal field (pink line, left-hand side scale increasing upward) and water flow rate at the "galleria Nova" (dark-blue line, right-hand side scale increasing downward). The minimum water flow rate at the "galleria Nova" during the years 1962–1964 corresponds to a maximum in vapour extraction from the geothermal field in the same period. Conversely, as the vapour extraction decreased in the following years, the water flow rate at "galleria Nova" increased again (vapour production from [28]; galleria Nova flowrate data are from a personal communication from Regione Toscana to a. Borgia).

located about 5 km from the geothermal fields northeast of Amiata Volcano (Poggio Zoccolino geothermal area, **Figure 1a**). The flow rate of this spring increased when the Piancastagnaio geothermal field was closed, and decreased again when the geothermal field was reopened. Similarly, the spring flow rate increased when the Bagnore geothermal field was closed and it dropped to zero when the geothermal field reopened with power production tripled. A parallel change in flow rate can be also observed in the flow rate of the "Galleria Nova" drainage tunnel (**Figure 6b**). Similar changes are also observed in the various piezometers.

To monitor the time evolution of the minimum in the water table, the local government and ENEL installed within the volcanic edifice a set of piezometers that continuously measure the water table, in addition to groundwater salinity, conductivity and temperature. Five of these piezometers are indicated in **Figure 1a**, which form the highest to the lowest elevations are: "Enel Inferno", "Lazzaretti", "Enel4", "Enel La Valle", "Enel Castagno". In addition, the draining tunnel of "Galleria Nova" constitutes the lower point of emergence of the water table. **Figure 7** shows the elevations of the water table for these piezometers in December 2018 projected along the purple line in **Figure 1a**. Two observations may be made:

1. From the original (before geothermal exploitation) elevation, the water table has dropped about 200–250 m in the two piezometers found at the higher elevations. Mineral precipitates (mainly goethite) in the fractures of the lavas of the cores of the "Lazzaretti" piezometer are found at about 200 m above today's water table (direct observations by the authors; cf. also [31, 32]). Because these precipitates can form only below the water table, this finding confirms that, since their precipitation, the water table has dropped by a similar elevation. Also, today's water table elevation at the "Lazzaretti" piezometer is about 50–100 m higher than the elevation measured by Compagnia Mediterranea Prospezioni [24], Marocchesi [29], and Manzella [30].
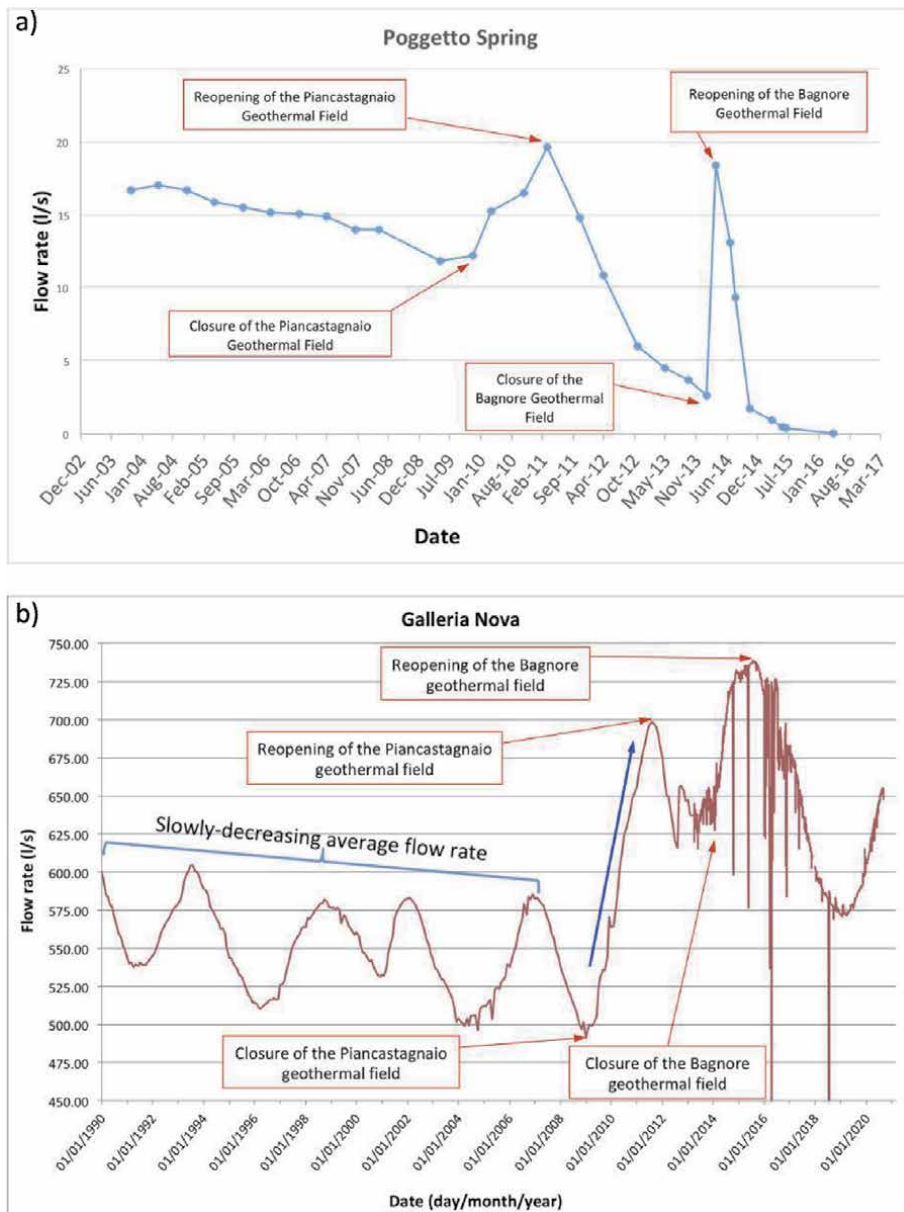
Figure 6.
*(a) Flowrate versus time of the spring "Poggetto" between 2003 and 2016. The spring flow rate varies inversely with geothermal fluids production of the Mt. Amiata fields. Data courtesy of Ing. Pagano. (b) Flow rate versus time of the galleria Nova drainage tunnel from 1990 to 2020. From 1990 to 2009, the flow rate has clear cycles with a 3–4 year periodicity. The anomalous 30% increase in flow rate that begins in the summer of 2010 (blue arrow) was just before the installation of the first piezometer (**Figure 1a**) and corresponded to the closure of the Piancastagnaio geothermal field. Also, the closure of the Bagnore geothermal field corresponds to a significant increase in flow rate, while the reopening of the fields matches decreases in flow rate. Data from Regione Toscana—Centro Funzionale Monitoraggio Idrologico-Idraulico.*

2. The water table has a strong inflexion in the gradient with the water table sloping toward the interior of the volcano—as determined from the piezometers Enel Castagno/Enel Valle toward Enel 4—.

These observations should be analysed in light of the following simplified conservation laws:
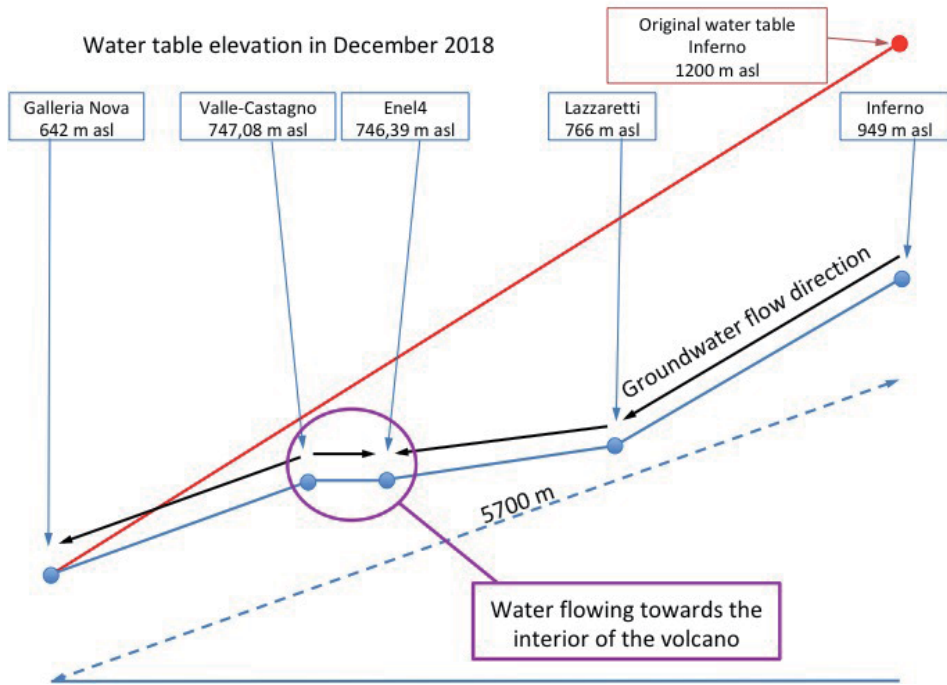
Figure 7.
Sketch of water table levels measured in December 2018. Red line is the approximate original water table from ***Figure 3a.*** *The elevation of the water table inferred by projected piezometer data from "ENEL Valle" and "ENEL Castagno" is the linear interpolation between their two elevations. Note: (1) the reduction in the water table and (2) the flow of water that is from the Valle-Castagno piezometers (located at lower topographic elevations) toward the ENEL4 piezometer (located at a higher topographic elevation) shows an inversion in the original direction of water flow in the aquifer. Data from Regione Toscana—Centro Funzionale Monitoraggio Idrologico-Idraulico.*

$$\frac{\partial v_x}{\partial x} + \frac{\partial v_z}{\partial z} = 0 \quad \text{2D−mass conservation,} \tag{1}$$

$$v_x = -\frac{k}{\mu}\frac{\partial p}{\partial x} \quad \text{x−momentum conservation,} \tag{2a}$$

or

$$v_x = -K\frac{\partial H}{\partial x}, \tag{2b}$$

where

$$K = \frac{k\rho g}{\mu} \tag{2c}$$

and v_x and v_z are the groundwater Darcy's velocities in the x and z directions respectively, k is the rock permeability, m and r are respectively the water viscosity and density, K is the hydraulic conductivity, $\frac{\partial p}{\partial x}$ and $\frac{\partial H}{\partial x}$ are respectively the pressure and head gradients in the x direction, and g is the acceleration of gravity.

Mass conservation (Eq. (1)) states that if the flow velocity changes in one direction, there must be an opposite change in the other direction. Momentum

conservation (Eq. (2); Darcy's law) states that the flow is in the negative direction of the pressure or head gradient, that is from high to low pressure or head.

From these observations and Eq. (2), we may see that, for constant hydraulic conductivity K, if the hydraulic gradient decreases in the x-direction (horizontal) so does the velocity. Therefore, from Eq. (2c), if the velocity decreases in the x-direction it must increase in the z-direction. That is, due to gravity, the groundwater can only flow to the minimum and than downward toward the geothermal system (indeed, there are no pumping wells in the area). This conclusion is made even more evident by the positive gradient between the piezometers Enel n.4 and Enel Castagno/Enel Valle that forces the groundwater to flow toward the interior of the volcano.

In addition, it can be observed that the temperature and salinity of the water at the ENEL "Castagno" piezometer substantially increases if the water table drops below about 748–757 m asl. In the first of these events, the salinity drops from 285 to 185 ppm as the water table rises from 754 to 767 m asl (**Figure 8a**). In the second event, the salinity rises from 170 to 210 ppm as the water table drops below 748 m asl; on the contrary, as the water table rises again in elevation to 755 m asl the salinity drops again to lower values. The changes in temperature during these events are even more pronounced (**Figure 8b**). In the first event, the temperature increases by 2°C as the water table drops from 762 to 749 m asl decreasing to the original temperature as the water table rises again. In the second event as the water table drops below 754 m asl the temperature increases by about 1.0°C, but when it drops below 746 m asl, there is a temperature increase of about 4.5°C. As the water table recovers to rise above 746 m asl, the temperature drops again by 2°C.

Both the salinity and temperature variations analysed in conjunction with the water table elevation changes indicate that as the water table falls below a given elevation, the pressure at the bottom of the aquifer decreases and, as suggested by Caparrini et al. [26], the hot saline fluids rise into the freshwater aquifer decreasing its quality. We point out that the piezometer ENEL "Castagno" is located at the intersection of two relevant faults (the "Le Mura" and "Poggio Pinzi" faults) created by the volcanic spreading processes (**Figure 1a**). These faults create particularly high-permeability pathways connecting the anhydrite and carbonate rocks of the geothermal field with the volcanic rocks of the freshwater aquifer.

Future work will attempt to quantify the actual volume of water that is drained from the superficial freshwater aquifers to the geothermal system. This calculation is at the moment hindered because flow rates from the various wells and the producing pressures and vapour/liquid water ratio in both geothermal systems are unknown.

4. Induced seismicity

An earthquake occurs when the shear stress (τ) accumulated on a fault plane exceeds its shear strength (τ_f), which opposes the relative motion along the fault and is mainly dependent on lithology, roughness of faults' surface and normal stress acting on it (e.g., [33]). The effective value of the normal stress (σ_n) acting on a fault surface is controlled by the local stress field (i.e., values and relative directions of principal stresses σ_1, σ_2 and σ_3) and by the pore pressure (p_p) in the neighbourhood of the fault.

$$\tau > \tau_f = C + \mu \left(\sigma_n - p_p \right), \tag{3}$$
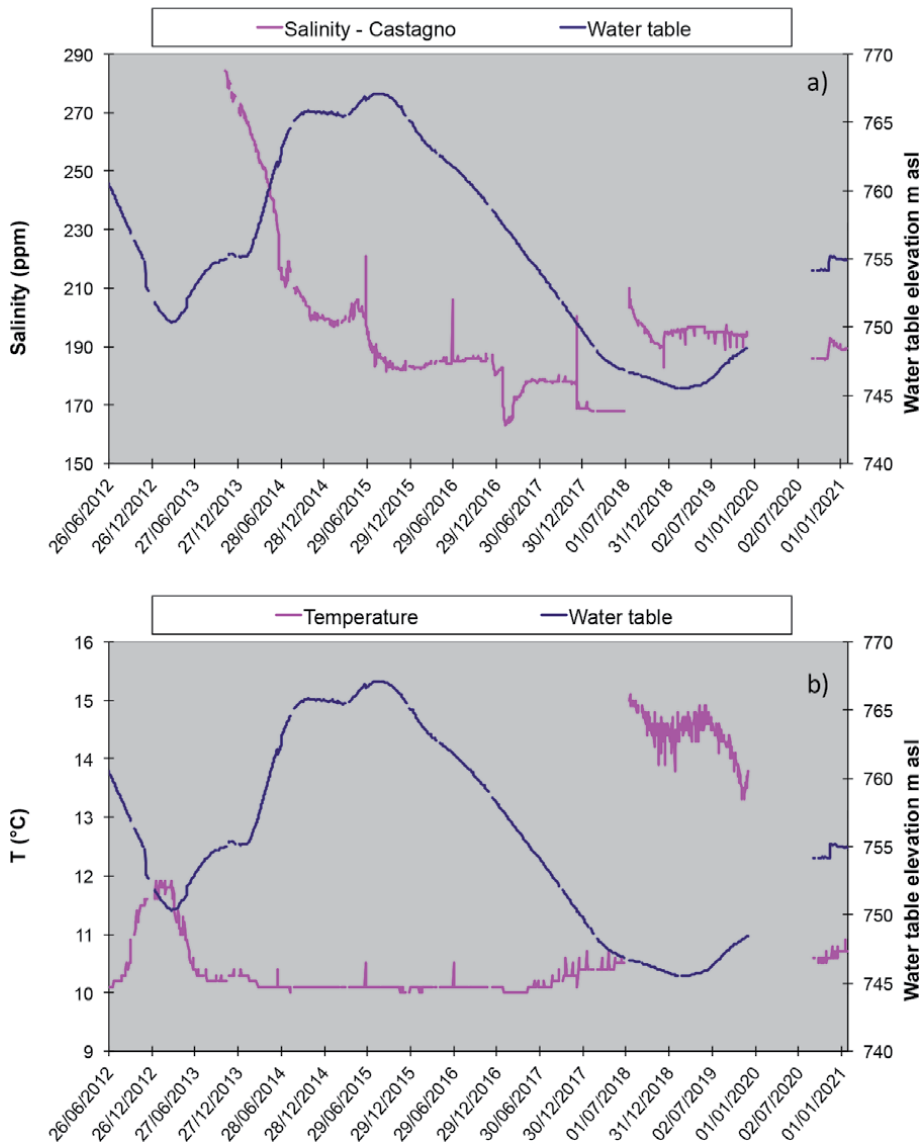
Figure 8.
Piezometer Castagno. (a) Water table elevation and salinity versus time. (b) Water table elevation and temperature versus time. Note the rapid changes in salinity and temperature as the water table drops to the lower values. Data from Regione Toscana—Centro Funzionale Monitoraggio Idrologico-Idraulico.

where C is cohesion and μ is friction coefficient [34]. When values of p_p increase—for example, due to anthropogenic operations, such as fluid injection, in the vicinity of the fault—pore pressure acts against σ_n, lowering the value of τ_f and thus allowing for the generation of a seismic event at relatively low values of shear stress (for $\tau > \tau_f$).

Seismicity is said to be "induced" when a pore-pressure-increase brought about by underground human activities (e.g., fluid injection) reaches a fault plane (possibly at some distance from the injection well) increasing the value of p_p and allowing the fault to slip, thereby releasing seismic energy accumulated on the fracture plane in the form of elastic strain [33]. The literature presents many past examples of seismicity induced by anthropogenic operations (e.g., [35, 36]) and, focus of this chapter, geothermal energy exploitation [37, 38]. In general, induced events are

usually of low intensity, because fault planes are not reactivated for their full extent [39], with hypocenters commonly located at relatively short distances from the injection well [37, 40, 41].

Seismicity is termed 'triggered' when the fault intersected by the pressure increase, due to gravity or tectonic loading, is already in a critical state in terms of shear stress (close to failure, i.e., critically stressed). In this case, τ is almost equal to τ_f on the fault plane and even a small increase of p_p activates a slip that interests the whole surface, releasing the entire stress accumulated on the structure in the form of seismic waves [39, 42]. A prerequisite for this to happen is the optimal orientation of the fault with respect to the principal stresses, with the normal to its surface lying in the plane $\sigma_1 \sigma_3$, where the differential stress is higher [38].

Previous studies (e.g., [33, 39, 43–45]) suggest that faults when in critically stressed conditions, can be more conductive to fluids (and to poroelastic stress changes). Barton et al. [45] present strong evidence that, in crystalline rocks, faults that are optimally oriented for shear failure and critically stressed have increased permeability and conduct fluid along their planes. Non-critically stressed faults appear to provide no fluid migration pathways. The concept of periodic fluid flow along growth faults (within sedimentary basins) was introduced by Sibson [43] and Hooper [45] who show how fluid motion along fault planes is restricted during periods of fault activity. At Paradox Valley, Colorado, USA, injection for disposal of high-salinity water induced seismicity (with several events of $M_L > 4$) which separated in two distinct zones: a principal one (>95% of events) asymmetrically surrounding the injection well and to a maximum radial distance of ~3 km, and a second zone covering an area of about 10 km^2 and centred ~8 km northwest of the injection [46]. Active faults and fractures at the edges of the valley allow for the stress change caused by the injection to reach the secondary seismic zone.

During the period 1982–2009, ENEL has recorded a large number of earthquakes with magnitudes in the range between 0 and 4 (**Figure 9**) [47]. These earthquakes, which appear to be induced by geothermal fluid production/
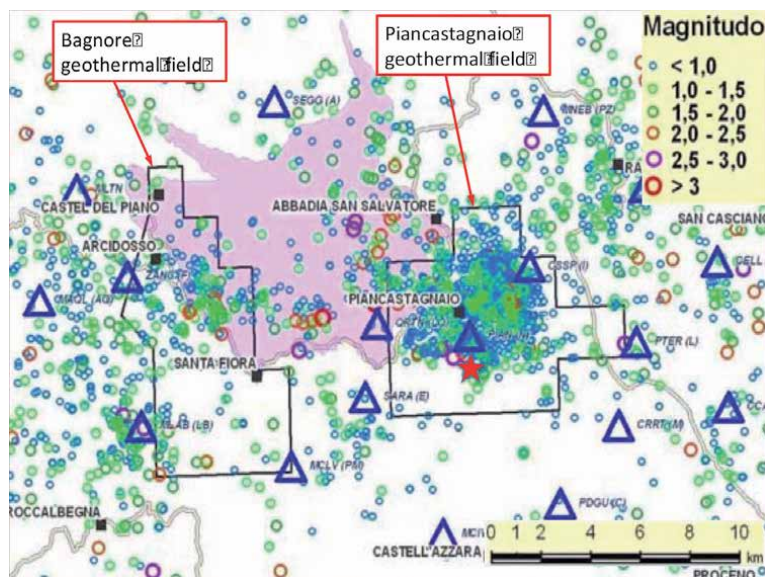
Figure 9.
Earthquakes epicentres recorded by ENEL from 1982 to 2009 (modified after [47]). The volcanic rocks are pink coloured; triangles are seismic stations. Note the large number of earthquakes that concentrate in and around the geothermal fields, most of which seem to be induced by geothermal exploitation; red star is the epicentre of the 1st April 2000 M = 3.9 earthquakes.

reinjection, are concentrated mainly within the geothermal fields and most of them are close to the production and injection wells. Some earthquakes even of significant magnitudes are located in proximity to extensional structures within the volcanic edifice.

Mazzoldi et al. [48] described the microseismic activity recorded in 2000–2001 around the Piancastagnaio geothermal field. They show how long-time geothermal fluid production with strong depressurization of the geothermal fields (see **Figure 4**) could have augmented the effective shear strength of faults and the potential magnitude of triggered or induced earthquakes. Perhaps this could have been the mechanism for the April 1st 2000 triggered earthquake in the Piancastagnaio Geothermal Field that had $M_L > 3.9$, damaging buildings in the Piancastagnaio and Abbadia San Salvatore municipalities and alarming the population [40, 41, 49].

During the last century, the strongest earthquake around Amiata Volcano occurred in 1919, with an epicentre at Piancastagnaio and with an estimated magnitude between 5.1 and 5.4. Two other events of magnitudes 5 and 4.6, with epicentres at Mt. Amiata (1948) and near Radicofani (some 10 km E of the volcano, 1958), respectively, have been reported. The latter is also the last event of $M > 4.5$ recorded in the area after the beginning of the geothermal exploitation (1959) [48].

During 14 months, Mazzoldi et al. [48] recorded about 600 seismic events of M_L between −1 and 3. The recorded events could be split into two groups: (a) tectonic events and (b) hydraulic-fracturing events. The largest part of the record (about 3/4 of them) were microseismic events ($M_L < 1$) belonging to group (a) with epicentres located within an area of 5 km in radius, centred within the geothermal field (around the PC16 injection well). Among microearthquakes, events with higher energies tended to be located within the area on the side of the volcano at very shallow hypocenter depths and close to the extensive structure of the edifice (cf. **Figure 1**). Hypocenter depths increase from the volcano toward the geothermal field where earthquake hypocenters are at and a few kilometres below exploitation depths (2–3 km). A small but significant part of the record (about 5%) consisted of group (b) events, which could not be accounted for by a pure brittle-fracture mechanism but rather seem indicative of hybrid events, generally related to fluid-filled fracture dynamics, typical of volcanic areas and geothermal fields [50]. Hypocenters of these events were tracked down with a grid-searching method based on the maximum energy distribution at the four stations [51] and were mainly concentrated within the geothermal field, on the south-eastern side of Amiata volcano still at exploitation depths.

Previous seismic analyses of recorded events [52, 53] and seismic observation by Mazzoldi et al. [48] show that the SE base of Mt. Amiata has the highest density of tectonic events in correspondence of the geothermal field location, the extensional structures that dissect the volcanic edifice (SE of the edifice) and the compressive structures at the base of the volcano—the last two formed by the volcanic spreading process [4].

Sorgenia [20] recorded microseismicity at the Eastern base of Amiata Volcano for 6-months. They located two distinct thrust-fault events (with a four-month delay between them) of approximate $M = 2$ and hypocenter depth of 8 km. These seismic events show active compression within the Siena-Radicofani Graben, which is consistent with the work of Bonini and Sani [18] and Borgia et al. [4].

Because of active volcanic spreading, after major earthquakes, faults tend to recover in time their critically stressed conditions according to the local Maxwell time (t) [54]. Using for the evaporites a Young's modulus $\lambda = 10^9$ Pa [55] and a viscosity $\mu = 10^{18}$ Pa s [4], this recurrence time is found to be:

$$t = \frac{\mu}{\lambda} = 10^9 \text{ s} = 31.7 \text{ a.} \qquad (4)$$

Given the approximations in Eq. (4) and using the Gutenberg-Richter curve given by Mazzoldi et al. [48], this recurrence time corresponds to earthquakes magnitudes between 4 and 5. These values of volcanic-spreading earthquake magnitudes, although on the smaller side, are comparable to the magnitudes given by Mazzoldi et al. [48]. Assuming our approximation for recurrence time is correct, and considering that the latest earthquake with a magnitude of about 4 occurred in 2000, we may suggest that a similar earthquake is expected to occur in the next few decades. Experience suggests that geothermal exploitation could perhaps trigger such an earthquake.

5. Atmospheric emissions

Currently, there are six flash-type 20-MWe power-plant units at Amiata Volcano, three for each of the two geothermal fields of "Bagnore" and "Piancastagnaio" (cf. **Figures 1** and **2**). In addition, for both fields, there is a secondary use of the residual heat for home and greenhouse heating.

To force evaporation of the geothermal fluid, the three fans of each cooling tower pump about 4–6 (*10^6 Nm^3/h) of fresh air into the base of the tower (cf. **Figure 2b**) [9, 56], and emit the same amount of air plus a fraction of geothermal fluid (much of which is evaporated into the airflow) from the top of the towers (**Figure 2b**). Because from about one-half to three-quarters (cf. [7, 9]) of the geothermal fluid that enters a power plant is emitted to the atmosphere from the cooling towers, a total in the range of 360–585 t/h of geothermal fluids is lost to the atmosphere. In addition to carbon dioxide (CO_2), and even if there are abatement technologies for mercury (Hg) and hydrogen sulphide (H_2S) (the AMIS—Abatement of Mercury and Hydrogen Sulphide) and for ammonia (NH_3) (with the addition of sulphuric acid) the emissions still have high contents of these pollutants and of additional pollutants such as sulphur dioxide (SO_2), methane (CH_4), arsenic (As), antimony (Sb), boric acid (H_3BO_3), selenium (Se), cadmium (Cd), chromium (Cr), manganese (Mg), nickel (Ni), lead (Pb), copper (Cu), and vanadium (V) (**Table 2**).

In particular, CO_2 and CH_4 emissions are over 6.7×10^5 and 1.4×10^4 t/a, respectively. These two compounds produce an equivalent greenhouse-gas effect that is calculated to be comparable to the emissions of gas-fired power plants per Mega Watt of electrical energy produced [57]. Orlando et al. [58] suggest that this CO_2 is generated by the interaction of the geothermal fluids with magnesian siderite in the phyllites of the geothermal reservoir. In addition, the emissions of H_2S that amount to 1.2×10^3 t/a, of SO_2 that consist of 2.7 t/a, and of boric acid have an acid-rain potential that is about twice that of coal-fired power plants per MW of electrical energy produced [57].

In addition, the emissions of NH_3 amount to 2.1×10^3 t/a (**Table 2**) and constitute a notable contribution to the formation of secondary fine particles (aerosols). In 2017 these emissions were close to half of the total Tuscany ammonia emissions [5, 59]. Relative to mercury, the emissions are indeed relevant even with the abatement technology in place; including mercury and mercury compound, they total 1.17 t/a. While the emissions of arsenic and arsenic compounds sum to about 79 kg/a. To better emphasise the relevance of these values, the only mercury and arsenic emissions are, respectively, 42.5% and 7.5% of the total emissions of these pollutants from all Italian industries [5]. Note that an amount approximately equal to that of

	Bagnore	Piancastagnaio	Total
H_2S Hydrogen suphide (t/a)[+]	4.86E+02	7.25E+02	1.21E+03
CO_2 Carbon dioxide (t/a)[+]	3.77E+05	2.97E+05	6.74E+05
SO_2 Sulphur dioxide (t/a)[+]	0.61	2.07	2.68E+00
NH_3 Ammonia (t/a)[+]	1.21E+03	9.51E+02	2.16E+03
CH_4 Methane (t/a)[+]	1.03E+04	4.10E+03	1.44E+04
CO Carbon monoxide (t/a)[+]	57.29	29.17	86.46
H_3BO_4 Boric acid (t/a)[*]	4.50	12.18	16.68
As Arsenic (kg/a)[+]	24.49	9.99	34.48
Arsenic compounds (kg/a)[*]	13.98	27.49	41.47
Hg Mercury (kg/a)[+]	106.7	258.07	364.77
Mercury compounds (kg/a)[*]	85.15	722.52	807.67
Sb Antimony (kg/a)[+]	24.28	24.07	48.35
Se Selenium (kg/a)[*]	9.20	20.46	29.66
Cd Cadmium (kg/a)[*]	0.02	0.01	0.03
Cr Chromium (kg/a)[*]	0.13	0.86	0.98
Mg Manganese (kg/a)[*]	0.18	0.11	0.29
Ni Nickel (kg/a)[*]	0.36	0.50	0.86
Pb Lead (kg/a)[*]	0.14	0.04	0.18
Cu Copper (kg/a)[*]	0.20	0.12	0.32
V Vanadium (kg/a)[*]	0.10	0.04	0.14

[*]*Data derived from: Ref. [57].*
[+]*Data derived from: Ref. [2].*

Table 2.
Today's approximate emissions per year of some compounds and metals from the power plants of the two Amiata volcano geothermal fields of "Bagnore" and "Piancastagnaio".

the Amiata Volcano area is emitted by the geothermal power plants of the Larderello area in central Tuscany. Before the emplacement of the mercury abatement technology, the emissions for mercury were probably an order of magnitude higher. The actual amount of mercury emitted from geothermal power plants as a total in the Amiata Volcano geothermal area is not known. However, a gross estimate can be made based on the available data published yearly by the Agenzia Regionale per la Protezione Ambientale della Toscana (ARPAT) since 2002, and the set of measurements made by ENEL [60]. Based on these measurements the total Mercury emitted by the Amiata Volcano power plants could be in the order of 50–60 t in the past 60 years.

Regarding the composition of the fine particles collected in the Piancastagnaio area Tommasini et al. [9] show that they are enriched relative to the fine particles collected in Firenze and Arezzo (these are among the Italian cities that have the largest concentrations of fine particles in the air) in sodium, vanadium, zinc, phosphorous, sulphur, tantalum, caesium, thallium, thorium, uranium, and arsenic (**Figure 10**). Barazuoli et al. [61] report a set of analyses of the condensates produced by several geothermal wells in the Bagnore and Piancastagnaio geothermal fields. From these data, we calculate that the condensate from the geothermal fluids can have a total solid concentration (C_s) in solution that is in the order of 1 g/l.
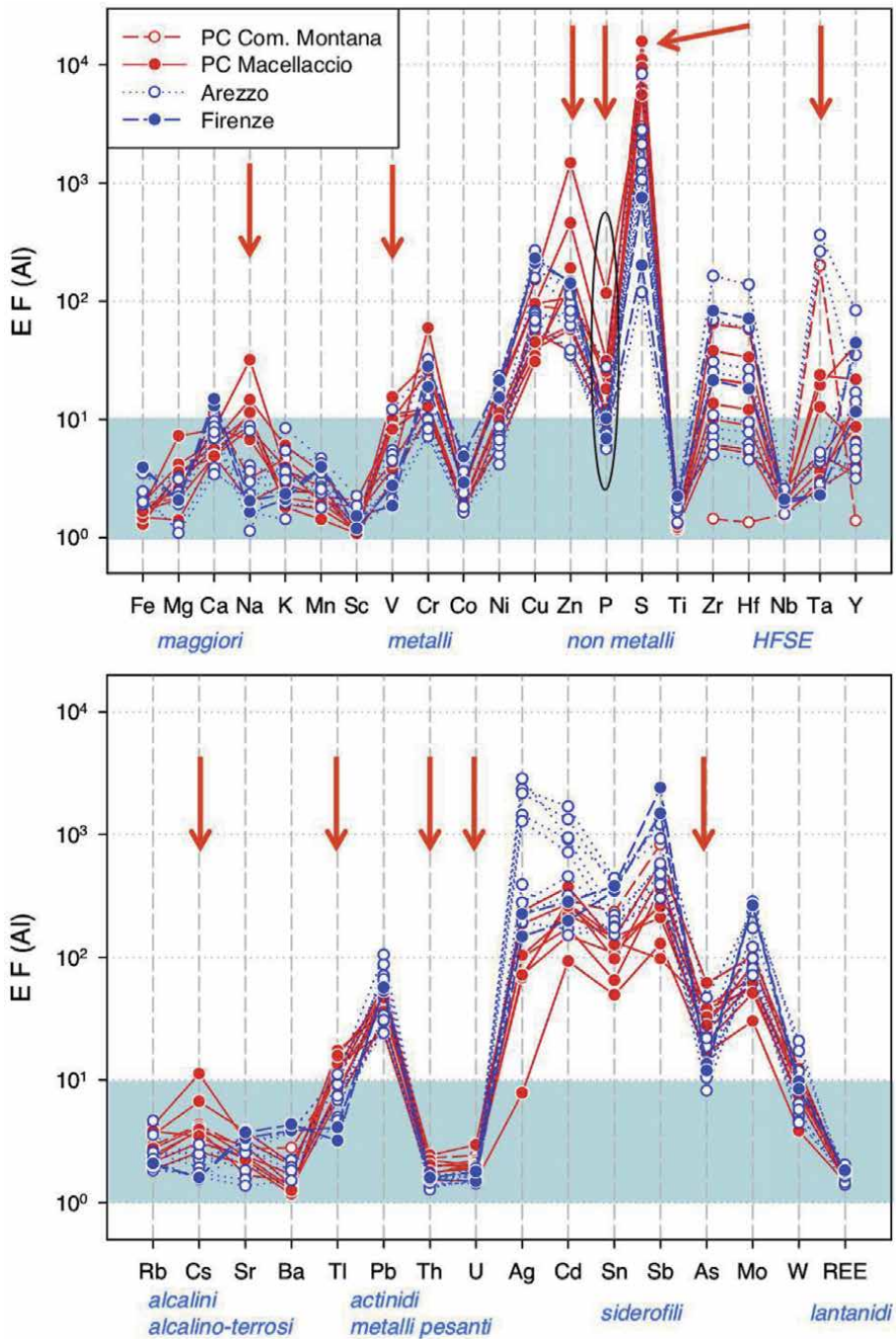
Figure 10.
Enrichment factor (EF) of heavy metals in the fine particles collected at Piancastagnaio geothermal field (after [9]). The arrow point to the elements that are enriched in the Piancastagnaio area in comparison to the concentrations found at Firenze (traffic station) and Arezzo (urban background station). Note that the EF scale is logarithmic: Small upward increases in the positions of points on the graph correspond to significant enrichments.

Recalling that the volume of condensate emitted to the atmosphere (V_c) is estimated to be in the order of two-third of the about 130 t/h of geothermal fluid used in a 20 MWe geothermal power plant and that the airflow through the cooling towers

(A_f) is about 5 Mm^3/h, doing the appropriate units conversion and assuming an equivalence between litres and kg for liquid water solutions, we may calculate:

$$C_{PM} = \frac{C_s \times V_c}{A_f} = \frac{10^6 (\mu g/l) \times 87 * 10^3 \ (l/h)}{5 \times 10^6 \ (m^3/h)} \approx 17 * 10^3 \ (\mu g/m^3). \qquad (5)$$

That is, the order of magnitude estimates of fine particles concentration (C_{pm}) emitted from the cooling towers of a 20–MWe geothermal power plant should be in the order of 17 * 10^3 ($\mu g/m^3$), which is a significant amount. This value should be incremented by the fine particles that are present in the non-condensable gas stream [9]. The primary and secondary fine particles resulting from the geothermal power plant emissions seem to be visible in the haze that is left after the evaporation of the H$_2$O cloud (**Figure 11**). During periods that the power plants are out-of-service emissions to the atmosphere are even more significant and are unaccounted for (**Figure 12**). In fact, during these periods, because the vapour production from the geothermal wells cannot be stopped, the geothermal fluids are emitted directly to the atmosphere without any pollutant abatement technology.

At the moment, there is no available direct measurement of the concentration of fine particles at the exit of the cooling towers of each power plant. Thus, we can only compare the value calculated above with the fine-particle concentrations of 10–30 μg/m^3 (average 15 μg/m^3) measured by Tomassini et al. [9] in the Piancastagnaio geothermal field area approximately 1–2 km uphill of the power plants. Given the approximations made and the fact that we are calculating a potential maximum fine-particle concentration in the emissions, to find a dilution factor of about a thousand, from the emission towers to the place where measurements were taken (1–2 km uphill of the power plants), appears to be consistent with atmospheric modelling of the power plant emissions (cf. [6]). In this respect, we observe that the power plants are located all around the village of Piancastagnaio from NE to E to SW and to S at a distance smaller than 2 km. In addition, in the western direction there are the three power plants of the Bagnore geothermal field at just over 10 km distance. Therefore, no matter from what direction blows the wind (apart from NW and N) the fumes from the power plants always reach the village of Piancastagnaio. It is only when there are strong winds from the north and northwest that the concentration of fine particles decreases [9]. We think that during winter thermal inversion events, when the fumes of the power plants can accumulate and linger in the lower atmosphere even for a few days, the concentration of fine particles could increase significantly above the values that have been occasionally measured up to now.

Finally, we have to recall that some of the elements emitted to the atmosphere, in addition to radon, are radioactive. Geothermal energy production has been included already many years ago [62] among the human activities that generate Technologically Enhanced Naturally Occurring Radioactive Materials (TENORM). In this respect, very little is known about the geothermal power plants of Amiata Volcano.

6. Discussion and conclusions

Geothermal exploitation for the production of electricity at Amiata Volcano uses flash-type power plants with cooling towers that evaporate much of the geothermal fluid to the atmosphere with minor reinjection, that is from about one-quarter to one-half, of the fluid produced [7, 9]. In addition, the flash of the geothermal fluid is mainly occurring at depth forcing a significant depressurization of the geothermal system from the original undisturbed conditions (cf. [21]).
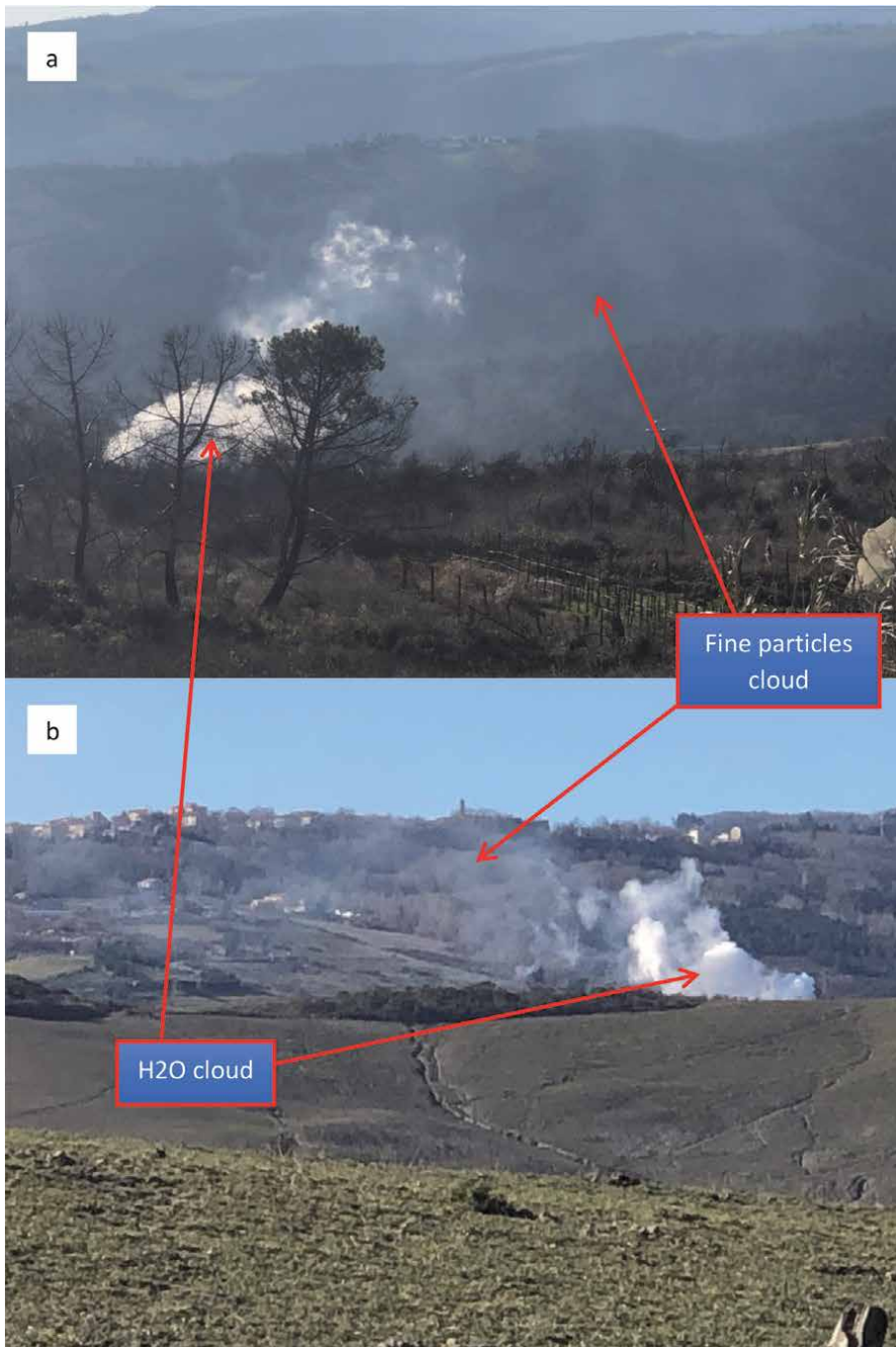
Figure 11.
Emissions from (a) the PC3 (b) the PC4-PC5 geothermal power plant units with the village of Piancastagnaio in the background. Note how after the evaporation of the water vapour in the atmosphere, a cloud of fine particles persists, much like the fumes emitted from major coal- or oil-fired power plants.

As a consequence, this depressurization propagates upward inducing a corresponding decrease in pressure at the base of the freshwater aquifer contained in the volcanic edifice [26]. Accordingly, the water table has substantially dropped, reaching in the centre of the volcano a decline of about 250 m (compare

Figure 12.
(a) The emissions during the out-of-service of the PC3 geothermal power plant occurred on the 10 of may 2005.
(b) Cloud of toxic geothermal fluids, emitted from the Bagnore 25 geothermal well, flowing toward home on 21 November 2007; the inhabitants had run away from their houses.

Figure 3a and **b**) and forming in the Southeastern sector of the volcanic edifice a minimum in the water table (**Figure 3b**), as it has been measured by Compagnia Mediterranea Esplorazioni [24], Marocchesi [29], and its time changes monitored by Manzella [30] with oscillations between 700 and 600 m asl. In December 2018, this minimum had an elevation of 746.39 m asl at the ENEL4 piezometer (**Figure 8**). The presence of this minimum demonstrates that the water is drained downward from the volcano into the rocks that contain the geothermal systems (the Anhydrites and the metamorphosed Tuscan Units; **Figure 1b**) via the many faults and the

volcanic conduits that cut the edifice and its basement (cf. [4, 8], and references therein). This impact of geothermal fluid production on freshwater aquifers need to be evaluated in detail when commissioning geothermal power plants. On the other hand, if a balanced production-reinjection volume of geothermal fluids were to become mandatory, for instance by using air-coolers in place of the evaporative towers, the impact on the superficial aquifers would be substantially reduced because the recharge from freshwater aquifers would need to compensate, as a first-order approximation, only for the reduced volume of the cold water reinjected relative to hot-water produced.

At Amiata Volcano, geothermal fluid production with its associated small amount of reinjection results in several induced earthquakes that are rarely felt by the population. However, a M_L = 3.9 induced earthquakes occurred on April 1st 2000 [40, 41, 49], which generated significant damages to houses and buildings in general but luckily no deaths. Given the volcanic spreading process, we suggest that an M_L = 4–5 earthquake could be triggered in the next few decades. Even if these magnitudes are not indeed large, the fact that the buildings of the many medieval villages in the area are old and not constructed to modern seismic standards, there is the likelihood of significant damages and potential deaths. Thus, increasing the amount of reinjected fluid relative to produced geothermal fluid could increase the earthquake risk, because it has been suggested that earthquake magnitude is related to the volume of fluids reinjected [63]. The suggestion of increasing reinjection to reduce the impact on the freshwater aquifer runs counter to reducing induced seismicity. Retrofitting all buildings, although very expensive, could be in the long term a reasonable answer because even larger-magnitude earthquakes unrelated to geothermal energy production, may occur in this area.

The non-condensable gases, in addition to the evaporation of a large fraction of the geothermal fluid in the cooling towers, produce significant emissions to the atmosphere [2, 5, 57]. In the first place, the CO_2 and CH_4 emissions produce green-house effects that are calculated to be comparable to the emissions of gas-fired power plants per electrical energy produced; therefore, we are forced to consider that the Amiata volcano geothermal power plants are not adequate to substantially reduce greenhouse gas emissions per electric energy produced. In addition, the emissions of H_2S, SO_2 and H_3BO_4, have an atmospheric acidification potential (acid rain) that is also similar to coal-fired power plants per electrical energy produced. Also, the emissions of NH_3, a notable contribution to secondary fine particles formation, in 2017 were close to half the whole emissions in Tuscany of such pollutant. Relative to Mercury, the emissions are relevant even with the abatement technology in place. Before, the emplacement of the Mercury abatement technology (AMIS) in the years two-thousands, the emissions were around an order of magnitude higher. The emissions of Arsenic and Arsenic compounds are also significant. While these emissions are generally monitored only for about a few hours per year, no controls are made for the rest of the time, even when the AMIS is not adequately functioning. In addition, the emissions that occur as fine particles (aerosol) are unaccounted for since there are no limits imposed by law for them. Primary and secondary fine particles related to the geothermal power plants could account for the relatively high level of fine particles (on average about 15 μg/m^3) in the air of this, by all means, rural area that practically has no large emissions from other industries. In the Piancastagnaio area fine particles are enriched in Sodium, Phosphorous, Sulphur, Zinc, Tantalum, Caesium, Thallium, Thorium, and Uranium relative to the particles sampled in Florence and Arezzo [9] suggesting a direct contribution from the geothermal power plants.

Although the concentrations of fine particles measured in the air have been sporadically measured below the law limits, the pollutants contained in these

particles tend to be toxic metals, making these aerosols potentially dangerous for the health of the population living in the area. The WHO REVIHAAP [64], states that all the studies conducted to date show that there is no threshold level below which the effects of pollution on health are not evident. Therefore, in the application of the precaution principle, we suggest that the emissions from the geothermal power plants, in combination with an increase in pollutant content in the freshwater and soil, could be a concomitant cause for the excesses in hospitalizations and deaths in the Amiata Volcano geothermal area (cf. [65]).

In conclusion, the use of air-coolers in place of the evaporative cooling towers, like the ones used today, would drastically reduce the potential impact on the health of the population residing in the Amiata Volcano geothermal area. This technical solution has been already indicated in 2010 by the local government of Tuscany [66], but it has not been applied yet. This technology, which is now proposed for most binary-cycle geothermal power plants in Italy, would substantially reduce both the impact on the superficial freshwater aquifers because all the produced fluid would be reinjected reducing the need for recharge from the superficial volcanic aquifer, and on the atmosphere. After all, the emissions would practically be minimal. On the contrary, the much larger volume of reinjected fluid may increase the risk of inducing or triggering earthquakes. We think that future Life-cycle assessments of the geothermal power plants should attempt at including the environmental impacts reported in this paper and the consequent health risk for the residing population. We stress that the new emerging technologies, such as the deep-borehole heat exchangers should receive more attention and incentives; they produce less energy per unit time but on the other hand, the energy production could probably last for much longer than conventional geothermal power plants, with a minimal environmental impact.

Acknowledgements

Conflict of interest

As a technical consultant, Borgia has served the Public Prosecutor of Grosseto, and worked for the Regione Toscana, the Comunità Montana Amiata Val d'Orcia, the municipalities of Piancastagnaio, Arcidosso and Radicofani, Macchia Faggeta, and several citizens to define the pollution and the environmental impact induced by the geothermal power plants.

Micheli has worked for 35 years in the geology and hydrogeology sections of the Regione Toscana and is now retired.

Carlo Balducci lived his whole life at the foot of Amiata Volcano and is now retired and in the process of creating a public comprehensive database of scientific and government documentation on the geothermal power plants of Amiata.

Notes

This paper is dedicated to the memory of Alice, Emidio, and all Amiata citizens that become ill and died.

Author details

Andrea Borgia[1*], Alberto Mazzoldi[1], Luigi Micheli[2], Giovanni Grieco[3],
Massimo Calcara[4] and Carlo Balducci[2]

1 EDRA, Roma, Italy

2 Independent Scientist, Firenze, Italy

3 Dipartimento di Scienze della Terra, Università degli Studi di Milano, Milano,
Italy

4 Istituto Nazionale di Geofisica e Vulcanologia, Roma, Italy

*Address all correspondence to: andrea.borgia@edra.us

IntechOpen

References

[1] Manzella A, Bonciani R, Allansdottir A, Botteghi S, Donato A, Giamberini S, et al. Environmental and social aspects of geothermal energy in Italy. Geothermics. 2018;**72**: 232-248

[2] Parisi ML, Ferrara N, Torsello L, Basosi R. Life cycle assessment of atmospheric emission profiles of the Italian geothermal power plants. Journal of Cleaner Production. 2019;**234**: 881-894

[3] Basosi R, Bonciani R, Frosali D, Manfrida G, Parisi ML, Sansone F. Life cycle analysis of a geothermal power plant: Comparison of the environmental performance with other renewable energy systems. Sustainability. 2020;**12**: 2786. DOI: 10.3390/su12072786

[4] Borgia A, Mazzoldi A, Brunori CA, Allocca C, Delcroix C, Micheli L, et al. Volcanic spreading forcing and feedback in geothermal reservoir development, Amiata volcano, Italia. Journal of Volcanology and Geothermal Research. 2014;**284**:16-31

[5] Basosi R, Bravi M. Geotermia d'impatto. QualEnergia, giugno/luglio, 2015. pp. 96–99

[6] Somma R, Granieri D, Troise C, Terranova C, De Natale G, Pedone M. Modelling of hydrogen sulphide dispersion from geothermal power plants of Tuscany (Italy). Science of the Total Environment. 2017;**583**:408-420. DOI: 10.1016/j.scitotenv.2017.01.084

[7] Agenzia Regionale per la Protezione dell'Ambiente della Toscana (ARPAT). Rapporto sulla campagna di misure svolta da ARPAT presso la central geotermoelettrica BAGNORE 3 finalizzata alla "verifica della tecnica sperimentale per l'abbattimento dell'ammoniaca, progettata dalla Società Enel Green Power S.p.A." 2010. p. 6

[8] Calamai A, Cataldi R, Squarci P, Taffi L. Geology, geophysics and hydrogeology of the Monte Amiata geothermal fields. Geothermics. 1970; **1**:150

[9] Tommasini S, Capecchiacci F, Zoppi M, Cabassi J, Marchionni S, Tassi F, et al. Progetto Regionale PATOS-2—Particolato Atmosferico. In: TOScana Linea di ricerca 7—Individuazione di marker specifici delle centrali geotermoelettriche. Report Regione Toscana. Firenze. 2015. p. 109

[10] Ferrari L, Conticelli S, Burlamacchi L, Manetti P. Volcanological evolution of the Monte Amiata, Southern Tuscany: New geological and petrochemical data. Acta Vulcanologica. 1996;**8**(1):41-56

[11] Brogi A. The structure of the Monte Amiata volcano-geothermal area (Northern Apennines, Italy): Neogene-quaternary compression versus extension. International Journal of Earth Sciences. 2008;**97**(4):677-703. DOI: 10.1007/s00531-007-0191-1

[12] Borgia A, Mazzoldi A, Brunori CB, Allocca C, Delcroix C, Micheli L, et al. Reply to: Barazzuoli P., Bertini G., Brogi A., Capezzuoli E., Conticelli S., Doveri M., Ellero A., Gianelli G., La Felice S., Liotta D., Marroni M., Manzella A., Meccheri M., Montanari D., Pandeli E., Principe C., Ruggieri R., Sbrana A., Vaselli V., Vezzoli L., 2015. COMMENT ON: "Borgia, A., Mazzoldi, A., Brunori, C.A., Allocca, C., Delcroix, C., Micheli, L., Vercellino, A., Grieco, G., 2014. Volcanic spreading forcing and feedback in geothermal resorvoir development, Amiata Volcano, Italia. J. Volc. Geoth. Res. 284, 16-31". Journal of Volcanology and Geothermal Research. 2015;**303**:209-215. DOI: 10.1016/j.jvolgeores.2015.08.006

[13] Garzonio CA. Paesaggi Geologici della Toscana—Regione Toscana. Pisa: Pacini Editore; 2008. p. 175

[14] Principe C, Vezzoli L. In: Principe C, Lavorini G, Vezzoli LM, editors. Vulcano-tettonica e morfologie vulcaniche del Monte Amiata, Il Vulcano di Monte Amiata. Nola (NA): Edizioni Scientifiche e Artistiche; 2017. p. 399

[15] Mazzuoli R, Pratesi M. Rilevamento e studio chimicopetrografico delle rocce vulcaniche del Monte Amiata. Atti - Società Toscana di Scienze Naturali Memorie Serie A. 1963;**70**:355-429

[16] Betz A. Osservazioni Geologiche sulle ricerche minerarie per cinabro effettuate nel permesso "Le Bagnore" negli anni 1959–1961. SICEDISON s.p.a. Sezione Ricerche Minerarie—Milano. Rimin Archives. 1962. p. 34

[17] Acocella V, Mulugeta G. Surface deformation induced by pluton emplacement: The case of Amiata (Italy). Physics and Chemistry of the Earth. 2000;**26**(4–5):355-362

[18] Bonini M, Sani F. Extension and compression in the Northern Apennines (Italy) hinterland: Evidence from the late Miocene–Pliocene Siena–Radicofani Basin and relations with basement structures. Tectonics. 2002;**21**(3):1-28

[19] Bonini M, Sani F, Stucchi EM, Moratti G, Benvenuti M, Mennano G, et al. Late Miocene shortening of the Northern Apennines back-arc. Journal of Geodynamics. 2014;**74**:1-31

[20] Sorgenia. Impianto geotermico Val di Paglia—Studio Impatto Ambientale—Rapporto sulla sismicità. 2019. p. 47. Available from: https://www.regione.toscana.it/-/procedimento-coordinato-e-provvedimento-unico [Accessed: 02 May 2021]

[21] Cataldi R. Remarks on the geothermal research in the region of

Monte Amiata (Tuscany, Italy). In: Paper Presented at the IAV International Symposium on Volcanology (New Zealand). 1965

[22] Consiglio Nazionale delle Ricerche (CNR). Contributo alla conoscenza delle potenzialità geotermiche della Toscana e del Lazio. CNR-PFE-RF 15. Roma. 1982. p. 47

[23] ENEL. Reference notes on geothermal areas of Tuscany and Latium (Italy). Biblioteca UNG, n. 86. 1986. p. 31

[24] Compagnia Mineraria Prospezione. Prospezioni Geoelettriche nella regione del Monte Amiata. Archivio Rimin, n. 234. 1966. p. 42

[25] Delcroix C, Browny K, Borgia A, Vercellino A, Grieco G, Moratti G. Rilievo geostrutturale preliminare dell'apparato vulcanico del Monte Amiata. Report for Regione Toscana. 2006. p. 46

[26] Caparrini F, Castelli F, Ercolani G. Adattamento e implementazione del modello idrologico MOBIDIC per il bilancio dei bacini idrografici e dell'acquifero del Monte Amiata. Report for Regione Toscana. 2011. p. 78

[27] Fatarella G. La cascata d'Acqua d'Alto, dallo sfruttamento al disastro ecologico. Amiata Storia e Territorio n. 41/42. 2002. pp. 60–71

[28] ENEL. L'energia geotermica in Toscana e nel Lazio settentrionale—Due secoli di storia. 1976. p. 50

[29] Marocchesi M. Indagine geofisica Monte Amiata. 1°, 2° e 3° stralcio. Report for Provincia di Grosseto. 2003

[30] Manzella A. Convenzione tra la Regione Toscana e l'Istituto di Geoscienze e Georisorse del CNR per la realizzazione della campagna geofisica triennale tramite elettromagnetismo

relativa all'acquifero dell'edificio vulcanico del Monte Amiata. Report for Regione Toscana. 2006. p. 55

[31] La Felice S, Montanari D, Battaglia S, Bertini G, Gianelli G. Fracture permeability and water–rock interaction in a shallow volcanic groundwater reservoir and the concern of its interaction with the deep geothermal reservoir of Mt. Amiata, Italy. Journal of Volcanology and Geothermal Research. 2012;**284**:95-105

[32] La Felice S, Bertini G, Principe C. Stratigrafia e caratterizzazione delle vulcaniti attraversate dal pozzo David Lazzaretti. In: Principe C, Lavorini G, Vezzoli LM, editors. Il Vulcano di Monte Amiata. Nola (NA): Edizioni Scientifiche e Artistiche; 2017. pp. 213–220

[33] Keranen KM, Weingarten M. Induced seismicity. Annual Review of Earth and Planetary Sciences. 2018;**46**: 149-174

[34] Terzaghi K, Peck RB. Soil Mechanics in Engineering Practice. New York: John Wiley and Sons/Chapman and Hall; 1948

[35] Grigoli F, Cesca S, Piolo E, Rinaldi AP, Clinton JF, Stabile TA, et al. Current challenges in monitoring, discrimination, and management of induced seismicity related to underground industrial activities: A European perspective. Reviews of Geophysics. 2017;**55**:310-340

[36] Foulger GR, Miles PW, Gluyas JG, Julian BR, Davies RJ. Global review of human-induced earthquakes. Earth-Science Reviews. 2018;**178**:438-514

[37] Evans KF, Zappone A, Kraft T, Deichmann N, Moia F. A survey of the induced seismic responses to fluid injection in geothermal and CO_2 reservoirs in Europe. Geothermics. 2012;**41**:30-54

[38] Buijze L, van Bijsterveldt L, Cremer H, Paap B, Veldkamp H, Wassing BBT, et al. Review of induced seismicity in geothermal systems worldwide and implications for geothermal systems in the Netherlands. Netherlands Journal of Geosciences. 2019;**98**:e13. DOI: 10.1017/njg.2019.6

[39] Mazzoldi A, Rinaldi AP, Borgia A, Rutqvist J. Induced seismicity within geological carbon sequestration projects: maximum earthquake magnitude and leakage potential from undetected faults. International Journal of Greenhouse Gas Control. 2012;**10**: 434-442

[40] Braun T, Dahm T, Kruger F, Ohrnberger M. Does geothermal exploitation trigger earthquakes in Tuscony? Eos. 2016;**97**. DOI: 10.1029/2016EO053197

[41] Braun T, Cesca S, Kühnb D, Martirosian-Janssend A, Dahmb T. Anthropogenic seismicity in Italy and its relation to tectonics: State of the art and perspectives. Anthropocene. 2018;**21**: 80-94. DOI: 10.1016/j. ancene.2018.02.001

[42] Ellsworth LW. Injection-induced earthquakes. Science. 2013;**341**:1225942. DOI: 10.1126/science.1225942

[43] Sibson RH. Conditions for fault-valve behaviour. Geological Society of London, Special Publication. 1990;**54**: 15-28

[44] Hooper ECD. Fluid migration along growth faults in compacting sediments. Journal of Petroleum Geology. 1991; **14**(2):161-180

[45] Barton CA, Zoback MD, Moos D. Fluid flow along potentially active fault in crystalline rock. Geology. 1995;**23**: 683-686

[46] Ake J, Mahrer K, O'Connell D, Block L. Deep-injection and closely

monitored induced seismicity at Paradox Valley, Colorado. Bulletin of the Seismological Society of America. 2005;**95**(2):664-683

[47] ENEL. Approfondimenti in merito ad alcuni aspetti di geologia e idrogeologia. SIA Bagnore 4, Integrazioni Volontarie. 2011. p. 19

[48] Mazzoldi A, Borgia A, Ripepe M, Marchetti E, Ulivieri G, Della Schiava M, et al. Faults strengthening and seismicity induced by geothermal exploitation of a spreading volcano, Mt. Amiata, Italia. Journal of Volcanology and Geothermal Research. 2015; **301**(2015):159-168

[49] Mucciarelli M, Gallipoli M, Fiaschi A, Pratesi G. Osservazioni su danneggiamento nella zona del Monte Amiata a seguito dell'evento del 1 Aprile 2000. X Congresso Nazionale "L'Ingegneria Sismica in Italia". Potenza-Matera 9-13 Settembre 2001

[50] Bame D, Fehler M. Observation of long period earthquakes accompanying hydraulic fracturing. Geophysical Research Letters. 1986;**13-1**:149-152

[51] Marchetti E, Ripepe M. Stability of the seismic source during effusive and explosive activity at Stromboli Volcano. Geophysical Research Letters. 2005; **32**(3):1-5

[52] Batini F, Fiordelisi A, Moia F. Main features of the seismicity in the Monte Amiata and Latera geothermal areas (Italy). XII General Assembly, European Seismological Commission. Barcelona, September 1990. pp. 17–22

[53] Chiarabba C, Amato A. Upper crustal tomographic images of the Amiata–Vulsini geothermal region, central Italy. Journal of Geophysical Research. 1995;**100-B3**:4053-4066

[54] Alessssandrini B, Filippi L, Borgia A. Upper-crust tomographic structure of

the Central Appennines, Italy, from local earthquakes. Tectonophysics. 2001;**339**:479-494

[55] Carmichael RS. Handbook of Physical Properties of Rocks. Vol. **3**. Boca Raton, FL: CRC Press Inc.; 1984. p. 340

[56] Agenzia Regionale per la Protezione dell'Ambiente della Toscana (ARPAT). Moitoraggio delle aree geotermiche—Controllo emission—Qualità aria. 2009. p. 74

[57] Bravi M, Basosi R. Environmental impact of electricity from selected geothermal power plants in Italy. Journal of Cleaner Production. 2014;**66**: 301-308

[58] Orlando A, Conte AM, Borrini D, Perinelli C, Gianelli G, Tassi F. Experimental investigation of CO_2-rich fluids production in a geothermal area: The Mt Amiata (Tuscany, Italy) case study. Chemical Geology. 2010;**274**: 177-186

[59] Piano Regionale per la Qualità dell'Aria ambiente (PRQA). Valutazione Ambientale Strategica del Piano Regionale per la Qualità dell'Aria Ambiente (PRQA)—Rapporto Ambientale. Regione Toscana. 2017. p. 191

[60] ENEL. Indagini per la valutazione degli effetti sul ambiente delle emission aerodisperse degli impianti geotermoelettrici del area Amiatina—Team emission e bilanci di massa. 1996. p. 71

[61] Barazuoli P, Baroni F, Brogi A, Di Lella LA, Fabbrini L, Frau I, Gaggi C, Gobbini M, Manzo C, Meccheri M, Montauti A, Munzi S, Nannoni F, Nicolardi V, Pisani A, Protano G, Riccobono F, Rossi S, Salleolini M, Salvini R, Scala A. Studio geostrutturale, idrogeologico e geochimico ambientale dell'area amiatina—Università degli

Studi di Siena. Report for Regione
Toscana. 2008. p. 369

[62] Istituto Superiore per la Protezione
e la Ricerca Ambientale (ISPRA),
Ministero dell'Ambiente e della Tutela
del Territorio e del Mare (MATTM).
Task 03.01.01—Censimento attività/siti
con NORM e raccolta delle analisi di
rischio. 2014. p. 129

[63] McGarr A. Seismic moments and
volume changes. Journal of Geophysical
Research. 1976;**81**:1487-1494

[64] REVIHAAP. Review of evidence on
health aspects of air pollution. World
Health Organization Technical Report.
2013. p. 302

[65] Minichilli F, Amadori M, Bustaffa E,
Romanelli AM, Protti MA, Michelassi C,
Vigotti MA, Cori L, Pierini A, Minniti C,
Marrucci S e Bianchi F. Progetto di
ricerca epidemiologica sulle popolazioni
residenti nell'intero bacino geotermico
toscano, 'Progetto Geotermia',
Allegato 6. Agenzia Regionale di Sanità
della Toscana. 2010. p. 205

[66] Delibera di Giunta Regionale
Toscana (DGRT). Decreto di Giunta
Regionale Toscana—Allegato A—Criteri
direttivi per il contenimento delle
emission in atmosfera delle centrali
geotermoelettriche. 344/2010. p. 88

Chapter 3

Tropical Volcanic Residual Soil

Prahara Iqbal, Dicky Muslim, Zufialdi Zakaria,
Haryadi Permana, Arifan Jaya Syahbana,
Nugroho Aji Satriyo, Yunarto Yunarto, Jakah Jakah
and Nur Khoirullah

Abstract

In West Lampung, Sumatra, Indonesia, tropical volcanic residual soils are formed from weathering of volcanic breccias in hydrothermal alteration areas with a thickness of up to 20 m. This soil has the characteristics of clayey silt, low to high plasticity, brownish-red color, has the potential to swelling, easily eroded, and slide when it is saturated, and contains the minerals kaolinite, halloysite, illite, dickite, nacrite, montmorillonite, despujolsite, hematite, and magnetite. The results showed that this soil can cause corrosion of steel and is widely used by the community as a medium for growing plants and vegetables and as a foundation for infrastructure (for example, houses). The volcanic residual soil of the research area had Low Rare Earth Element (LREE) potential and specific uses. The soil with characteristic low plasticity has Liquid Limit (LL) brine value <50% will be suitable for agriculture purposes, building foundations, and earth construction. At the same time, the other category is soil with intermediate to high plasticity characteristics, which has an Liquid Limit (LL) brine value >50%, was more ideal for the primary forest.

Keywords: Corrosion, eroded, LREE, soil plasticity, West Lampung

1. Introduction

The soil (Greek: pedon; Latin: solum) is a part of the earth's crust made up of minerals and organic matter. The soil originates from rocks' physical and chemical weathering and has particle sizes ranging from clay to boulders. In general, the soil is divided into two types: residual soil and sedimentary soil [1].

Residual soil is soil formed directly from the rock source due to rock chemical weathering, dominated by the hydrolysis process (reaction between silicate minerals and acids) due to high rainfall and temperature conditions. The soil is above and in contact with the source rock or, in other words, does not undergo a transport process [1–4]. Based on the degree of rock weathering, this soil is within or equal to zone VI [5–8] (**Figure 1**).

Residual soil is mainly formed in tropical climates and has high rainfall and is formed in areas with many quaternary volcanic rock formations, such as Indonesia (tropical volcanic residual soil) [9–12]. In Indonesia, these deposits occupy 53% of the land area and form the basis for constructing various types of infrastructure [9, 13–15].
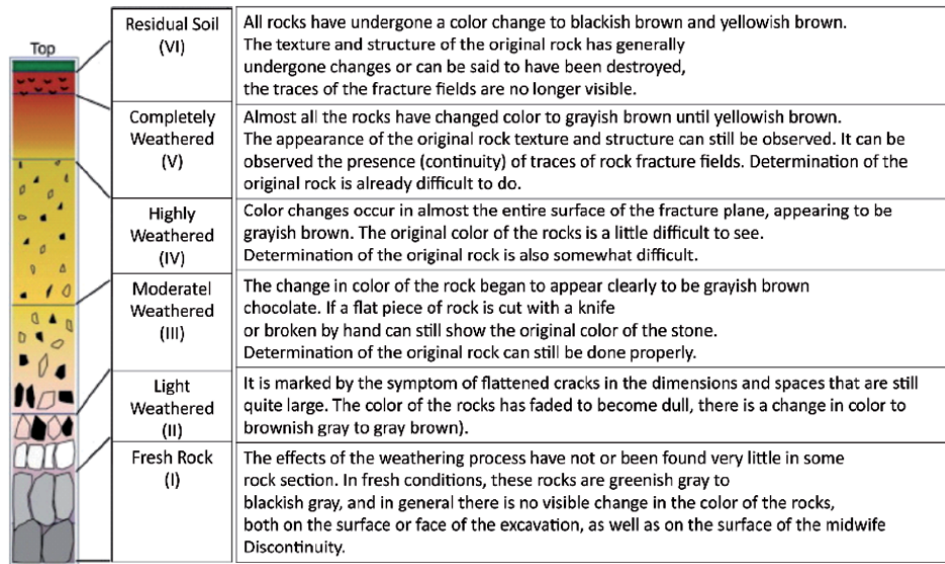
Figure 1.
Rock weathering profile and residual soil formation (Modification from [7]).

Geologically, the residual soils have a unique mineral composition of clay. Allophane, halloysite, kaolinite, illite, and montmorillonite are some minerals of clay found in the residual soil [13, 16]. The formation of residual soil will produce its own physical and engineering characteristics [10, 17]. Rahardjo et al. and Huat et al. [10, 18] have revealed that the soil has complex and diverse properties. Depending on the characteristics and history of eruptions, residual soils, in particular volcanic residual soils, may be layered or massive, coarse-grained or fine-grained, bonded or unbound, cracked or not broken. Volcanic residual soil can cover flat or sloping areas, reaching thicknesses of up to tens of meters. This soil covers an essential part of the world's surface, including the formation of slopes, areas occupied by urban settlements, structures, and infrastructure, and can create environmental problems, such as landslides, erosion, and land degradation [19–30].

The remainder of this chapter deals with genetics, characteristics, advantages and disadvantages, land suitability, soil improvement, and comparison with tropical volcanic residual soils. This research was conducted in West Lampung Transect Road, West Lampung, Lampung Province, Sumatra, Indonesia (**Figure 2**).
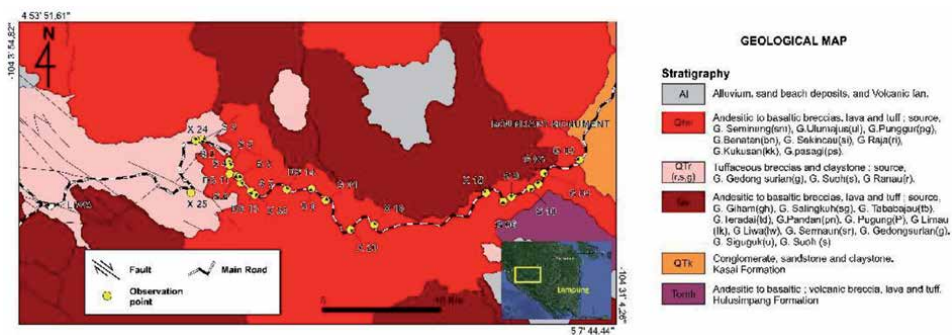
Figure 2.
Research area observations and geological map. (Modified from Soehaimi et al. [31]).

2. Genetic

The research area was on tropical wet climate [18]. Annual precipitation in this area was more than 2000 mm per year [32]. The region's geography is characterized by rolling hills with a V valley shape, a medium to a steep slope, and an altitude of 850–1150 meters above sea level (see **Figure 2**). The landscape regulates the flow patterns of regional research into radial, parallel, and sub-dendritic (see **Figure 2**). An important aspect that forms the romance of the research area today is the Sumatra Fault that passes through the area. Geographical conditions of the research area and

Figure 3.
Tropical volcanic residual soil.

Figure 4.
Volcanic breccias.
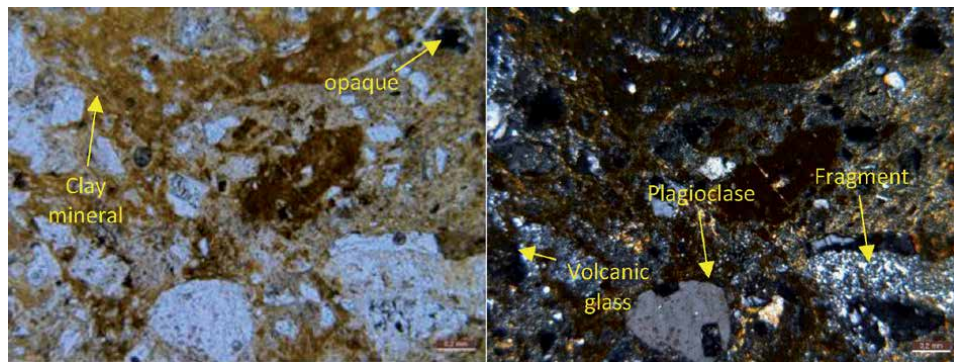
Figure 5.
Rock photomicrograph.

earth dynamics processes formed volcanic soil with a thickness of more than 20 m [28] (**Figure 3**).

Based on field findings and petrographic analysis, the research area consists of volcanic breccias with tuff components embedded in the tuff, sand, and clay matrix. (see **Figures 2** and **4**).

Tuff, the dominant rock, is characterized by crystal tuff and lithic tuff. Those tuff exhibit welded and flow structures, porphyritic and clastic textures, consisting of fragments and cement. The fragments consist of feldspar (partially insulated and alkaline feldspar type), quartz (showing embayment), plagioclase (andesine type), pyroxene, epidote, sericite, iron oxide, opaque minerals, and biotite embedded in the flow-textured volcanic glass base (**Figure 5**).

The rocks that make up the research area are deposited on land. The rock is deposited in a hydrothermal alteration environment. Evidence of hydrothermal alteration in the presence of geothermal manifestations around the research area, namely in the Mt. Seminung to the north and in the Suoh area, Mt. Sekincau, to the south [33].

3. Soil geochemistry

Volcanic glass, mica, and feldspar, as the main components of the rock source, are mainly submerged in clay minerals [34]. Based on XRD analysis, clay minerals are made up of kaolinite, dickite, nacrite, halloysite, illite, montmorillonite, and chlorite. Other minerals, including quartz, hematite, magnetite, and cristobalite, were present (**Figure 6**).

Kaolinite, dickite, nacrite, and halloysite are kaolinite groups {Al2Si2O5 (OH)4} [31]. Hunt and Yuan et al. [35, 36] noted that the occurrence of kaolinite and halloysite indicates soil extracted from volcanic rocks with a felsic composition. They described the forming climate at tropical temperatures, neutral to acidic pH conditions, free drainage, and porous rocks. Kaolinite and halloysite are secondary minerals commonly present in Andisols [37]. Both minerals are derived from feldspar and chlorite weathering [38]. Nacrite and dickite are clay minerals from the rarest group of kaolinites. The mineral is a transition from an illite mineral. Chen et al. [39] revealed that the presence of nacrite and dickite was associated with tuff deposition. These minerals are produced in the hydrothermal alteration environment.

The illite mineral {(K, H3O)(Al, Mg, Fe)2(Si, Al)4O10[(OH)2, (H2O)} is defined as clay-sized mica contained in clay rocks. Illite is a clay mineral formed in areas with mild climate characteristics or in mountain tropics. This kind of clay is made from weathering rocks rich in K and Al under high pH conditions. Generally,
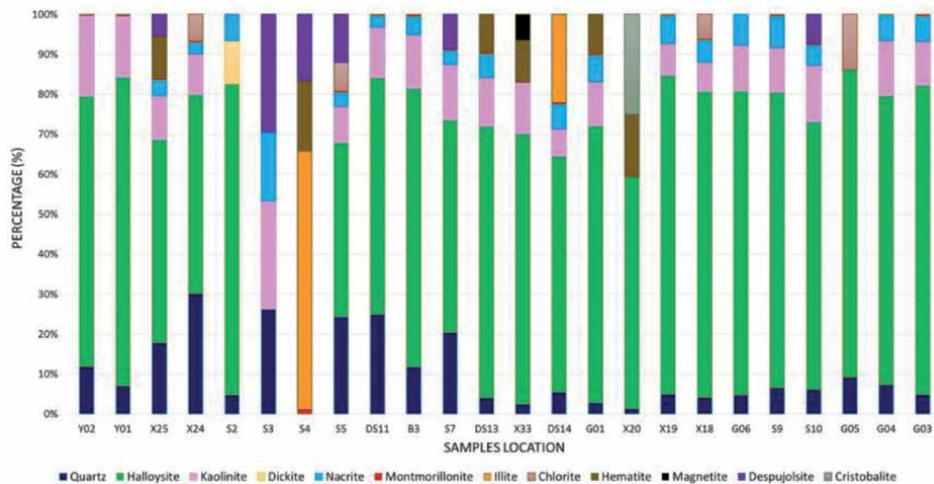
Figure 6.
Soil composition of mineralogy.

these minerals are formed by weathering mica minerals such as muscovite and feldspar. Chlorite {(Mg, Fe)3 (Si, Al)4O10(OH)2 • (Mg, Fe)3 (OH)6} is a secondary mineral, typically found in igneous rock, formed from primary Fe-Mg minerals.

Montmorillonite {(Na; Ca)0:3(Al; Mg)2Si4O10(OH)2. NH2O} is a mineral subclass of the smectite group, formed from the intemperate mica, feldspar, and volcanic ash. The mechanism that acts on the shape of these minerals is the process of neoformation. This phase is typical in source rocks of volcanic glass composition [40, 41]. Ryan and Huertas [42] have proposed that the occurrence of kaolinite-montmorillonite in soil suggests that the soil parent material is andesitic that influenced by hydrothermal alteration.

Hematite (Fe2O3) is an iron (III) oxide mineral. Hematite minerals of the clay size can also occur as secondary minerals produced by soil weathering processes and iron oxides or other oxyhydroxides, such as goethite, responsible for the red color of the soil in the tropics [43].

Magnetite (Fe3O4) is a mineral and one of the three most common iron oxides in nature. This mineral has magnetic properties. Magnetite, black, a relatively common metallic mineral, is also one of the most important iron ores of modern society, occurring in various igneous, pegmatite, contact metamorphic rocks hydrothermal veins [44].

Cristobalite (SiO2) is the stable form of silica. This mineral is formed at very high temperatures in medium-acid volcanic rocks [45, 46]. Despujolsite {Ca3Mn4 + (SO4) 2 (OH) 6 • 3H2O} is a mineral formed in hydrothermal manganese deposits [47].

4. Characteristics

Centered on Hardjowigeno [48]; Subardja et al. [49], the West Lampung Semi-Detailed Soil Map on a scale of 1:50,000 in 2016 released by the Agricultural Research and Development Agency, and WRB map (https://www.isric.org/explore/wrb accessed on January, 01st, 2021) the research area are made up of Andosol-type soil. The soil is acidic, PH <6, CEC is medium - Low, storage capacity and water absorption are very high; N, P, K, Ca, Mo, Mg content and microbial activity low-very low, and moderate to good drainage conditions/well-drained soils.

Figure 7.
Soil cracking.

Based on observations in the field, generally, the soil in the research area has a brownish-red color, the characteristics of it loose when it is dry and sticky when it is wet, groove erosion can be observed, and it is easy to break off if there is additional water in the rainy season. The soil surface can be seen as the soil severely degraded with very large angular or platy aggregates and restricted pore space (see **Figures 3** and 7).

Based on laboratory analysis (**Table 1**), the soil of the research area is included in the high plasticity silt type (MH) [50]; has characteristics low to medium plasticity characteristics (LL Brine 32.12% - 68.66%) [51, 52]. This soil has a specific gravity of 2.41–3.03. According to Bowles [53], the soil of the research area consists of mica and iron. Next, the soil has a wet unit weight of 1.27 g/cm^3–2.15 g/cm^3 and porosity 35.25% to 67.00%, based on de Castro et al. [54] these characteristics belonged to the soil which has clayey silt and uniform grain size, and inorganic soil type. The soil has a liquid limit >50%, has a plasticity index>17%. Prakash and Jain [55] categorize this type of soil as soil with high plasticity. The permeability of this soil is 4.63E-11 to 5.54E-05 m/s (soil with small to sufficient permeability) [56]. The engineering characteristics of this soil are cohesion values of 0.008 kg/cm^2 to 1,675 kg/cm^2 and internal shear angles 18.36° to 39.26°. These values represent that the soil of the research area is in a very loose to solid state/good and slide hazard [57].

5. Soil microstructure

The soil microstructure investigation was carried out using a scanning electron microscope (SEM), and SEM images at different magnifications are shown in **Figure 8**. SEM photos show that the soil microstructure of the soil of the research area is an aggregation of soil particles with fractures and pores (see **Figure 8**). The percentage of soil aggregation compared to fractures and pores is 70:30. This Figure implies that soil aggregation is dominant against fractures and pores, causing the soil permeability of the volcanic residue in the research area to be small to relatively permeable.

From **Figure 8**, it can be seen that the soil aggregate is kaolinite in the form of platy, illite in the form of curved and spongy sheets, and halloysite in the form of

No	Code	Specific Gravity (GS)	Porosity (%)	Liquid Limit (%)	Plasticity Index (IP) (%)	Permeability (m/s)	Wet Unit Weight γs (g/cm^3)	Cohesion (Kg/Cm^2)	Internal Friction Angle (Deg)	LL Brine (%)
1	X25	2,84	54,66	79,70	29,74	7,15E-08	1,78	0,00829	32,4118	53.55
2	S1	2,59	55,60	70,37	36,03	1,65E-09	1,61	0,06626	39,2644	50.00
3	X24	2,72	59,53	94,51	28,85	1,48E-10	1,68	1,67528	24,2048	40.19
4	S2	2,41	53,20	67,65	33,78	2,11E-06	1,69	1,03402	18,6025	101.17
5	S3	2,65	62,70	56,70	22,16	2,05E-10	1,46	1,15602	19,7825	46.64
6	S4	2,78	64,30	54,75	15,59	1,39E-07	1,27	0,71624	34,9597	68.66
7	S5	2,70	51,34	53,35	23,19	3,24E-07	1,80	1,5752	20,8547	48.68
8	DS11	2,80	56,17	71,50	30,75	5,54E-05	1,63	0,23531	20,2978	43.11
9	S6	2,45	45,87	59,22	27,84	3,19E-06	1,67	0,25504	34,5343	52.00
10	S10	2,50	48,57	61,00	26,95	4,63E-11	1,70	0,67808	33,5389	51.93

Table 1.
Some soil samples and their physical properties.
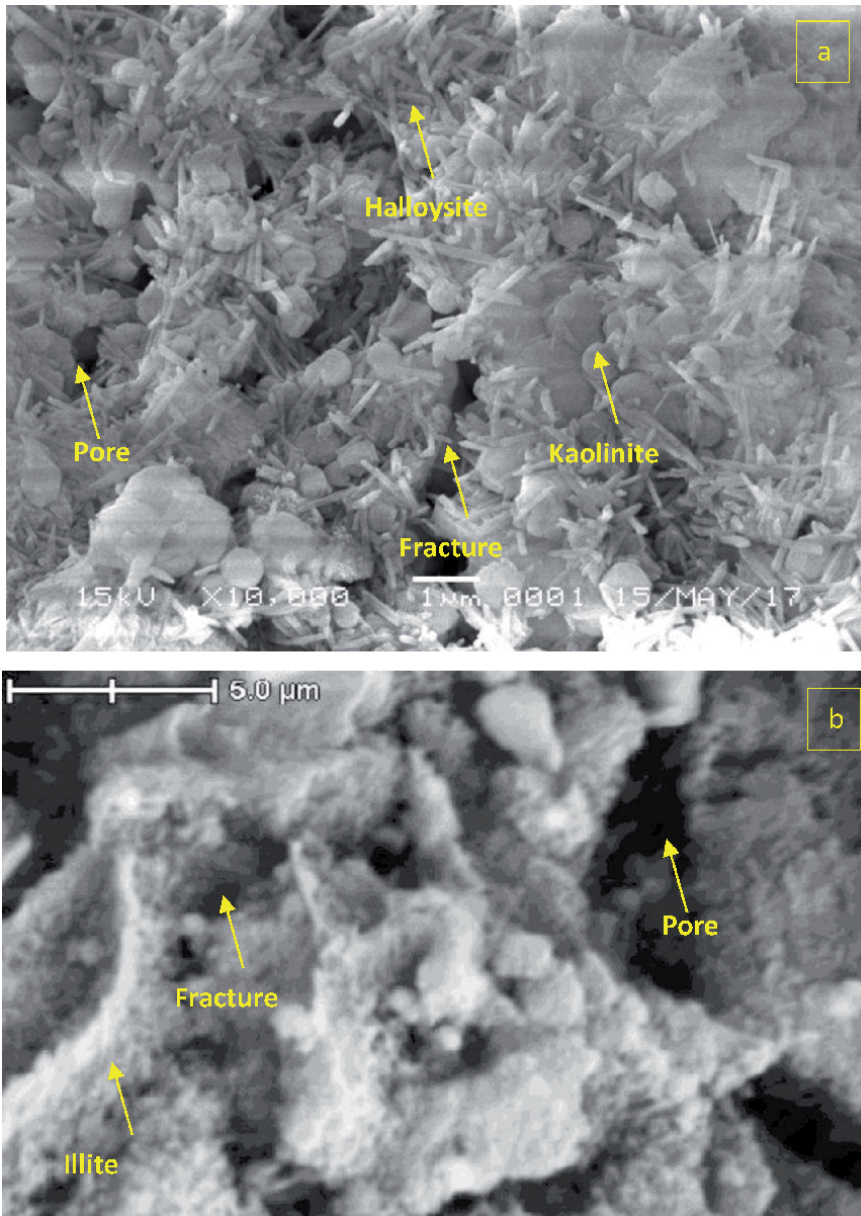
Figure 8.
a-b SEM tropical volcanic residual soil.

tubes. The three minerals are bound/cemented by iron oxide. Plate-shaped particles will be susceptible to degradation due to mechanical efforts and forces acting in nature. The shape of the plate particles causes the shear strength of the volcanic residual soil in the research area to be not so large [58, 59].

6. Advantages and disadvantages

People usually use volcanic residual soil as a growing medium for different kinds of plants [60, 61] because the soil has an organic layer and organic minerals [62]. Priddle et al. [63] argued that volcanic soil, especially red soil, is one of the

most fertile soils in the world as a product of volcanic material. This soil is very suitable for growing root crops such as potatoes and ginger. In some countries, such as Japan and China, volcanic residual soil is a critical resource with significant consequences for sustainable agricultural production and stable economic growth. These countries use this soil as a basis for infrastructure (roads, buildings, etc.) and landfills [64–67].

Because this type of soil is widely used for agriculture, fertilizers for plant fertilization will be intensive. One source said that the use of fertilizers in the West Lampung area was 17,845 tonnes. The subsidized fertilizer consists of urea of 9,365 tons, SP36 1,300 tons, ZA 1,230 tons, NPK (nitrogen, phosphorus and potassium) Fonseka 5,150 tons, and organic 800 tons. (https://www.liputan6.com/bisnis/read/4464775/alokasi- pupuk-bersubsidi-lampung-barat-tahun-2021-naik accessed on March 03, 2021). Hu et al. [68] and Ramos et al. [69] state that fertilizers in the soil will increase the likelihood of REE forming. The main areas with an increase of REE in the soil are restricted to regions where agriculture is intense. In agricultural areas, the main REE entrance is caused by the application of phosphate fertilizers. These factors form REE in addition to the parent material that forms the soil and the mineralogical content of the soil. REE will form in all types of rock and soil. Soils originated from igneous rocks, schists, and sandstone tend to contain more REE when compared to those originated from other materials. The adsorption of REE in soils is influenced by clay type and content, especially the concentrations of aluminum silicates and iron and manganese oxides. These last ones have the most remarkable adsorption capacity.

Because the soil type in the research area comes from Quaternary volcanic rock, dominant clayey soils, and contains manganese oxide (Despujolsite), we hypothesize that in the soil of the research area, there is an Low Rare Earth Element (LREE) type. One of the benefits of Rare Earth Element (REE) is in the electronics industry. REE will be used as a chemical catalyst for the manufacture of portable electronic device batteries.

On the other hand, volcanic residual soil still has its disadvantages. Iqbal et al. [28] observed that the liquid limit of volcanic residual soil is >50%, while some researchers [70–73] found that liquid limits >40% would decrease the shear strength of the soil and cause landslides (**Figure 9**). Landslides usually occur during the rainy season. Landslide due to soil lack of strength as rainwater infiltration induces positive pore water pressure and reduces the safety factors (FoS).

Figure 9.
Landslide event.

Many residual soils in the tropics exhibit abnormally high internal shear angles, which can be explained by soil particles randomly arranged by weathering [58]. Another reason the residual soil angle has a large enough internal shear angle is iron oxide in the soil. Zhang et al. [23] revealed that iron oxides in residual soils are present due to local enrichment and exist in the form of layers of clay aggregates binding them to coarser aggregations. Zhang et al. [58] stated that iron oxide in residual soil would cause poor compacting properties, but it is an agent to increase cementation and structural strength of the soil. The presence of iron oxide will make the internal friction angle in the soil quite large. The weakness of the bonds (cementation) formed by iron oxide is that when the soil is saturated with water, the cementation can be damaged or destroyed. The event will reduce soil cohesion. If the soil forms a slope, there will be a possibility of landslides.

Darajaat et al. [74] revealed that one of the factors that influence the stability of the volcanic residual soil slope is rainwater with an intensity condition of 10–43 mm/hour and 120–168 hours. This condition will reduce the slope safety factor by 2–30%. Another, Widisaputra et al. [75] simulated the stability of the volcanic residual soil slopes that were affected by earthquakes. The result is that the safety factor of the volcanic residual soil slopes will decrease by 1/3 to ½.

The observations of Iqbal et al. [76] concluded that the volcanic residual soil in the West Lampung area has swelling potential. This potential is due to the volcanic residual soil containing clay minerals such as kaolinite, halloysite, illite, and montmorillonite. The swelling-shrinking features that belong to this type of soil result in cracking, which occurs during the dry season. The fractures that occur would affect the local hydrological conditions. These conditions can impact the stability of slopes, agricultural production, and plantations [77–81]. On the other side, the mechanism of swelling and shrinking of the soil can cause considerable damage to the walls of the buildings [27, 82, 83].

Another thing that is concerned about is the corrosion process of steel. Veleva et al. [84]; Norhazilan et al. [85]; Noor and Al-Moubaraki [86]; Lim et al. [87]; Wasim and Shoaib [88]; Liu et al. [89] revealed that soil composed of silt and clay will have the highest level of corrosion compared to soil composed of rough grains (gravel to sand), this is related to the water content, the corrosion process will be high in soils with high water content. Iqbal et al. [29] stated that the properties of soil engineering (plasticity index, water content, and clay content) impact the corrosion process of steel. Their paper found that the water content had an adequate contribution of 24.79% to the corrosion process. The corrosion process (in this case, the corrosion rate) will increase if 1% of the index plasticity and water content is added.

Since the soil characteristic of the research area is silt and clay, this process should be taken into account when building infrastructure (such as water/gas/oil buried pipelines or building foundations).

7. Land suitability

According to several researchers [90–94], there have been very drastic shifts in land use in West Lampung, Sumatra, Indonesia over the last ten years (2000–2010). Primary forests have declined significantly, while dryland agriculture (coffee-based farming), rice fields, and residential areas have grown. These adjustments cause soil erosion and surface runoff. According to the author's observations in the region, soil depletion resulted in erosion and landslides during the rainy season (see **Figure 9**). Meanwhile, during the dry season, there is drought and soil cracking (**Figure 7**). This phenomenon indicates the occurrence of soil quality issues in the West Lampung

region. As a result of these issues, it is assumed that the volcanic residual soil of the study area has unique characteristics for specific land use.

Based on our research, using a statistical approach (K-Means Clustering) (**Tables 2** and **3**) and qualitative analysis, the soils of the research area are divided into two clusters (**Figure 10**). The first cluster soils with low plasticity, LL brine value of 50% or less (low to intermediate salt content). This cluster included soils with the inactive soil category (< 1) and contained minerals: despujolsite, hematite, chlorite, montmorillonite ($< 0.4\%$), and quartz. While the second cluster soils with intermediate to high plasticity have LL brine values greater than 50% (intermediate to high salt content), and soils with the normal to active soil category (> 1). Despujolsite, hematite, magnetite, illite, montmorillonite ($> 0.4\%$), dickite, and quartz are the minerals that can be found in this cluster.

The following is an example of soil suitability. The first cluster includes swell-shrink features ranging from zero to intermediate. This soil type has well-structured soil, strong consistency, low seepage losses, and a limited pore area [67, 95]. The soils would be ideal for agriculture, building foundations, and earth construction due to their characteristics [67].

The second cluster is distinguished by intermediate to high swell-shrink characteristics [96]. These soils are dispersed because of their high Natrium content. The soils had been heavily eroded, and platy aggregates had formed [95]. These traits contribute to slow seedling emergence and germination [97]. These soils have insufficient soil intensity [98]. Infiltration in these soils can be rapid at first, but they later stay wet for long periods, causing erosion, infrastructure destruction, and trafficability problems [99]. Because of their characteristics, soils in this cluster are well suited for primary forest growth.

No	Sample Code	Soil Activity	LL_brine	Montmorillonite	Clusters
1	X25	1.25	53.55	0.6	2
2	X24	0.82	40.19	0.4	1
3	S2	0.92	101.17	0.9	2
4	S3	1.51	46.64	0.4	2
5	S4	1	68.66	0.9	2
6	S5	0.91	48.68	0.4	1
7	DS11	0.92	43.11	0.4	1
8	S10	0.97	51.93	0.4	2
9	G05	1.26	59.17	0.6	2
10	G03	0.99	47.26	0.5	2

Table 2.
Tropical volcanic residual soil cluster.

	Cluster		Error		F	Sig.
	Mean Square	**df**	**Mean Square**	**df**		
Soil_Activity	37.354	1	.327	54	114.313	.000
LL_brine	18.026	1	.685	54	26.327	.000
Montmorillonite	20.784	1	.634	54	32.800	.000

Table 3.
ANOVA.
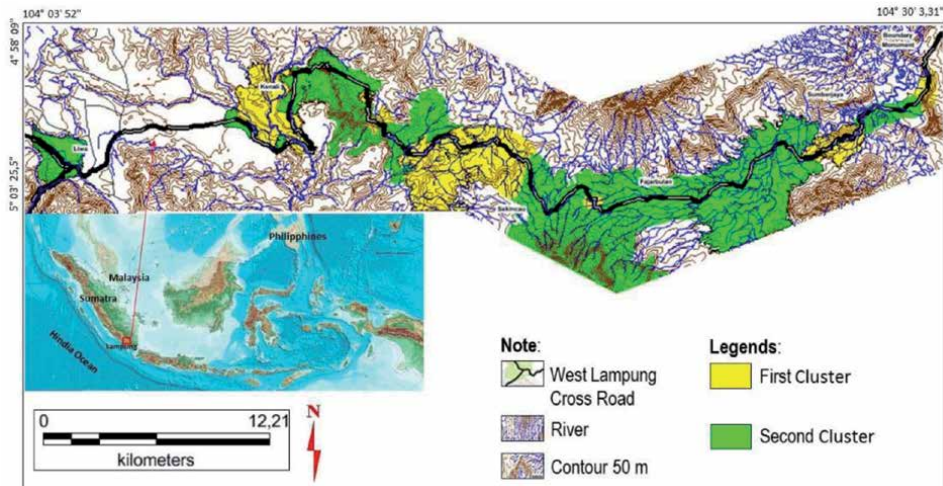
Figure 10.
Soil cluster map.

8. Soil improvements

Volcanic residual soil is unique for engineering purposes. For engineering purposes, much volcanic residual soil is compacted to increase soil strength and/or decrease permeability. This is done to increase density, reduce porosity, and shrink pores. Volcanic residual soil exhibits wretched incompetence, but this property can often be overcome by drying. Significant changes in cohesion and internal friction angles can be induced during drying to make volcanic residual soil suitable for engineering purposes.

One example is that a Road Engineer would dry volcanic residual soil in the sun to irreversibly reduce its moisture content or apply calcined lime (CaO), gypsum, cement, and/or bitumen to create an exothermic dehydration reaction [67, 96, 100].

Another way to improve the physical properties of volcanic soil is by using agro-ecological methods, which is not allowing volcanic residual soil to be bare, the goal is to prevent the soil from being easily eroded [67, 96, 101, 102]. Planting elephant grass is an agro-ecological effort. In addition to helping increase soil cohesion, elephant grass can also be used as animal feed.

9. Comparison

In several years, Buurman, P. [103], Northmore, et al., [104], and Prasetyo and Gilkes [105], research on the characteristics of volcanic residual soils in Indonesia was conducted. Case studies involved soils on andesitic volcanic material between 100 and 1000 m altitude in West and East Java, West Sumatra acid volcanic tuffs, and South-East Sulawesi ultramafic rocks in Indonesia. Discussions are mainly on soil classification, soil genetic, engineering characteristics, and engineering use.

On West Java, Indonesia, Latosols in a toposequence between 40 and 1020 m altitude on andesitic rocks and derived sediments were classified according to Soil Taxonomy. Although soils can be classified according to Soil Taxonomy, several of the boundaries in Soil Taxonomy units are inconvenient for practical use. It is proposed to define Red and Yellowish Red Latosols. The Location of the research took place on the Salak and Gede Volcanoes, West Java. This area consists

of intermediary volcanic tuffs (andesite). Soil, which is the result of weathering of the source rock, contains halloysite as the main mineral that already shows some kaolinite characteristics (metahalloysite). This mineral is accompanied by fair amounts of interstratified illite-vermiculite, some illite-chlorite, goethite, and quartz.

The subsequent research is on the west and north to east slopes of the Lawu Volcano, East Java, Indonesia. The physical chemistry and mineralogy were studied of two sequences of soils: Andosols, Latosols, Mediterranean Soils, and Grumusols on the west slope and Mediterranean Soil on the north-east slope of the Lawu Volcano. Soils are developed from pyroxene andesite parent material on Upper Pleistocene and Holocene surfaces. Weathering gradually increases downslope. Andosols are the least weathered soils, while Mediterranean Soils at the lowest altitude are most strongly weathered. Downslope, free iron in soils, and particularly iron concretions in the sand fraction increase considerably, hence, perhaps the red color of soils at lower altitudes. Weathering with the prevailing high rainfall and constantly high (isohyperthermic) temperature produces deep soils with predominantly halloysitic mineralogy. Gibbsite is formed in medium acid soils. Smectite appears in neutral to mildly alkaline soils with a high supply of bases.

The presence was demonstrated of Oxisols on felsic and ultramafic parent materials on South-East Sulawesi. On ultramafic rocks, there was an association of Inceptisols, Alfisols, Ultisols, and Oxisols governed by topography. The rocks are mainly peridotites with a varying degree of serpentinization. They are separated from the main body by a fault zone with schists and phyllites. Montmorillonite minerals predominate in the clay fractions with additional vermiculite-illite, margarite, illite, and quartz following a high supply of bases—mainly magnesium—by weathering of peridotite. Montmorillonites form in contact with the disintegrating rock or in places with magnesium-rich groundwater. As soon as Mg becomes depleted, interstratified minerals form that finally change to kaolinite.

The soils studied in West Sumatra occur on Tertiary or Early Quaternary volcanic tuffs of dacitic and liparitic composition. The landscape is an undulating dissected peneplain, and erosion is only slight. The soil Colors were mainly strong brown and redder. Textures were very clayey. The soils were strongly desaturated. Clay fractions were invariably dominated by kaolinite, showed minor amounts of gibbsite, chlorite, goethite, and quartz.

Based on the literature review above, the soil in the research area has several similarities and differences in characteristics. The equation lies in the color reddish brown-brownish red, iron, and soils with predominantly halloysitic mineralogy. Its distinguishing characteristic is the content of other minerals. This difference is due to differences in geographical location and surrounding geological conditions. It is known that an area with mountainous conditions, tropical climates, bypassed by fault structures, and there is a manifestation of the geothermal/hydrothermal alteration environment, will produce soil with a sufficiently varied and concentrated clay mineral content, as well as minerals that are characteristic of the hydrothermal alteration region (e.g., Despujolsite) as in the research area.

10. Conclusions

Tropical volcanic residual soils of the research area have several similarities and differences in characteristics compared to other volcanic residual soils in the Indonesian area. The equation lies in the color reddish brown-brownish red, iron, and soils with predominantly halloysitic mineralogy. Its distinguishing characteristic is the content of other minerals. This difference is due to differences in

geographical location and surrounding geological conditions. It is known that an area with mountainous conditions, tropical climates, bypassed by fault structures, and there is a manifestation of the geothermal/hydrothermal alteration environment, will produce soil with a sufficiently varied and concentrated clay mineral content, as well as minerals that are characteristic of the hydrothermal alteration region (e.g., Despujolsite) as in the research area.

The soil has a specific use. For the first cluster, the community can use the soil to growing some plants and vegetables because it is very fertile. The soil can be used for building foundations, but the soil can cause steel corrosion, requiring special attention when using it. Another particular concern is for the soil in the second cluster. This soil type has the potential to swelling and landslide during the rainy season. Soil improvements are needed when the community will use them. Finally, the soil in the research area has Rare Eart Element (REE) potential. Low Rare Earth Element (LREE) is the type that is likely to be in the soil.

Acknowledgements

Conflict of interest

This statement is to certify that all authors have seen and approved the manuscript being submitted. We warrant that the article is the Authors' original work. We warrant that the article has not received prior publication and is not under consideration for publication elsewhere. On behalf of all Co-Authors, the corresponding Author shall bear full responsibility for the submission.

This research has not been submitted for publication, nor has it been published in whole or in part elsewhere. We attest that all authors listed on the title page have contributed significantly to the work, have read the manuscript, attest to the validity and legitimacy of the data and its interpretation, and agree to its submission to IntechOpen.

All authors agree that the author list is correct in its content and order and that no modification to the author list can be made without the formal approval of the Editor-in-Chief. All authors accept that the Editor-in-Chief's decisions over acceptance or rejection or in the event of any breach of the Principles of Ethical Publishing in the IntechOpen being discovered of retraction are final.

Notes/thanks/other declarations

In particular, we would like to thank M.S. Sadewo, Abdul W. Asykarullah, FTG UNPAD 2016 students, and all those who have helped so that this paper can be completed properly.

Author details

Prahara Iqbal[1,2]*, Dicky Muslim[1], Zufialdi Zakaria[1], Haryadi Permana[2], Arifan Jaya Syahbana[2], Nugroho Aji Satriyo[2], Yunarto Yunarto[2], Jakah Jakah[2] and Nur Khoirullah[1]

1 Padjadajaran University, Bandung, Indonesia

2 Indonesian Institute of Sciences, Bandung, Indonesia

*Address all correspondence to: praharaiqbal123@gmail.com

IntechOpen

References

[1] Wesley LD. Fundamentals of soil mechanics for sedimentary and residual soils. John Wiley & Sons; 2009.

[2] Blight G. Origin and formation of residual soils. Mechanics of Residual Soil. 1997;1:15.

[3] Wesley L. Residual soils and the teaching of soil mechanics. In 2013.

[4] Sunarminto S, Bambang H, Nurudin M, Sulakhudin S, Wulandari C. Peran Geologi dan Mineralogi Tanah untuk Mendukung Teknologi Tepat Guna dalam Pengelolaan Tanah Tropika. Yogyakarta, Indonesia: Gadjah Mada University Press; 2014.

[5] Little A. The engineering classification of residual torpical soils. In 1969.

[6] Dearman W, Baynes F, Irfan T. Engineering grading of weathered granite. Engineering Geology. 1978;12:345-374.

[7] Sadisun I, Bandono B. Pengenalan derajat pelapukan batuan guna menunjang pelaksanaan berbagai pekerjaan sipil dan operasi penambangan. Bul Ilmiah Gakuryoku. 1998;10-22.

[8] Sudarsono U, Hasibuan G. Karakteristik Geologi Teknik Tanah Residu Batuan Sedimen Kuarter Bawah Daerah Kertajati, Majalengka, Jawa Barat Engineering Geological Characteristics of the Residual Soil, Lower Quaternary Sediments in Kertajati Region, Majalengka, West Java. Jurnal Geologi Indonesia. 2011;6(3): 177-189.

[9] Elifas D. Geologi Kuarter Kaitannya Dengan Gerakan Tanah Sebagai Salah Satu Bencana Alam yang Menonjol di Indonesia. Makalah Dalam Loka Karya Geologi Kuarter,(Kerjasama PPPG-JICA). 1989;16-18.

[10] Rahardjo W, Sukandarrumidi, Rosidi H. Peta geologi gersistem Jawa lembar Yogyakarta, Jawa, skala 1:100.000, edisi 2. Pusat Penelitian dan Pengembangan Geologi. 1995;

[11] Sukamto R, Ratman N, Simandjuntak TO. Peta Geologi Indonesia Skala 1:5.000.000. Bandung, Indonesia: P3G; 1996.

[12] Ali A, Huang J, Lyamin A, Sloan S, Griffiths D, Cassidy M, et al. Simplified quantitative risk assessment of rainfall-induced landslides modelled by infinite slopes. Engineering Geology. 2014;179: 102-116.

[13] Wesley LD. Fundamentals of soil mechanics for sedimentary and residual soils. Wiley Online Library; 2010.

[14] Saroso BS. Geology and Landslide in Indonesia. Proceeding of National Seminar Slope Bandung. 2002;1-13.

[15] Wibawa Y, Sugiarti K, Soebowo E. Characteristics and engineering properties of residual soil of volcanic deposits. In IOP Publishing; 2018. p. 012041.

[16] Wilson M. The origin and formation of clay minerals in soils: past, present and future perspectives. Clay minerals. 1999;34(1):7-25.

[17] Fredlund DG, Rahardjo H. An overview of unsaturated soil behaviour. Geotechnical special publication. 1993;1-1.

[18] Huat BB, Toll DG, Prasad A. Handbook of tropical residual soils engineering. CRC Press; 2012.

[19] Jia J, Zhou C, Jiang N, Lu S. Analysis of Stability of Residual Soil Slope and Treatment Measure. Electronic Journal of Geotechnical Engineering. 2014;19:3889-3898.

[20] Lee C, Byun Y-H, Lee J-S. Geotechnical and Geoacoustic Properties of Volcanic Soil in Ulleung Island, East Sea of Korea. Marine Georesources & Geotechnology. 2016;34(7):659-667.

[21] Faridlah M, Tohari A, Iryanti M. Hubungan Parameter Sifat Magnetik Dan Sifat Keteknikan Tanah Pada Tanah Residual Vulkanik. Wahana Fisika. 2016;1(1):54-76.

[22] Taboada T, Rodríguez-Lado L, Ferro-Vázquez C, Stoops G, Cortizas AM. Chemical weathering in the volcanic soils of Isla Santa Cruz (Galápagos Islands, Ecuador). Geoderma. 2016;261:160-168.

[23] Zhang X, Kong L, Yin S, Chen C. Engineering geology of basaltic residual soil in Leiqiong, southern China. Engineering Geology. 2017;220:196-207.

[24] Lemougna PN, Wang K, Tang Q, Nzeukou A, Billong N, Melo UC, et al. Review on the use of volcanic ashes for engineering applications. Resources, Conservation and Recycling. 2018;137:177-190.

[25] Zolkepli M, Ishak M, Zaini M. Analysis of slope stability on tropical residual soil. International Journal of Civil Engineering and Technology. 2018;9(2):402â.

[26] Xia J, Cai C, Wei Y, Wu X. Granite residual soil properties in collapsing gullies of south China: spatial variations and effects on collapsing gully erosion. Catena. 2019;174:469-477.

[27] Stell E, Guevara M, Vargas R. Soil swelling potential across Colorado: A digital soil mapping assessment. Landscape and Urban Planning. 2019;190:103599.

[28] Iqbal P, Muslim D, Zakaria Z, Permana H, Syahbana AJ, Yunarto J. Geotechnical Characteristics of Volcanic Red Clay Soil Related to Geoengineering Problem in Sekincau, Sumatra, Indonesia. International Journal of Advanced Science and Technology. 2020;29(7):3166-3173.

[29] Iqbal P, Muslim D, Zakaria Z, Permana H, Yunarto Y. RELATIONSHIP BETWEEN SOIL ENGINEERING PROPERTIES AND CORROSION RATE IN ANDESITIC VOLCANIC SOILS, WEST LAMPUNG, SUMATRA, INDONESIA. Jurnal Teknologi. 2020;83(1):117-125.

[30] Uyeturk CE, Huvaj N, Bayraktaroglu H, Huseyinpasaoglu M. Geotechnical characteristics of residual soils in rainfall-triggered landslides in Rize, Turkey. Engineering Geology. 2020;264:105318.

[31] Soehaimi A, Muslim D, Kamawan I, Negara RS. Microzonation of the Liwa City on the Great Sumatera Active Fault and Giant Ranau Volcanic Complex in South Sumatera, Indonesia. In: Engineering Geology for Society and Territory-Volume 5. Springer; 2015. p. 1015-9.

[32] Iqbal P. Geologi Kuarter dan Cuaca Daerah Lampung Barat, Kaitannya dengan Kejadian Longsor (Studi Kasus Jalur Jalan Transek Lampung Barat). Jurnal Geologi dan Sumberdaya Mineral. 2018;19(3):163-169.

[33] Energi K, Mineral SD. Potensi Panas Bumi Indonesia Jilid 1. Direktorat Panas Bumi, Ditjen EBTKE dan Pusat Sumber Daya Mineral, Batubara, dan Panas Bumi, Badan Geologi Jakarta (ID): Kementerian Energi dan Sumber Daya Mineral. 2017;

[34] Churchman GJ, Lowe DJ. Alteration, formation, and occurrence of minerals in soils. CRC press; 2012.

[35] Hunt RE. Geotechnical engineering investigation handbook. Crc Press; 2005.

[36] Yuan P, Tan D, Annabi-Bergaya F. Properties and applications of halloysite nanotubes: recent research advances and future prospects. Applied Clay Science. 2015;112:75-93.

[37] Joussein E, Petit S, Churchman J, Theng B, Righi D, Delvaux B. Halloysite clay minerals—a review. Clay minerals. 2005;40(4):383-426.

[38] Wilson M. Factors of soil formation: parent material. As exemplified by a comparison of granitic and basaltic soils. Soils: basic concepts and future challenges Cambridge University Press, Cambridge. 2006;113-129.

[39] Chen FH. Foundations on expansive soils. Vol. 12. Elsevier; 2012.

[40] Chesworth W. Encyclopedia of soil science. Springer Science & Business Media; 2007.

[41] Frolova JV, Gvozdeva IP, Kuznetsov NP. Effects of hydrothermal alterations on physical and mechanical properties of rocks in the Geysers Valley (Kamchatka Peninsula) in connection with landslide development. In 2015. p. 1-6.

[42] Ryan P, Huertas FJ. The temporal evolution of pedogenic Fe–smectite to Fe–kaolin via interstratified kaolin–smectite in a moist tropical soil chronosequence. Geoderma. 2009;151(1-2):1-15.

[43] Cornell RM, Schwertmann U. The iron oxides: structure, properties, reactions, occurrences and uses. John Wiley & Sons; 2003.

[44] Harrison RJ, Dunin-Borkowski RE, Putnis A. Direct imaging of nanoscale magnetic interactions in minerals. Proceedings of the National Academy of Sciences. 2002;99(26):16556-16561.

[45] Bishop JL, Ethbrampe EB, Bish DL, Abidin ZL, Baker LL, Matsue N, et al. Spectral and hydration properties of allophane and imogolite. Clays and Clay Minerals. 2013;61(1):57-74.

[46] Matsui M, Sato T, Funamori N. Crystal structures and stabilities of cristobalite-helium phases at high pressures. American Mineralogist. 2014;99(1):184-189.

[47] Gaudefroy C, Granger M-M, Permingeat F, Protas J. La despujolsite, une nouvelle espece minerale. Bulletin de Minéralogie. 1968;91(1):43-50.

[48] Hardjowigeno S. Klasifikasi Tanah dan Pedeogenesis. 1993;

[49] Subardja D, Ritung S, Anda M, Sukarman ES, Subandiono R. Petunjuk Teknis Klasifikasi Tanah Nasional. Balai Besar Penelitian dan Pengembangan Sumberdaya Lahan Pertanian, Badan Penelitian dan Pengembangan Pertanian, Bogor. 2014;22.

[50] Casagrande A. Classification and identification of soils. Transactions of the American Society of Civil Engineers. 1948;113(1):901-930.

[51] Jang J, Carlos Santamarina J. Fines classification based on sensitivity to pore-fluid chemistry. Journal of Geotechnical and Geoenvironmental Engineering. 2016;142(4):06015018.

[52] Santamarina JC, Park J, Terzariol M, Cardona A, Castro GM, Cha W, et al. Soil properties: physics inspired, data driven. In: Geotechnical fundamentals for addressing new world challenges. Springer; 2019. p. 67-91.

[53] Bowles JE. Engineering Properties of Soils and their Measurements 4th edition. New Delhi: McGraw Hill Education (India) Private Limited; 2012.

[54] de Castro J, Ballesteros F, Méndez A, Tarquis AM. Fractal analysis of Laplacian pyramidal filters applied to segmentation of soil images. The Scientific World Journal. 2014;2014.

[55] Prakash K, Sridharan A. Free swell ratio and clay mineralogy of fine-grained soils. Geotechnical Testing Journal. 2004;27(2):220-225.

[56] Igwe O, Mode W, Nnebedum O, Okonkwo I, Oha I. The analysis of rainfall-induced slope failures at Iva Valley area of Enugu State, Nigeria. Environmental earth sciences. 2014;71(5):2465-2480.

[57] Kaniraj SR. Design aids in soil mechanics and foundation engineering. Tata McGraw-Hill; 1988.

[58] Zhang X, Liu X, Chen C, Kong L, Wang G. Engineering geology of residual soil derived from mudstone in Zimbabwe. Engineering Geology. 2020;277:105785.

[59] Heidemann M, Bressani LA, Flores JA. Hydrothermal clays and their influence on slope stability in residual soils of Southern Brazil. Bulletin of Engineering Geology and the Environment. 2021;80(2):795-811.

[60] Leamy M. International committee on the classification of Andisols (ICOMAND). Circular Lett 10, 29 Feb. 1988;

[61] Shoji S, Nanzyo M, Dahlgren R. Volcanic ash soils: genesis, properties and utilization. Elsevier; 1994.

[62] Richmond RH, Golbuu Y, Shelton III AJ. Successful management of coral reef-watershed networks. In: Coasts and Estuaries. Elsevier; 2019. p. 445-459.

[63] Priddle J, Lacey D, Look B, Gallage C. Residual Soil Properties of South East Queensland. Australian Geomechanics Journal. 2013;48(1):67-76.

[64] Hino T, Lejeune A. Pumped storage hydropower developments. 2012;

[65] Yu H-Y, Li F-B, Liu C-S, Huang W, Liu T-X, Yu W-M. Iron redox cycling coupled to transformation and immobilization of heavy metals: implications for paddy rice safety in the red soil of South China. In: Advances in Agronomy. Elsevier; 2016. p. 279-317.

[66] Oji AS, Akinbiyi OA, Olayiwola KO. Geotechnical Characterization of Soil, a Tool in Determining The Suitability of Soil for Construction Purpose, A Case Study of Federal Polytechnic Ede, Osun State, Southwestern Nigeria. IJOSEET. 2016;1(2):16-23.

[67] Danso H. Suitability of Soil for Earth Construction as Building Material. Advancements in Civil Engineering & Technology. 2018;2(3):199-211.

[68] Hu Z, Haneklaus S, Sparovek G, Schnug E. Rare earth elements in soils. Communications in Soil Science and Plant Analysis. 2006;37(9-10): 1381-1420.

[69] Ramos SJ, Dinali GS, Oliveira C, Martins GC, Moreira CG, Siqueira JO, et al. Rare earth elements in the soil environment. Current Pollution Reports. 2016;2(1):28-50.

[70] Nengsih S. Pengaruh Kadar Air Terhadap Kestabilan Lereng (Kampus Politeknik Negeri Padang). Jurnal Ilmiah Rekayasa Sipil. 2015;12(2):36-45.

[71] Fan C-C, Chang H-W. The role of time in the hydrological behavior of residual soil slopes during rainfall events. Catena. 2015;124:1-8.

[72] Bidyashwari I, Kushwaha R, Chandra M, Okendro M. Physical properties of soil and its implication to slope stability of Nungbi Khunou, NH-150, Manipur. International Journal of Geosciences. 2017;8:1332-1343.

[73] Kristo C, Rahardjo H, Satyanaga A. Effect of hysteresis on the stability of residual soil slope. International soil and water conservation research. 2019;7(3):226-238.

[74] Darajaat MR, Iqbal P, Zakaria Z, Muslim D. PENGARUH INTENSITAS DAN DURASI HUJAN TERHADAP KESTABILAN LERENG TANAH RESIDUAL VULKANIK DI JALUR LIWA-KEMUNING, LAMPUNG BARAT. Geoscience Journal. 2020;4(2):181-190.

[75] Widisaputra R, Zakaria Z, Sophian RI, Iqbal P, Permana H. PENGARUH BEBAN GEMPA TERHADAP KESTABILAN LERENG TANAH DAERAH LIWA DAN SEKITARNYA, KABUPATEN LAMPUNG BARAT, LAMPUNG. Geoscience Journal. 2020;4(5):411-419.

[76] Iqbal p, Muslim D, Zakaria Z, Permana H, Satriyo NA, Syahbana AJ, Yunarto, Khoirullah N, Asykarullah AW. Swelling potential of volcanic residual soils in Sumatra (Indonesia) in relation to environmental issues. Environ. Socio.-econ. Stud. 2020; 8(4): 1-10.

[77] Kirby J, Bernardi A, Ringrose-Voase A, Young R, Rose H. Field swelling, shrinking, and water content change in a heavy clay soil. Soil Research. 2003;41(5):963-978.

[78] Yoo K, Amundson R, Heimsath AM, Dietrich WE. Spatial patterns of soil organic carbon on hillslopes: Integrating geomorphic processes and the biological C cycle. Geoderma. 2006;130(1-2): 47-65.

[79] Jiang H, Wang B, Inyang HI, Liu J, Gu K, Shi B. Role of expansive soil and topography on slope failure and its countermeasures, Yun County, China. Engineering geology. 2013;152(1): 155-161.

[80] Qi S, Vanapalli SK. Influence of swelling behavior on the stability of an infinite unsaturated expansive soil slope. Computers and Geotechnics. 2016;76:154-169.

[81] Stewart RD, Abou Najm MR, Rupp DE, Selker JS. Modeling multidomain hydraulic properties of shrink-swell soils. Water Resources Research. 2016;52(10):7911-7930.

[82] Pusch R, Yong RN. Microstructure of smectite clays and engineering performance. CRC Press; 2006.

[83] Al-Yaqoub TH, Parol J, Znidarcic D. Experimental investigation of volume change behavior of swelling soil. Applied Clay Science. 2017;137:22-29.

[84] Veleva L. Soils. ASTM International. OH; 2005. 387-404 p. (Corrosion Tests and Standards: Application and Interpretation).

[85] Norhazilan M, Nordin Y, Lim K, Siti R, Safuan A, Norhamimi M. Relationship between soil properties and corrosion of carbon steel. Journal of Applied Sciences Research. 2012;8(3): 1739-1747.

[86] Noor EA, Al-Moubaraki AH. Influence of soil moisture content on the corrosion behavior of X60 steel in different soils. Arabian Journal for Science and Engineering. 2014;39(7): 5421-5435.

[87] Lim KS, Yahaya N, Md Noor N, Mior Mohd Tahir SNF, Paik JK, Mohd MH. Effects of soil properties on the corrosion progress of X70-carbon steel in tropical region. Ships and Offshore Structures. 2017;12(7): 991-1003.

[88] Wasim M, Shoaib S. Influence of Chemical Properties of Soil on the Corrosion Morphology of Carbon Steel Pipes. Metals in Soil-Contamination and Remediation. 2019;

[89] Liu H, Dai Y, Cheng YF. Corrosion of underground pipelines in clay soil with varied soil layer thicknesses and aerations. Arabian Journal of Chemistry. 2020;13(2):3601-3614.

[90] Dariah A, Agus F, Arsyad S, Sudarsono S, Maswar M. Erosion and

surface runoff in coffee-based agricultural land in Sumberjaya, West Lampung. Agrivita. 2004;26(1):52-60.

[91] Dariah A, Agus F. Soil Quality of the Land under Coffee-Based Farming System (Case Study at Sumberjaya, West Lampung). Jurnal Tanah dan Iklim. 2012;(23).

[92] Dariah A, Agus F, Arsyad S. Relationship Between Soil Characteristics and Rate of Soil Loss on Coffee Base-Farming System at Sumberjaya, West Lampung. 2012;

[93] Astuti JW. Deteksi Perubahan Penggunaan Lahan di Kabupaten Lampung Barat. Thesis Institut Pertanian Bogor. 2016;

[94] Yustika RD, Somura H, Yuwono SB, Arifin B, Ismono H, Masunaga T. Assessment of soil erosion in social forest-dominated watersheds in Lampung, Indonesia. Environmental monitoring and assessment. 2019;191(12):1-15.

[95] Agriculture and Horticulture Development Board and British Beet Research Organisation. Principles of Soil Management. AHDB; 2019. 20 p.

[96] Ipswich City Council and Ipswich Rivers Improvement Trust. Ipswich Soil Management Guidelines. Amec Foster Wheeler; 2014 p. 51.

[97] Lal R, Stewart B. Soil Management for sustaining ecosystem services. Chapter 19. Principles of Sustainable Soil Management in Agroecosystems Lal R, Stewart B(eds) CRC Press Taylor & Francis Group, Boca Raton, FL. 2013;521-533.

[98] Fernández-Getino A, Duarte A. Soil management guidelines in Spain and Portugal related to EU Soil Protection Strategy based on analysis of soil databases. Catena. 2015;126:146-154.

[99] FAO. Voluntary guidelines for sustainable soil management. 2017;

[100] Neall VE. Volcanic soils. Land use, land cover and soil sciences. 2009;7:23-45.

[101] Perret S, Michellon R, Boyer J, Tassin J. Soil rehabilitation and erosion control through agro-ecological practices on Reunion Island (French Overseas Territory, Indian Ocean). Agriculture, ecosystems & environment. 1996;59(3):149-157.

[102] Perret S, Dorel M. Relationships between land use, fertility and Andisol behaviour: examples from volcanic islands. Soil Use and Management. 1999;15(3):144-149.

[103] Buurman P. Red soils in Indonesia. Pudoc; 1980.

[104] Northmore K, Culshaw M, Hobbs P, Hallam J, Entwisle D. Engineering geology of tropical red clay soils: summary findings and their application for engineering purposes. 1993.

[105] Prasetyo B, Gilkes R. Properties of iron-oxides from red soils derived from volcanic tuff in West Java. Soil Research. 1994;32(4):781-794.

Participatory Contingency Plan to Covid 19 Adaptation of Merapi Volcano Eruption - Indonesia

Eko Teguh Paripurno

Abstract

The contingency plan was carried out for the seven highest villages in Sleman Regency, Yogyakarta Special Region, as areas prone to eruption of Merapi Volcano. This contingency plan was prepared based on a scenario with a volcanic eruption index of 3, in the form of the collapse of a lava dome of 5 million cubic meters. The collapse of the lava dome formed a hot cloud that moved 6–9 km towards the Gendol River, Opak River, Kuning River, Boyong River and Krasak River. The number of exposed residents is 18,880. The emergency situation period is estimated to be 30 days, from the time the status is increased to Alert. This contingency plan was prepared in a participatory and collaborative manner, under the coordination of the Sleman Regency Regional Disaster Management Agency (RDMA). This process includes: (1) Updating the village level contingency plan as materials for the district level. (2) Formation of a substance team from local government, universities and non-governmental organizations, and (3) Conducting a series of workshops for related organizations to compile documents and equate perceptions on the adaptation of contingency plans with the Covid 19 health protocol. The preparation of this document also involves the participation of children, in order to express their opinions and needs in implementing emergency management.

Keywords: Participatory contingency plan, covid-19 adaptation, children participation

1. Introduction

Sleman Regency is on the southern slopes of Merapi Volcano, at an altitude between 100 and 2,500 meters above sea level. This regency consisting of 17 districts, 86 sub-districts and 1,212 hamlets. The boundaries of Sleman Regency, to the north, are bordered by Boyolali Regency, Central Java Province. In the east, it is bordered by Klaten Regency, Central Java Province. In the south, it is bordered by Bantul Regency and Yogyakarta City, Yogyakarta Special Region. In the west, it is bordered by Kulon Progo Regency, Yogyakarta Special Region and Magelang Regency, Central Java Province.

Merapi Volcano has been the most active volcano during Holocene time. As strato volcano, Merapi exhibit altwrnating volcanic activities of effusive and axplosive character and self destruction. The explosivity index has involved during the last ten tousand years. The effusive activities were characterized by the occurence

of lava flow, the development of lava dome, and the production of the nuee ardente d'avalanche, called Merapi type (69–74, [1]).

Merapi Volcano since 1768 has recorded more than 80 eruptions. Among them are large eruptions with a Volcano Eruption Index (VEI) of more than 3. Major eruptions occurred in 1768, 1822, 1849, 1872 and 1930–1931. The eruption of Merapi Volcano in 1872–1931 led to the west-northwest. From the big eruption in 1930 until the eruption in 2001 the direction of the eruption changed to the southwest. The 1994 eruption occurred a deviation to the southwest - south, namely upstream of the Boyong River, between the Turgo and Plawangan hills (69–138, [2]).

Of 1.1 million people living on the flanks of the active Merapi volcano, 440,000 are at relatively high risk in areas prone to pyroclastic flows, surges, and lahars. For the last two centuries, the activity of Merapi has alternated regularly between long periods of viscous lava dome extrusion, and brief explosive episodes at 8–15 year intervals, which generated dome-collapse pyroclastic flows and destroyed part of the pre-existing domes. Violent explosive episodes on an average recurrence of 26–54 years have generated pyroclastic flows, surges, tephra-falls, and subsequent lahars. The 61 reported eruptions since the mid-1500s killed about 7000 people (479–502, [3]).

The distribution and run-out distances of these flows have frequently exceeded those of the classic Merapi-type nuées ardentes of the recent activity. Widespread pumiceous fallout deposits testify the occurrence of moderate to large (subplinian) eruptions (VEI 3–4) during the mid to late Holocene. VEI 4 eruptions, as identified in the stratigraphic record, are an order of magnitude larger than any recorded historical eruption of Merapi, except for the 1872 AD and, the October–November 2010 events (1213–1233, [4]). The last eruption in 2010 was one of the most explosive eruptions with a hot cloud range of up to 15 km.

The geologic record suggests the latter, which would place several hundred thousand people at risk. We know of no reliable method to forecast when an explosive eruption will interrupt the present interval of low-level activity. This conclusion has important implications for hazard evaluation (9–50, [5]).

Volcanic eruption contingency plans that address Covid 19 adaptation and involve the participation of children, so as to express their opinions and needs in implementing disaster emergency management.

2. Merapi Volcano Eruption Scenario

The eruption of Merapi Volcano is characterized by the release of surface magma to form a lava dome in the middle of an active crater around the peak. The emergence of new lava is usually accompanied by the destruction of old lava, which blocks the flow, causing lava to fall. The new lava that reaches the surface forms a dome that can grow bigger. The growth of the lava dome is proportional to the magma flow rate which varies up to hundreds of thousands of cubic meters per day. The lava dome that grows in the crater and enlarges causes instability. The lava dome which is unstable in position and pushed by gas pressure from inside causes part of it to collapse, thus forming pyroclastic flows that slide into rivers that originate at Merapi Volcano. The movement speed reaches 60–100 km/hour and will stop when the energy of the motion runs out. Pyroclastic flows are a primary hazard, directly affecting the population, and the most destructive of all types of hazards.

The scenario for the future eruption of Merapi Volcano begins with the formation of a lava dome in the center of the crater on the southeast side. The maximum volume is 10 million cubic meters, and half, as much as 5 million cubic meters, collects into pyroclastic flows. This scenario refers to a large chronology of eruptions in 1992, 1994, 1995, 1996, and 2001. Another scenario is the formation of a lava dome

with the same volume in the center of the crater on the west – northwest side. The growth of the dome is large enough to cause instability/collapse of the crater wall in the western sector and the southern sector close to the crater opening. This scenario is consistent with the eruptive behavior of 1998 and 2006.

After the phreatic eruption on May 21, 2018, the Geological Agency increased the activity status of Merapi Volcano from Level 1 to Level 2, with a recommendation that there should be no population activity within a radius of 3 km from the summit. Furthermore, in 2019 there were 4 eruptions. On September 22, 2019, the eruption column formed ±800 meters. October 14, 2019, formed a ± 3,000 meter eruption column. November 9, 2019, a hot cloud glided into the Gendol River as far as 2 km, with an eruption column of ±1,500 meters. November 17, 2019 formed a 1,000 meter eruption column. After the eruption on June 21, 2020, there was a shortening of the baseline distance of the Electronic Distance Measurement (EDM) in the northwestern sector of Babadan, with an average rate of up to 11 mm/day. The seismicity increased so that on November 4 2020 average shallow volcano-tectonic event earthquake (VB) was 29 times/day, multyphase earthquake (MP) 272 times/day, avalanche (RF) 57 times/day, gusts (DG) 64 times/day, total earthquake energy (Vt and MP) in a year amounting to 58 GJ. Based on these data, the Geological Agency has increased the status of Merapi Volcano activity from Level 2 to Level 3.

The Sleman Government responded and followed up on the change in status by establishing the Merapi Volcano Disaster Emergency Response Status. This determination is the basis for preparing a Disaster Emergency Management Operational Plan. Seven villages in Disaster Prone Area (DPA) III, were designated as potential affected areas, namely the areas of Glagaharjo, Kepuharjo, Umbulharjo, Hargobingan, Purwobinangan, Girikerto, and Wonokerto villages.

In this scenario, people evacuate to reduce risks. Communities are shifting from their higher-risk dwellings to lower-risk shelters. The relationship between the level of risk which is influenced by the position in the disaster-prone area with the status of the volcano is shown in **Figure 1**.

Figure 1.
Level of risk, relation of disaster prone area (X) and volcano status (Y).

3. Prediction of event and impact

Merapi Volcano eruption assumed to be on May 14, 2021, Hours: 23.30 WIB with VEI 2. Merapi Volcano eruptions towards the crater opening to the South - Southeast, namely the Gendol River, Opak River, Kuning River and Woro River. The potential for hot cloud avalanches leads to the South-Southeast, West and Southwest sectors, namely the Gendol River, Opak River, Kuning River, Boyong River, and Krasak River.

The coverage of the Sleman Regency is affected by the danger of pyroclastic flow along the upstream river channels on Merapi Volcano that lead to the South - Southeast, West-Southwest, namely the Gendol River, Opak River, Yellow River, Boyong River, and Krasak River.

No	River	Village	Hamlet	People
1	Gendol (9 km)	Glagaharjo	Kalitengah Lor (5,5 km)	537
			Kalitengah Kidul (6 km)	459
			Srunen (8 km)	459
			Singlar (9 km)	339
			Gading (9 km)	282
	Gendol (9 km) Opak (6 km)	Kepuharjo	Kopeng (7 km)	469
			Jambu (8,4 km)	390
			Batur (8,4 km)	528
			Pagerjurang (10 km)	535
			Kepuh (8,7 km)	386
			Manggong (9,9 km)	286
2	Opak (6 km) Kuning (7 km)	Umbulharjo	Pelemsari (8,5 km)	241
			Pangukrejo (6,5 km)	300
3	Kuning (7 km) Boyong (6,5 km)	Hargobinangun	Kaliurang Timur (7 km)	1.198
			Kaliurang Barat (6 km)	1.406
			Ngipiksari (7 km)	1.146
			Boyong (8 km)	980
4	Boyong (6,5 km)	Purwobinangun	Turgo (5,7 km)	507
			Ngepring (8 km)	951
			Kemiri (8 km)	700
			Ngelosari (9 km)	385
			Tawangrejo (10 km)	663
5	Krasak (7 km)	Wonokerto	Tunggularum (8,5 km)	617
			Gondoarum (9 km)	588
			Sempu (9,5 km)	1078
			Manggungsari (9,5 km)	656
6	Krasak (7 km)	Girikerto	Ngandong Tritis (7 km)	758
			Nganggring (8,7 km)	260

Table 1.
Number of people potentially affected by pyroclastic flows.

The primary hazard in the form of pyroclastic flow is the most destructive compared to other types of hazards. Pyroclastic flow is a flow of hot mass (300–800 degrees Celsius) in the form of a mixture of gas and volcanic material consisting of various sizes of clots moving down turbulently with speeds of up to 100–150 km/hour. The number of affected people is 18,880 people in 33 hamlets from 7 villages, from Turi District, Pakem District and Cangkringan District, according to **Table 1**.

4. Merapi volcano status and community activities

In accordance with the Indonesian National Standard (SNI) 8751–2018 concerning Volcanic Eruption Hazard Preparedness Training Management, at Normal status, Level 1, people in DPA I and DPA II, can carry out their daily activities. Communities in DPA III, can carry out daily activities while still complying with local government regulations according to the Geological Agency's technical recommendations (298–310, [6]; 307–320, [7]). In this status, activities in the community are advised to disseminate the DPA map, understand the character of volcanic hazards, understand the location of residence in the DPA, collect data on residents in prone areas, collect data on resources in disaster-prone areas, compile regular procedures, prepare routes and signs for evacuation routes and train preparedness.

At Level 2 status, people in DPA I can still carry out their activities by increasing awareness. People in DPA II can still carry out their daily activities by increasing their awareness of dangers. People in DPA III are advised not to do activities around the crater. Communities in this status are advised to disseminate information on Alert Status, update population data in disaster-prone areas, update vulnerable populations in disaster-prone areas, collect data on resources in disaster-prone areas, prepare equipment and communication systems, prepare evacuation plans,
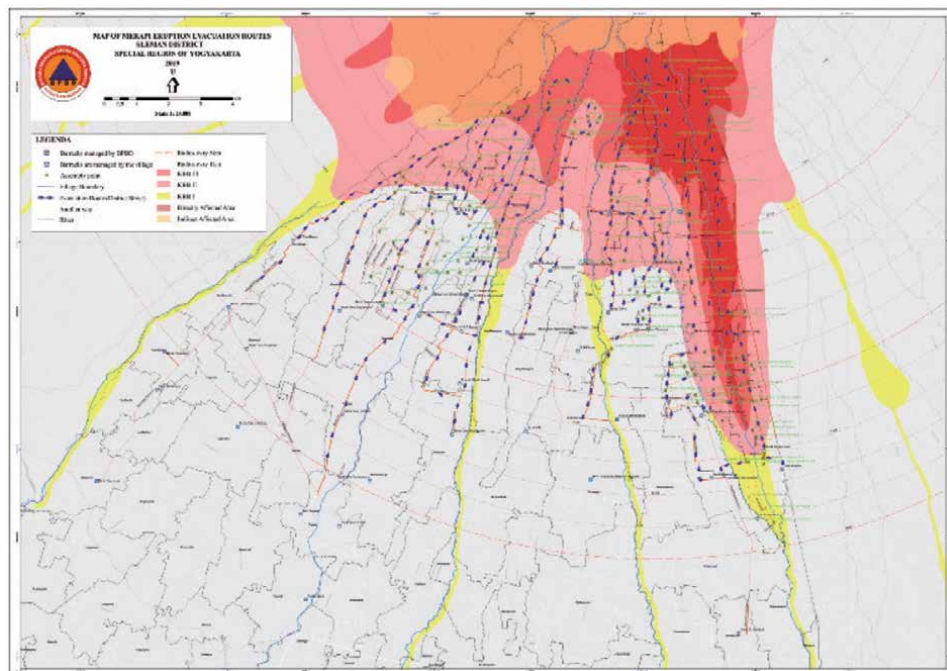
Figure 2.
Disaster Prone Area III (red), II (orange), I (yellow) and evacuation route figure.

prepare evacuation transportation tools, prepare refugee camps, preparation of public kitchens, explanation to the community and division of evacuation groups.

At Level 3 status, the people in DPA I increase their awareness by not doing activities around the river valley that is upstream in the peak area. The people in DPA II began to prepare themselves to evacuate while waiting for orders from the local government according to technical recommendations from the Geological Agency. People in DPA III are not allowed to carry out activities and begin to prepare themselves to evacuate. Communities at this level must disseminate Alert Status information, operate warning signs, operate evacuation transportation equipment, operate evacuation shelters, operate public kitchens ready, activate security, activate fixed procedures, activate communication systems, establish and activate command post for emergency response.

At Level 4 status, people in DPA I, II, and III immediately evacuate based on recommendations from the local government according to technical recommendations from the Geological Agency. In this status the community must disseminate information on Alert Status, sound warning signs, give verbal and written evacuation orders from the emergency response commander, activate regular procedures, carry out evacuations, activate evacuation sites, operate public kitchens, operate security and crisis centers. The DPA I, II and III is shown in **Figure 2**.

5. Emergency management

At level 3 status, the Sleman Government determined a Disaster Emergency Status through a Regent Decree, as well as activated the contingency plan to "Operation Plan for Emergency Management of Merapi Volcano Eruption with Adaptation to the Covid-19 Health Protocol". This activity is carried out to ensure protection and fulfillment of basic needs for survivors including vulnerable groups, including women, children, the elderly and people with disabilities. Henceforth, each component works in accordance with the description of its function, according to **Table 2**.

No	Function	Explanation
1	Command, Control, Coordination, Communication and Information	1. Command of disaster emergency response organization 2. The Command Post is located at the Pakem Sub-District Main Command Post. 3. Command Post as a control center, information center, resource management center as well as a center for coordination, services and complaints.
2	Planning, Handling and Prevention of Covid 19	1. Conducting a situation assessment and making daily progress reports 2. Manage Covid 19 data, information and public relations centers 3. Planning for the needs of refugees / survivors for three days. 4. Planning for the implementation of the Covid 19 health protocol 5. Perform consolidation and coordination 6. Planning and managing volunteers from outside the area 7. Determine treatment priorities 8. Provide assistance to sub-district field posts and village emergency response posts 9. Identify the economic potential that is owned 10. Develop a strategy to strengthen the economy of the community in refugee camps 11. Develop an early economic recovery strategy.

No	Function	Explanation
3	Operation	1. Carry out the process of evacuation and rescuing residents 2. Carry out a process of searching and helping residents 3. Isolating the patrol area and installing portable traffic signs 4. Implement the Covid-19 health protocol in all surgical procedures 5. Support the evacuation and rescue of livestock 6. Supports community livestock management
4	Sub-District Operational Unit Field Post	1. Supporting disaster emergency response 2. Supporting the fulfillment of the basic needs of residents and affected livestock in each village. 3. Ensuring the implementation of the Covid 19 health protocol in villages
6	Village Implementing Unit	1. Implementing Disaster Emergency Management 2. Fulfilling the basic needs of residents and affected livestock is carried out according to procedures 3. Implement Covid 19 health protocol enforcement 4. Providing self-isolation / quarantine for Covid 19
7	Logistic	1. Managing logistics to meet operational needs includes: personnel, facilities, transportation, food, facilities and infrastructure needs 2. Carry out logistics management functions (recording, sorting, storage distribution) 3. Implement the Covid 19 health protocol in all actions / activities
8	Administration and Finance (Secretariat)	1. Carrying out administrative governance functions that meet the principle of accountability 2. Prepare regulations for administrative and financial mechanisms in accordance with applicable laws and regulations 3. Provide support for administrative and financial governance processes

Table 2.
Fungtion and explanation of emergency management.
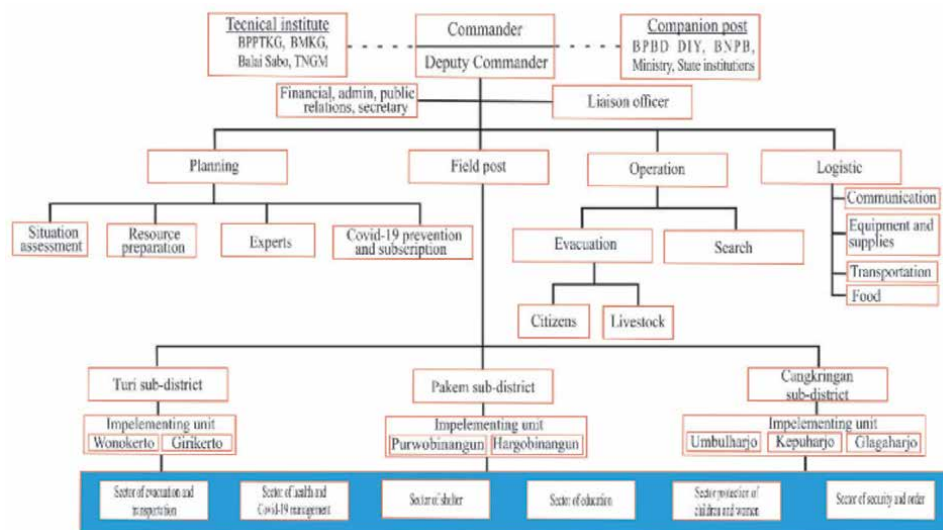
Figure 3.
Emergency Management Structure in Sleman District.
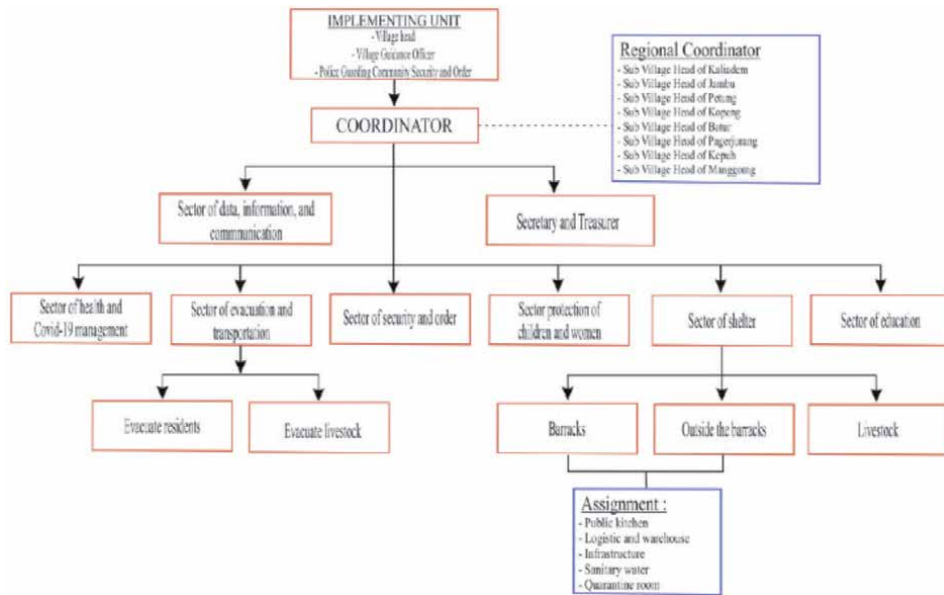
Figure 4.
Emergency management structure in village level.

Coordination is carried out following up the decree determining the emergency status. Therefore, all parties involved in the command structure for disaster emergency handling are urgently required to carry out their respective duties and functions to: (1) activate the information communication and reporting system at the post for disaster emergency management; (2) Mobilizing resources; (3) Determine the emergency response period for 30 days; (4) Prioritizing handling of vulnerable groups; and (5) Implementation of the Covid Health Protocol 19. The organizational structure for implementing emergency management at the district level is shown in **Figure 3**, and the structure at the village level is shown in **Figure 4**.

6. Child participation

Children's participation in the preparation of contingency plans is realized by including a declaration of the results of the children's forum discussion, sebagai berikut: (1). In disaster management, the vulnerable groups are prioritized; (2) The needs for clothing, food and shelter are adjusted; (3) Avoid sexual violence against children; (4) Periodic disaster mitigation activities for children; (5) Basic rights to education, spatial health, sharing and assembly are provided by the government; (6) Increase signposts that are easy for children to understand and lighting for evacuation roads; (7) Making an evacuation map; (8) Ensuring a comfortable place of refuge for vulnerable groups; (9) Involving children as caregivers for others; (10) Children need food that is varied and different from adults; when in evacuation; (11) The government opens the opportunity to cooperate with other parties and does not exploit children when a disaster occurs; (12) Speed up the creation of lost documents; (13) Mode of transportation for vulnerable people; (14) Increase the number of toilets in the evacuation posts and differentiate sanitation facilities for children and adults; (15) Availability of health experts and psychologists for children; (16) There are trauma healing activities as a priority; (17) Additional internal displace person/refugee rooms for children; (18) Use of social media as a means of communication.

7. Conclusion

This participatory and child-friendly contingency plan is a model for emergency response to volcanic eruptions during the COVID-19 pandemic. This document may be adapted for other comparable natural disaster contingency plans. This contingency plan will be easy to implement once it is completed with the Operational Plan document.

Acknowledgements

Author details

Eko Teguh Paripurno
University of Pembangunan Nasional Veteran Yogyakarta, Indonesia

*Address all correspondence to: paripurno@upnyk.ac.id

IntechOpen

References

[1] Adjat Sudradjat, Idlrem Syafri, Eko Teguh Paripurno; The characteristics of lahar in Merapi Volcano, Central Java as the indicator of the explosivity during Holocene, Jurnal Geologi Indonesia (Indonesian Journal of Geology), 2010, 69-74

[2] Barry Voight, EK Constantinem S. Siswowijoyo, R. Torley, Historical eruption of Merapi volcano, Central Java, Indonesia, 1768-1998, Journal of Volcanology and Geothermal Research, 2000, 69-138

[3] Jean Claude Thouret, Frank Lavigne, Kelfon Karim, Sutikno Bronto, Toward a revised hazard assesment at Merapi volcano, Central Java, Journal of Volcanology and Geothermal Research, 2000, 479-502

[4] Ralf Gertisser, Sylvain J. Charbonnier, Jorg Keller, Xavier Quidellur, The geological evolution of Merapi volcano, Central Java, Indonesia, Bulletin of Volcanology, 2012, 1213-1233

[5] Chris G Nehall, Sutikno Bronto, B. Alloway, et.al, 10,00 Years of explosive eruptions of Merapi volcano, Central Jaca: archaeological and modern implications, Journal of Volcanology and Geothermal Research, 2000, 9-50

[6] Supriyati Andreastuti, Eko Teguh Paripurno, Hendra Gunawan, Agus Budianto, Devy Syahbana, John Pallister: Character of community response to volcanic crises at Sinabung and Kelud volcanoes, Journal of Volcanology and Geothermal Research, 2019, 382, 298-310

[7] Supriyati Andreastuti, Agus Budianto, Eko Teguh Paripurno: Integrating social and physical perspectives of mitigation policy and practice in Indonesia, Observing the Volcano World, 2017 307-320.

Volcanic Sedimentology, Geochemistry and Petrology

Chapter 5

Effusive Badi Silicic Volcano (Central Afar, Ethiopian Rift); Sparse Evidence for Pyroclastic Rocks

Dereje Ayalew, David Pyle and David Ferguson

Abstract

We report field observation, textural description (thin section and scanning electron microscope (SEM)) and mineral chemistry (backscattered electron imaging and dispersive X-ray analysis) for rhyolitic obsidian lavas from previously under described effusive Badi volcano, central Afar within the Ethiopian rift. These rhyolitic obsidian lavas are compositionally homogeneous and contain well developed flow bands. Textural analysis is undertaken to understand the formation of flow band, and to draw inferences on the mechanism of emplacement of this silicic volcano. Flow band arises from variable vesicularity (i.e., alternating domains of vesicular, light glass and non-vesicular, brown glass). Such textural heterogeneities have been developed during distinct cooling and degassing of the melt in the conduit.

Keywords: Afar, Badi, flow band, lava, pyroclastic

1. Introduction

Many rhyolite lavas are usually associated with pyroclastic deposits [1–3]. In fact each lava eruption is almost invariably associated with preceding phases of explosive pyroclastic activity [4–6]. This suggests that lavas could be a terminal event of many explosive eruptions during which most of the volatiles of the magma have been removed. Even while the rhyolite lavas being growing explosive activity may continue, as evidenced by the presence of unusually large amounts of obsidian ejecta among the pyroclastic deposits [4].

The principal requirement for the effusive (not explosive) eruption of magma as coherent lava is that the exsolved volatile content of the magma immediately before eruption should be sufficiently low to prevent the build-up of a gas pressure which could cause explosive fragmentation of magma and country rock [7]. Nevertheless, sufficient water is initially available in the magma source regions [3]. Therefore, for coherent magmas to be erupted from magma sources with high volatile contents the magma has to degas [7].

Volcanologic and petrologic studies on the silicic centres which lie within the Afar axial range or off the axis are very scarce. This is partly because of the remoteness and inaccessibility of the area that practically inhibits field investigation. The very few previous studies mainly focused on the extensive basaltic flow fields
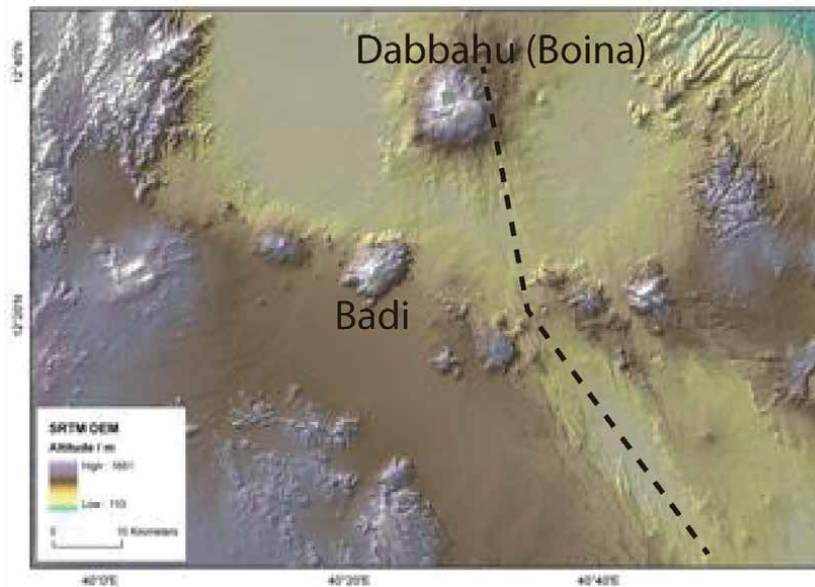
Figure 1.
Topographic relief map of central Afar, showing the location of the off-rift axis Badi volcano. Dashed line represents the 2005 dyke injection (after [21]).

[8–13], which have been interpreted as incipient oceanic ridges. However, there are also comparable volumes of silicic magmas to that of the basaltic counterparts in the region [14–16]. Very little is known about these silicic centers which form a conspicuous central edifice in the axial range of the Afar magmatic segments [15, 17–20].

This study presents field observation; textural description (thin section and scanning electron microscope); and mineral chemistry (backscattered electron imaging and dispersive X-ray analysis) for previously undescribed Badi volcanic edifice from central Afar, Ethiopia (**Figure 1**). Contrary to many localities, whereby rhyolitic lava domes and flows are usually associated with pyroclastic deposits, the Badi volcanic edifice contains several clusters of coalescing silicic domes and lava flows, and sparse evidence for pyroclastic rocks. Thus, this volcano offers a relatively rare opportunity to study effusive silicic volcanic phenomena. The motivation of this work is to understand the mechanism of emplacement of Badi silicic domes and flows with hope to draw inferences on the formation of the flow bands. In order to address these questions we employ textural analysis of the lavas using petrographic microscope and scanning electron microscope (SEM), accompanied by mineral chemistry. To the knowledge of the authors, there are no earlier studies of this kind documented in the literature from the region so far. Petrologic and geochemical studies of some silicic volcanic rocks from Afar including those from Badi have been considered elsewhere [17–20, 22] and are omitted from the forthcoming discussion.

2. Geologic background

Afar depression (the Afar triple junction), roughly 300 km wide, marks the intersection of three rifts: the Red Sea, Gulf of Aden and east African rifts. This extensional province formed within a Palaeogene Ethiopian flood basalt province associated with the Afar mantle plume [23, 24]. Rifting within the Red Sea and Gulf of Aden arms of the triple junction has progressed to oceanic spreading [25], whereas the less-evolved Ethiopian rift is transitional from continental rifting to

oceanic seafloor spreading [26]. The crust of the Afar depression is highly extended and intruded with mafic dykes [27]. Crustal thickness ranges from 16 km in the north beneath Erta'Ale range to 24 km in the south [28].

Within the southern Red Sea rift and Afar, the initial development of border faults was roughly coincident with the 31–29 Ma flood basalt sequences in the same area [29]. Strain migrated riftward from 19 to 12 Ma [29], and by ~5 Ma, an oceanic spreading ridge had developed within the south central Red Sea rift [30]. Southward propagation (south of 16°N) of the ridge runs inland through Ethiopia, whereby extension (faulting and dyking), seismicity and volcanism are localized in discrete narrow (<10 km wide) ~60 km long rows/zones within the Afar depression [31]. These rows are referred to as magmatic segments and are characterized by aligned chains of basaltic cones with associated flow fields, shield volcanoes, shallow seismicity and positive gravity anomalies [26]. The available K-Ar data for basaltic and silicic rocks along the terrestrial portion of the Red Sea rift system indicate an age range of 1.46–0.52 Ma [32]. Within these magmatic segments, volcanism tends to be bimodal, with extensive basaltic flow fields and axial silicic centers [15, 18–20, 22]. Profuse fissure basalt volcanism, referred to as "Stratoid Series" [33] covering most of the central and southern part of the Afar depression, occurred about 5 Ma ago where it was most active between 4.5 and 1.5 Ma [34].

3. Methods

Fresh, unaltered obsidians (twelve samples) were collected from Badi volcano, and were examined under petrographic microscope and scanning electron microscope (SEM) at Department of Earth Sciences, University of Oxford, UK. SEM images and chemical analysis (backscattered electron imaging and dispersive X-ray analysis) of samples were acquired.

4. Result

4.1 Field relation

Badi volcano (located at 12.387°N and 40.366°E) lies off the axis of the main rift and is associated with a deviation in the strike of the faults (**Figure 1**). It is a well-defined rounded volcanic center with diameter of emerging from fissural basaltic lava fields. The summit of the center is about 1280 m high above mean sea level (msl) and the base is around 640 m high above msl. The total volume of the volcano is estimated to be about 31.5 km^3. The silicic lava consists of a cluster of several rhyolite domes and flows. There is no central vent; rather each dome/flow has its own vent. The only age constraint available for the silicic part of the Badi edifice is a K-Ar age of 290 Ka for one of the basal silicic domes [32].

The sub-aerial Badi volcanic edifice has essentially two parts (**Figure 2**): the base of silicic domes and flows and then, the upper basaltic flows which have been erupted on to the silicic material. There are no exposed explosive products associated with the effusive activity in Badi volcano, unlike many rhyolitic obsidian flows and domes in the Ethiopian rift valley which are commonly associated with pyroclastic deposits [4, 6, 35–37]. It has been noted that in most volcanic centers of Afar, pryroclastic products are scanty [15]. However, there are large silicic caldera complexes in Afar away from the rift axis [16]. The absence of fragmental magmatic materials at Badi volcano clearly reflects that the effusion of lava domes and flows resulted from the different rheology of the magma.

Figure 2.
Outcrop photos illustrating the eruptive sequence of Badi volcano; Basal silicic domes and flows, and upper basaltic flow.

During our preliminary field investigation, we found evidence for a single, coarse-grained pumice cone deposit, on the side of the volcano. The pumice fall deposits are quite high up elevation wise and lay directly on top of some basaltic scoria cones (**Figure 2**), so they post-date at least some of the later basaltic volcanism and have been erupted after almost all of the silicic domes/flows that make up the main body of the Badi Mountain. Accordingly, the volcanic stratigraphy of Badi volcano from old to young is silicic dome, then basaltic scoria and finally pumice fall deposit. There are certainly no silicic flows interbedded with the pyroclastic material (**Figure 2**). The very large pumices (0.5 m in size or more) suggest reasonably close to the vent. All of the dates for the late stage basaltic activity are around 50 Ka and younger (Ar-Ar and cosmogenic ^{3}He datings, [13]). This indicates that the pyroclastic deposits are much younger than 50 Ka. An interpretation might be that the pumice deposit is the product of a small explosive eruption, sourced from a body of silicic melt that was rejuvenated by the later injection of basaltic magma.

4.2 Texture of flow bands

Field inspection reveals that the rhyolite lavas show a vertical zonation of lava textures related to the mechanism of emplacement (**Figure 3a**). The upper surface of obsidian usually fractures into blocks, probably related to the movement and cooling of the interior of the flow. Beneath these layers is the core (interior) of the dome which is unlaminated and shows columnar joints. The upper outer surface of the dome is made up of obsidian layer which displays a very pronounced layers, or flow bands (**Figure 3b**) defined by a color variation (i.e., alternating domains of light and brown glasses). The flow bands are frequently folded (**Figure 3c**) and exhibit intricate fluidal textures as indicated by highly contorted and intensively crenulated layers (**Figure 3d**). Folds arise as flow layering deforms during flow advance [38].

Petrographic observation of the flow bands (**Figure 4**) shows that the boundaries between the light and brown glass bands are abrupt, reflecting laminar flow state. The brown lamella is relatively thickener than the light one. The flow banding is locally deflected around phenocrysts (**Figure 4**), suggesting that crystallization took place before the cessation of flowage of the lava.

As seen both in the hand specimen and thin section, SEM observation (**Figure 5**) illustrates that the Badi lavas have flow banding/layering defined by alternating lamellae of light and black glasses. Black bands are represented by non-vesicular obsidian, while light layers are vesicular glass. The obsidian domain shows abundant, very small microlites of mainly alkali feldspar, quartz

Figure 3.
Outcrop photos illustrating the lithological variability (a) Textutal differences through a rhyolite lava, with a chilled glassy carapace top and a columnar jointed bottom. (b) Black, vitreous obsidian occurring as interbanded layers. (c) Flow-folded obsidian. (d) Fluidal characteristic as evidenced by contorted and crenulated layers.
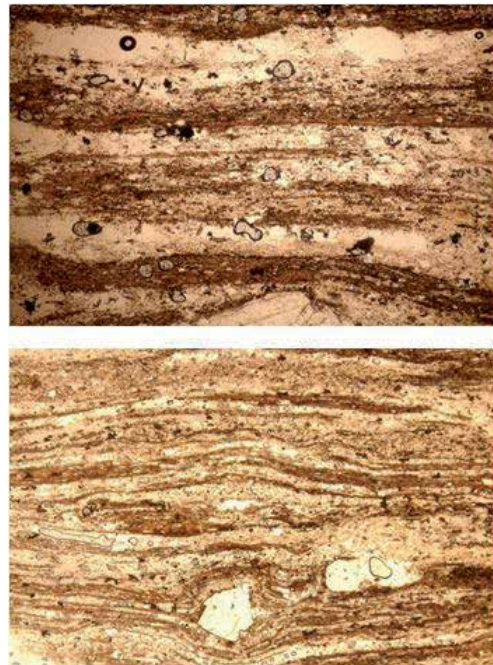
Figure 4.
Photomicrographs illustrating flow banding defined by alternating domains of brown and light glasses (×30, ordinary light). Note flow bands deflected around phenocrysts.
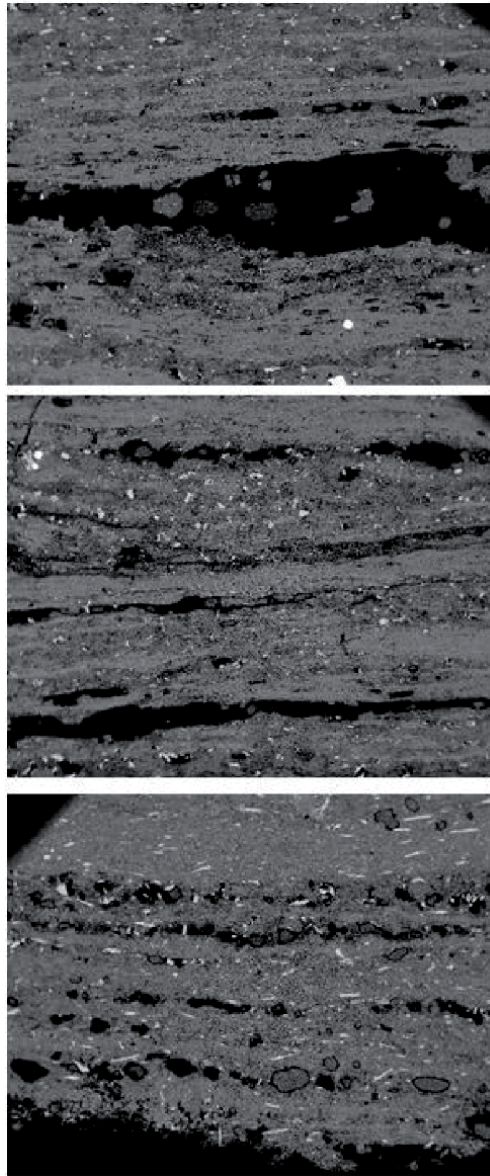
Figure 5.
SEM image illustrating the differences in abundance of vesicles between the flow bands. Note microlites are randomly oriented. Field of view is 9 μm.

and pyroxene set in a glassy matrix. Microlites are generally randomly oriented. It is important to note that there is no notable difference in the abundance of microlites between the two glass domains. Furthermore, the Badi lavas contain neither xenocrystic nor xenolithic materials.

4.3 Petrography

The rhyolite lavas, which form the main part of the Badi edifice, display a wide variety of textures ranging from sparsely porphyritic through aphyric to almost completely glassy obsidians (**Figure 6**). The phenocrysts are unbroken which provides textural evidence that distinguish the flows and domes as lava rather than rheomorphic ignimbrite. They appear to have been in equilibrium without
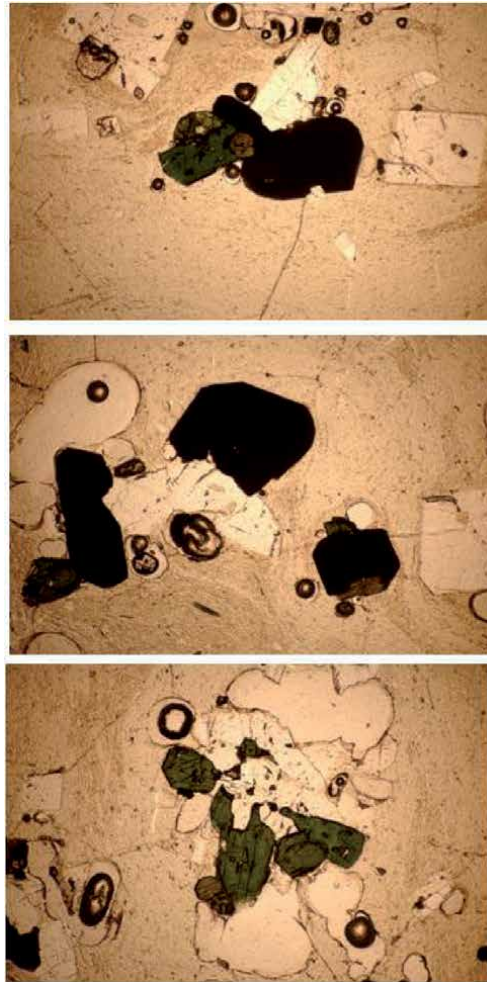
Figure 6.
Photomicrographs illustrating the petrographic characteristics of pertalkaline rhyolites from Badi volcano with phenocrysts of alkali feldspar (euhedral), quartz (rounded), aegirine (green) aenigmatite (dark brown) set in a microcrystalline or glassy matrix (×30, ordinary light).

embayment or resorption. The porphyritic lavas (e.g., samples 01–04, 02–06, 25–02) contain very few phenocrysts or microphenocrysts (< 5 vol.%) of alkali feldspar, quartz, green clinopyroxene and aenigmatite enclosed in a microcrystalline or glassy groundmass which is mainly alkali feldspar, quartz and pyroxene. The aphyric lavas (e.g., samples 01–07, 02–04, 29–03) exhibit very scarce microphenocrysts of alkali feldspar, quartz and green pyroxene embedded in a microcrystalline groundmass which mainly contains alkali feldspar and quartz. They are slightly altered as indicated by a dirty appearance of feldspar. The rhyolitic obsidians (e.g., samples 01–09, 02–04, 03–01, 30–04(1), 30–12, 31–01) contain microlites of alkali feldspar, quartz and pyroxene set in a glassy matrix. The groundmass/matrix is relatively fresh and unaltered devoid of post eruption divetrification and hydration products such as spherulites.

The mineral assemblage in Badi lavas, in order of decreasing abundance, includes alkali feldspar, quartz, green clinopyroxene and aenigmatite, although not all phases are found in every sample. **Table 1** reports the main petrographic characteristics of phenocrysts and matrix of the Badi rhyolite lavas. Accessory Fe-Ti oxides and apatite are present in trace amount and occur as inclusions. Fe-sulfide, possibly

Phase	Mode (vol.%)	Petrographic description
Phenocrysts	(1–5%)	
Alkali feldspar	up to 3%	Typically tabular and prismatic euhedral phenocrysts (1–4 mm in length); unbroken showing simple twinning; rarely cloudy appearance. Equant microphenocrysts (< 1 mm in size).
Quartz	<2%	Subhedral to rounded crystals.
Alkali pyroxene	<2%	Aegirine forms elongated (skeletal) and prismatic crystals (up to 3 mm in length); showing green to brownish-yellow color and pleochroism, and only one perfect cleavage. Aegirine-augite occurs as small euhedral; Equant microphenocrysts (0.6 mm in size); shows both cleavages.
Aenigmatite	<1%	Euhedral crystal with typical dark brown color.
Groundmass/matrix		Generally fresh and unaltered; ranges from entirely glassy to microcrystalline groundmass; alkali feldspar, quartz and pyroxene are the principal microlite minerals; display flow banding defined by variation of vesicle abundances.

Table 1.
Main petrographic characteristics of phenocrysts and matrix of the Badi rhyolites.

pyrrhotite occurs as tiny bleb inclusions within oxides. Alkali feldspar, quartz, green clinopyroxene, and aenigmatite are ubiquitous in the phenocrysts and microphenocrysts. Alkali feldspar is volumetrically the most abundant crystal in the Badi lavas. Phenocryst and matrix compositions of the Badi rhyolite lavas are presented in **Table 2**. Composition of alkali feldspar is anorthoclase or sanidine. Alkali-pyroxene is the most abundant mafic mineral and is mostly aegirine and subordinate aegirine-augite. Aenigmatite is commonly the second most abundant mafic mineral.

The modal presence of alkali pyroxene and aenigmatite, which are considered to be index minerals in the peralkaline salic rocks [39], in Badi rhyolites surely confers a peralkaline affinity. Nicholls and Carmichael [40] indicated that aegirine is the dominant phase in strongly peralkaline composition (pantellerite), whereas hedenbergite seems to be dominating in less peralkaline composition (comendite).

	Anorthoclase	Sanidine	Aegirine	Aenigmatite	Glass
Sample	01–/04	25–/02	01/–04	01/–04	
SiO_2	66.52	66.55	53.84	40.15	67.60
TiO_2			1.22	9.39	
Al_2O_3	17.19	18.22	0.72	0.66	12.87
FeO	1.41	0.78	29.67	41.66	5.49
MnO	0.10	0.07	0.34	1.40	
MgO	0.23		0.21	0.05	0.27
CaO	0.04	0.16	1.22	0.38	0.05
Na_2O	7.12	6.77	12.00	6.41	5.82
K_2O	6.68	7.49	0.09		6.93
Total	99.29	100.04	99.32	100.11	99.03

Table 2.
Representative energy dispersive (EDS-SEM) x-ray analyses of minerals and glass of rhyolites from Badi volcano.

The presence of modal aegirine in Badi lavas implies a pantelleritic composition. This affinity is also supported by chemical composition (Hutchinson et al., 2018) in which the silicic lavas from Badi volcano are predominantly pantellerite with minor comendite. The absence of Fe-Ti oxides in the mineral assemblage suggests that the magma was crystallized at low oxygen fugacity which lies at or below the FMQ buffer curve in the T-f_{O2} space [41]. Recent works (e.g., [42]) have shown that the nature of co-existing phases, especially pyroxene, in peralkaline rhyolites is controlled by the redox conditions; aegirine crystallizes in more reduced conditions (i.e., in no-oxide field). The co-existence of aenigmatite and aegirine in Badi rhyolites strongly suggests that the original silicic magma was generated, evolved and crystallized in a more reduced condition; at low oxygen fugacity which lies at or below the FMQ buffer in no-oxide field.

It becomes increasingly apparent that some workers (e.g., [37]) have shown the presence of fayalite, hedenbergite and plagioclase in the mineral assemblage of peralkaline rhyolites from Ethiopian rift valley. These minerals are not found in Badi rhyolites. We only observed plagioclase and hedenbergite as xenocrysts in xenolithic material in a single specimen (30-01(4)). These less-evolved inclusions show angular contacts, suggesting that they were solid while the host rhyoltic lava was liquid. We emphasize the importance of indentifying the mineral assemblage found in rhyolites as phenocrysts and xenocrysts.

5. Discussion

5.1 Origin of flow banding

Thin flow banding, defined by discrete lamellae/layers with contrasting color, is a common feature of many effusive volcanic rocks. It is a ubiquitous texture in very viscous, highly siliceous lavas, such as rhyolites (e.g., [3, 43, 44]). Flow band in rhyolite lavas has been described from varying crystallinity and vesicularity [45]. Differences in abundance of microlites and/or vesicles appear to develop either during flow of the melt in the conduit or during late stage cooling and degassing during flow emplacement [45, 46]. Flow banding is thought to be a reflection of laminar flow.

Flow banding in rhyolite lavas may have a variety of origins, including mixing of compositionally distinct magmas [47, 48], or incorporation of xenolithic material in a shear flow [49], or fracture-healing processes of texturally distinct magma [46, 50]. Another type of flow banding origin seems to arise from deformation of domains in the melt that had contrasting water concentration in the melt prior to flow [43]. There is yet little consensus on any of these alternatives.

One of the most important questions to answer is whether or not the banding displayed by the Badi rhyolite lavas is due to textural (i.e., differences in abundance of vesicles) or compositional (i.e., differences in abundance or preferred orientation of microlites) heterogeneities. Flow banding in Badi lavas is defined by alternating domains/layers of contrasting glass colors (light and brown glasses). Brown bands are represented by non-vesicular obsidian, while light layers are vesicular glass (**Figure 5**). Our data set shows that there are no extreme differences in mineral composition or proportion between the light and brown glasses. This appears to indicate that the banding observed in the studied lavas is not due to compositional heterogeneities at least on the basis of mineralogical grounds. Instead it is due to textural differences, caused by variations in vesicle concentration of the glass bands (**Figure 5**).

Such textural heterogeneities due to differences in the abundance of vesicles of the glass may develop either during magma flow in the conduit [46], or during

flow emplacement [49]. All of the samples from Badi volcano surveyed both in thin section and SEM do not contain xenocystic and/or xenolithic material. This further provides evidence against incorporation of xenolithic material during the course of the flow of Badi lavas at the Earth's surface. Hence, this textural (vesicularity) heterogeneity could not have developed during late stage cooling and degassing during flow emplacement. Rather such textural variations (heterogeneities) imply distinct cooling and/or degassing histories, and must have formed during flow in the conduit prior to magma extrusion.

5.2 Emplacement of rhyolite domes and flows

Many rhyolitic obsidian flows and domes are commonly preceded or accompanied by explosive episodes [2, 3, 36, 37]. Two contrasting models have been proposed to explain the common sequence of initial, explosive plinian eruptions followed by quite effusions of lava: (1) the volatile stratification model; and (2) permeable foam model. In the former case, a stratification of volatiles in the source magma body is invoked to explain the initially explosive phase [1]. In the later case, one envisions a fairly uniform batch of magma that can release gas as it ascends through the fracture and porous conduit rock [7].

The Badi volcanic edifice is entirely constituted by several clusters of coalescing silicic domes and lava flows; there are no any explosive products associated with the effusive activity. This is in contrary to many rhyolitic obsidian flows and domes (e.g., Fentale and Gedemsa, Ethiopia; Inyo Dome, USA; Pantelleria, Italy) which are commonly associated with pyroclastic deposits [1–3]. These features are also common in most silicic volcanic centers of Afar in which pyroclastic rocks are usually scarce [15].

The fundamental question is whether extrusive rhyolite lavas of Badi volcano represent quenched dry rhyolite magma or have somehow degassed during ascent and eruption to prevent build-up of a magmatic gas pressure. The lack of hydrothermal manifestation, represented by direct escape of exsolving volatiles through the vent immediately before eruption, strongly suggests that the coherent lavas from Badi did not erupt from degassed magma source. Furthermore, amphibole phases are not observed in Badi rhyolites. The absence of amphibole phase in Badi rhyolites demonstrates that the water content of the pre-eruption magma was not enough to stabilize amphibole which requires about 3 wt.% H_2O in a silicic magma to crystallize [3]. The absence of amphibole phase suggests that the Badi rhyolite domes and flows resulted from initially volatile-poor silicic magmas. Hence, the lack of progression from tephra ejection to lava extrusion, contrary to many rhyolite eruptive sequences, at Badi volcano reflects the lava must be nearly as dry as obsidian to escape fragmentation up on extrusion.

Effusions of silicic lavas often pile up over the vent area rather than traveling long distances (e.g., [1–3]), due to their high viscosity that prevents them from flowing far from the vent from which they extrude. It seems that the Badi rhyolites advanced outward. This might be related to their composition (**Table 1** and **Figure 6**) in that the Badi rhyolites are predominantly pantellerite with relatively high Na^+ and K^+ ion concentrations which act as network modifier (i.e., lowering the degree of melt polymerization) thereby relatively lowering the viscosity of the silicic magma [51]. Once extruded, the Badi lava flows outward (the average Badi flow is about 1.5 km) due to their relatively low viscosity.

In addition, the Badi rhyolite lavas are aphyric (with total phenocryst contents of <5%, **Table 1**), suggesting an extremely high magma temperature at the time of eruption. The high emplacement temperature implies that the rhyolite lavas reached the surface through a circular conduit, which presents a much smaller cooling surface to the country rocks [52]. The aphyric condition of rhyolite lavas has been

ascribed to unusually low viscosity [53]. The Badi lavas have flowed outward up to 1.5 km. Hence, these lavas may have had reduced viscosity due to their high magma temperature and peralkaline affinity, as the cause of the increased fluidity.

6. Conclusions

The rhyolite lavas from effusive Badi volcano, central Afar, show peralkaline affinity (predominantly pantellerite), as evidenced by the presence of modal aegerine and aenigmatite in the mineral assemblage. These lavas display flow banding defined by alternating lamellae of brown, non-vesicular (obsidian) and light, vesicular glasses. Flow banding is thought to arise from differences in vesicle abundances between the brown and light glasses. Such textural heterogeneity might have developed during magma flow in the conduit prior to magma extrusion. The scarcity of explosive products is explained by the fact that the Badi rhyolite domes and flows resulted from initially volatile-poor silicic magma that prevents build-up of a magmatic gas pressure which could cause explosive fragmentation. The Badi lavas flowed outward due to their high magma temperature and peralkaline affinity as the cause of the increased fluidity.

Acknowledgements

Author details

Dereje Ayalew[1*], David Pyle[2] and David Ferguson[3]

1 School of Earth Sciences, Addis Ababa University, Addis Ababa, Ethiopia

2 Department of Earth Sciences, University of Oxford, Oxford, UK

3 School of Earth and Environment, University of Leeds, Leeds, UK

*Address all correspondence to: dereayal@yahoo.com

References

[1] Fink, J.H., 1983. Structure and emplacement of a rhyolitic obsidian flow: Little Glass Mountain, Medicine Lake Highland, northern California. Geol. Soc. Am. Bull. 94, 362-380.

[2] Fink, J.H., Anderson, S.W., Manley, C.R., 1992. Textural constraints on effusive silicic volcanism: beyond the permeable foam model. J. Geophys. Res. 97, 9073-9083.

[3] Swanson, S.E., Naney, M.T., Westrich, H.R., Eichelberger, J.C., 1989. Crystallization history of obsidian dome, Inyo domes, California. Bull. Volcanol. 51, 161-176.

[4] Fontijn, K., McNamara, K., Tadesse, A.Z., Pyle, D.M., Dessalegn, F., Hutchison, W., Mather, T.A., Yirgu, G., 2018. Contrasting styles of post-caldera volcanism along the main Ethiopian rift: implications for contemporary volcanic hazards. J. Volcanol. Geotherm. Res. 356, 90-113.

[5] Siegburg, M., Thomas M., Gernon, T.M., Bull, J.M., Keir, D., Barfod, D.N., Taylor, R.N., Abebe, B., Ayele, A. 2018. Geological evolution of the Boset-Bericha Volcanic Complex, Main Ethiopian Rift: ^{40}Ar/^{39}Ar evidence for episodic Pleistocene to Holocene volcanism. J. Volcanol. Geotherm. Res. 351, 115-133

[6] Tadesse, A.Z., Ayalew, D., Pik, R., Yirgu, G., Fontijn, K., 2019. Magmatic evolution of the Boku volcanic complex, main Ethiopian rift. J. Afr. Earth Sci. 149, 109-130.

[7] Eichelberger, J.C., Carrigan, C.R., Westrich, H.R., Price, R.H., 1986. Nonexplosive silicic volcanism. Nature 323(6089), 598-602.

[8] Barberi, F., Civetta, L., Varet, J., 1980. Sr isotopic composition of Afar volcanics and its implication for mantle evolution. Earth Planet. Sci. Lett. 50, 247-259.

[9] Barrat, J.A., Fourcade, S., Joron, J.L., 1989. Isotope (Sr, Nd, Pb, O) and trace-element geochemistry of volcanics from the Erta'Ale range (Ethiopia). J. Volcanol. Geotherm. Res. 80, 85-100.

[10] Barrat, J.A., Joron, J.L., Taylor, R.N., Fourcade, S., Nesbitt, R.W., Jahn, B.M., 2003. Geochemistry of basalts from Manda Hararo, Ethiopia: LREE-depleted basalts in central Afar. Lithos 69, 1-13.

[11] Betton, P.J., Civetta, L., 1984. Strontium and neodymium isotopic evidence for the heterogeneous nature and development of the mantle beneath Afar (Ethiopia). Earth Planet. Sci. Lett. 71, 59-70.

[12] Ferguson, D.J., Barnie, T.D., Pyle, D.M., Oppenheimer, C., Yirgu, G., Lewi, E., Kidane, T., Carn, S., Hamling, I., 2010. Recent rift-related volcanism in Afar, Ethiopia. Earth Planet. Sci. Lett. 292, 409-418.

[13] Medynski, S., Pik, R., Burnard, P., Williams, A., Vye-Brown, C., Ferguson, D., Blard, P.H., France, L., Yirgu, G., Seid, J.I., Ayalew, D., Calvert, A., 2013. Controls on magmatic cycles and development of rift topography of the Manda-Hararo segment (Afar, Ethiopia): insights from cosmogenic ^{3}He investigation of landscape evolution. Earth Planet. Sci. Lett. 367, 133-145.

[14] Barberi, F., Chedeville, E., Faure, H., Giglia, G., Marinelli, G., Santacroce, R., Tazieff, H., Varet, J., 1973. Geology of northern Afar (Ethiopia). Rev. Géogr. Phys. Géol. Dynam. 2, 443-490.

[15] Barberi, F., Santacroce, R., Varet, J., 1974. Silicic peralkaline volcanic rocks of the Afar depression (Ethiopia). Bull. Volcanol. 38, 755-790.

[16] Wiart, P., Oppenheimer, C., 2005. Large magnitude silicic volcanism in

north Afar: the Nabro volcanic range and Ma'alalta volcano. Bull. Volcanol. 67, 99-115.

[17] Barberi, F., Santacroce, R., Ferrara, G., Treuil, M., Varet, J., 1975. A transitional basalt-pantellerite sequence of fractional crystallization, the Boina center (Afar rift, Ethiopia). J. Petrol. 16, 22-56.

[18] Field, L., Barnie, T., Blundy, J., Brooker, R.A., Keir, D., Lewi, E., Saunders, K., 2012. Integrated field, satellite and petrological observations of the November 2010 eruption of Erta Ale, Bull. Volcanol. 74, 2251-2271.

[19] Field, L., Blundy, J., Calvert, A., Yirgu, G., 2013. Magmatic history of Dabbahu, a composite volcano in the Afar rift, Ethiopia. Geol. Soc. Am. Bull. 125, 128-147.

[20] Hutchison, W., Mathera, T.A., Pyle, D.M., Boycec, A.J., Gleeson, M.L.M., Yirgu, G., Blundy, J.D., Ferguson, D.J., Vye-Brown, C., Millar, I.L., Sims, K.W.W., Finch, A.A., 2018. The evolution of magma during continental rifting: new constraints from the isotopic and trace element signatures of silicic magmas from Ethiopian volcanoes. Earth Planet. Sci. Lett. 489, 203-218.

[21] Wright, T.J., Ebinger, C., Biggs, J., Ayele, A., Yirgu, G., Keir, D., Stork, A., 2006. T.J. Magma-maintained rift segmentation at continental rupture in the 2005 dyking episode. Nature 442, 291-294.

[22] Ayalew, D., Pik, P., Bellahsen, N., France, L., Yirgu, G., 2019. Differential fractionation of rhyolites during the course of crustal extension, western Afar (Ethiopian rift). Geochem. Geophys. Geosys. 20(2), 571-593.

[23] Hofmann, C., Courtillot, V., Feraud, G., Rochette, P., Yirgu, G., Ketefo, E., Pik, R., 1997. Timing of the Ethiopian flood basalt event and implications for

plume birth and global change. Nature 389, 338-341.

[24] Marty, B., Pik, P., Yirgu, G., 1996. Helium isotopic variations in Ethiopian plume lavas; nature of magmatic sources and limit on lower mantle contribution. Earth Planet. Sci. Lett. 144, 223-237.

[25] Manighetti, I., Tapponnier, P., Gillot, P.Y., Jacques, E., Courtillot, V., Armijo, R., Ruegg, J.C., King, G., 1998. Propagation of rifting along the Arabia-Somalia plate boundary: into Afar. J. Geophys. Res. 103(B3), 4947– 4974.

[26] Hayward, N.J., Ebinger, C., 1996. Variations in along-axis segmentation of the Afar rift system. Tectonics 15, 244-257.

[27] Dugda, M.T., Nyblade, A.A., 2006. New constraints on crustal structure in eastern Afar from the analysis of receiver functions and surface wave dispersion in Djibouti. Geol. Soc. Spec. Publ. 259, 239-251.

[28] Stuart, G.W., Bastow, I.D., Ebinger, C.J., 2006. Crustal structure of the northern main Ethiopian rift from receiver function studies. In: Yirgu, G., Ebinger, C.J., Maguire, P.K.H., eds. The Afar volcanic province within the east African rift system, Geol. Soc. Spec. Publ. 259, 55-72.

[29] Wolfenden, E., Ebinger, C., Yirgu, G., Renne, P.R., Kelley, S.P., 2005. Evolution of a volcanic rifted margin: southern Red Sea, Ethiopia. Geol. Soc. Am. Bull. 117, 846-864.

[30] Cochran, J., 1983. A model for development of the Red Sea. Am. Assoc. Pet. Geol. Bull. 67, 41-69.

[31] Stab, M., Bellahsen, N., Pik, R., Quidelleur, X., Ayalew, D., Leroy, S., 2016. Mode of rifting in magma-rich settings: tectono-magmatic evolution of Central Afar. Tectonics 35, 2-38.

[32] Lahitte, P., Gillot, P.Y., Courtillot, V., 2003. Silicic central volcanoes as precursors to rift propagation: the Afar case. Earth Planet. Sci. Lett. 207, 103-116.

[33] Varet, J. 1978. Geology of central and southern Afar (Ethiopia and Djibouti Republic) Edition CNRS, Paris.

[34] Kidane, T., Carlut, J., Courtillot, V., Gallet, Y., Quidelleur, X., Gillot, P.-Y., Haile, T., 1999. Paleomagnetic and geochronological identification of the Reunion subchron in Ethiopian Afar. J. Geophys. Res. 104(B5), 10,405-10,419.

[35] Hutchison, W., Biggs, J., Mather, T.A., Pyle, D.M., Lewi, E., Yirgu, G., Caliro, S., Chiodini, G., Clor, L.E., Fischer, T.P., 2016. Causes of unrest at silicic calderas in the east African rift: new constraints from InSAR and soil-gas chemistry at Aluto volcano, Ethiopia, Geochem. Geophys. Geosys. 17(8), 3008-3030.

[36] Rampey, M.L., Oppenheimer, C., Pyle, D., Yirgu, D. 2010. Caldera-forming eruptions of the Quaternary Kone volcanic complex, Ethiopia. J. Afr. Earth Sci. 58, 51-66.

[37] Ronga, F., Lustrino, M., Marzoli, A., Melluso, L., 2010. Petrogenesis of a basalt-comendite-pantellerite rock suite: the Boseti volcanic complex (main Ethiopian rift). Mineral. Petrol. 98, 227-243.

[38] Castro, J., Cashman, K.V., 1999. Constraints on rheology of obsidian lavas based on mesoscopic folds. J. Struct. Geol. 21, 807-819.

[39] Gibson, I.L., 1970. A pantelleritic welded ash-flow tuff from the Ethiopian rift valley. Contrib. Mineral. Petrol. 28, 89-111.

[40] Nicholls, J., Carmichael, I.S.E., 1969. Peralkaline acid liquids: a petrological study. Contrib. Mineral. Petrol. 20, 268-294.

[41] Marsh, J.S., 1975. Aenigmatite stability in silica-undersaturated rocks. Contrib. Mineral. Petrol. 50, 135-144.

[42] Markl, G., Marks, M.A.W., Frost, B.R., 2010. On the controls of oxygen fugacity in the generation and crystallization of peralkaline melts. J. Petrol. 51, 1831-1847.

[43] Seaman, S.J., Dyar, M.D., Marinkovic, N., 2009. The effects of heterogeneity in magma water concentration on the development of flow banding and spherulites in rhyolitic lava. J. Volcanol. Geotherm. Res. 183, 157-169.

[44] Smith, J.V., 2002. Structural analysis of flow-related textures in lavas. Earth Sci. Rev. 57, 279-297.

[45] Gonnermann, H.M., Manga, M., 2005. Flow banding in obsidian: a record of evolving textural heterogeneity during magma deformation. Earth Planet. Sci. Lett. 236, 135-147.

[46] Castro, J.M., Dingwell, D.B., Nichols, A.R.L., Gardner, J.E., 2005. New sights on the origin of flow bands on obsidian. In: Manga, M., Ventura, G., eds. Kinematics and dynamics of lava flows. Geol. Soc. Am. Spec. Paper 396, p. 55-65.

[47] Gibson, R.G., Naney, M.T., 1992. Textural development of mixed, finely porphyritic silicic volcanic rocks, Inyo Domes, eastern California. J. Geophys. Res. 97, 1541-1559.

[48] Seaman, S.J., Scherer, E.E., Standish, J.J., 1995. Multistage magma mingling and the origin of flow banding in the Aliso lava dome, Tumacacori Mountains, southern Arizona. J. Geophys. Res. 100 (B5). doi.org/10.1029/94JB03260.

[49] Rust, A.C., Cashman, K.V., Wallace, P.J., 2004. Magma degassing buffered by vapor flow through brecciated conduit margins. Geology 32(4), 349-352.

[50] Tuffen, H., Dingwell, D.B., Pinkerton, H., 2003. Repeated fracture and healing of silicic magma generate flow banding and earthquakes? Geology 31(12), 1089-1092.

[51] Mysen, B.O., Virgo, D., Seifert, F.A., 1982. The structure of silicate me;ts: implications for chemical and physical properties of natural magma. Rev. Geophys. Space Phys. 20, 353-383.

[52] Clough, B.J., Wright, J.V., Walker, G.P.L., 1982. Morphology and dimensions of the young comendite lavas of La Primvera volcano, Mexico. Geol. Mag. 119, 477-485.

[53] Bailey, R.A., Dalrymple, G.B., Lanphere, M.A., 1976. Volcanism, structure, and geochronology of Long Valley Caldera, Mono County, California, J. Geophys. Res. 81, 725-744.

Miocene Volcaniclastic Environments Developed in the Distal Sector of the Bermejo Basin, Argentina

José L. Lagos and Ana M. Combina

Abstract

During the Miocene, in the distal sectors of the Bermejo Basin, a complex relationship developed between a floodplain and contemporary volcanic activity. Seven stages of sedimentation are established to interpret this paleoenvironmental relationship. Stage I corresponds to the development of the floodplain previous to pyroclastic activity; in Stage II, pyroclastic activity is manifested by fall deposits and dry pyroclastic surges. A probable calm in the volcanic activity, associated with exceptional rains, generates laharic deposits (Stage III). Stage IV is dry pyroclastic surges that collapse the floodplain. Subsequently, the river system is reestablished (Stage V) under a regime of low to null volcanic activity. During Stages VI and VII, thick deposits of dry and wet pyroclastic surges, which have records of contemporary seismic activity. The presence of deformational structures within the pyroclastic deposits and lahars indicate that the volcanic centers were in distant areas. The volcanism that generated these deposits is probably associated with the migration to the east of the Miocene volcanic arc of the Cordillera de Los Andes or could be associate with the volcanism of the Sierra de Famatina.

Keywords: Miocene, pyroclastic rocks, floodplains, Bermejo basin

1. Introduction

The study area is located southwest of Campo de Talampaya, La Rioja Province, Argentina. In this sector, there is a topographic high called Alto de San Nicolás, in which the Grupo San Nicolás [1] emerges. The San Nicolás Group is made up of the Rio Mañero and Desencuentro Formations, both of continental origin (**Figure 1b** and **c**), which together have a thickness greater than 2000 meters [4]. The pyroclastic sediments in these units were dated by [5], in $15,0 \pm 1,2$ Ma and $7,54 \pm 1,56$ Ma placing this sequence in the middle-late Miocene.

The Desencuentro Formation was divided into four informal Members named D1, D2, D3 and D4 [1, 2, 4] based on their facies and paleoenvironmental evolution, emphasizing the description of clastic sediments. However [6, 7], the study and interpretation of the important pyroclastic deposits present within this Formation, calling it Member P. These authors point out that member P is interdigitated within members D2 and D3. Paleontological and paleoenvironmental papers indicate that
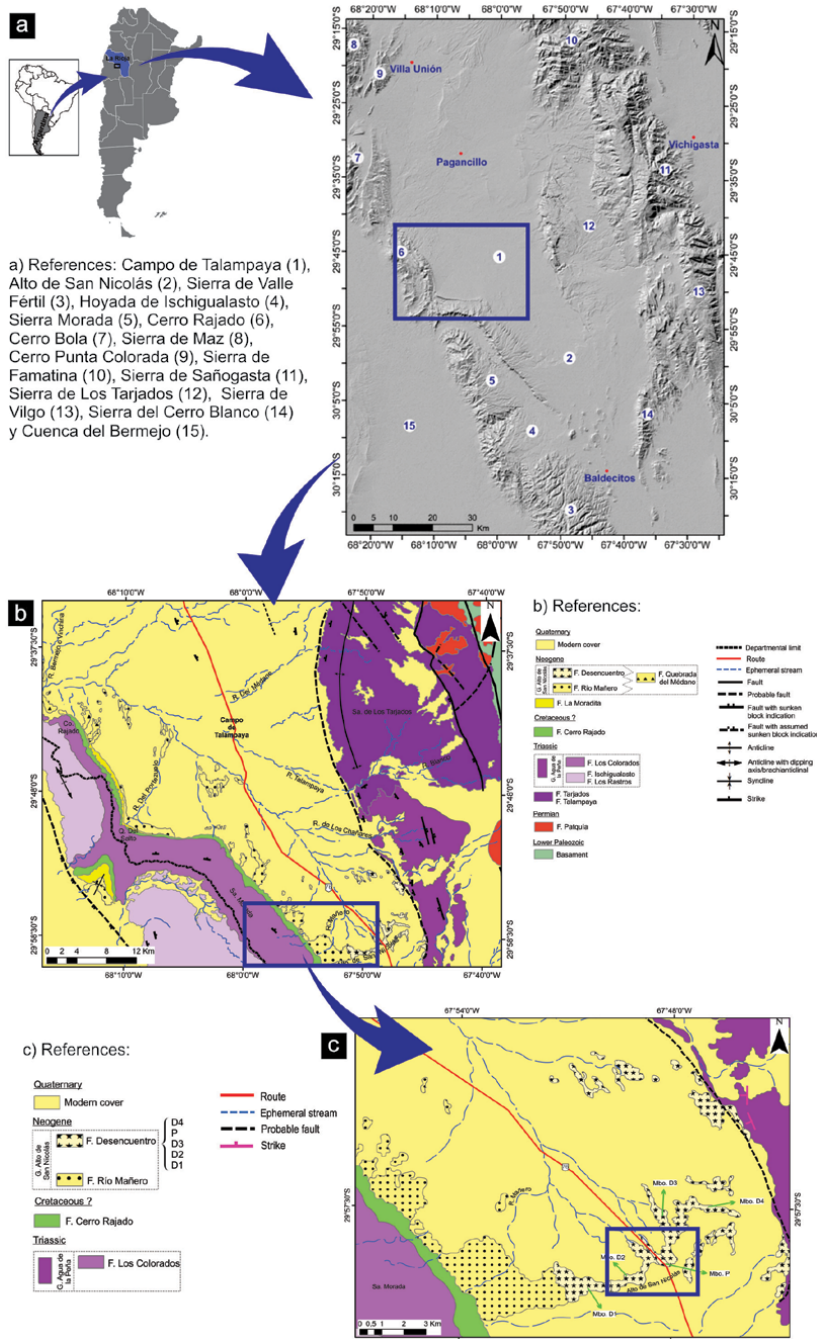
Figure 1.
(a) Topographic map and its environments with map of South America and Argentina; (b) Local geology of study area (modified of [2, 3]); (c) Detailed geological map of study area.

the prevailing climate for that period was warm, seasonal with torrential rains [1, 2, 8].

The objective of this contribution is to determine the prevailing paleoenvironmental conditions during the late Miocene and their evolution, through detailed sedimentological studies, in the middle section of the Desencuentro Formation in Campo de Talampaya, La Rioja Province, Argentina.

2. Geology and tectonic evolution

Since the beginning of the Andean Orogeny (Maastrichtian-Danian), the extensional basins of southwestern South America have changed their tectonic configuration. Most of them went from extensional to compressive regimes, and those near the elevated front became foreland basins (Austral Basin, Neuquina, Cuyana, and Bermejo Basin, etc.).

The Alto de San Nicolás Group deposits in what was the distal sector of the Bermejo basin correspond to this stage of sedimentation of a predominantly continental character [1, 4]. The basal section of the Alto de San Nicolás Group is conditioned by the elevation of the Cordillera Frontal and by the ascent and migration of the continuous and folded belt in the Precordillera. On the other hand, the upper section is associated with the elevation of the Sierras Pampeanas, more precisely with the Sierra de Velasco [1]. Finally, with the ascent between the end of the Miocene and the Pliocene of the Sierra de Valle Fértil, Sierra Morada and Sierra de Los Tarjados produces the disconnection of the most distal parts of the basin (Campo de Talampaya Basin) with the main depocenter of Bermejo [9].

Currently, in the central-western sector of Argentina (Pampean segment), the low inclination (5°-10°) with which the Nazca Plate subducts below the South American Plate conditions the tectonics of the sector [10, 11]. This Pampean segment is characterized by the development of foreland basins, which are fragmented by elevated basement blocks and originate intermountain depressions. Among the foreland intermontane basin that develops on the Pampean segment is the Campo de Talampaya which is related to the uplift of the Sierra de Los Tarjados [1].

In the southwestern sector of Campo de Talampaya (**Figure 1a,b** and **c**), there is a topographic high that extends in a NE–SW direction called Alto de San Nicolás (**Figure 1a,b** and **c**), which consists of a succession of continental Neogene (Alto de San Nicolás Group) age strata, 2320 m thick, which also exhibit a dip to the east that varies between 5° and 21° [1, 4]. In this sector, the Alto de San Nicolás Group (**Figure 1a,b** and **c**) comprises the Río Mañero and Desencuentro Formations. The base of this stratigraphic unit rests paraconformity or by angular unconformity upon Cerro Rajado Formation (Cretaceous?) depending on which is the sector of the Campo de Talampaya [4]. Discordant on the neogenic units are an alluvial fan, ephemeral fluvial systems, and eolian deposits of the Quaternary [12].

The Desencuentro Formation (upper Miocene) consists of a clastic sequence that overlaps the Río Mañero Formation through a transitional passage, which consists of sandstones, mudstones, few conglomerate lenses, and tuff levels deposited in a saline mud-flat environment which are finally covered by sand-flat/mudflat [1]. This unit was divided into four informal Members (D1, D2, D3, and D4) emphasizing the description of the widely developed clastic sediments [1, 2, 4], but not in the case of the rocks of volcanic origin, since these, they are only mentioned as participants in the sedimentary record. Subsequently, a new member (called P) is included for the Desencuentro Formation, depending on its pyroclastic/volcaniclastic character, leaving the stratigraphic column composed of D1, D2, P and D3, D4 [6]. The recognition of Member P indicates characteristic volcanic participation during the deposition of the Desencuentro Formation in the distal sector of the Bermejo Basin [7].

3. Methodology

Five field works were performed in the middle section of Alto de San Nicolás, where traditional field techniques were used: description of detailed stratigraphic

profiles (lithology, grain size, contacts, geometry, color, and sedimentary structures/biogenic were the data taken) and measurement of strike and dip of strata with Brunton compass. Subsequently, the different lithofacies were classified and interpreted, which were grouped into associations of facies and architectural elements to interpret the depositional environments. In the case of clastic and volcaniclastic lithofacies, the associations will be interpreted as architectural elements, following what was stated by [13, 14]. Pyroclastic lithofacies, their genetic processes will be interpreted in a general way, following the methodology of [15] and other authors [16, 17].

The identified pyroclastic lithofacies were coded adapting the proposal of [15]. The capital letter is used for the grain size classes and the lower case for the sedimentary structures: (T) tuffs, (L) lapillita, (m) massive, (b) lamination, (db) diffuse lamination, (//b) parallel lamination, (xb) cross-lamination, (ob) sinusoidal ripple-drift lamination, (dob) diffuse sinusoidal ripple-drift lamination, (r) deformational structures, (ch) chute and pool, (esc) climbing structures, (acc) accretional lapilli. For the clastic and volcaniclastic lithofacies, they were coded by adapting the scheme of [13, 14]. Also, for these lithofacies the capital letter is used for the grain size classes and the lower case for the sedimentary structures and identification of volcaniclastic rocks: (F) claystone, (S) sandstone, (G) conglomerate; (m) massive, (pl) planar cross-lamination, (ps) planar cross-stratification (t) tangential cross-stratification, (h) parallel lamination, (v) volcaniclastic (s) matrix supported.

In this work, sedimentary rocks without the content of volcanic fragments will be called clastic rocks. Following the scheme [18], rocks or pyroclastic deposits will be called those that demonstrate a mode of fragmentation, transport and deposition [fall, surge or flow] directly related to volcanic activity. The term volcaniclastic will be used, following the criteria of [18], to refer to those deposits that have a connection with volcanism, but that result from the transport and deposition of exogenous cycle agents (mudflows, river currents, etc.), regardless of the fragmentation mechanism (during the eruption or if they are new particles formed by the weathering of older rocks). For this reason, for their classification, they will be considered as clastic rocks to which the qualifying noun volcaniclastic will be added.

For the granulometric classification of the sedimentary particles, the Udden-Wentworth classification and Phi scale were used and for the pyroclastic particles the modified proposal of [17] was used.

4. Sedimentological and paleoenvironmental analysis

A total of **23** facies were identified in the deposits of the middle section of the Desencuentro Formation in Alto de San Nicolás, which were grouped into three facies associations (pyroclastic facies) and six architectural elements (clastic and volcaniclastic facies). The nomenclature used in the identification of lithofacies is indicated in **Tables 1–4**, together with the sedimentary structures and other characteristics of each one; and the terminology applied for the associations of facies (DPS, WPS and PF) and architectural elements (FF, CH(FF), CR, CH and SG) is indicated in **Table 5**. The different interpretations that were inferred from the identified lithofacies, associations of facies and architectural elements are briefly described below:

The presence of sismites (fluid leaks, flaming structures, ball pillow, etc.) in the sediments originated by the humid pyroclastic surges, allows us to infer, following what was stated by [19] that the sedimentation area would be in a distal sector with respect to the eruptive center (**Figure 2k**).

Pyroclastic lithofacies			
Code	**Description**	**Interpretation**	
//bT1	Coarse tuffs, well-selected, grayish, in tabular bodies, with variable thickness (0,8 to 1,50 m), exhibiting wavy, net, and transitional boundaries. Internally they present parallel lamination, which is sometmes better denoted by observing layers that individually exhibit whitish pumice clasts or dark lithic clasts.	The development of sharp parallel lamination and good selection suggest that these deposits were formed from a high flow regime [15].	Dry pyroclastic surges
obT	Coarse tuffs, well-selected and grayish in bodies with irregular geometries, exhibiting wavy and net contacts, with thicknesses of approximately 10 to 50 cm. Internally, they present sinusoidal ripple-drift laminations (**Figure 2a**) and sometimes shows concretions, some pumiceous clasts and pipes (**Figure 2j**) that cut to the lamination.	The development of sinusoidal ripple-drift laminations and bodies with marked and erosive limits indicates a genesis associated with surges [20]. The different pipes that cross the base of this lithofacies indicate different forms of fluid expulsion. On the one hand, you can see "classic" vertical pipes that cut the pre-existing structure [15], implying a vertical rise of the fluids that have not encountered resistance to their passage, probably due to lack of cohesion in the pre-existing sediments, while there are pipes that modify the vertical layout, becoming horizontal and vertical again.	Dry pyroclastic surges
escTL	Coarse tuffs and coarse lapilli, grayish-white, which occur in irregular bodies, with wavy transitional limits and thicknesses of approximately 8 to 12 cm. Internally these tuffs present "scaling structures", marked by intercalations of thin to thick laminae (**Figure 2d**). In some sectors, these scaling structures consist of clast-support pumiceous sigmoid bodies.	The climbing structures observed originate from these types of pyroclastic surges that slide over topographic irregularities [21, 22]. When this lithofacies develops clast-support deposits, its origin within the surges is punctual and does not condition their dynamics. In this point space, a granular deposit is produced.	Dry pyroclastic surges
bL	Coarse and medium/coarse lapilli, grayish, which develop bodies of tabular to slightly irregular geometries, with thicknesses that vary between approximately 10 to 35 cm and planar and wavy transitional limits. Internally, this bodies have thin and thick, parallel or sinusoidal, clast-support, which show variations in the proportion of lapilli pumiceous (**Figure 2g**). The white laminae are characterized by having a greater amount of pumice than lithic clasts. In some sectors, weakly laminated whitish pumice lenses are found at the base of the bodies. Lenses sometimes have reverse or normal gradation.	The alternation of enriched or depleted levels in pumiceous clasts originates from successive surges with variations in the clast populations, from sustained currents over time [15]. The development of pumiceous lenses at the base of the bodies probably responds to punctual and local flow regime changes, which deposit the clasts of greater granulometry, the rest of the particles are carried as bed load by turbulence, generating, in this way, the lamination observed.	Dry pyroclastic surges
pmL	Medium and coarse lapilli, massive, moderately selected, clast-support, which occur in tabular bodies. These lapillitic bodies have thicknesses ranging from 4 to 15 cm and exhibit	They are interpreted as deposits originated from pyroclastic fall [15, 16]. The presence of units with contrasting granulometry (in this case, thick and fine lapilli) is related to non-sustained	Pyroclastic falls

Pyroclastic lithofacies		
Code	Description	Interpretation
	planar, net, and transitional contacts. In some sectors, includes a set of strata made up of intercalations of medium and coarse lapilli that together present a growing grain arrangement (**Figure 2f**). Lapilli are white in color and arranged randomly, although few imbricated clasts can be observed.	eruptions that have several short-duration pulses or to partial collapses of the eruptive column [23]. At interruptive moments, rework may have occurred by tractive agents, which produced imbrication of clasts in certain sectors of the deposit.	
mT	Fine tuffs, massive, white that develop into mantiform bodies (**Figure 2i**). These tuff deposits have thicknesses ranging from 20 to 50 cm and have lateral extensions that can be followed for more than 80 m and planar net limits.	The development of massive, mantiform bodies that extend great distances are associated with deposits that correspond to pyroclastic fall (PF) [23].	Pyroclastic falls

Table 1.
Table of pyroclastic lithofacies and their codes adapting from the proposal by [15].

Pyroclastic lithofacies		
Code	Description	Interpretation
rL dbTacc	Coarse tuffs (well-selected) and fine lapilli, grayish that develop irregular or tabular geometries, exhibiting wavy, net and transitional contacts, with thicknesses of approximately 0,4 to 1,20 m. Internment they present diffuse lamination (**Figure 2c**). The original lamination can be deduced by the presence of levels enriched in fine pumiceous lapilli and other levels enriched in lithics. This lamination is deformed by fluid leaks (**Figure 2h**), flame and load structures. Other deformational structures are sedimentary folds and convolute lamination. They also observed accretional lapilli (**Figure 2e**) and specks of oxides.	The presence of accretional lapilli would indicate the union of ash particles by condensation of water in humid eruptive clouds [16, 24–26]. In this pyroclastic currents, the vapor, by accompanying the sediment during its transport, is retained in the pores and, when it cools, it becomes water, which causes the sediment to be embedded in fluids, giving it plasticity and ease for the liquefaction. Deformational structures (convolute lamination, flame structures, etc.) are interpreted sismites [19, 27, 28]. Another genesis for these structures is associated with a rapid sedimentary loading of denser sediments [29].	Wet pyroclastic surges
dobT	Coarse tuffs, well-selected, grayish that develop irregular geometries with wavy and transitional contacts, and thicknesses of approximately 0,1 to 1,10 m. They present diffuse sinusoidal ripple-drift lamination, with a wide wavelength that in some sectors graded laterally to sheets with horizontal lamination. It also has rust specks of oxides, accretional lapilli, concretions, and few white pumiceous clasts. The concretions are subequant, with diameters ranging from 2 to 10 cm. The core of the anterior structures is formed by claystone intraclasts. In	The presence of thin bodies with transitional boundaries could represent rapidly stacked and partially amalgamated flow units [30]. The concretions are formed by precipitation or segregation of minerals around a core (in this case of claystone intraclasts). The claystones intraclasts located at the base of the bodies are consistent with the turbulent character of these pyroclastic currents, which would have eroded previous clastic sedimentary environments. The preservation of the primary lamination in concretions	Wet pyroclastic surges

Pyroclastic lithofacies			
Code	Description	Interpretation	
	addition, concretions can be aligned or located at the base of the bodies.	indicates that concretions are postdepositional [31].	
xbT	Coarse tuffs, well-selected, grayish, generating tabular bodies with a thickness of 0,4 m, with wavy net bases. Internally they develop tangential cross-lamination (**Figure 2l**), which varies vertically to parallel lamination. These deposits also exhibit specks of oxides, pipes of various sizes and concretions.	Tangential cross-lamination and parallel lamination are interpreted as the product of two or more pyroclastic surges pulses, with different speeds. The specks of oxides originate from the instantaneous oxidation of the pyroclasts during their transport/ deposition, generating instantaneous metasomatic oxidative processes [32].	Wet pyroclastic surges
//bT2	Coarse tuffs, well-selected, grayish, which develop bodies of tabular and irregular geometries, with thicknesses that vary between approximately 0,25 to 1 m and with wavy, net, and transitional contacts. They present thin and thick, parallel (**Figure 2b**) and deformational lamination, in addition to sinusoidal ripple-drift laminations of short wavelength in phase. These deposits also exhibit, ripples in phase, specks of oxides and concretions (**Figure 2k**).	Sinusoidal ripple-drift laminations of short wavelength are associated with these pyroclastic currents [20].	Wet pyroclastic surges
chT	Coarse tuffs, well-selected grayish, and with irregular bodies, which develop net and wavy contacts. Internally they present chute and pool structures (**Figure 2m**), denoted by intercalations of thin and thick sheets that present angularity.	Chute and pool are associated with wet pyroclastic surges [18], and also point out that they are indicators of high flow regimes [20].	Wet pyroclastic surges
mTacc	Coarse tuffs, grayish, in approximately tabular bodies, with a thickness of 40 to 60 cm and transitional and wavy contacts. Internally they are massive, exhibiting specks of oxides and accretion lapilli.	The development of massive bodies and the presence of accretional lapilli are associated with wet pyroclastic surges [32]. The presence of moisture in the cloud that accompanies these flows that counteracts the effects of elutriation due to fluid leaks [15].	Wet pyroclastic surges

Table 2.
Table of pyroclastic lithofacies and their codes adapting from the proposal by [15].

5. Sedimentary model

For the development of the paleoenvironmental model that involves the genesis of Member P and part of Members D2 and D3 [6, 7], the different sedimentation moments were divided into seven temporarily consecutive stages.

5.1 Stage I

The first sedimentation event is made up of fine clastic deposits, represented by the architectural elements FF, SG, CR and CH (FF) (**Figures 4** and **5**). The element FF represented by claystone, tabular bodies and of great extension, corresponds to wide flood plains. The interdigitation between FF and SG
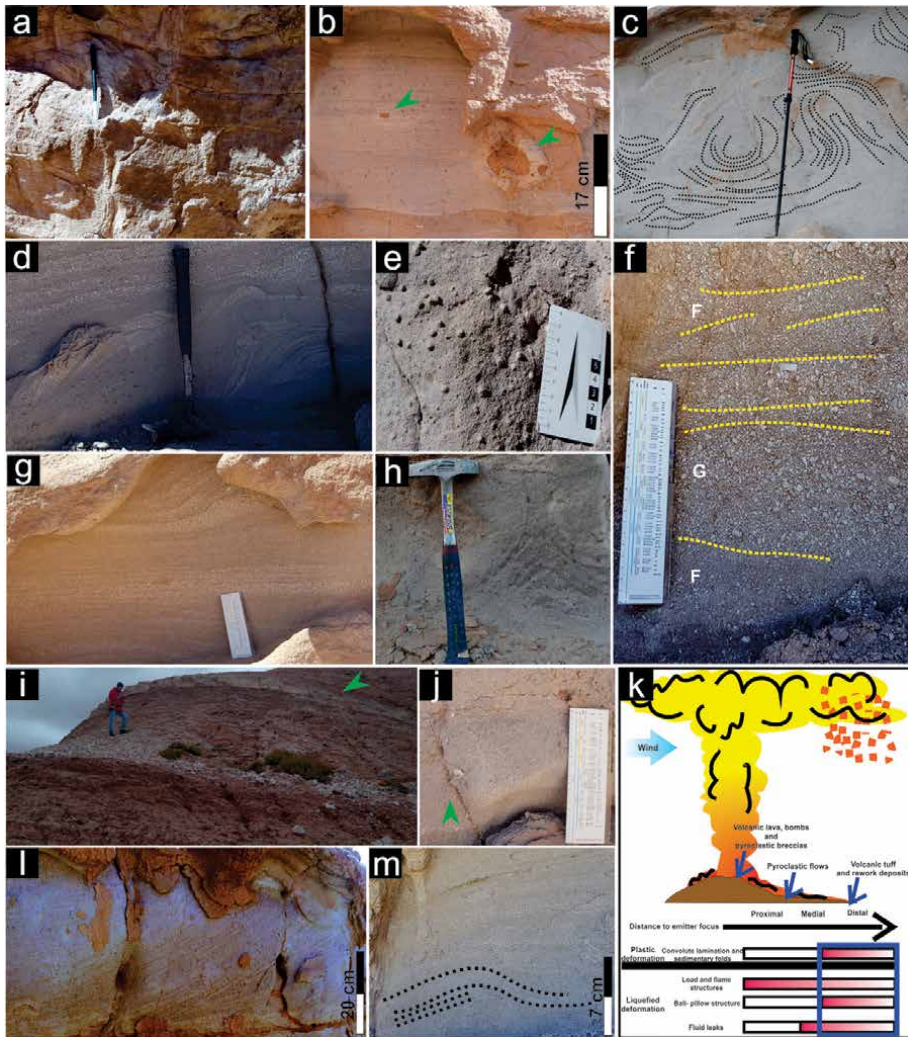
Figure 2.
(a) Bodies exhibiting internally ripple-drift laminations, the pen measures 15 cm; (b) level with internally parallel lamination and concretions (indicated by green arrows); c) level with diffuse sedimentary folds, the cane measures 1 m; d) level that presents scaling structures and where, in addition, the direction of flow is indicated; e) Accretional lapilli; f) outcrop showing intercalations of levels with medium (M) and coarse (G) lapilli; g) outcrop where intercalations of tabular to slightly irregular levels are observed, which internally present sheets with variations in the proportion of pumiceous clasts; h) fluid exhaust structure, the pickaxe measures 33 cm; i) outcrop where one level of fall are observed (indicated by green arrow); the person is 1.65 m tall; j) level that is crossed by a pipe that presents elutriation of fines and a vertical trajectory (indicated by green arrow); k) scheme where the structures found in the field are indicated with a table and from which the distance to the emitter focus can be inferred (modified from [19]); l) tabular body exhibiting internally tangential cross-lamination; m) level with parallel lamination structures and chute and pool.

indicates that these floodplains are intermittently invaded by hyperconcentrated flows, represented by approximately tabular bodies of great thickness (more than 1.5 m), probably amalgamated. The origin of these mass movements (sheet flood) would be associated with humid times, where the pluvial discharge peaks generate floods, which can transport considerable amounts of sand and pellets. These laminar processes [38] can sometimes generate deposits of more than 2 m thick [4]. In an arid climate or dry seasons, the plains would have dried out, generating levels with desiccation cracks observed in the Fm lithofacies.

Clastic lithofacies			
Code	Description	Interpretation	
Gm	Conglomerates, clast-support, reddish-brown in color, appear in irregular bodies with irregular net boundaries and thicknesses of approximately 5 to 7 cm. They are made up of claystone intraclasts, brown in color and which are also imbricated.	They are interpreted as lag [14]. These originate from high flow regimes, capable of transporting even cohesive fragments of the floodplain [33].	Lag
Sm	Fine and medium grayish sandstones, which occur in tabular bodies, with thicknesses that vary between 0.20 to 2 m and lateral extensions that exceed 20 meters (**Figure 3k**). These bodies exhibit net planar and deformational limits, although sometimes these can be transitional, in which case they form amalgamated bodies. This facies tends to have a massive structure, however, in some sections of these deposits, diffuse parallel lamination (**Figure 3c**) and incipient low angle cross-lamination can be observed. Likewise, small and isolated levels of whitish pumiceous paraconglomerates are observed. In addition, it presents clastic dikes, load structures and pinch and swell (**Figure 3l**), the latter denoted by reddish-brown claystone levels, immersed in a sandy matrix.	It is interpreted as deposits of gravitational flows [13] corresponding to hyperconcentrated flows. The massive structure is the result of the high concentration of particles and the rapid deposition, however, the presence of diffuse parallel lamination and incipient low-angle cross-lamination could be signaling the dilution of these flows and a change in dynamics in the transport of the sediment [34]. The presence of small and isolated levels of pumiceous paraconglomerates would indicate the remobilization of previous pyroclastic deposits.	Gravity flows
Spl	Fine and medium sandstones, reddish-brown in color, present in tabular bodies, with thicknesses ranging from 0.10 to 1 m and lateral extensions of approximately 1 to 5 m. These deposits exhibit wavy, net, and transitional contacts. Internally they develop planar cross-lamination (sometimes diffuse) (**Figure 3h**). In some sectors, this lithofacies has reddish-brown claystone intraclasts at the base.	They are interpreted as bottom charge deposits, the result of the migration of megawaves from straight ridges in a low flow regime [13, 14].	Bars
Sh	Fine and medium sandstones, well-selected and with parallel lamination (sometimes incipient), which occur in irregular to slightly tabular bodies, brown (**Figure 3e**). These bodies exhibit thicknesses that vary between 30 to 70 cm and net, irregular and planar limits. When the limits are transitional the bodies appear amalgamated.	This facies is interpreted as flat layer deposits with a high flow regime as a result of the decrease in water hair [13]. Upper regime plane lamination	Planar bed flow
Fm	Massive reddish-brown claystones that develop tabular bodies, with thicknesses ranging from 0.6 to 2 m and lateral extensions ranging from 8 to 25 m approximately (**Figure 3a**). The limits of these claystone deposits are net planar. Internally, this facies is massive, although in some sectors bioturbations can be observed, rhizolites, and	The massive claystone deposits (Fm) are generated by settling fine suspended sediments under conditions of very low energy [14].	Flood plains

Clastic lithofacies		
Code	**Description**	**Interpretation**
	desiccation cracks (**Figure 3d**) that are mainly concentrated on the roof of the bodies.	
Fl	Parallel lamination claystone, of lighter reddish-brown colors, that form tabular bodies with thicknesses of 2 to 10 cm and lateral extensions ranging from 2 to 8 m (**Figure 3f**). In addition, they present net planar limits, although they can sometimes be deformational. Internally they present thin and thick, parallel and deformational laminaes. The deformational structures can have different scales; from small to large scale, the latter comes to separate sandstone bodies (lithofacies Sm). Raindrop marks, load structures (**Figure 3g**), and isolated whitish pumice clasts are observed in some sectors on the roof of these claystone bodies (**Figure 3c**). Occasionally the pumiceous clasts form very thin pumiceous sheets.	This lithofacies can be interpreted as deposits formed by decantation in shallow water bodies where the sediment has been transported by suspension [13]. Flood plains

Table 3.
Table of clastic lithofacies and their codes adapting from the proposal by [13, 14].

Volcaniclastic lithofacies		
Code	**Description**	**Interpretation**
Gmsv	Volcaniclastic conglomerates with an abundant fine sandy matrix of light brown color, which develop tabular bodies, with thicknesses that vary between 40 and 80 cm (**Figure 3a** and **k**). These bodies have net and planar boundaries. Internally, in sectors, very diffuse thick lamination can be observed (**Figure 3b**). The few gravel clasts are white pumice, with diameters ranging from 0.5 to 3 cm, white, subangular to subrounded, and with semi-equant and tabular shapes. These clast swarms can exhibit diffuse reverse gradation (**Figure 3b**). This spatial arrangement of the pumice clasts could be interpreted as boundaries of bodies with similar textural characteristics that appear amalgamated. Sometimes the pumiceous clasts are arranged vertically. In some sectors, this facies limits inferiorly with the lithofacies Fm. In this limit, claystone intraclasts and flame structures can be observed.	The facial features described correspond to the deposits formed under conditions of hyperconcentrated flows, directly or indirectly related to contemporary volcanic activity. The presence of massive deposits with incipient lamination, with generally flat limits, moderate textural selection, vertical pumiceous clasts, and accumulation are common characteristics in laharic deposits [35]. The observed accumulations of pumiceous clasts mark the upper limits of these laharic events that form amalgamated bodies. The transitional and wavy contacts that are observed in some levels could respond to load structures, probably caused by the rapid deposition of one level on a less competent one that causes its deformation. Lahars

Volcaniclastic lithofacies			
Code	Description	Interpretation	
Gtv	Volcaniclastic conglomerates polymictic, clast-support, which occur in tabular bodies, whitish brown and with thicknesses of approximately 25 to 40 cm, which exhibit planar net lower limits (**Figure 3i**). Internally they present tangential cross-stratification (sometimes deformed) represented by levels with varying proportions in pumiceous clasts and to a lesser extent by claystone clasts. In some sectors, these deposits have perforating bioturbations on the roof.	They are interpreted as product deposits from the migration of gravelly accretion bars downstream or longitudinal bars during periods of high discharge [14]. The presence of pumiceous clasts indicates the remobilization and/or reworking of pyroclastic deposits, and in the case of claystone clasts of the sediments of previous plains.	Bars
Shv	Fine to coarse volcaniclastic sandstones that occur in tabular to slightly irregular bodies, light brown in color, with thicknesses ranging from 10 to 15 cm and wavy planar or transitional net limits (**Figure 3i**). Internally they exhibit thin parallel lamination (diffuse), formed by whitish pumiceous clasts and some claystone intraclasts.	It is interpreted as bottom charge deposits, probably originated by currents with relatively low flow velocities [13, 36]. Parallel lamination of low flow regime can be interpreted as part of 2D megaondules (dunes with straight ridges), with a view perpendicular to the flow direction.	Sandwaves
Spsv	Coarse volcaniclastic sandstones, which appear in tabular bodies, light brown, which exhibit powers of approximately 15 to 20 cm and planar net limits. Internally they develop thick and fine planar cross-stratification (**Figure 3j**), represented by levels with varying proportions in pumiceous clasts and lithic clasts.	They are interpreted as deposits of low flow regime bedforms [14, 37] resulting from the migration of straight crested megaondules (2D) [13].	Sandwaves

Table 4.
Table of volcaniclastic lithofacies and their codes adapting from the proposal by [13, 14].

In some sectors, interacting with the flood plains, sandy channels develop, of little thickness (between 50 and 70 cm) and tabular to slightly lenticular geometries, interpreted as probable channel systems belonging to crevasses (corresponding to the architectural element CR), originated by erosion of the edges of the main channel during flood events. These channeled systems are sometimes laterally amalgamated, a circumstance that could indicate the topographic compensation of different episodes of flooding-breakdown of the sloping-crevasse formation. The channels are filled by deposits of sand bars (SB), originated from currents with low flow regimes. Interdigitated with FF and SB, sporadically, there are bodies with concave bases filled with fine material (silts and clays), interpreted as deposits of abandoned channels CH (FF). Based on the architecture, spatial relationships and interrelationship that the element FF, CR and CH(FF) present, considered as overbank deposits, it is possible to indirectly infer that the canal system that would have originated them would correspond to an anastomosed fluvial system [13].

5.2 Stage II

Gradually, this sedimentary system began to be influenced by the volcanism of the region (**Figure 5**). The record of this volcanic activity begins in the study area
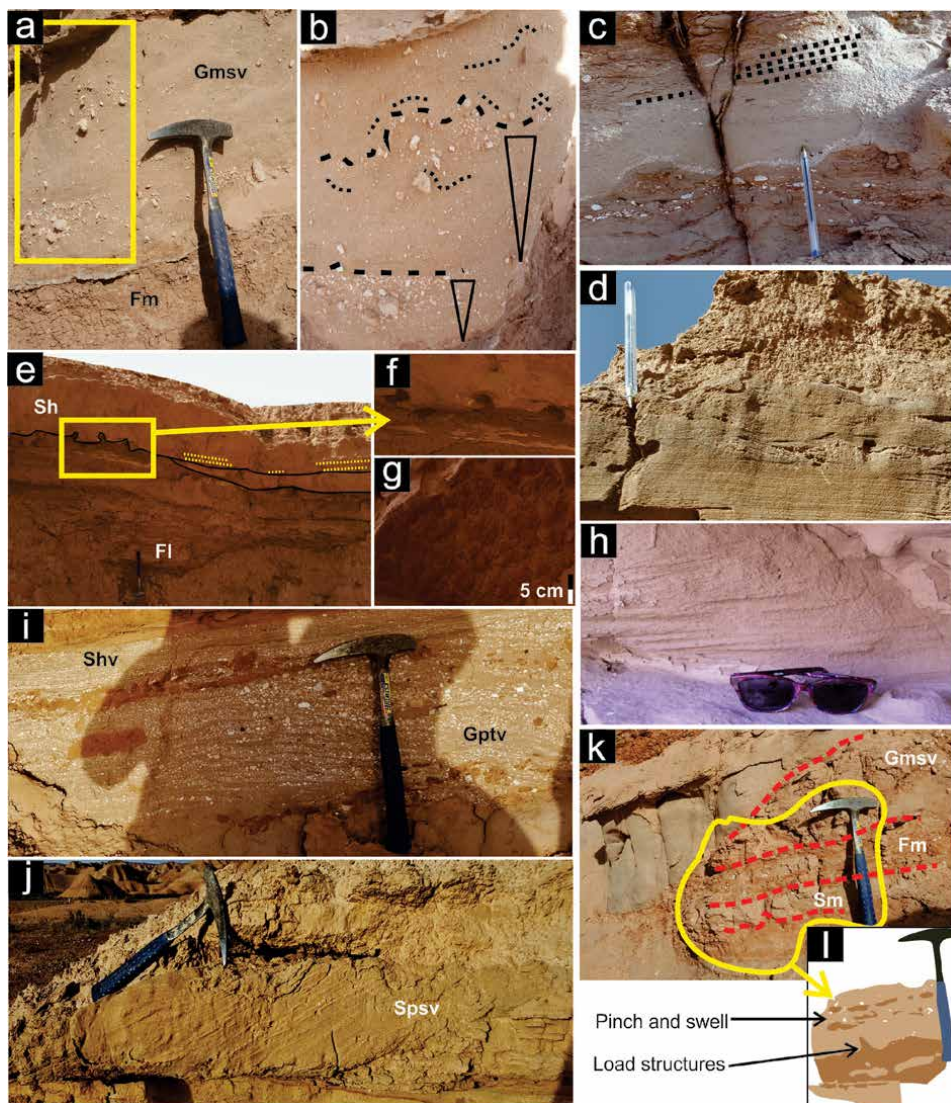
Figure 3.
(a) Outcrop where the lithofacies Fm and Gmsv are indicated; b) figure b corresponds to an enlargement of figure a, where lahars levels are observed with inverse gradation and also very diffuse lamination; c) outcrop where claystone levels are observed that internally present pumiceous clasts and, in addition, a level of fine sandstone that presents diffuse parallel lamination, the pen measures 14 cm; d) level featuring parallel lamination; e) outcrop where the Sh and Fl facies are indicated; f) figure f corresponds to an enlargement of figure e, where the load structures are better observed (indicated with yellow arrows); g) desiccation crack structures; h) level internally featuring planar cross lamination, glasses are 13 cm wide; i) outcrop where the lithofacies Gptv and Shv are indicated. The Gtv lithofacies internally presents tangential cross-stratification, denoted by levels with varying proportions of pumiceous and claystone clasts; j) outcrop where the lithofacies Spsv is indicated, which internally presents planar cross-lamination; k) outcrop where the lithofacies Gmsv, Sm and Fm are indicated; l) scheme of figure k, where the load structures and pinch and swell are indicated.

with falling pyroclastic deposits (facies association PF). The facies association PF (**Figure 4**) is interpreted as a product of the gravitational fall of material from pyroclastic clouds, formed during high-energy explosive eruptions. The energy condition mentioned above would be indicated by the grain size (ash and lapilli) that the lithofacies mT and pmL present [17]. The contribution of pyroclastic material would have caused changes in the dynamics of the fluvial system, by observing a decrease in the size and frequency of crevasse systems. These changes

		Facies associations and architectural elements	
Code	**Facies**	**Description**	**Interpretation**
DPS	//bT1 obT escTL bL	Tuffs (coarse and fine) and lapillita (medium and coarse), grayish, in tabular and irregular bodies, which generally exhibit wavy, net and transitional. The presence of parallel lamination, sinusoidal ripple-drift lamination, scaling structures, etc. indicate that these pyroclastic surges are dry. This association is generated by turbulent flows with low concentrations of particles.	Dry pyroclastic surges
WPS	dbTacc rL dobT xbT //bT2 chT mTacc	Coarse tuffs, grayish, which occur in tabular and irregular bodies, with wavy, net and transitional contacts. Internally present tractive structures (tangential cross-lamination, chute and pool, etc.), deformational structures (convolute lamination, fluid leaks, flame structures, etc.). Sometimes they appear as massive deposits. This association is generated by turbulent and dilute flows. The presence of accretional lapilli, specks of oxides and other structures indicates generated by wet pyroclastic surges.	Wet pyroclastic surges
PF	mT pmL	Fine tuffs and lapillita (medium and coarse), grayish, in tabular bodies, with planar, net, and transitional contacts. They are characterized by being massive deposits and with a clast-support texture. This association is interpreted as deposits of pyroclastic falls from pyroclastic clouds where the sediments are transported by the turbulence and gases of the cloud at different distances. During this transport, the sediments fall in free fall, depending on their size.	Pyroclastic falls
FF	Fm Fl	Massive and/or laminated claystone, of a reddish-brown color, that occur in tabular bodies, which generally develop large extensions ($\sim$25 m) and exhibit planar net limits, although sometimes they can be deformational. Internally, they present desiccation cracks, bioturbations, raindrop marks, load structures, and rhizolites, among others. This architectural element consists of plains (areas with very little slope), which intermittently flood and dry out [13].	Floodplain fines
CH(FF)	Fm Fl	Claystone units, reddish-brown in color, in canaliform bodies, which exhibit concave basal limits and are filled with laminated or massive-looking claystone material. This element represents abandoned channels [14].	Abandoned channels
CR	Sh Shv Sp	Clastic and volcaniclastic sandstones (fine to coarse), which present planar parallel and planar cross-lamination that develop lenticular to slightly tabular bodies, with net irregular contacts and sometimes planar. It is interpreted as deposits of crevasses splays (spill lobes), originated by the erosion of the edges of the main channel [13, 14].	Crevasses splays
CH SB	Sp Spv Shv	Set of fine to coarse clastic and volcaniclastic sandstones, exhibiting planar cross-lamination. These deposits develop in tabular bodies, which generally exhibit planar and sometimes irregular, net, and transitional contacts. Element SB1 represents background shapes, the result of the migration of crossbars (2D). When these facies present pumiceous clasts, it is assumed that the currents eroded and/or remobilized previous pyroclastic deposits.	Sand bars
CH GB	Gtv Gm	Coarse volcaniclastic sandstones and volcaniclastic and clastic clast-support conglomerates. They are presented in tabular bodies, with net planar contacts. Internally they develop lamination and tangential cross-stratification and present variable amounts of pumiceous and lithic clasts. This set of intrinsically related facies is interpreted as bar and	Grave bars

Facies associations and architectural elements			
Code	Facies	Description	Interpretation
		channel bottom deposits (lag). Both bottom structures originate from high flow regimes and normally form in the deepest areas of active channels [13, 33].	
SG	Sm Gmsv	Fine and medium sandstones and matrix-support conglomerates form tabular bodies, often amalgamated, which generally develop large extensions (~20 m) and exhibit planar net contacts and/or transitional. These deposits are characterized by being massive, although in some sectors they can present diffuse parallel lamination and deformational structures (pinch and swell, clastic dikes, load-bearing structures, etc.). This set of characteristics are typical of the SG element [14]. The genesis of this element is related to hyperconcentrated flows. If the deposit has pumiceous clasts, these are considered lahars.	Lahars and hyperconcentrated flows

Table 5.
Table of facies associations (pyroclastic facies) and architectural elements (clastic and volcaniclastic facies).

could be associated with the migration of the river system and/or the loss of its identity, as it has to transport a greater sedimentary load (pyroclastic), under the same tectonic and climatic conditions. In this way, interdigitated volcaniclastic deposits (represented by crevasses) begin to appear in the sedimentary record with the facies association PF and the FF architectural element, the latter element sometimes carrying few pumiceous clasts.

Subsequently, a new volcanic episode represented by the lithofacies bL (association facies DPS) records the activity of dry pyroclastic surges on these plains. The association DPS is interleaved with the FF element. The variations in the content of pumiceous clasts that each of the sheets that make up these pyroclastic deposits (bL) present, allows us to infer that they would have originated from successive surges with oscillations in the populations of clasts, a product of currents fluctuating sustained over time [15].

The plains are areas that are characterized by developing gentle slopes, so a greater contribution of sediments, from pyroclastic falls and successively surges, has probably caused an even greater loss of slope of these plains, being the topographic features very scarce.

5.3 Stage III

In these plains sedimentary events occur (**Figure 5**) whose characteristics are high fluid discharge and high sedimentary load (SG architectural element), which can be interpreted as lahars and hyperconcentrated flows. The origin of both types of gravitational flows is associated with floods as a result of exceptional rains, which allow the generation of hyperconcentrated currents, which by remobilizing pyroclastic materials generate lahars. The deposits product of these processes of mass movements is characterized by being tabular, of great lateral extension (greater than 25 m) and being internally massive, although sometimes they can present tractive structures (for example, diffuse parallel lamination), which could be explained due to dilution of these flows due to loss of sedimentary head, which results in a different fluid/head ratio of the event.

Sometimes the interdigitation of the Gmsv and Sm lithofacies with the FF element generates bodies that present deformational basal contacts and structures

Figure 4.
Composite stratigraphic column and facies of the middle section of the Desencuentro formation. From left to right, the sections from the base to top are described. The lithofacies codes corresponds to Tables 1–4; and the facies associations and architectural elements to Table 5.
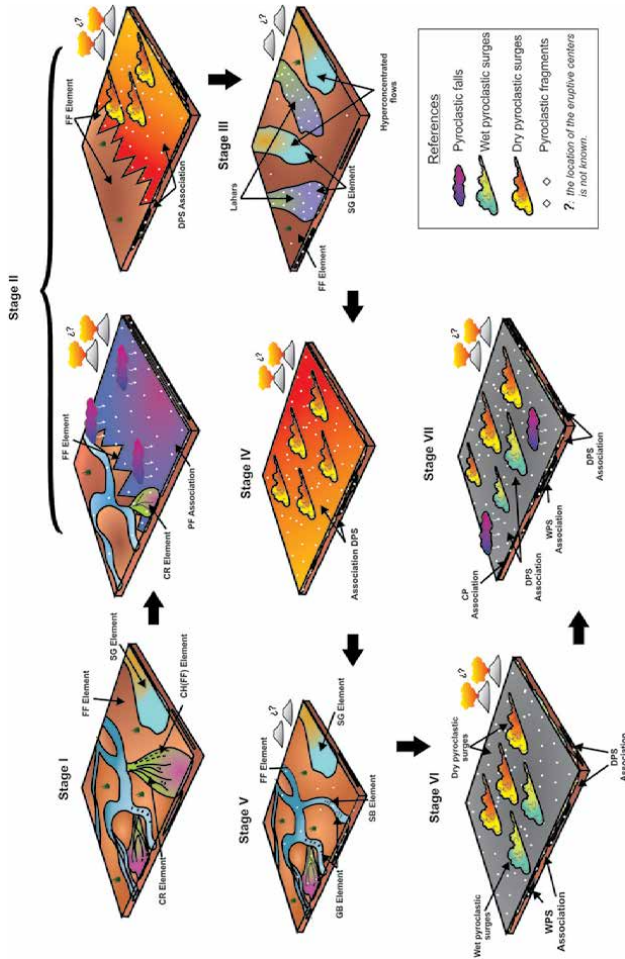
Figure 5.
Scheme unscaled outline showing the seven sedimentary stages and their evolution over time.

such as clastic dikes, pinch and swell, structures in flame, among others; which indicate that these sediments would have been embedded in fluids and that, due to differences in densities and pressures, the aforementioned structures are produced.

5.4 Stage IV

A new volcanic event, also represented by explosive eruptions, gives rise to dry pyroclastic surges (facies association DPS), which are deposited again on these plains (**Figure 5**). The pyroclastic deposits resulting from this eruptive moment, internally develop sharp tractive structures and high flow regime (e.g. parallel lamination, scaling structures, etc.), which correlate with dry pyroclastic surges, which probably respond to a rapid stacking and amalgamation of successive pyroclastic events. This is indicated by the transitional contacts between the different bodies.

5.5 Stage V

On top of this pyroclastic sedimentation, a new volcaniclastic sedimentation cycle begins that shows an interuptive period (**Figure 5**). This period of mixed sedimentation is represented by the architectural element FF that interdigitates with SB and SG vertically, which would indicate that the river system would be recovering its old position within the area. Fluvial deposits consist of conglomerate and coarse sandy lithofacies. The development of these deposits could correspond to new crevasses that, by vertical accretion, continue to generate the floodplain.

Later, massive, mantiform and sandy bodies are deposited, whose origin is related to hyperconcentrated flows caused by torrential rains.

5.6 Stage VI

In this sedimentary stage, the area is influenced by pyroclastic(s) event(s) which are registered as deposits of wet surges (facies association WPS) and dry (facies association DPS) that once again cover the extensive plains (**Figure 5**). The associations of WPS and DPS facies interdigitate with each other, and together present power of approximately 25 to 30 m, with a great absence of clastic sedimentation. In the deposits produced by wet pyroclastic surges, deformational structures develop (e.g. fluid leaks, sedimentary folds, convolute lamination, flame structures, etc.), observed in the dbTacc and rL lithofacies. The origin for these deformational structures is associated with seismic waves; gravity and inertia effects by pyroclastic flows and/or differential gas pressures [30]. Seismic waves can be attributed to contemporary volcanic activity, which causes unconsolidated and plastic sediments to deform and/or undergo liquefaction. However, a probable deformation generated by a rapid stacking of successive surges should not be ruled out.

The facies association DPS corresponds to dry pyroclastic surges, where no deformational structures have been observed, which implies a different behavior when passing seismic waves. This behavior would be related to the lack of interporal fluid in the sediments. In the sedimentary record, the dry and wet surge deposits are interdigitated, however, in the upper terms of the sequence, those of the DPS association prevail.

5.7 Stage VII

On the surge deposits (DPS and WPS indistinctly), tabular and low-power deposits (4 to 8 cm approximately) develop, interpreted as deposits of gravitational fall from pyroclastic clouds, which present levels with contrasting granulometry (CP association) (**Figures 4** and **5**). This type of deposition is related to non-

sustained eruptions that have several pulses of short duration or to partial collapses of the eruptive column [23]. The last pulse of volcanic activity is recorded, in the study area, as a new wet surge event, followed by dry surges.

6. Conclusions

- These pyroclastics, clastic and volcaniclastic paleoenvironments in the section were developed in the most distal areas of the Bermejo Basin, and later were fragmented from the main part of the basin.

- The middle section of the Desencuentro Formation (Member P and part of Members D2 and D3) consists of clastic, volcaniclastic and pyroclastic sediments that generate a complex pattern of mixed paleoenvironmental evolution, which indicates interruptions in the volcanic activity of the Miocene arc in more distal areas of the Bermejo Basin.

- The detailed study of the sequences indicates the presence of an anastomosed river system (stage I), with the development of flood plains and mass removal events. This fluvial system, probably ephemeral with seasonal reactivations, develops in arid climatic conditions.

- The presence of fall deposits with dry pyroclastic waves in the floodplain (stage II) signals the beginning of the interaction of the river system with contemporary pyroclastic deposits. A probable lull in volcanic activity, coupled with exceptional rains (common in arid climates), generated lahars deposits (stage III). Stage IV represents a new hydromagmatic eruptive period, which consists of dry pyroclastic surges that cause the collapse of the river system. The river system begins to recover (stage V), with the development of SB and GB, as volcanic activity decreases. The presence of deposits associated with mass removal (SG element) confirms cycles in the climate. Later, thick deposits of wet and dry pyroclastic surges intercalated with fall deposits, indicate greater participation of pyroclastic sedimentation on fluvial sedimentation. However, the presence of levels of claystone intraclasts indicates that there were moments of development of plains with fine to very fine sedimentation of little importance, which was eroded by the pyroclastic surges (stages VI and VII).

- Sedimentation in the study area was not only controlled by the prevailing climatic conditions, but also by a rapid collapse of the river system due to the high load of pyroclastic sediments, which could not be transported to other areas, due to peneplanization generated by the volcanic deposits and the distal position within the Bermejo Basin.

- These paleogeographic conditions (peneplanization) prevailed in the formation of the posterior paleoenvironments (shallow lagoons with high evaporation and fluvial environments with very low energy and little channeling) described by [2] in member D4.

- The volcanic system contemporary to these sedimentation stages was not recognized, however, the general characteristics of the pyroclastic deposits described suggest that the volcanic events that generated the DPS, WPS and PF facies associations correspond to magmatic or hydromagmatic eruptions.

- The presence of sismites (fluid leaks, flaming structures, ball pillow, etc.) in the pyroclastic rocks allows us to infer that the sedimentation area would be in a distal for the eruptive(s) center(s).

- The volcanic focus (s) would be related to the Miocene volcanism that would have occurred at these latitudes. In the Miocene, the arc was migrating to eastern positions [39], we consider that these pyroclastic activities show the arc activity in the area; although it is not clear if these pyroclastic deposits are associated with the Miocene volcanism of Sierra de Famatina, to the east of the study area. The authors are currently conducting further studies to determine the origin of the volcanites.

Acknowledgements

Author details

José L. Lagos[1,2]* and Ana M. Combina[1,2]

1 Instituto de Geología y Recursos Naturales [INGeReN], Universidad Nacional de La Rioja, La Rioja, Argentina

2 Departamento de Geología, Universidad Nacional de Río Cuarto, Instituto de Ciencias de la Tierra, Biodiversidad y Ambiente (ICBIA; CONICET-UNRC), Córdoba, Argentina

*Address all correspondence to: joselgs24@gmail.com

IntechOpen

References

[1] Malizzia, D.C., Reynolds, J.H., Tabbutt, K.D. Chronology of Neogene sedimentation, stratigraphy and tectonism in the Campo de Talampaya region, La Rioja Province, Argentina. Sedimentary Geology, 1995. 96: 231-255. DOI: 10.1016/0037-0738(94)00132-E

[2] Georgieff, S.M., Herbst, R., Esteban, G., Nasif, N. Paleoenvironmental analysis and paleontological record of the Desencuentro Formation (Upper Miocene), Alto de San Nicolás, La Rioja Argentina. Ameghiniana, 2004. 41: 45-56. ISSN 0002-7014

[3] Fauqué, L., Limarino, C.O., Vujovich, G.I., Férnandez Dávila, L., Cegarra, M. y Escosteguy, L., Hoja Geólogica 2964-IV, Villa Unión. Provincias de La Rioja y San Juan. Boletín 345. Buenos Aires, Instituto de Geología y Recursos Minerales, Servicio Geológico Minero Argentino. 2018 ISSN 0328-2333

[4] Malizzia, D. C. Contribución al conocimiento geológico y estratigráfico de las rocas terciarias del Campo de Talampaya, Provincia de La Rioja, Argentina. Tesis Doctoral. Universidad Nacional de Tucumán, 1987

[5] Reynolds, J.R. Chronology of Neogene tectonics in the Central Andes (27°-35°S) of western Argentina, based on the magnetic polarity stratigraphy of foreland basin sediments. Tesis Doctoral Dartmouth College, Hannover, New Hampshire, 1987

[6] Lagos, J. L., Bravo Cura, N. F., Combina, A. M., Falcon, C. M., Horta, L. R. Estudio de las secuencias piroclásticas neógenas tardías del Alto de San Nicolás, Campo de Talampaya, La Rioja. In Actas 10° congreso de exploración y desarrollo de Hidrocarburos-Programa de Estudiantes-Trabajos Técnicos, Argentina. 2018. p. 45-55

[7] Lagos, J.L. 2020. Estratigrafía de la sección media de la Formación Desencuentro, Mioceno tardío, Campo de Talampaya. Tesis de Grado. Universidad Nacional de La Rioja. Unpublished

[8] Cusminsky, G.; García, A., Herbst. Ostrácodos (Crustacea, Ostracoda) y carófitos (Chlorophyta, Charales) de la Formación Desencuentro (Mioceno superior), provincia de La Rioja, Argentina Ameghiniana 2006 43 (2): 327-338. ISSN 0002-7014

[9] Ramos, V.A. Las Provincias Geológicas del territorio argentino. In: Caminos, R. Editor. Geología Argentina. Servicio Geológico y Minero. 1999. 41-96. ISSN 0328-2325.

[10] Ramos, V.A., Cristallini, E.O., Pérez, D.J. The Pampean flat-slab of the Central Andes. Journal of South American Earth Sciences. 2002.15: 59-78. ISSN: 0895-9811

[11] Ramos, V.A., Folguera, A. Andean flat-slab subduction through time. Geological Society, London, Special Publications. 2009. 327: 31-54p. DOI: 10.1144/SP327.3

[12] Caselli, A. T., Talampaya. Viento, agua y tiempo, diseñadores de una arquitectura deslumbrante. In: CSIGA (Ed.) Sitios de Interés Geológico de la República Argentina. Instituto de Geología y Recursos Minerales. Servicio Geológico Minero Argentino, 2008. Anales 46, I, Buenos Aires, 131-144 ISSN 0328/2325

[13] Miall, A.D. The Geology of Fluvial Deposits. Springer, Berlin. 2006. 528 p. DOI: 10.1007/978-3-662-03237-4

[14] Miall, A.D. The Facies and Architecture of Fluvial Systems. Springer Geology. Springer, 2014. 316 p. DOI: 10.1007/978-3-319-00666-6

[15] Branney, M.J., Kokelaar, P. Pyroclastic density currents and the sedimentation of ignimbrites. Geological Society London Memoirs. 2002. 27, 143 p. DOI: 10.1017/S0016756804329171

[16] Németh, K., Martin, M. Practical Volcanology. Lecture notes of understanding volcanic rocks from field-based studies. Geological Institute of Hungary, Ocassional Papers, 27, 2007. 220p. ISBN 978-963-671-259-4

[17] Petrinovic, I. A., D'Elia, L. Rocas Volcaniclásticas: Depósitos, Procesos y Modelos de facies. Argentina. Asociación Argentina de Sedimentología, 2018. 172 p. ISBN 978-987-96296-6-6

[18] Cas, R.A.F., Wright, J.V. Volcanic Successions Modern and Ancient. Chapman y Hall, 1987, 528 p. DOI: 10.1007/978-94-009-3167-1

[19] Zhou, Y-Q., Y Peng, T-M., Zhou, T-F., Zhang, Z-K., Tian, H, Y Liang, W-D, Yu, T., Sun, L-F. Soft-sediment deformation structures related to volcanic earthquakes of the Lower Cretaceous Qingshan Group in Lingshan Island, Shandong Province, East China. Journal of Palaeogeography. 2017. 6 (2): 162-181. DOI: 10.1016/j.sedgeo.2018.05.012 0037-0738

[20] Wohletz, K., Sheridan, M. A model of pyroclastic surge. Geological Society of America. Special Paper. 1979. 180: 177-194

[21] Douillet, G., Bernard, B., Bouysson, M., Quentin, C., Y Dingwell, D., Gegg, L., Hoelscher, I., Kueppers, U., Mato, C., Ritz, V., Schlunegger, F., Witting, P. Pyroclastic dune bedforms: macroscale structures and lateral variations. Examples from the 2006 pyroclastic currents at Tungurahua (Ecuador). Sedimentology, 2018. 66: 1531-1559. DOI: 10.1111/sed.12542

[22] Smith, G., Rowley, P., Williams, R., Giordano, G., Trolese, M., Silleni, A., Parsons, D., Capon, S. A bedform phase diagram for dense granular currents. Nature Communications. 2019. 2873. DOI: 10.1038/s41467-020-16657-z

[23] Houghton, B., Carey, R.J., Pyroclastic Fall Deposits. En: Haraldur Sigurdsson, Editor. The Encyclopedia of Vocanoes. 2nd Edition., Academic Press. 2015. 1456 p. ISBN: 9780123859389

[24] James, M.R., Lane, S.J., Gilbert, J.S., Density, construction, and drag coefficient of electrostatic volcanic ash aggregates. Journal of Geophysical Research, 2003. 108 (B9). DOI: 10.1029/2002JB002011

[25] Scolamacchia, T., Macías, J., Sheridan, M. Y Hughes, S. Morphology of ash aggregates from wet pyroclastic surges of the 1982 eruption of El Chichón Volcano, Mexico. Bulletin of Volcanology. 2005. 68: 171-200. DOI: 10.1007/s00445-005-0430-x

[26] Adams, P. M., Lynch, D. K., Buesch, D. C. Accretionary lapilli: what's holding them together?. Desert Symposium. 2016. p. 256-265.

[27] Douillet, G., Taisne, B., Tsang-Hin-Sun, E., Müller, S., Kueppers, U., Dingwell, D., Syn-eruptive, soft-sediment deformation of deposits from dilute pyroclastic density current: triggers from granular shear, dynamic pore pressure, ballistic impacts and shock waves. Solid Earth, 2015. 6 (2): 553-572 DOI: 10.5194/se-6-553-2015

[28] Üner, S., Aliriz, M. G, Özsayin, E., Sağlam A.S., Y Karabiyikoglu, M. Earthquake Induced Sedimentary Structures (Seismites): Geoconservation and Promotion as Geological Heritage (Lake Van-Turkey). Geoheritage. 2016. 9: 133-139. DOI: 10.1007/s12371-016-0186-z

[29] Lowe, D.R., Water escapes structures in coarse-grained sediments.

Sedimentology, 1975. 22: 157-204. DOI: 10.1111/j.1365-3091.1975.tb00290.x

[30] Kuno, H., Characteristics of deposits formed by pumice flows and those formed by ejected pumice. Tokyo University Earthquake Research Institute Bulletin, 1941. 19, 144-149.

[31] Boggs, S. Petrology of Sedimentary Rocks, 2nd Ed. Cambridge University Press. 2009 600 p. DOI: 10.1017/CBO9780511626487

[32] Martí, J., Araña, V. La Volcanología Actual. CISC. 1993. 578 p. ISBN: 978-84-00-07363-3

[33] Dabrio, C. J., Estructuras sedimentarias primarias. In: Sedimentación fluvial / M. Díaz Molina. Sedimentación lacustre / P. Anadón Monzón. Sedimentación en costas siciclásticas, deltas y mares someros / C. J. Dabrio González. Ciclo de Seminarios de Sedimentología – IGME (1). Servicio de Publicaciones, Ministerio de Industria y Energía, 1984. Madrid, pp. 13-26.

[34] Nemec, W. y Muszynski, A. Volcaniclastic alluvial aprons in the Tertiary of Sofia district (Bulgaria). Ann. Soc. Geol. Poloniae, 52: 239-303. 1982

[35] Vallance, J.W., Iverson, R.M. Lahars and Their Deposits. In: Haraldur Sigurdsson. Editor, The Encyclopedia of Volcanoes 2nd Edition, Academic Press. 2015. 1456 p. ISBN: 9780123859389

[36] Nichols, G. Sedimentology and Stratigraphy, 2nd. Edition. Blackwell, 2009. 419 p. ISBN: 978-1-405-13592-4

[37] SOUTHARD, J. B., "Experimental determination of bed-form stability". Annu. Rev. Earth Planet. Sci. 19: 423-55. 1991.

[38] Zavala, C. Hyperpycnal (over density) flows and deposits. Journal of Palaeogeography, 9: 1-21. 2020 DOI: 10.1186/s42501-020-00065-x

[39] Ramos, V., F. Nullo. El volcanismo de arco cenozoico. In V. Ramos (Ed). Geología y Recursos Naturales de Mendoza. XII Congreso Geológico Argentino y II Congreso de Exploración de Hidrocarburos. 1993 Relatorio, I (12): 149-160

Hydrogeochemistry of the Pidong Crater Lake, Jos Plateau Volcanic Province, Nigeria: Constraints on Chemical Elements Sources

Longpia Cedric Bernard and Lar Uriah Alexander

Abstract

The occurrence and recurrence of floating 'mat' vegetation around the Pidong Crater Lake and intermittent change in the color of the lake water from natural blue to brown-yellowish color call for a better understanding of the factors controlling these biological and physico-chemical changes. As a result of these changes, a hydrogeochemical monitoring regime was employed where the lake water samples were collected and analyzed on a monthly basis over a period spanning for 3 years. The hydrogeochemical results for the lake water when plotted in the piper trilinear diagram display predominantly Mg-Ca-HCO_3 type with minor water types of Na-K-HCO_3, Na-K-Cl and Na-K-SO_4 types ($\leq 20\%$), suggesting a derivation from water-rock interaction processes (hydrolysis). The visible dominance of the alkali earth metals ($Mg^{2+} + Ca^{2+}$) over the alkali metals ($Na^+ + K^+$) is expected from a basaltic host rock aquifer due to the dissolution of its constituent ferromagnesian minerals and plagioclase respectively. The general depletion of LILE (Ba, Rb, Sr) (1–10 x Chondrite) and that of High Strength Elements (HSE) (Nb-Yb) (0.001 to <1 Chondrite values) suggest that these elements are from sources (basaltic rocks) highly depleted in these elements. Study of Oxygen-18 ($\delta^{18}O$) and Deuterium (δ^2H) study of the lake water shows that it is of meteoric origin and of relatively recent age (230 ± 30 yrs. before present). The increase in PCO_2 in the lake water triggers the increase in Fe concentration (335 ppb to 429 ppb) which is manifested by the sporadic color change and increased acidity in the lake from pH 7.35 to pH < 6.71.

Keywords: Pidong Crater Lake, Jos Plateau, hydrogeochemistry, water color changes, fumaroles (CO_2), meteoric water

1. Introduction

The volcanoes of the Jos Plateau are aligned in four specific volcanic lines-namely Miango, Kassa, Panyam (Sura) and Gu volcanic lines [1]. There is no record of any actual activity in the Nigerian volcanic provinces in the recent past [2–5]. Recent K-Ar dating the volcanoes of the Kassa volcanic line revealed recent eruption during the Pleistocene ages [6].

Recently, biological and physico-chemical changes were observed within the Jos Plateau Volcanic Province within and around the Pidong Lake which is

characterized by the occurrence and recurrence of floating 'mat' vegetation (Plate I & II). The physical changes are dominated by the intermittent color changes from its natural bluish to yellow brownish color and these activities call for a comprehensive study of these phenomena. In light of the intermittent activities in the lake, this study seeks to determine- (1) the hydrogeochemical characteristics of the lake, (2) constraint the origin and source (s) of the lake water and its chemical elements (3) to ascertain the factors responsible for the observed color change in the lake.

2. Location and geography

The Jos Plateau is located in the Northcentral area of Nigeria. It is the second largest volcanic province in Nigeria after the Biu Plateau [4, 7] and consists of about 22 volcanoes [3, 8]. The Panyam Volcanic Line is the second Southwest end member of the Jos Plateau volcanic region. The Pidong volcano is the southernmost of a series of 7 volcanoes of the Panyam Volcanic Line located in the southwestern segment of the Jos Plateau. The Pidong volcanic crater lake is located on the summit of the Pidong volcano within the southernmost of the 3 crater and lies on longitude $9^0 12'20''$-$9^0 12'40''$ and latitude $9^0 18'50''$- $9^0 19'10''$ at an altitude of 1300 m. The lake's morphological and bathymetric data shows that the lake has a length of 160 m with maximum depth of 6 m [9, 10].

2.1 Geology of the Pidong maar

The Pidong volcano is hosted by medium to coarse grained granite gneiss rocks of PreCambrian age [11]. The volcano extrudes through three craters arranged in a N-S direction with the southernmost breached by water. The Pidong maar is bounded to the south and southeast by granite gneiss rocks and to the west, north and northeast by pyroclastic surge deposits explosively ejected during formation (**Figure 1**). The volcanic ejecta consists mainly of pyroclastic materials, scoria, basaltic lava, pulverized granite materials, and volcanic ash [3, 9, 12]. Beside the lake's crater rim to the extreme south-east are characterized by deposits of large boulders of granite rocks and this is evident of the high explosion that characterized the eruption of the Pidong Maar/Lake [9].
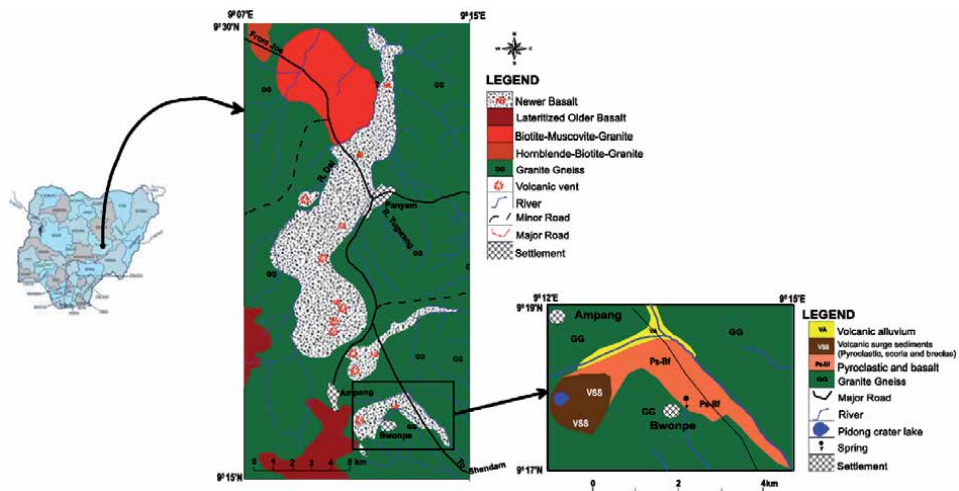

Figure 1.
Location and geological map of Panyam Volcanic Province and Pidong crater Lake area.

3. Methodology

3.1 Water sampling and hydrogeochemical analysis

A hydrogeochemical monitoring regime of the Pidong Crater Lake was carried out by sampling the water on a monthly basis to determine any hydrogeochemical changes over the 2 to 3 year study period. The physical parameters of Temperature, pH, Electrical Conductivity (EC), Total Dissolved Solids (TDS) were carried out directly in the field using an MT 806/pH/EC/TDS/Temperature portable meter. The major, trace and rare earth elements analysis (Mg, Ca, Na, K, Cr, Ni, Co, Sc, V, Cu, Pb, Zn, Bi, Cd, Sn, W, Mo, AS, Sb, Rb, Cs, Ba, Sr., Ga, Li, Ta, Nb, Hf, Zr, Y, Th, U, B, Fe, La, Ce, Pr, Nd, Sm, Eu, Gd, Tb, Dy, Ho, Er, Tm, Yb, and Lu) were carried out using ICP-MS method. The anions (SO_4, Cl, HCO_3, NO_3, F, Br and PO_4) concentrations were determined using colorimetric method at Bureau Veritas Minerals Laboratory Ltd., Canada. The oxygen and hydrogen isotopes analyses of the lake, local rainfall and volcanic spring water was carried out at Activation Laboratory Ontario Canada using cavity ring down spectroscopy with V-SMOW as standard and reported in per mill notation ($_{0/00}$).

The Carbon-14 dating of the lake water was determined by single stage accelerator mass spectroscopy (Source: Activation Laboratories, Canada).

4. Results

4.1 Hydrogeochemical analysis of the crater lake

4.1.1 Physico-chemical parameters

The physico-chemical analyses of the lake water are presented in **Table 1**. The physico-chemical characteristics show slight variability over the 2 to 3 year monitoring period. The pH values for the lake water range from 6.20 to 7.7. The pH is more acidic (< 7) during the dry season (March–June) and becomes more alkaline (rises to >7) during October–December period. Temperatures are highest during the month of March–April (27^0-30°C) and correlates well with highest EC (340-390 µs/cm) and TDS (150-170 mg/l) values. In general, there is a gradual decrease in temperature from 30°C in March to 20°C in December each year.

4.1.2 Major cations

The major cations (Mg, Ca, Na and K) concentrations are in the order of-Mg > Ca > K > Na. The highest concentration of Mg range from 30 mg/l to 40 mg/l, Ca from 21 mg/l to 25 mg/l, Na from 8 to 11 mg/l and K from 5.38 to 15 mg/l and are observed during the dry season (January to April) while the lowest concentration of Mg (16 to ≥25 mg/l), Ca (10 to 15 mg/l), Na (3 to 5.25 mg/l) were observed during the rainy season (August to October) (**Table 2**). Comparative analysis of Fe concentration with Patterson 1986 [9] show that the Fe concentration have increased from 0.27 to 0.612 mg/l over the last 29 yrs. It is observed that Fe concentration progressively increased from 0.332 mg/l in October, 2014 to 3.249 mg/l within the period of lake color change activities from November 2014 to February 2015. From the physico-chemical concentrations of the lake over the study period shows that it is seasonally dependent. However, a comparison of the pH values in the present study with that reported by Patterson [9] showed a decrease in pH from 9.35 to ≤7 with corresponding decrease in alkalinity ($CaCO_3$) from 335 mg/l to 187 mg/l.

Date	pH	Temp.°C	EC (ms/cm)	TDS (ppm)	Mg (mg/l)	Ca (mg/l)	Na (mg/l)	K (mg/l)	SO₄ (mg/l)	Cl (mg/l)	F (mg/l)	Br (mg/l)	HCO₃ (mg/l)	PO₄ (mg/l)	NO₃ (mg/l)
25/05/13	7.08	27.4	0.49	240	41.85	23.66	8.80	14.52	3.67	6.2	—	0.018	200	0.0117	<2.0
27/06/13	7.70	28.0	0.39	140	41.53	25.35	9.23	15.27	<0.50	11	—	0.017	185	0.0116	<2.0
22/07/13	6.99	26.6	0.23	110	—	—	—	—	—	—	—	—	—	—	—
30/08/13	6.94	26.5	0.031	160	31.16	19.03	7.52	11.84	1.54	6.3	—	0.019	210	0.0220	<2.0
27/09/13	7.09	24.6	0.23	110	23.23	16.53	4.97	9.00	<0.50	0.53	—	<0.01	110	0.0452	<2.0
28/10/13	7.1	24.4	0.31	150	30.40	19.23	7.62	12.26	1.19	8.7	—	0.022	220	0.0152	—
27/11/13	7.42	26.5	0.29	150	32.29	18.75	5.96	10.80	0.51	5.2	—	0.015	147	0.0175	<2.0
18/12/13	7.66	20.3	0.36	190	32.82	19.39	6.03	10.93	0.55	5.2	—	0.016	143	0.0311	<2.0
30/01/14	7.19	23.1	0.26	130	33.74	17.63	7.08	11.30	<0.5	5.3	0.290	—	200	0.0906	<2.0
14/03/14	7.18	27.6	0.37	180	38.05	22.24	7.69	13.35	<0.5	5.8	0.320	—	190	0.0163	<2.0
28/03/14	6.86	28.2	0.38	190	39.17	25.71	7.84	13.73	<0.5	5.9	0.330	—	180	0.0321	<2.0
24/04/14	6.89	28.9	0.39	190	39.11	23.37	8.54	14.26	<0.5	8.6	0.320	<0.10	215	0.0161	0.035
24/5/14	7.06	26.2	0.35	170	35.36	21.29	7.18	13.07	<0.50	7.0	0.290		240	0.0081	<0.020
28/6/14	7.16	28.5	0.33	160	31.85	19.53	6.67	12.19	<0.50	5.8	0.28	0.018	218	<0.05	<0.02
29/7/14	7.0	24.9	0.29	140	29.13	18.45	5.84	10.55	<0.50	5.2	0.250	0.016	200	0.0086	0.023
14/8/14	6.9	25.8	0.28	140	25.74	17.48	5.15	9.80	<0.50	4.9	0.240	0.017	185	<0.005	<0.02
30/9/14	6.95	25.5	0.22	110	16.47	10.86	3.01	5.34	<0.5	2.1	0.140	0.011	103	<0.05	<2.0
29/10/14	7.37	27.8	0.24	110	23.72	15.92	4.26	7.42	4.38	1.4	0.118	—	—	—	<2.0
28/11/14	6.71	26.3	0.25	120	25.22	16.31	4.78	8.10	<0.5	4.0	0.200	0.020	174	0.0117	<2.0
17/12/14	6.86	22.6	0.25	120	25.64	18.94	6.21	8.74	0.53	4.1	0.200	0.021	169	0.0157	<2.0
29/01/15	6.96	22.1	0.28	140	19.68	16.15	11.5	4.87	4.13	5.3	0.180	0.011	138	0.0644	2.11
26/02/15	7.0	24.3	0.32	160	31.54	21.15	6.17	19.52	<0.5	7.1	0.270	0.022	211	0.165	0.629

Date	pH	Temp.°C	EC (ms/cm)	TDS (ppm)	Mg (mg/l)	Ca (mg/l)	Na (mg/l)	K (mg/l)	SO₄ (mg/l)	Cl (mg/l)	F (mg/l)	Br (mg/l)	HCO₃ (mg/l)	PO₄ (mg/l)	NO₃ (mg/l)
18/03/15	7.10	24.1	0.30	150	30.26	25.35	9.08	11.69	<0.5	7.8	0.270	0.023	211	0.0439	0.778
23/04/15	7.08	30.5	0.34	170	34.22	22.69	7.04	12.73	<0.5	6.3	0.290	0.022	225	0.0193	0.205
27/05/15	7.15	28.01	0.24	170											
21/06/15	7.04	25.3	0.211	165											
22/07/15	6.96	24.7	0.24	163											
31/08/15	7.05	25.2	0.23	168											
24/09/15	7.15	24.9	0.21	170											
25/10/15	6.83	25.4	0.22	110											
23/11/15	6.93	24.8	0.24	120											
23/12/15	6.99	25.1	0.23	130											
27/01/16	7.13	23.4	0.24	140											
28/02/16	7.18	24.8	0.211	150											
29/03/16	7.08	27.3	0.21	160											
30/04/16	6.97	27.4	0.211	170											
24/09/16	6.2	25.9	0.22	173											

Table 1.
Physico–chemical parameters of the Pidong volcanic crater Lake (may 2013–April 2015).

Period	pH	Temperature °C	EC µs/m	Mg (mg/l)	Ca (mg/l)	Na (mg/l)	K (mg/l)	Zn (mg/l)	Fe (mg/l)	Cu (mg/l)	Al (mg/l)	SO₄ (mg/l)	Cl (mg/l)	Alkalinity (CaCO₃) (mg/l)	F (mg/l)
Patterson (1986) report	9.35	28.50	410	36.40	13.65	12.80	25.80	0.065	0.270	< 0.004	—	< 0.33	2.50	335.0	—
Present study (2013–2015)	7.17	26.10	299	29.680	39.670	6.890	11.390	0.064	0.612	0.004	0.456	1.030	5.607	141.500	0.249

Table 2.
Comparative hydrogeochemical data of 1986 and present study (after Lar [12]).

4.1.3 Trace elements concentrations

Some of the trace elements (Cu & Zn) show wide variability in concentration varying from 13.4 mg/l, 0.003 to 0.088 mg/l respectively (**Table 2**). The spider graphs (**Figures 2** and **3**) of the Light Ion Lithophile Elements (LILE) (Ba, Rb, Sr) normalized to chondrite values show enrichment (1–10 X chondrite values) while Nd to Yb are impoverished (0.001 to <1 X chondrite). These elements display variations in concentration over the study period.

4.1.4 Rare earth elements concentrations

The REE concentrations displayed in the spidergraph (**Figure 4**) show slight variability during the study period and are rarely depended on the seasons (**Table 3**). The concentration variations for La, Ca, Pr, Nd, and Sm is 0.01 to 0.5 ppb, 0.06 to 1.09 ppb, < 0.01 to 0.12 ppb, and < 0.02 to 0.08 ppb respectively. However, Gd-Lu concentration range between ≤ 0.01 and with few deviations >0.01 ppb which is not dependent on season. The sum average concentration for the REE (La to Lu) is 0.54 ppb and varies between <0.01 and 1.09 ppb. The REE are impoverished relative to chondrite values (< 1 X chondrite). There are significant variations (0.03 to 0.18 X chondrite) for La-Sm in the LREE concentration relative to HREE (Gd to Lu). An important characteristic of the variations is the relative similarities in the geochemical spectra indicating similar source.

4.1.5 Anion concentrations

The major anions of the lake water are HCO_3^-, Cl^-, SO_4, and NO_3 with average concentration of 141.4 mg/l, 5.65 mg/l, 0.845 mg/l. The minor anions are F, Br and PO_4 with average concentration of 0.24 mg/l, 0.017 mg/l, 0.03 mg/l respectively. Generally, the highest (193.675 mg/l) and the lowest (186.5 mg/l) sum of the major anions concentrations are observed during the dry and wet seasons respectively.

A comparative hydrochemical concentration of the anions of chloride (Cl^-) and sulphate (So_4^{-2}) in the present study with Patterson [9] values (**Table 1**) showed Cl and SO_4 have increased from 2.5 mg/l to 5.67 mg/l and < 0.33 mg/l to 1.03 mg/l respectively.
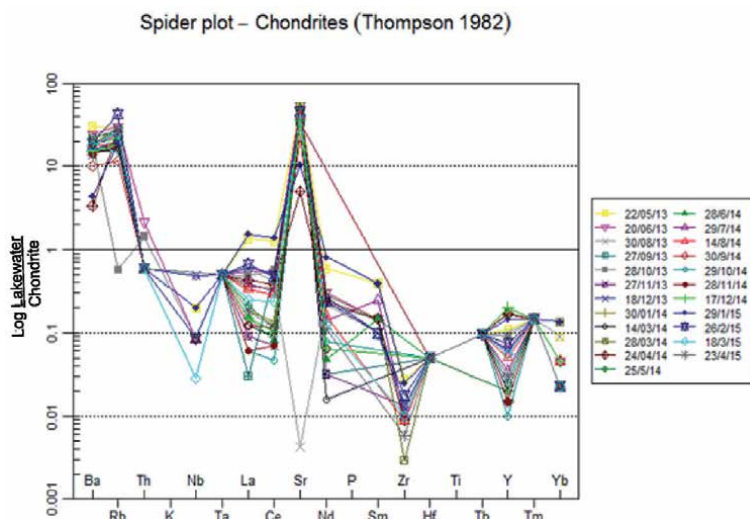

Figure 2.
Spidergraph of incompatible trace element concentrations of Pidong crater Lake normalized to chondrite.
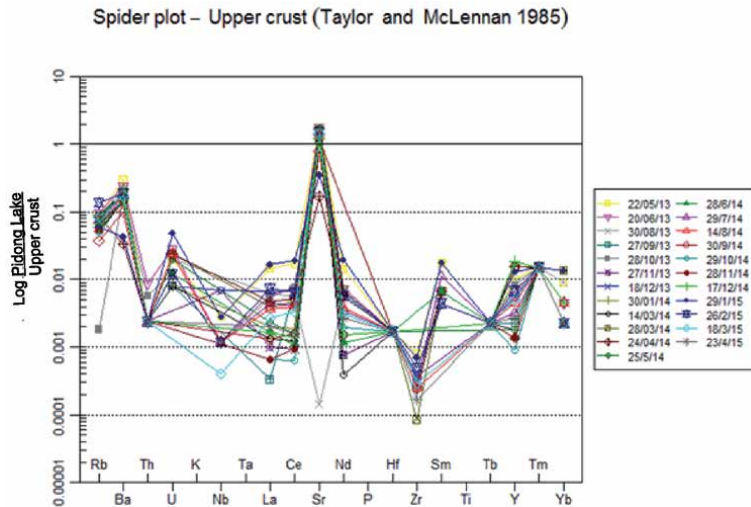
Figure 3.
Spidergraph of incompatible trace element concentrations of Pidong crater Lake normalized to upper crust abundance.
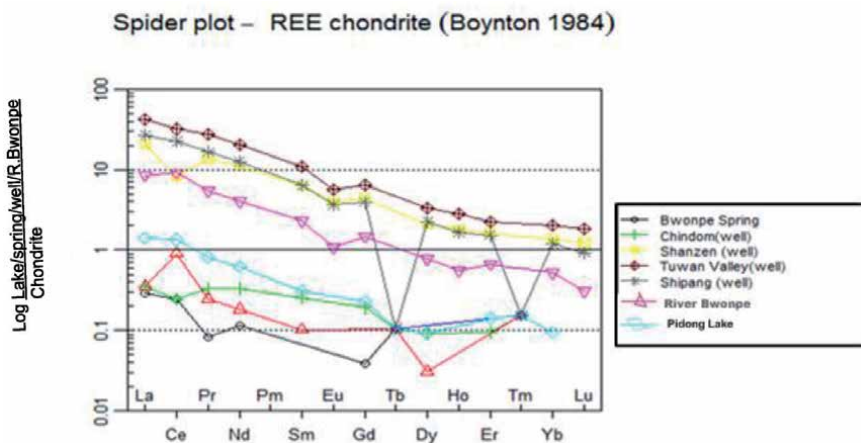

Figure 4.
Spidergraph of REE of Pidong crater Lake, Bwonpe volcanic spring, wells and river Bwonpe normalized to chondrite.

4.2 Oxygen, hydrogen and carbon isotopes

The Pidong Crater Lake isotope composition of oxygen-18 and deuterium are $-4.9_{0/00}$ and $-25_{0/00}$ respectively and that of the rainfall within the upper River Ndai basin are $\delta^{18}O$ ($-4.75_{0/00}$) and δ^2H ($-31_{0/00}$) (**Table 4**). The plot of the $\delta^{18}O$ versus δ^2H falls close to Standard Meteoric Water Line (**Figure 5**). The hydrocarbon age of the lake water is 230 ± 30Bp (**Figure 6**).

4.3 Lake color change activities

The Pidong Crater Lake intermittently display color changes from its natural bluish color to brown-yellowish color (**Figure 7**). The lake color change activities were observed in November 2014, October 2015 and September 2016. During

Date	La	Ce	Pr	Nd	Sm	Eu	Gd	Tb	Dy	Ho	Er	Tm	Yb	Lu	∑REE
22/05/13	0.44	1.09	0.10	0.37	0.08	<0.01	0.06	<0.01	0.03	<0.01	0.03	<0.01	0.02	<0.01	2.22
20/06/13	0.18	0.46	0.05	0.19	0.03	<0.01	0.03	<0.01	0.03	<0.01	0.02	<0.01	0.01	<0.01	1.0
22/07/13	—	—	—	—	—	—	—	—	—	—	—	—	—	—	—
30/08/13	0.19	0.36	0.04	0.14	0.02	<0.01	0.02	<0.01	0.02	<0.01	0.01	<0.01	0.02	<0.01	0.82
27/09/13	0.01	0.44	<0.01	0.02	<0.02	<0.01	0.01	<0.01	0.01	<0.01	<0.01	<0.01	<0.01	<0.01	0.49
28/10/13	0.16	0.49	0.03	0.14	0.03	<0.01	0.02	<0.01	0.01	<0.01	<0.01	<0.01	<0.01	<0.01	0.88
27/11/13	0.03	0.06	<0.01	0.02	<0.02	<0.01	<0.01	<0.01	<0.01	<0.01	<0.01	<0.01	<0.01	<0.01	0.11
18/12/13	0.20	0.44	0.04	0.17	0.02	<0.01	<0.01	<0.01	<0.01	<0.01	<0.01	<0.01	<0.01	<0.01	0.87
30/01/14	0.06	0.12	0.01	0.04	<0.02	<0.01	<0.01	<0.01	<0.01	<0.01	<0.01	<0.01	<0.01	<0.01	0.23
14/03/14	0.04	0.08	0.01	0.01	<0.02	<0.01	0.01	<0.01	<0.01	<0.01	<0.01	<0.01	<0.01	<0.01	0.15
28/03/14	0.12	0.30	0.03	0.18	0.03	<0.01	0.05	<0.01	0.05	<0.01	0.03	<0.01	0.03	<0.01	0.82
24/04/14	0.14	0.33	0.04	0.15	0.03	<0.01	0.06	<0.01	0.05	<0.01	0.04	<0.01	0.01	<0.01	0.85
24/05/14	0.07	0.10	0.01	0.04	<0.02	<0.01	<0.01	<0.01??	<0.01	<0.01	<0.01	<0.01	<0.01	<0.01	0.22
28/06/14	0.05	0.07	0.02	0.03	0.03	0.02	0.02	<0.01	<0.01	<0.01	<0.01	<0.01	<0.01	<0.01	0.29
29/07/14	0.13	0.27	0.03	0.09	0.05	0.02	0.03	<0.01	<0.01	<0.01	<0.01	<0.01	<0.01	<0.01	0.62
14/08/14	0.11	0.25	0.03	0.10	<0.02	<0.01	<0.01	<0.01	0.02	<0.01	0.01	<0.01	0.01	<0.01	0.53
30/09/14	0.04	0.10	<0.01	0.04	<0.02	<0.01	0.02	<0.01	<0.01	<0.01	<0.01	<0.01	<0.01	<0.01	0.2
29/10/14	0.02	0.04	<0.01	0.05	<0.02	<0.01	<0.01	<0.01	0.01	<0.01	<0.01	<0.01	<0.01	<0.01	0.12
29/11/14	0.02	0.06	<0.01	<0.01	<0.02	<0.01	<0.01	<0.01	0.02	<0.01	<0.01	<0.01	<0.01	<0.01	0.1
17/12/14	0.05	0.09	<0.01	0.04	<0.02	<0.01	<0.01	<0.01	<0.01	<0.01	<0.01	<0.01	0.01	<0.01	0.19
29/01/15	0.5	1.21	0.12	0.51	0.08	0.01	0.07	<0.01	0.05	<0.01	<0.01	<0.01	0.03	<0.01	0.258
26/02/15	0.22	0.41	0.04	0.15	0.02	<0.01	0.03	<0.01	<0.01	<0.01	<0.01	<0.01	<0.01	<0.01	0.87

Date	La	Ce	Pr	Nd	Sm	Eu	Gd	Tb	Dy	Ho	Er	Tm	Yb	Lu	∑REE
18/03/15	0.08	0.21	0.01	0.08	<0.02	<0.01	0.02	<0.01	0.01	<0.01	<0.01	<0.01	<0.01	<0.01	0.41
23/04/15	0.06	0.10	<0.01	0.07	<0.02	<0.01	<0.01	<0.01	<0.01	<0.01	<0.01	<0.01	<0.01	<0.01	0.23

Element concentration in ppb.

Table 3.
REE (Rare earth elements) concentration in Pidong volcanic crater Lake (may 2013–April 2015). NB- All element concentration in parts per billion.

lake color change activities pH were observed to have decrease from 7.39 to 6.71, 7.15 to 6.83 and 7.18 to 6.20 in November 2014, October 2015, and September 2016 respectively.

Location/source	Date of sampling	Analyte		
		$\delta^{18}O_{H2O}$ (‰)	δ^2H_{H2O} (‰)	δ^3H_{H2O} (‰)
Pidong Crater Lake	June, 2014	−4.8	−25.0	17.0
Bwonpe Volcanic Spring	June, 2014	−4.7	−26.0	34.0
Rainfall	June, 2014	−4.9	−31.0	12.0

Table 4.
Oxygen and hydrogen isotope composition of Pidong crater Lake, Bwonpe volcanic spring and rainfall.
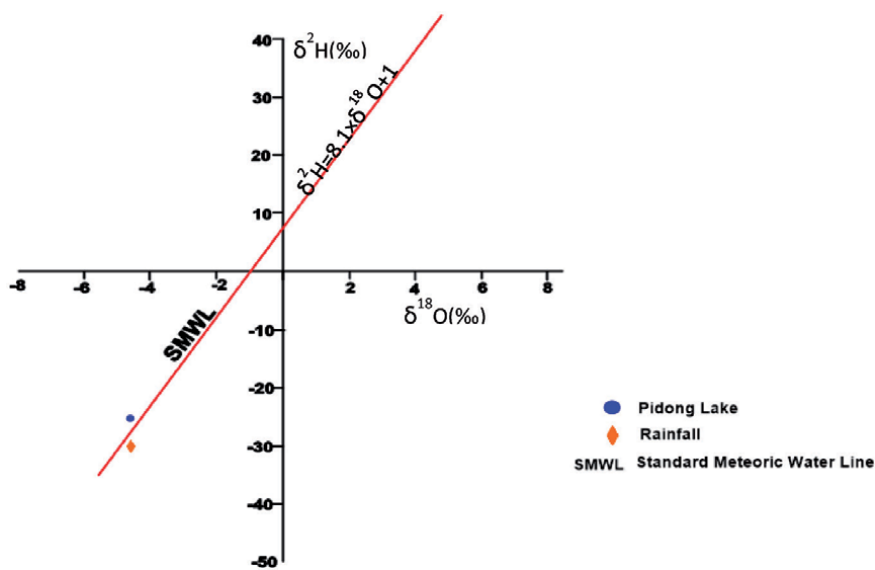
Figure 5.
δ2H versus δ18O diagram for Pidong crater Lake, Bwonpe volcanic spring, rainfall and standard mean ocean water (SMOW).
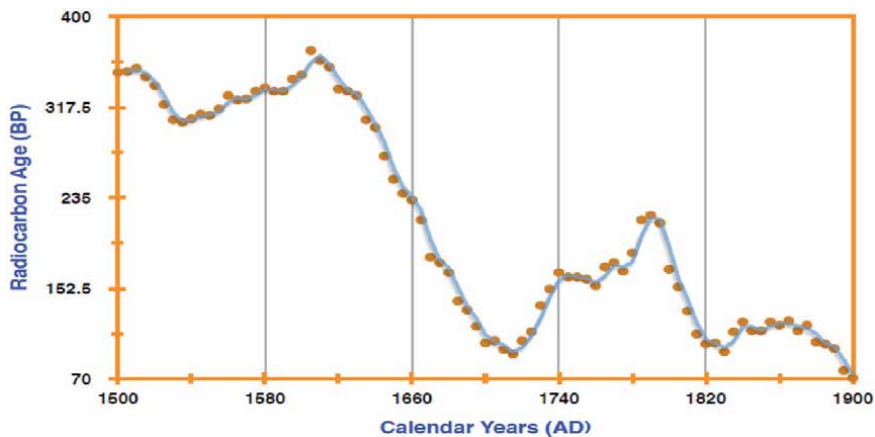
Figure 6.
Radio carbon (^{14}C) age of Pidong crater Lake.

Figure 7.
(a) Natural bluish water color of Pidong crater Lake; (b) Pidong crater Lake water color change activities in November 2014, October 2015 and September 2016.

4.4 Lake water types and sources of major ions

The Piper Trilinear diagram (**Figure 8**) for the lake water plots predominantly in the Mg-Ca-HCO$_3$ segment. The minor water types which constitutes only about 10–20% and include Na-K-Cl and Na-K-SO$_4$ water types.

The major element concentration abundance of the lake is in the order of Mg^{2+} > Ca^{2+} > K$^+$ > Na$^+$. Similarly, the major element oxide distribution order for the volcanic ejecta materials (Basalts, pyroclastic, ash) for the Pidong volcanic rocks is in order of MgO > CaO > Na$_2$O > K$_2$O [12, 13]. The major cation concentration order
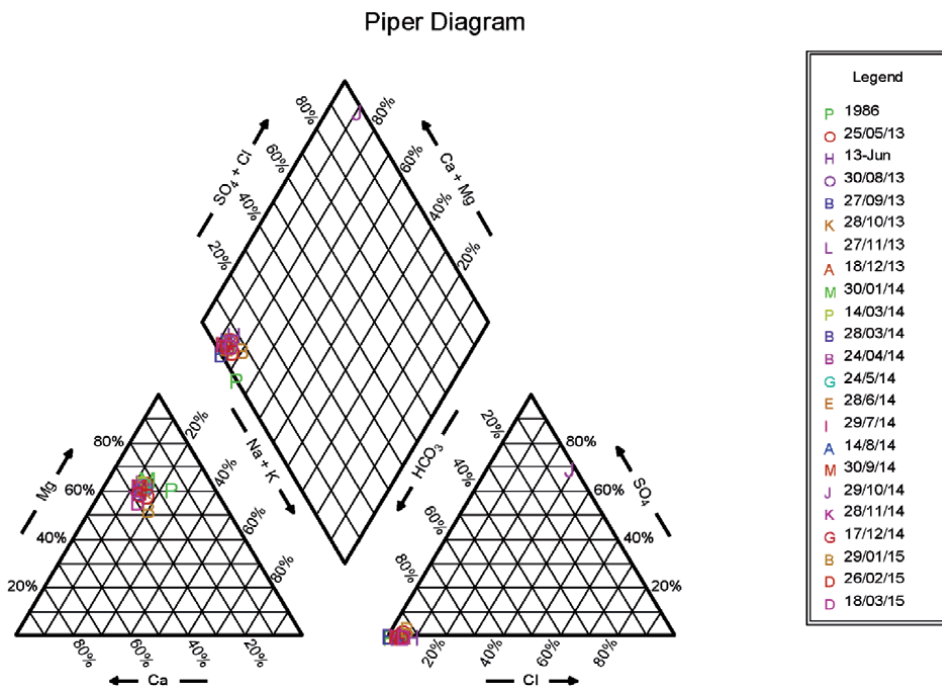
Piper Diagram

Figure 8.
Piper trilinear diagram for Pidong crater Lake.

of the lake water and that major oxides of the Pidong volcanic rocks show similarity in the concentration abundance.

The Gibbs diagram is an illustration of the mechanism controlling the chemistry of groundwater samples in crystalline aquifers. The plot is that of the ratios of $\dfrac{Na^+}{Na + Ca^+}$ vs. Total Dissolved Solids and $\dfrac{Cl^-}{Cl^- + HCO_3}$ vs. Total Dissolved Solids. The Gibbs diagrammatic plot for the Pidong Crater Lake water shows it is controlled predominantly by water-rock dominance processes (**Figure 9**).

4.5 Partial carbon dioxide pressure (PCO$_2$)

Partial carbon dioxide pressure of crater lake water is the partial pressure of carbon dioxide in equilibrium with lake and saturated atmospheric pressure. PCO$_2$ is based on the equilibria of carbon specie in solution. The PCO$_2$ plot for the two year observation for the Pidong Lake shows zit is constantly and several orders of magnitude higher than air saturated water pressure except June, 2013 (**Figure 10**). The highest PCO$_2$ of 4.5 X 10^{-2} and 2.5 X 10^{-2} bars were observed in March and November, 2014 respectively and correlate with highest decreases in pH from 7.38 to 6.71 in November 2014. The lowest decreases in pH were observed during lake watercolor change activities (**Table 2**). Generally, increases in pH and PCO$_2$ were observed to be linked with decrease in pH and lake color change activities.
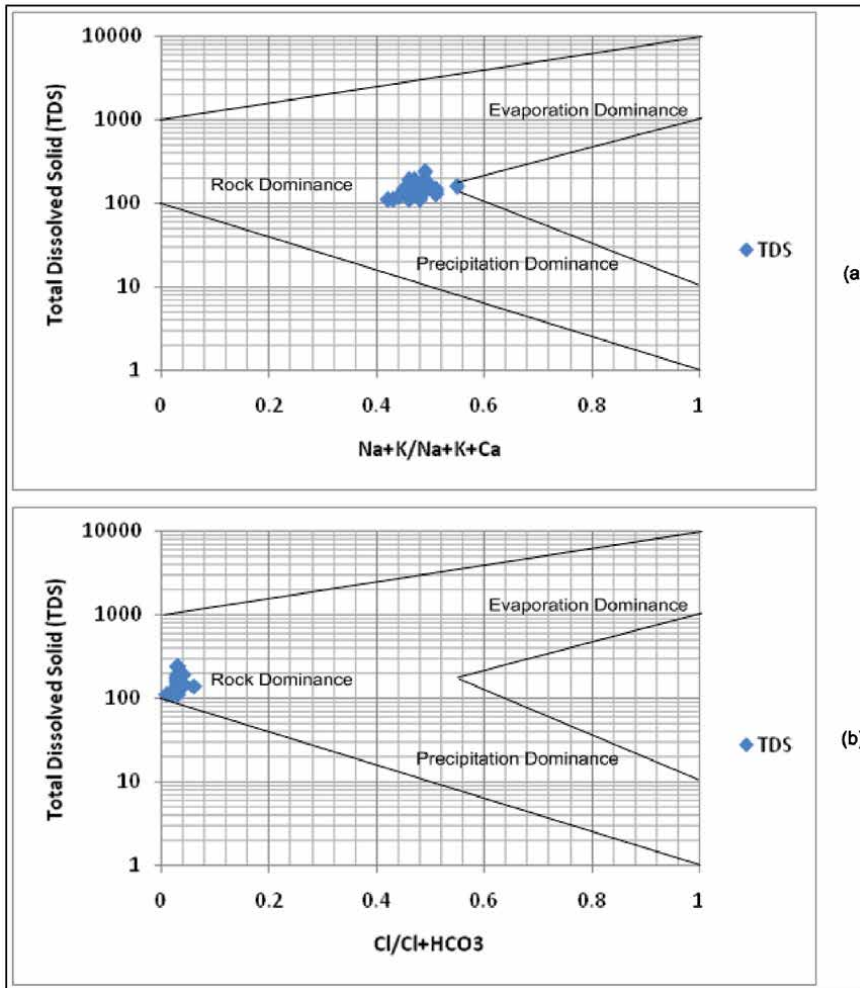
Figure 9.
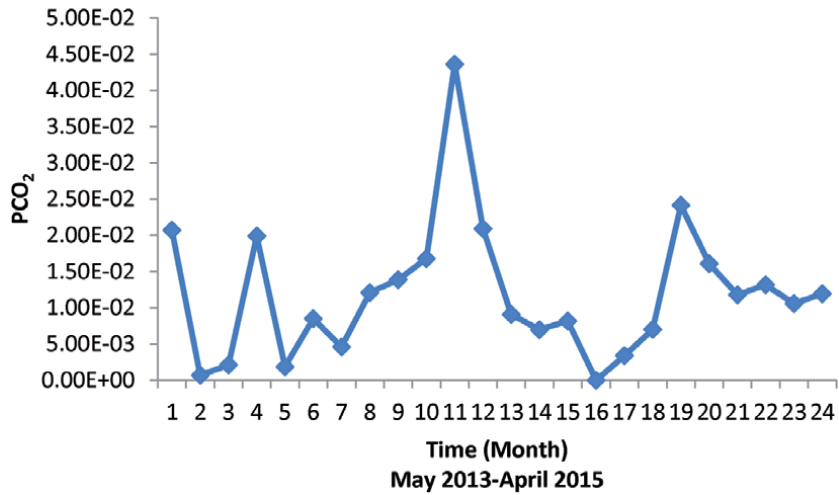*Gibbs diagram for Pidong crater Lake.*

Figure 10.
PCO2 versus time for Pidong crater Lake.

5. Discussion

5.1 Sources of major ions

The Gibbs diagram for the Pidong Crater Lake shows that the lake water is characterized mainly by water-rock interaction processes [14]. The hydrogeochemical abundance order of the lake ($Mg^{2+} > Ca^{2+} > Na^+ > K^+$) and that of the host rock ($MgO > CaO > NaO > K_2O$) show similarity and may suggests derivation from the overlaying volcanic rocks. Similarities in hydrogeochemical spectral patterns of lake and host volcanic rocks are indicators of sources of derivation [4, 15, 16]. The major cations of groundwater are derived mainly from chemical weathering [17]. Generally, the silicate minerals present in the basalts, pyroclastic materials, ash and pulverized granite get weathered by hydrolysis producing mainly Mg-HCO_3 and Na^+ and K^+ depleted groundwater. Groundwater containing CO_2^{2-} can easily react with orthoclase to release Magnesium ion, Calcium bicarbonate ions (Mg^{2+}, Ca^{2+}, HCO_3^-) [18]. The Na^+ and K^+ alkali appear to originate from hydrolysis of plagioclase in the basalt and granite rocks. In water-rock interaction processes the following chemical reaction of volcanic rocks may occur and hence the chemical sources are derivable from these processes.

1. Hydrolysis of plagioclase minerals

$$CaAl_2SiO_8 + HCO_2 + \tfrac{1}{2}O_2 \rightarrow Al_2Si_2\,4(OH) + CO_3^{2-} \tag{1}$$
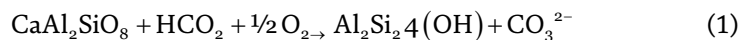
2. Oxidation (chemical weathering) for ferromagnesium minerals (Pyroxene)

$$(Mg,Fe,Ca)SiO_3\,9H_2CO_3 \rightarrow (Mg^{2+},Fe^{2+},Ca^{2+}) + 4HCO_3^- + HCO_3 + H_4SO_4 \tag{2}$$
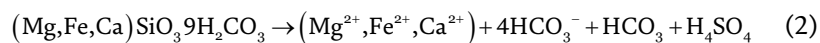
5.2 Trace elements concentration

It is observed that Fe concentration have significant increase by 200% from 0.27 mg/l in 1986 to 0.612 mg/l in present study [12]. Lake water, Fe concentration gradually increases from 423 ppb in November, 2014 to 3249 ppb in March 2015 during the lake color change activities. This phenomenon is similar to the Lake Nyos CO_2 gas disaster episode of 1986 [19, 20]. The lake color change phenomenon was attributed to upliftment of deep anoxic water carried upwards to shallow lake level where oxidation of ferrous iron precipitates to form murky water.

The spider plot for the LILE normalized to upper crustal values (UC) (**Figure 2**) displays strong positive anomalies in Sr. (>1x UC values), Ba (>0.1x UC values) and enrichment in Rb (0.1x UC values). There is a visible negative anomaly in Zr (0.0001 x UC values), all together suggesting that these elements are originally from a source that is highly depleted in these elements (probably deep mantle source) [21]. The dominant rock types that comprise of the crater lake/maar are basalts, pyroclastics and volcanic ash. Generally, hydrogeochemical constituents of any groundwater are signatures of the background rock types the water precolates through [17, 22].

5.3 Rare earth elements concentrations

Generally, REE spidergraph of the Pidong lake water normalized to chondrite values show high impoverishment or depletion (< 0.01 to <1 X chondrite) (**Figure 4**). The slight enrichment in the LREE (La-Sm) is suggestive of influence by crustal rocks materials (host granitic basement rock) rich in these elements (**Figure 4**).

There is high similarity in the REE patterns in the well waters compared to that of the lake and the spring water. The well waters generally exhibit higher REE concentrations (. > 1x Chondrites) but maintain similar LREE enrichment relative to HREE suggestive of significant influence from the surrounding basement complex host rocks. The impoverishment in REE in the lake and spring water suggests a derivation from a mantle source depleted in these elements [4, 15, 16, 22].

5.4 Anion concentrations

The concentration of the SO_4, Cl and F are generally influenced by the water-rock interaction processes between rainfall and host volcanic/granitic rocks. Generally, HCO_3^- is derived from dissolution of silicate minerals of orthoclase, plagioclase, hornblende, diopsite, olivine and biotite of country rock by carbonic acid [18, 23–25]. A comparative analysis of the hydrogeochemical anion concentrations of the lake in this study with that of Patterson [9] show that there is significant increase in Cl, SO_4 and Fe and corresponding decrease in alkalinity and pH over the last 29 years. These increases have been attributed to intermittent CO_2 degassing (fumaroles) into the lake from the subsurface hydrothermal system [12].
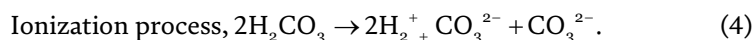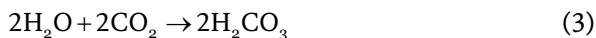
5.5 Origin and age of water

The $\delta^{18}O$ and δ^2H compositional values for the lake (**Table 2**) falls within meteoric water composition values [12, 26] and this is further affirmed by the plot (**Figure 5**) of the SMOW line in the $\delta^{18}O$ and δ^2H correlation diagram [26–28]. The hydrocarbon-14 (^{14}C) age of the lake water is calculated to be 230 ± 30 yrs. and this affirm, that the lake water is relatively young and suggests constant replenishment by precipitation.

5.6 Lake color and hydrogeochemical changes

The Pidong Lake color change activities are characterized by decrease in pH values 7.39 to 6.71, 7.15 to 6.83 and 7.18 to 6.20 as observed in November 2014, October 2015 and September 2016 respectively. The intermittent lake color changes associated with CO_2 degassing into the lake and its dissolution forming weak acid. The HCO_3^- specie increases over time and resulting in decrease in pH from 9.35 to neutral or slightly acidic as seen in the comparative study (**Table 1**). This process can be explained as follows:

$CO_{2\,(gas)}$, $CO_{2\,(aq)}$, HCO_3, CO_3^{2-}, specie are related to pH and temperature of fluid [28]. When $CO_{2\,(gas)}$ undergoes hydration and ionization, hydration of CO_2 forms $H_2^-CO_3^{2-}$, CO_2 gas dominated sub aqueous relevant with the lake

$$2H_2O + 2CO_2 \rightarrow 2H_2CO_3 \tag{3}$$

$$\text{Ionization process, } 2H_2CO_3 \rightarrow 2H_2{}^+{}_+ CO_3{}^{2-} + CO_3{}^{2-}. \tag{4}$$

It is observed that the highest ionization correlates with the lowest pH (6.71) during the period of lake color change. This result suggests a magmatic gas/fumaroles (CO_2) connecting upwards below the lake from shallow mantle and mixing with shallow groundwater and controlled by meteoric recharge. This similar phenomenon was observed in Popocapetl volcanic springs [28]. The intermittent CO_2 gas and associated gas input into the lake during color change activities over time is

suggestive of the cause of the decrease in pH from 9.35 to neutral or near acidic as well as alkalinity from 330 mg/l to 147 mg/l [9] as compared with present study.

5.7 Partial carbon dioxide pressure (PCO_2)

Generally, the PCO_2 versus saturated atmospheric pressure for the lake is above equilibrium for the study period. However, several peaks (4.5×10^{-2} and 2.5×10^{-2} bar) were observed during the lake color change in November 2014 etc. with corresponding pH decreases (6.71). Similarly, these characteristics where increases in PCO_2 are characterized by decrease in pH were observed in Popocapetl volcanic activities [28]. The increased PCO_2 and decreased in pH characterized by lake water color change activities suggest low pressure CO_2 gas influx or bubbling degassing input and its ionization to form weak carbonic acid.

6. Conclusion

The Pidong Crater Lake water is majorly meteoric origin probably coming from percolating meteoric waters of relatively young age (230 ± 30 years before present). The chemical element composition of the Lake is dominantly of Mg-HCO$_3$ water type, influenced mainly by the interaction between meteoric water and basaltic rocks with surrounding granitic host rock from relatively deeper aquifers. In addition, the chemical composition of the lake water is further influenced by minor CO_2 degassing, attributable to minor intermittent fumaroles activities possibly from deep mantle source.

Acknowledgements

Author details

Longpia Cedric Bernard[1]* and Lar Uriah Alexander[2]

1 Department of Mineral and Petroleum Resources Engineering, Plateau State Polytechnic, Barkin Ladi, Nigeria

2 Department of Geology, University of Jos, Nigeria

*Address all correspondence to: cblongpia@gmail.com

IntechOpen

References

[1] Centre for Geodesy and Geodynamics (CGG). Preliminary report on geohazard map of Nigeria, 2007, pp 1-108

[2] Carter, J. D, Barber, W and Tait, E.A. The geology of parts of Adamawa, Bauchi and Bornu provinces in northeastern Nigeria. Geological Survey of Nigeria Bulletin No. 30, 1963.

[3] Schoeneich, K. and Ugodulunwa, F.X.O., 1994, April. Guide book on the field trip to Panyam Volcanoes. 30th Annual Conference of Nigerian Mining and Geosciences Society, Jos, Plateau State, pp 18.

[4] Lar, U. A. and Usman A. M. Environmental distribution of trace metals in the Biu Volcanic Province Nigeria: Exposure and associated human health problems. International Journal of Scientific & Engineering Research, 2012, 3(10), pp 1-16

[5] Lar, U.A., Lekmang, I.C., Shuaibu, M.T., Mahmud, U.M. and Yakubu T.A. *Volcanoes of Nigeria: A preliminary study.* Paper presented at the 7th Conference on African Geology. Assiut, Egypt, 2013, April.

[6] Tsalha, M., Lar, A.U., Yakubu, T.A., Blundy J. & Bart, H.W. (2014). Geochemistry and geochronology of the quaternary volcanisms of the Kassa volcanic field, Jos Plateau, North central Nigeria. IOSR Journal of Applied Geology and Geophysics, 2 (3), 51-63.

[7] Lar, UA, Mohammed TS, Yakubu TA, Mahmud UM, Haruna ST, Samuel T. Development of geohazards map of Nigeria, mapping of volcanic edifices in Nigeria CGG. In: Toro Project; 2007. Unpublished Manuscript

[8] Wright, J.B. (1976). A critical review of geology of Nigeria. InC. A Kogbe (Ed,), *Geology of Nigeri*a (pp 309-317).

Lagos: Elizabethan Publishing Company.

[9] Patterson G. Lake Pidong-A preliminary survey of a volcanic crater lake. Dept. of Geography, University of Durham, UK, 1986.

[10] Longpia, C.B 2021. Hydrogeochemistry of Pidong Volcanic Crater Lake, Jos Plateau, Nigeria: Constraints on Chemical Elements Sources. Unpublished PhD Thesis University of Jos, Nigeria.

[11] Macleod, W. N, Turner, D. C and Wright, E.P. The geology of the Jos Plateau. General geology. Bull. Geological Survey of Nigeria, 1971, 32 vol. 1.

[12] Lar, U., Lekmang, I., Longpia, C. and Tsalha, M. Is a volcanic eruption possible in Nigeria? In A. Paone and Yun, S. (Eds.), Forecasting Volcanic Eruptions, pp (5-27). London: Intech open, 2020.

[13] Lekmang, I.C., 2019. Geochemistry of the basalts of Kerang twin volcanoes within the Panyam Volcanic Line, Jos Plateau, Nigeria: Implications for their origin and evolution. PhD Thesis, pp 176, University of Jos, Jos.

[14] Gibbs, R. J. (1970). Mechanism controlling world water chemistry. Science, 170, 1088-1090.

[15] Martinez Cruz, M. *Geochemical evolution of the acid crater lake Poas Volcano, (Costa Rica): Insights into volcano-hydrothermal process.* Unpublished PhD Thesis, University of Costa Rica, Costa Rica, 2008.

[16] Lar, U.A. and Gusikit, R.B. Environmental health impact of potentially harmful elements distribution in Panyam (Sura) Volcanic Province, Jos Plateau, Central Nigeria.

Environmental Earth Sciences. Springer, 2015.

[17] Ghadami F, Mahmoud Nirzaei, Mohammed Ghomi, Najid Minna. Hydrochemical Properties of the Thermal water of Mahalat Abgarm, Iran. GRC Transactions, 2012, vol. 36.

[18] Ghiglieri, G, Pitals D, Cerr G, Oggiano G. Hydrogeology and hydrogeochemistry of an alkaline volcanic area: the NE Mt Merunslope (East African Rift-Northern Tanzania). Journal of Hydrology and Earth System Sciences, 2012, 16, 529-541.

[19] Evans, W.C., White, L.D., Tuttle, M.L., Kling, G.W., Tanyileke, G. & Michel, R.L. (1994). Six years of change at Lake Nyos, Cameroon, yield clues to the past and cautions for the future. Geochemical Journal, 28, 139-162.

[20] How volcano works. Retrieved March 15, 2016 from http://www. geology.sdsu.edu/how_volcanoes_work/ Nyos.html

[21] Taylor S. R and Mclennan S.M. The celential crust: its composition and evolution. Blackwell Scientific publication, Oxford, 1985, pp 312.

[22] Offodile, M.E. (2002). *Groundwater study and development in Nigeria* (2nd eidition). Jos: Mecon Geology and Engineering Services Ltd.

[23] Mackenzie, F. J. and Garells, R. H. Silicates: Reactivity in water science, 1965. 150, 57-58.

[24] Chourasia, L. P. Hydrogeochemistry of groundwater in part of the hardrock terrain of Central India, *Proceedings of symposium HS 2005 at IUGG Perugia:* IAHS Publishing 314: 2007, pp 286-292

[25] Rajmohan, N., Al-Futaisi and Al-Tougi, S. Geochemical process regulating groundwater quality in coastal region with complex

contamination sources: Barca, Sultante, Oman, Environmental Earth Science, 2009, 59, 385-398.

[26] Craig, H. Isotopic variations in meteoric waters. Science, 1961. 133(3465), 1702-1703

[27] Rosanski, K., Araguas-Araguas, L. and Gonfitiatini, R. *Isotopic patterns in modern global precipitation.* American Geophysical Union Monograph, 1993, No. 78.Washington: AGU.

[28] Martin-Del Pozzo, A.L, Inguagiato S, Aceves F, Saenz H, and Aguayo A. Spring water and CO_2 interaction at Popocatepetl volcano, Mexico, 2002, Vol. 41 (3), pp 345-351.

Petrology and Geochemistry of Nakora Ring Complex with Emphasis on Tectonics and Magmatism, Neoproterozoic Malani Igneous Suite, Western Rajasthan, India

Naresh Kumar and Radhika Sharma

Abstract

The present contribution reports on the field, petrographical and geochemical observations of the volcano-plutonic rocks of the Nakora Ring Complex (NRC) from the Neoproterozoic, Malani Igneous Suite (MIS) (Northwestern Peninsular India) and confers about their magmatic evolution and tectonic implications. Three magmatic phases are notable in the NRC which is Extrusive, Intrusive and Dyke phase where with small quantities of basaltic flows was initiated and accompanied by extensive/voluminous acidic flows. Petrographically, rhyolite shows flow bands, porphyritic, spherulitic, aphyritic and perlitic textures whereas basalt flows are distinguished by the presence of labradorite in lath-shaped crystals (plagioclase feldspar) and clinopyroxene (augite). The presence of high silica and total alkalis in NRC rocks, as well as high field strength elements (HFSE), enrichment of trace elements and negative anomalies of Sr., Eu, P, and Ti indicates that the emplacement of the lava flows was controlled by complex magmatic processes such as fractional crystallization, crustal contamination and partial melting. The association of basalt-trachyte-rhyolite means that the magma chamber was supplied a significant amount of heat to the crust before the eruption. Moreover, a volcanic vent was also reported at NRC where rhyolite was associated with agglomerate, volcanic breccia, perlite and tuff. The current research proposed that the Neoproterozoic magmatism at NRC was controlled by rift-related mechanism and produced from crustal source where the heat was supplied by mantle plume.

Keywords: Volcano-plutonic, Petrology, Nakora, Malani Igneous Suite

1. Introduction

Volcano mentions as the magma and associated ingredients erupt to the surface from the vent and also refer to the landform formed by solidified lava and volcanic debris near the vent. Abundant volcanic rocks in the Earth's upper continental crust are broadly studied because they are closely related to with magmatic processes,
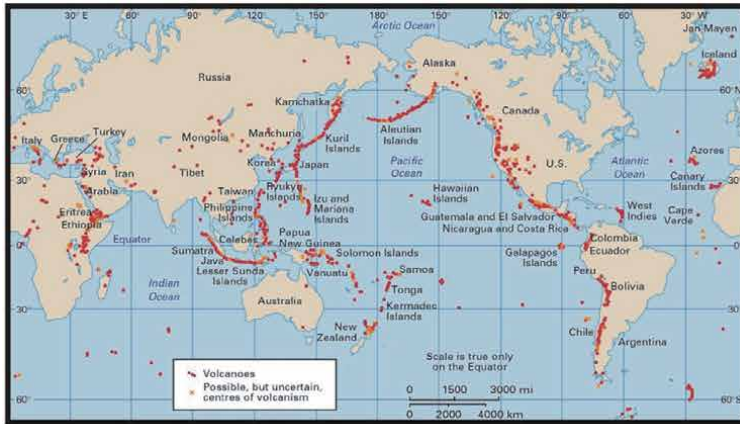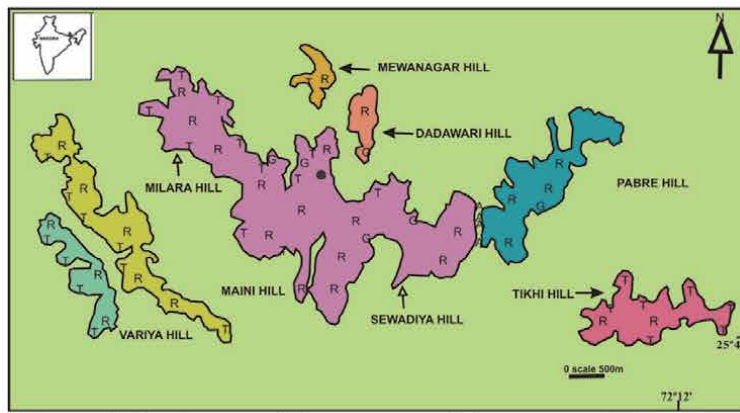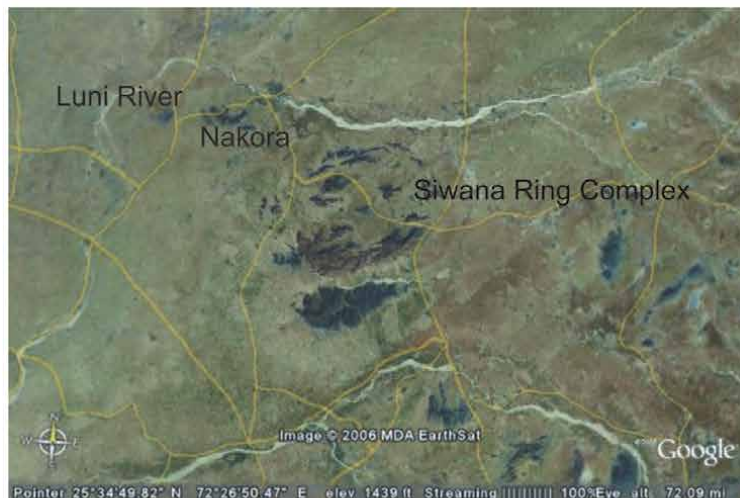
Figure 1.
(A) Global map showing location of volcanoes and centers of valcanism on lithospheric plates and related to crustal evolution (modified after Encyclopedia Britannica, 2008). (B) Geological map of Nakora area, Western Rajasthan, India. (C) Aerial view of Nakora Ring Complex, Siwana Ring Complex and Luni lineament, Rajasthan, India.

crustal evolution, tectonics and geodynamics [1]. Volcanoes are almost located where tectonic plates diverge or converge on Earth surface/subsurface, and the majority of them are found underwater. Volcanic vent were documented from diverse settings of the world and they are sketched with crustal provinces, platforms, shield areas and orogenic belts (**Figure 1**). The volcanoes such as Mid-Atlantic Ridge and Pacific Ring of Fire are superlative example of divergent and convergent tectonic plates respectively. Volcanoes can also found in the East African Rift, Rio Grande Rift (North America), Hawaii, Arizona, Iceland, Mount Fuji (Japan), Stromboli (Italy), Valles Caldera and Yellowstone National Park in New Mexico and Narcondam Island (India). As isolated magma bodies ascend from large magma source regions, small volcanic vents are discovered within the Tharsis Volcanic Province [2]. The cooling efficiency inside the parent fountain determines the pyroclastic products are generated by basaltic Hawaiian fountaining [3, 4]. Big Ben lavas identified in Heard Island (Subantartic volcanic) are dominated by basalt, basanite and trachybasaltic rocks and discharge rate of average magma is very truncated [5].

On survey of India topographic sheet no. 45C/1; Scale 1: 50000; 25°45′– 25°50′ N; 72°05′–72°15′ E Nakora Ring Complex is located in Western Rajasthan. NRC divided in many hills, i.e., Milara, Nakora, Dadawari, Variya, Sewadiya, Tikhi, Maini and Pabre which consists of granite, basalt, trachyte, rhyolite, tuff, gabbro and dolerite (**Figure 1B**). The NRC's rocks are related to the Malani Igneous Suite (MIS, Neoproterozoic) in the Trans Aravalli Block (TAB) of Indian Shield. The major period of anorogenic (A-type) is an exclusive event in the geological evolution of Indian Shield with the characteristics of bimodal in nature, high heat producing and Intraplate magmatism.

TAB consists of peralkaline, metaluminous to mildly peralkaline and peraluminous granites of Siwana, Jalor, Jhunjhunu and Tosham respectively with cogenetic association of acid volcanics [6–8]. MIS is India's largest anorogenic acid volcanism and the world's third largest with the characteristics of distinctive ring structures and radial dykes. It has a range of ~55,000 sq. Km with a broad initial phase of felsic and mafic volcanism, accompanied by granitic plutonism. MIS owes its origin to hot spot tectonics and is governed in the TAB by NE–SW trend lineaments [9, 10]. The objective of this research is to provide a relation between magmatism and tectonism by using petrological and geochemical data in Nakora area of MIS.

2. Geological setting

MIS (~780–750 Ma) spread in NW India which is a silicic large igneous province (Precambrian) and characterised by Pan-African thermo-tectonic event [11–13]. This event showed volcanic and plutonic igneous multiphase assemblages during the Neoproterozoic period that were operated by hot-spot tectonism. In NW India, TAB is leading with A-type magmatic felsic rocks having specific geochemical characteristics i.e., alkaline, peralkaline, metaluminous and peraluminous [7–9, 14]. In Tosham (Haryana), Siwana, Jalor, Jhunjhunu, Nakora, Mokalsar, Jodhpur, Sirohi (Rajasthan) and even in Nagar Parkar (Sind-Pakistan), Kirana Parkar (Kirana), they are well exposed (Lahore-Pakistan) [6, 9, 10, 15].

The tectonic, magmatic and geodynamic characteristics of NRC are enlightened on the basis of geological field mapping, petrography and major and trace elements chemical data. Different rocks are classified into different phases based on the field relationships of the region. They are categorizing as Extrusive phase (trachyte,

rhyolite, basalt, tuff, perlite, breccia, ash and agglomerate), Intrusive phase (granite and gabbro) and Dyke phase (basalt, dolerite, rhyolite and microgranite). In NRC, region first phase includes basic flows which is latter outpoured the acidic volcanic rocks and contains pyroclastic explosive rocks, acid lava flows and pyroclastic ash fall. Second phase having granite which is intruded the acid flows (plutons, ring dykes and bosses) and third phase consists of felsic and mafic dykes which cut the rocks of earlier phases [16, 17]. The NRC hill is located along the Luni River and the Luni River suddenly turns 'U' from West to South, reflecting the continental rift [18]. The Sukri lineaments are followed by NE–SW trend parallel lineaments of the Luni River and are called major Luni-Sukri lineaments (**Figure 1C**). These types of lineaments are caused by the release of stress after the orogenic cycles of Aravalli-Delhi and MIS magmatism, caused by mantle plume [19]. In TAB, the Luni rift is an important tectonic lineament [20]. This lineament is linked to significant continental rift model crustal dislocations for magma extrusions and intrusions [21]. Luni rift has therefore acted as the path for magma to rise through various major fractures, followed by anorogenic volcanism that may precede/follow the position of ring complexes. The NRC field, which is a small part of the NW continental block, a very significant element in explaining the petro-genetic, geodynamic evolution of MIS.

3. Field observations

In field photos, numerous lithological rock-suits with field relationships are drawn and the genuine petrological research is performed. The detailed physio-chemical features of various hills are defined as:

3.1 Extrusive phase

3.1.1 Basalt

The basalt flow occurs predominantly in the inner parts of the NRC hills of Sewadiya, Maini and Dadawari. Basalt has a fine grained and colour is black/dark brown, light greyish brown, and dark greyish brown. Basalt forms with a maximum thickness of 10 m and the rhyolite and trachyte flows are underlying. The flows of rhyolite and basalt display radial pattern (**Figure 2A**) and sharp contact with themselves (**Figure 2B**). The basalt contains large vesicles (4–6 mm) and often calcite fills the vesicles. Basalt xenoliths in the rhyolite (**Figure 2C**) and trachyte are found to suggest that basalt is older than rhyolite and trachyte.

3.1.2 Trachyte

At the outer margin of each hill, the trachyte flow is observed and it is the second dominant form of rock after the rhyolite. Trachyte flows of porphyritic as well as non-porphyritic nature are dark/light bluish color. It occurs on Milara hill at a maximum thickness of 50 m. Sharp contact is observed between trachytes and rhyolites. Basalt xenoliths in trachytes suggest that the flows of trachyte are younger than basalt.

3.1.3 Rhyolite

Rhyolite occurs in almost all the hills in NRC with the pyroclastic assemblages and is the most prevalent rock form in NRC. The color of rhyolite is primarily dark brown (**Figure 3A**) with different hues of light brown, red brick, grey, green, black, blue and purple. It is considered in nature to be porphyritic and non-porphyritic. In
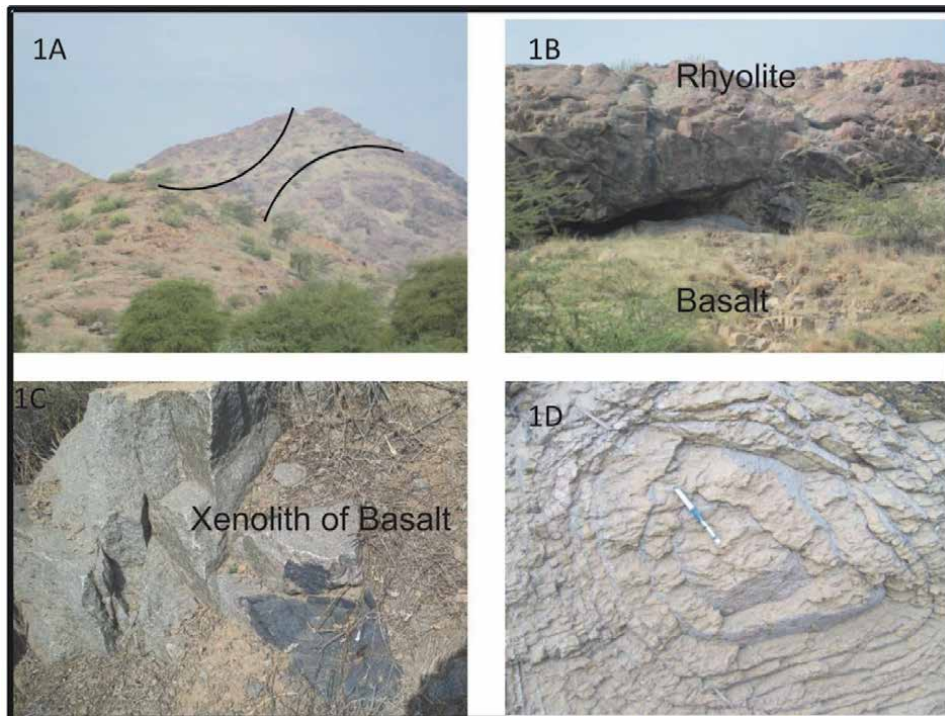
Figure 2.
(A) Radial pattern present in Sewadiya hill, (B) basalt underlies the dark color rhuolite, (C) xenolith of basalt present in the rhyolite, (D) spherical weathering of the rhyolite rock.

the Nakora area, the maximum flow thickness is 200 m, represented by dark brown rhyolite at Sewadiya and Maini hill.

On the Northeastern flank of Sewadiya hill, spheroidal rhyolite is exposed. It is light yellow to pale brown in color. In a region of 200 sq. meters, the spheroidal rhyolite is exposed. The spheroidal structure is up to 5 m in size and shows a large number (up to 65) of few cm thick concentric shells surrounding a nuclei (**Figure 2D**). The shells consist of concentric layers of light and dark colors. They occur mostly in circular/semicircular and square shapes as well. A sharp contact is observed between the spheroidal rhyolite and the brown rhyolite.

3.2 Pyroclastic assemblages

There are exposures of ash, welded tuff, blast breccia, agglomerate and perlite. In the inner part of Sewadiya hill, there is a small bed of volcanic ash (light yellow color). Tuff demonstrates different colors, viz. Light yellow to light grey, but glassy material and tiny vesicles are also noted in it in a few areas. Sharp contact with basalt (**Figure 3B**) and rhyolite is indicated by Tuff. In the foothills of the Maini hill, angular fragments of explosive breccia and agglomerate (rounded to elongate in form with a diameter of 6–10 cm) are observed.

3.3 Intrusive phase

3.3.1 Granite

Granite is primarily exposed at three NRC sites, i.e. the inner parts of Sewadiya, Maini, and Dadawari hill. The granites display varying shades of pink, dark pink
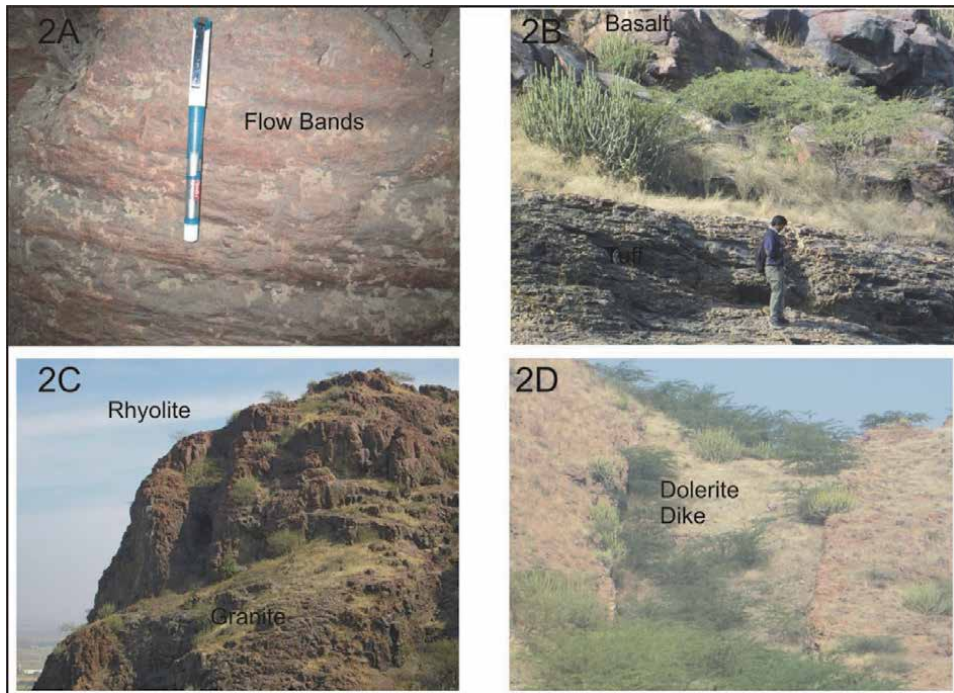
Figure 3.
(A) flow bands in non-porphyritic rhyolite, (B) contact between tuff and basalt, (C) contact between rhyolite and granite, (D) dolerite dyke.

and light pink, respectively. They are medium, large and compact grains. In the study zone, sharp contact of granite with rhyolite is observed. The intrusive aspect of granite in the rhyolite promotes volcanic plutonic association and sub-volcanic nature (**Figure 3C**).

3.3.2 Gabbro

Gabbro occurs in three locations i.e. Sewadiya hill, near Maini hill, and at Sewadiya hill and Pabre hill contact. Gabbro rocks types are connected to rhyolite as a small invasive body. Gabbro's color is dark black, coarse-grained and massive.

3.4 Dyke phase

3.4.1 Basalt

The basaltic existence of the dyke is found within the tuff and iron oxides encrusted porphyritic dark brown rhyolite in the Maini and Sewadiya hills. Basalt is observed in both the flow and the dyke shape. The color is black, fine grained with small (few cm) vesicles. The basalt dyke is 2 meters wide and 10–15 meters long.

3.4.2 Dolerite

In the inner circle of the research field, dolerite dykes are prevalent and have NE–SW patterns. In the study area, the radial pattern of dolerite dykes can easily be observed. They primarily cut through the rhyolites and trachytes. In color, the

dolerite dyke is black and medium grained. Dolerite dykes range in width from 1 m to a maximum of 50 m and can be tracked to a maximum of 300 m (**Figure 3D**).

3.4.3 Rhyolite and microgranite

The granite in Sewadiya hill has been cut by rhyolite (light brown) and microgranite (light pink). The granite is 100 m by 100 m in size. The rhyolite dyke has a width of between 1 m and 3 m and a length of up to 100 m. The rhyolite on the outcrop is marked by small bushes.

4. Petrography

This section contains the detailed petrographical characteristics of different rock types which are described as follows:

4.1 Extrusive phase

4.1.1 Basalt

Basalt reveals textures that are ophitic (**Figure 4A**) and sub-ophitic (**Figure 4B**). Plagioclase labradorite (feldspar) and augite (clinopyroxene) are the dominant in basalt flows (**Figure 4A**). As accessories minerals, fine grained quartz, hematite and magnetite are found in the groundmass. The lath-shaped crystal (plagioclase) takes place as a phenocryst and also occurs in ground mass (**Figure 4B**). In basalt, large vesicles (4–6 mm) are often packed with secondary minerals such as quartz and calcite. Labradorite is in shape from euhedral to subhedral and finely grained. It shows lamellar twinning and is changed to kaolin. Often it gives a cloudy appearance due to alteration. Augite has a medium grained and pale brown and grey color.

4.1.2 Trachyte

Trachyte illustrates the porphyritic texture (**Figure 4C**). Trachytic texture is often the directive flow and parallelism of elongated crystals (**Figure 4D**). Trachyte's petrographic properties are somewhat similar to rhyolite, with relatively less quartz and more ferromagnesian minerals viz. riebeckite, magnetite, arfvedsonite and hematite. It consists of quartz, orthoclase and riebeckite phenocrysts as important minerals in the groundmass of quartzofeldspathic. Orthoclase occurs in quartzofeldspathic groundmass as euhedral crystals. This illustrates the twinning and kaolin alteration of Carlsbad. The orthoclase phenocrysts are fractured and often filled with crystals of riebeckite. Quartz, with embayed margin and fractured shapes, happens as euhedral to subhedral crystals. The quartz veins cut the ground-mass quartzofeldspathic. The riebeckite is fine grained, blue in color, needle form and embedded in the ground mass.

4.1.3 Rhyolite

When viewed under a microscope, Rhyolite displays flow bands, porphyritic, aphyritic, spherulitic (radiating growth of feldspar and quartz from a common center) (**Figure 4F**) and perlitic textures. The rhyolite consists of orthoclase, quartz, and arfvedsonite phenocrysts as important minerals in the ground mass quartzofeldspathic. In some samples, high temperature alkali feldspar, i.e. euhedral
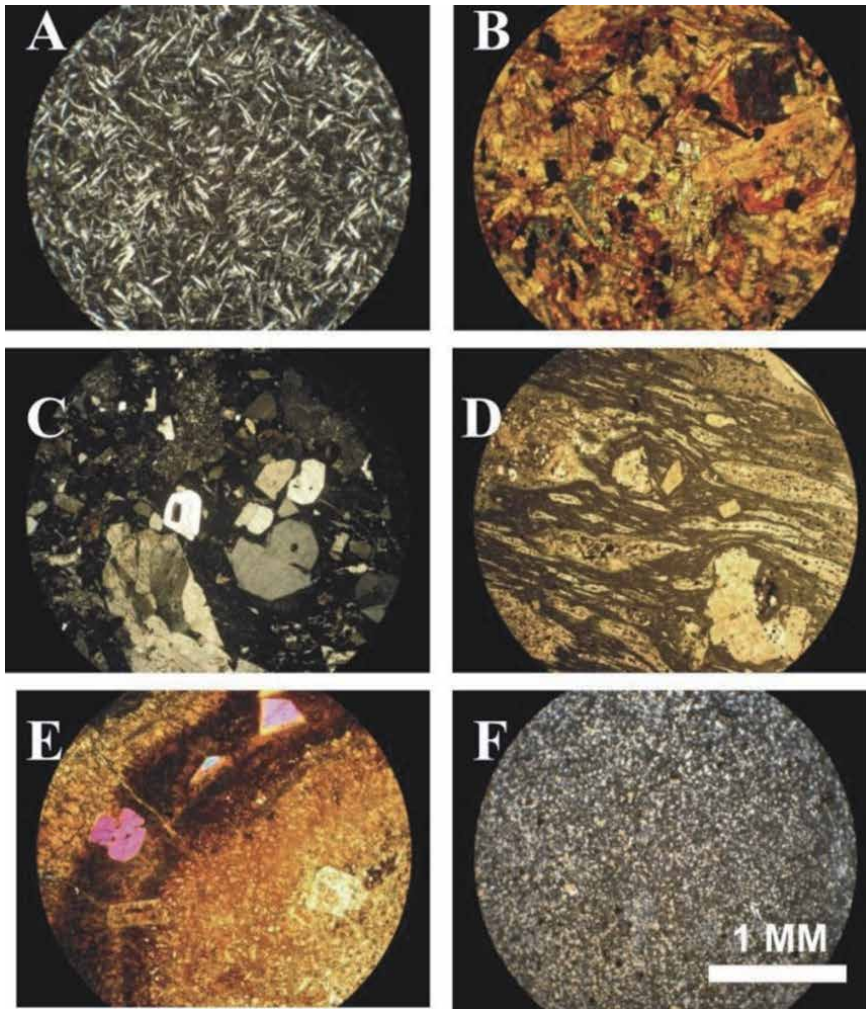
Figure 4.
(A). Labradorite and augite are present in basalt and shows ophitic texture; XPL. (B). Labradorite and augite are showing sub-ophitic texture in basalt; XPL. (C). Quartz, orthoclase which is showing Carlsbad twinning in trachyte; XPL. (D). Trachyte shows cryptocystalline nature of flow direction; PPL. (E). Quartz, orthoclase occur in a matrix of fine grained quartz and feldspar of rhyolite, which shows a little flow structures; PPL. (F). Quartz, orthoclase, aniegmatite shows equigranular texture by granite; XPL.

sanidine crystals, are also found. Microcrystalline aggregates of quartz, alkali feld-spar, blue amphibole (riebeckite), pyroxene (light green aegirine), blood red aenigmatite, magnetite, and hematite are de-vitrified to the ground mass. The fine quartz-feldspar ground mass reflects the lava flow directions.

Phenocrysts of quartz occur in different ways, i.e. drop like, fractured and embayed. The orthoclase and ground mass are cut by the quartz veins and parallel to the lava flow path (**Figure 4E**). Alkali feldspar phenocrysts illustrate twinning in Carlsbad. Altered and fractured orthoclase is also found at a few stages. Arfvedsonite's fine crystals are correlated with alkali feldspar. Bluish green arfvedsonite occurs with pleochroic (X = dark bluish green, Z = yellowish green) as fine to medium grained prismatic crystals.

The spheroidal rhyolite displays layers of mafic (dark/light brown) and felsic (light grey), reflecting the texture of the flow. Hematite, magnetite and arfvedsonite are formed of the mafic layer and they are fine grained. The felsic layer is composed of quartz, perthite, and orthoclase and medium-grained. Medium

grained, lath/prismatic shaped, colorless and showing Carlsbad twinning are the orthoclase crystals. Orthoclase is scattered, sericitised spontaneously and combined with quartz intergrowth. Fine quartz veins are cut by the sericitised feldspars and display high order interference colour.

5. Analytical techniques

Major, trace and rare earth elements contents (min., max. and mean) for representatives samples of plutonic and volcanic rocks are reported in the **Tables 1–3**, respectively. Major elements are analyzed by using wet chemical method using a UVV is spectrophotometer108 and Atomic Absorption Spectrophotometer (Varian 240 FS AAS) at Department of Geology, Kurukshetra University, Kurukshetra. Trace and rare earth elements are analyzed by ICPMS (PerkinElmer Sciex ELAN DRC II) at National Geophysical Research Institute (NGRI), Hyderabad. Standardization for major and trace elements including rare earth elements was based on USGS rock standards RGM—1, JG—2 and MRG—1.The analytical precision is found to be in the error level of <5% for major and <105 for trace elements.

6. Bulk geochemistry

The whole-rock geochemical data of major and minor oxides, trace elements and rare earth elements for the acid volcano-plutonic rocks, are carried out to justify our mineralogical and petrographical results [22]. They are high in SiO_2, $K_2O + Na_2O$, Al_2O_3, Ba, Th, U, Y, Rb, Zr, Nb, REEs (except Eu) and low in TiO_2, CaO, MgO, V, Sr., Ni, Cr, Ti, P, Eu; typically A-type affinity. Based on the mineral chemical databank, it was investigated that K-feldspar, plagioclase and biotite are important silicate minerals in rock-formation.

6.1 Extrusive phase

Average values of SiO_2, Al_2O_3, Na_2O, K_2O, Fe_2O_3, TiO_2, CaO, MgO, MnO and P_2O_5 (in wt %) are in basalts samples as 51.30, 3.18, 1.40, 3.46, 12.24, 3.18, 5.53, 5.70, 2.01 and 0.60 respectively, in trachyte, values are 67.93, 7.93, 1.07, 5.96, 9.00,

Major elements	Basalt	Trachyte	Rhyolite	Granite	Gabbro	Dolerite
SiO_2	45.59–54.00	66.7–69.4	64.80–71.90	66.20–69.60	45.49–53.20	54.5
TiO_2	2.34–4.12	2.67–2.93	1.61–2.84	1.11–3.80	1.67–2.66	2.83
Al_2O_3	11.20–17.40	6.1–10.5	7.20–13.10	7.10–11.90	14.90–15.60	13.5
Fe_2O_3	9.67–14.50	8.1–10.2	5.40–9.70	2.60–10.00	8.90–17.20	9.7
MnO	1.62–2.70	1.25–3.13	0.19–1.06	0.56–1.69	1.38–1.58	1.1
MgO	4.42–6.56	0.49–1.47	0.49–3.28	0.98–4.75	6.25–6.50	7.2
CaO	1.68–7.60	0.8–1.52	0.80–3.64	1.41–3.56	2.80–3.50	4.96
Na_2O	1.00–2.71	1.06–1.09	0.94–1.18	0.99–1.19	5.11–7.10	2.18
K_2O	1.85–4.46	4.3–7.28	4.48–6.81	4.07–7.96	1.44–2.41	2.09
P_2O_5	0.31–0.88	0.5–0.55	0.45–0.62	0.28–0.77	0.44–0.47	0.82

Table 1.
Major element concentrations of Nakora rocks.

Trace elements	Granite	Rhyolite	Trachyte	Basalt	Gabbro	Dolerite
Sc	5.77	1.64	2	30.23	20.99	28.4
V	6.5	3.35	4.15	201.58	149.31	206.89
Cr	3.31	5	23.68	37.55	57.11	55.1
Co	1.33	0.58	0.61	31.15	46.87	38.69
Ni	3.25	2.34	23.09	35.05	120.99	15.35
Cu	0.39	0.34	9.88	35.18	43.3	52.21
Zn	56.7	36.4	226.61	190.09	69.24	544.26
Ga	37	29.3	30.76	28.18	12.77	17.9
Rb	157	104	144.69	60.46	46.36	50.51
Sr	37.1	12.7	11.94	178.34	312.14	295.83
Y	216	154	227.51	74.86	18.84	42.86
Zr	1482	1459	2009.4	501.97	80.37	64.25
Nb	38.6	40.3	82.57	26.09	4.2	5.89
Cs	5.93	0.62	0.74	1.07	2.06	0.93
Ba	417	91.9	80.29	345.12	416.83	405.96
Hf	46.1	31.9	50.44	10.54	2.03	1.82
Ta	2.42	1.96	8.44	2.06	0.57	0.39
Pb	10.8	9.59	2.92	2.07	0.98	30.9
Th	16	11	17.39	2.92	0.3	1.11
U	4.93	2.8	1.78	0.41	0.07	0.11
Ba/Rb	3.15	0.9	0.55	6.45	8.99	8.04
Rb/Sr	4.88	8.46	12.12	0.35	0.15	0.17
Zr/Rb	7.02	14.7	13.89	6.79	1.73	1.27
Ba/Sr	10.9	7.59	6.72	1.98	1.34	1.37
Sr/Y	0.23	0.08	0.05	3.15	16.57	6.9
Nb/Y	0.2	0.26	0.36	0.31	0.22	0.14
Zr/Nb	27.7	33.6	24.34	17.23	19.14	10.91
Zr/Y	5.22	8.67	8.83	5.74	4.27	1.5
Y/Nb	5.17	4.18	2.76	4.8	4.49	7.28
K/Rb	0.03	0.05	0.02	0.04	0.02	0.03

Table 2.
Trace element concentrations of Nakora rocks.

2.84, 1.15, 1.09, 2.13 and 0.53 respectively whereas rhyolites show average values as 68.46, 9.73, 1.05, 5.65, 7.74, 2.40, 1.92, 1.62, 0.73 and 0.55 respectively.

6.2 Intrusive phase

The granites show (wt %) SiO_2 (66.20–69.60), Al_2O_3 (7.10–11.90), total alkalies (5.06–9.15), Na_2O (0.99–1.19), K_2O (4.07–7.96), total iron (2.60–10.00), TiO_2 (1.11–3.80), CaO (1.41–3.56) and MgO (0.98–4.75). Gabbros show a wide range of SiO_2 (45.49–53.20), Al_2O_3 (14.90–15.60), total alkalies (6.55–9.51), Na_2O

| Rare earth elements	Granite	Rhyolite	Trachyte	Basalt	Gabbro	Dolerite
La	71.5	39.06	94.05	29.13	7.85	10.78
Ce	392.99	101.81	243.67	73.34	19.74	32.58
Pr	37.7	16.84	26.55	9.11	2.7	4.3
Nd	170.72	75.96	133.58	50.16	15.5	26.97
Sm	40.17	17.39	30.08	11.61	3.98	7
Eu	4.23	1.35	2.24	3.4	1.7	2.46
Gd	33.89	14.66	29.27	12.25	4.11	8.28
Tb	6.04	2.9	4.5	1.78	0.57	1.3
Dy	40.27	21.6	33.37	10.84	3.94	6.88
Ho	4.63	2.6	7.14	2.18	0.77	1.41
Er	16.11	9.17	20.64	6.06	1.93	4.3
Tm	2.14	1.24	2.63	0.82	0.22	0.7
Yb	22.22	12.86	17	4.84	1.33	3.73
Lu	3.67	2.1	3.69	0.93	0.3	0.55
Ce/Nd	1.89	1.08	1.82	1.09	1.27	1.21
Ce/Sm	7.96	4.73	8.1	4.68	4.96	4.65
Gd/Yb	1.4	0.94	1.72	2.22	3.09	2.22
Ce/Yb	13.36	6.55	14.33	12.46	14.84	8.73
Eu/Eu*	0.14	0.07	0.08	0.24	0.42	0.32

Table 3.
REE element concentrations of Nakora rocks.
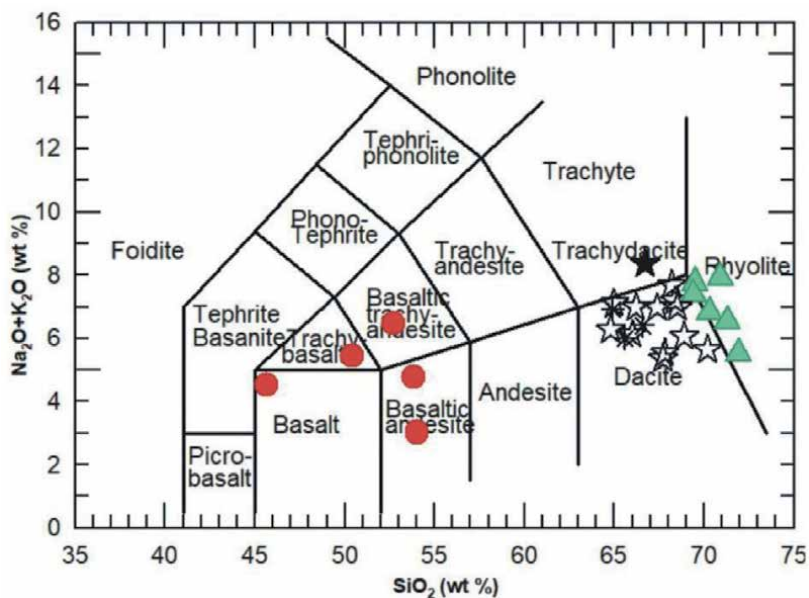
Figure 5.
Total alkali-silica diagram showing classification of Nakora volcanics. Symbols: Rhyolite (▲), Dacite (☆), Trachydacite (★), Basalt (●).

(5.11–7.10), K_2O (1.44–2.41), wide variation of total iron (8.90–17.20), high TiO_2 (1.67–2.66), CaO (2.80–3.50) and less variation of MgO (6.25–6.50) (wt%).

6.3 Dyke phase

6.3.1 Dolerite

As compare to basalts, the dolerite shows (wt %) high SiO_2 (54.50), low Al_2O_3 (13.50), low total alkalies (4.27), (Na_2O: 2.18, K_2O: 2.09), low total iron (9.70), low TiO_2 (2.83), low CaO (4.96) and high MgO (7.20).

On the basis of geochemical data, Nakora acidic volcanic and basic rocks are plotted in the TAS diagram (**Figure 5**) [23] in which rhyolites lie in the field of rhyolite and dacite however dacite is very close to rhyolite where basic rocks lie in the field of basalt, trachybasalt, basaltic trachy–andesite and basaltic andesite. In tectonic discrimination $R_1 – R_2$ diagram [24], the Nakora granites fall in the field of anorogenic (**Figure 6**). Usually, the intrusion of anorogenic felsic magma into upper crust follows a cycle of compressive tectonic activity and orogenic magmatism [25]. The clustering of the granites in the anorogenic field indicates the limited melting of a crustal source [24].

In the Harker diagram, 1909 [26], the SiO_2 (wt %) is plotted along the X axis and other oxide concentrations are plotted along Y axis. These diagrams reveal that Nakora rocks show four different distribution trends (**Figure 7**). The Nakora rocks show a regular decrease in Al_2O_3, MgO, Fe_2O_3 and CaO with increasing silica and continuous increase in K_2O with increasing value of silica. In the case of TiO_2 and P_2O_5, the rocks show constant distribution trend. In case of Na_2O, the rocks show totally constant Na_2O concentration with increasing silica content. The Nakora basalts contain more Al_2O_3, K_2O, Fe_2O_3, TiO_2, CaO and P_2O_5 as compared to other basic rocks. MgO and Na_2O are more in dolerite and gabbro respectively. Granites show high MgO, TiO_2, K_2O and P_2O_5 as compared to other acid volcanic rocks. Al_2O_3 and Fe_2O_3 are more in tuff and trachydacite respectively.
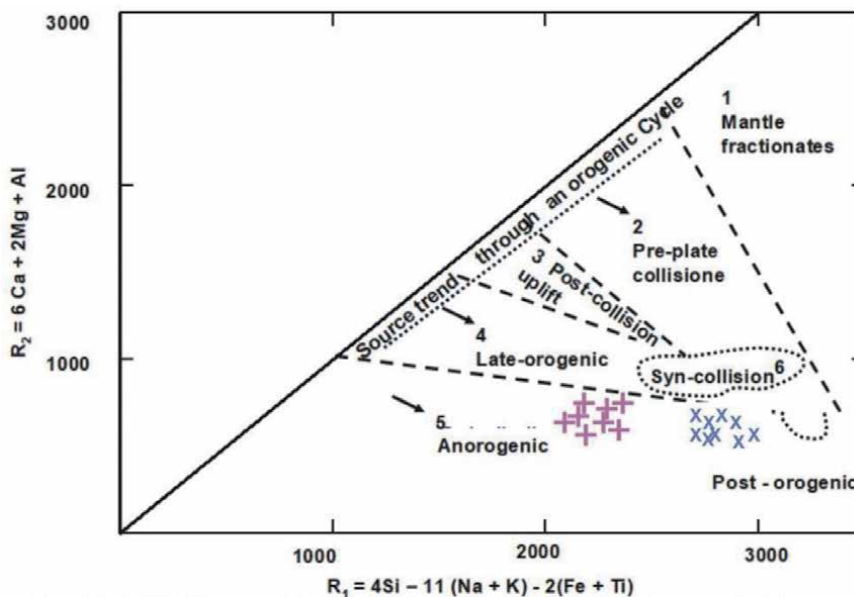

Figure 6.
R1-R2 diagram [24] of major granitoid association. Symbols: Grey granite (✚), Pink granite (✖).
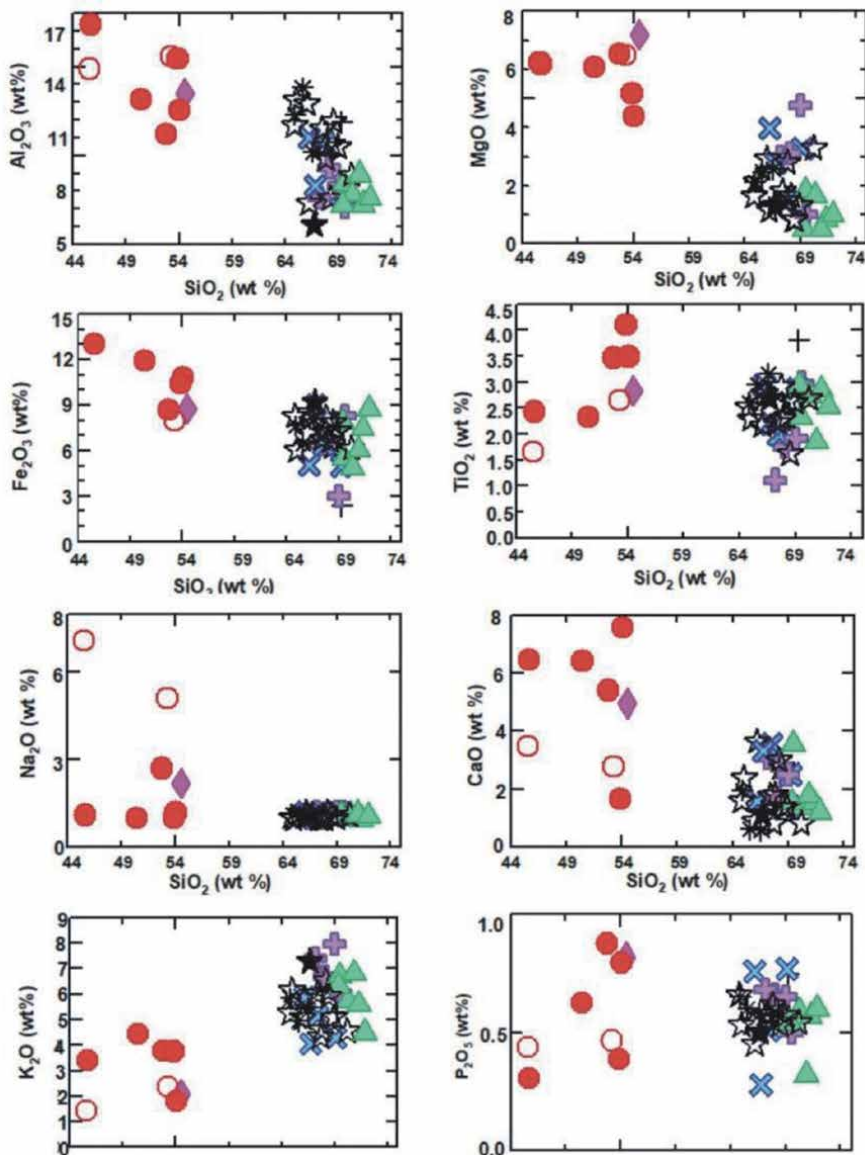
Figure 7.
Harker variation diagram of SiO vs. oxide showing the variation of Nakora rocks. Symbols: Peralkaline Granite (⬗), Metaluminous Granite (✖), Peraluminous granite (✚), Rhyolite (▲), Dacite (☆), Trachydacite (★), Tuff (✳), Basalt (⬤), Gabbro (◯), Dolerite (◆).

On the basis of different tectonic discrimination diagrams [27], which are based on mineral assemblages, the tectonic environment of the Nakora rocks is clarified. In the various tectonic discriminating diagrams (Y+Nb vs. Rb), when Nakora granites are plotted, they fall within plate granites (**Figure 8**). The above diagrams therefore demonstrate that this phase of magmatism was anorogenic. The primitive mantle normalized multi-element pattern (normalization values from Sun and McDonough [28]) for three Nakora basic rocks (2 basalts and 1 dolerite) displays similar pattern (**Figure 9**). However, the dolerite dyke is showing highly Pb enrichment as compared to basalts. The Nakora basic rocks show LREE enriched nature and they have consistent negative Nb, Ta, Sr. and Zr anomalies. The HREE pattern of dolerite dyke is showing parallel arrangement with HREE pattern of
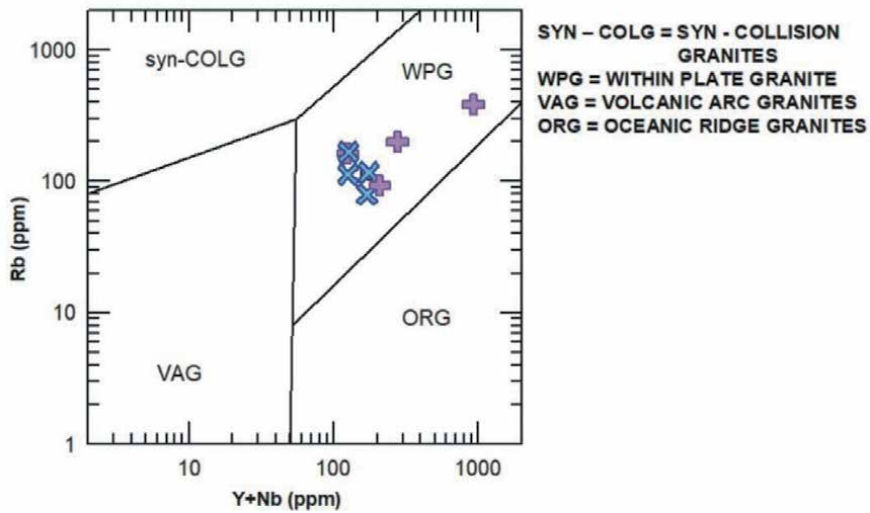
Figure 8.
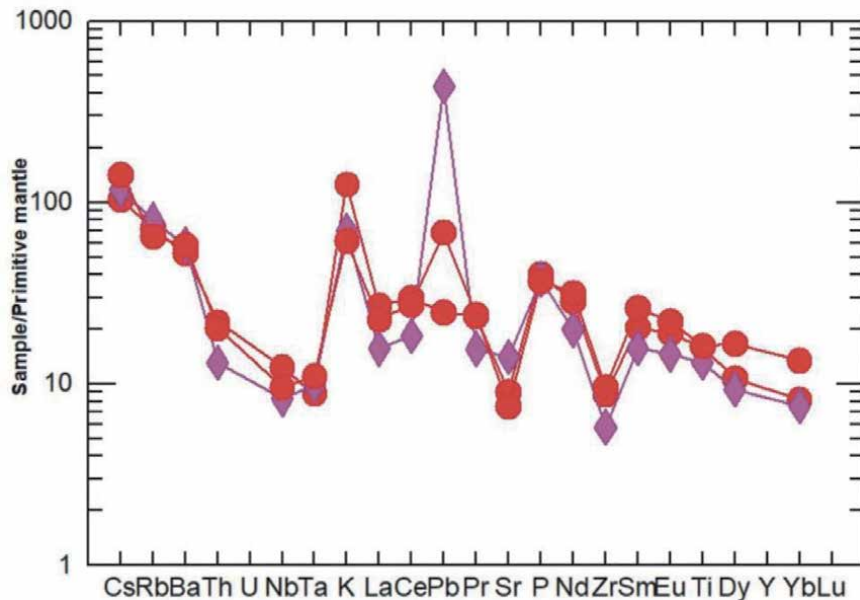*Y + Nb vs. Rb diagram of Nakora acidic rocks.*

Figure 9.
Primitive mantle normalized trace element patterns for Nakora basic rocks [28].

other basic rocks. Hence close resemblance is observed between the dolerite dyke and Nakora basalts in terms of their LREE enrichment and negative Nb, Ta and Zr anomalies. Thus based on the above observations we conclude that these rocks may be related to same source. The chondrite normalized REE patterns for all types of Nakora rocks are shown in **Figure 10**. REE patterns in the Nakora acid volcanics and basic rocks are characterized by sub-parallel patterns with strong negative Eu anomaly (Eu/Eu* = 0.06 to 0.12, avg. 0.08). But in basic, positive Eu anomaly (Eu/Eu* = 0.24 to 0.44, avg. 0.34) is observed. The Nakora basic rocks are less enriched in LREE and HREE as compared to acid volcanics. On the other hand, rhyolites and granites are showing almost similar abundances of REE which is probably due to
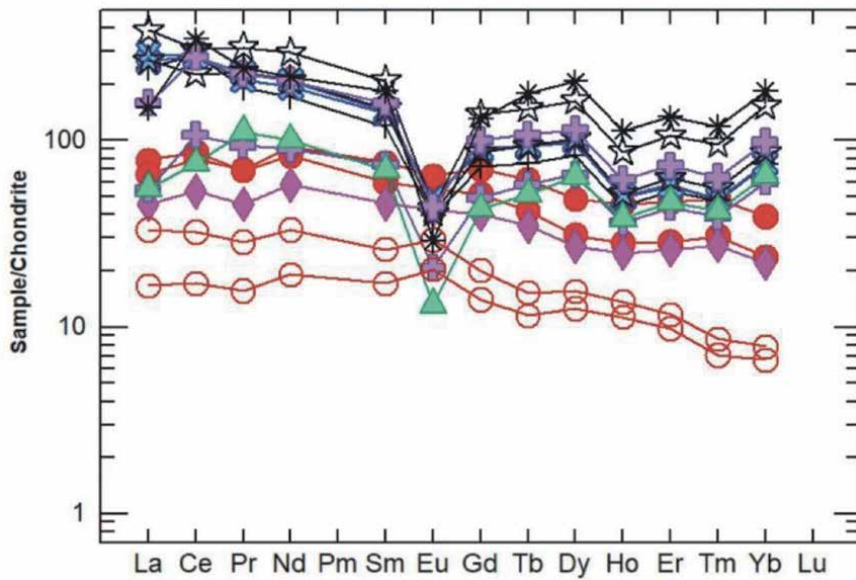
Figure 10.
Chondrite normalized REE patterns for Nakora rocks [28].

their comagmatic nature. In general, the fractionation is more in HREE as compared to LREE in Nakora acid volcanic rocks, whereas in basics, almost flat normalized patterns are observed. Thus the sub-parallel REE patterns of all Nakora rocks suggest a common magmatic source.

The Siwana magma is derived from the mantle and has A-type geochemical parameters [29]. With the assimilated Achaean crust, the Jalor complex suggests primary mantle derivation with a variable degree of crustal contamination [30]. The Jhunjhunu granites seem to have come from a granodioritic composition source [31].

In the **Figure 11**, the chondrite normalized pattern is derived for partial melt by 33% partial melting leaving a residue 48% plagioclase, 33% opx and 19% cpx which closely approaches the REE patterns of Nakora basalts. The Bhilwara mafic metavolcanic which is taken from outside the study area and mixed Nakora gabbros
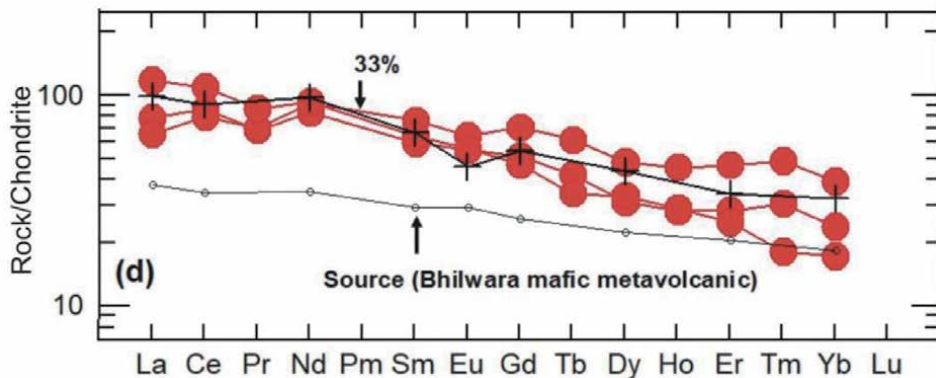

Figure 11.
Chondrite-normalized diagram showing the calculated REE patterns for melts produced by 33% batch partial melting of mafic metavolcanic from Bhilwara leaving a residue consisting of 48% plagioclase, 33% orthopyroxene and 19% clinopyroxene.

169

taken from the study area are showing maximum similarities with the REE patterns of the Nakora basalts. Hence, the Nakora basalts could have been derived by different degrees of partial melting of source rock similar to Bhilwara mafic metavolcanic/Nakora gabbros composition.

7. Magmatism and tectonism

MIS shows the within plate environment that is related to the activity of the hot spot and represents the tensional environment in its spot that is flanked by different elliptical/ring structures [17, 21]. About 700–900 m.y., the magma of the Trans Aravalli MIS erupted. Alkaline magmatism, like subalkaline subvolcanic complexes in lithospheric continents, represents the igneous activity, while the plume gives rise to basaltic oceanic chains/aseismic ridges in oceanic crustal regions. Intraplate, anorogenic existence and extensional tectonic environment are well known by MIS granites and Mahe (750 Ma) and Ste. Anne (764 Ma) Seychelles granites [32] show the similar environment. They are aligned with Siwana (732 Ma old) hypersolvus granites and subsolvus granites from Jalor (MIS).

The higher amount of Zr is reported by Kochhar et al., [33] in the Siwana rhyolites which formed during the Zr crystallization and Nakora area also exhibits the appreciable amount of Zr concentrations. Partial melting and enrichment of alkali elements initiate due to releasing of pressure at a depth which influx the volatiles in to the crust [20]. The peralkaline association of trachyte–rhyolite and basalt within–plate character denotes the zones of crustal extension [34]. The Arabian–Nubian shield shows the tensional tectonic environment which is formed by the bimodal magmatic activity during the uppermost Precambrian crustal evolution [35]. The Nakora area is characterized by the close association of trachyte, rhyolite, granite (peralkaline, peraluminous and metaluminous) with gabbro, basalt and dolerite. Close association of granite is observed with trachyte flows in Mokalsar [36] and Goliya Bhaylan area [37] of Siwana. Granites are associated with gabbro and basalt in Guru Nal area and Jalor area respectively [38]. In view of association of trachyte, rhyolite, basalt and gabbro, with the subsolvus and hypersolvus granite of the Malani area, it is suggested that the model of deep crustal hot zone which is suggested by Annen et al. [39] as outlined above can be applied to the area under study.

A deep crustal hot zone is created in the model by mantle-derived hydrous basalts accumulated as a series of sills into the lower crust. Melts are generated in Nakora area from two distinct sources; partial crystallization of basalt to produce residual H_2O-rich melts; and partial melting of pre-existing crustal rocks. Partially melting of the underlying crust, which may involve meta-sedimentary and meta-igneous basement rocks, as well as earlier basalt intrusions, is aided by heat and H_2O transfer from the crystallising basalt [39]. According to the evidence in the literature and the geochemical and petrological findings presented, MIS is the result of a complex series of geological processes that include partial melting, fractional crystallisation, magma mixing and assimilation, crustal contamination, and fluid-melt interactions. However, while Nakora is made up of common hydrous minerals such as biotite, amphiboles, apatite, and muscovite, it also contains volatile components in the form of halogens, indicating that the comagmatic rocks went through many phases during their evolution.

Kochhar [40] explained the similarities between Trans–Aravalli Block (TAB) and Arabian Nubian shield (ANS) in terms of granite emplacement, ring structures and cauldron subsidence. In both the terrines, the alkali granites mark the cratonisation of the shield and show evidences of Strutian glaciation. Western Central Madagascar granites near Ambistra were emplaced during extensional collapse of Pan–African orogen and indicate emplacement age of 804–775 Ma. They are

very similar to Jalor granites in terms of gabbroic sleeves [41]. 750 Ma alkaline magmatism which is widespread and well developed in the continents viz., TAB, Central Iran, Arabian–Nubian shield, Medagascar and South China, Somalia, Seychelles [40] were characterized by common crustal stress pattern, rifting and thermal regime, shrutian glaciation and dessiciation and similar paleolatitudinal positions which could be attributed to the existence of a Supercontinent–the Malani Supercontinent. Rogers [42] has also suggested the similarities of their development including production of alkali granites, subsidence of thick partly deformed basin on recently formed crust and ultimate development of platform cover sediments. Hence in future, the significance of mantle plume and crust–mantle interaction should be studied for the emplacement of MIS.

A volcanic vent is observed in NRC with steep slope. It is characterized by elongated or semicircular depression with various volcanic flow products. Volcano–plutonic associations of NRC are located along the Luni River which flows 2 km Northeast of NRC. The Luni River takes sudden 'U' turn from West to South direction which represents the continental rift. Luni rift is an important tectonic lineament in TABLE [19]. This lineament is related to major crustal dislocations of continental rift type for the exrusions and intrusions of the magma [20]. Hence Luni rift served the way for magma rising through various major fractures, it is accompanied by anorogenic volcanism which may precede/follow the emplacement of ring complexes. The Nakora peralkaline granites support the view of association of rifting of crust in the area [43]. The semi–circular ring structure of Nakora area indicates the emplacement of magma into tensional environment. Hence, NRC indicates the presence of rift mechanism operated in the area in their emplacement vis–a–vis the tectonism and volcanism (**Figure 12**).
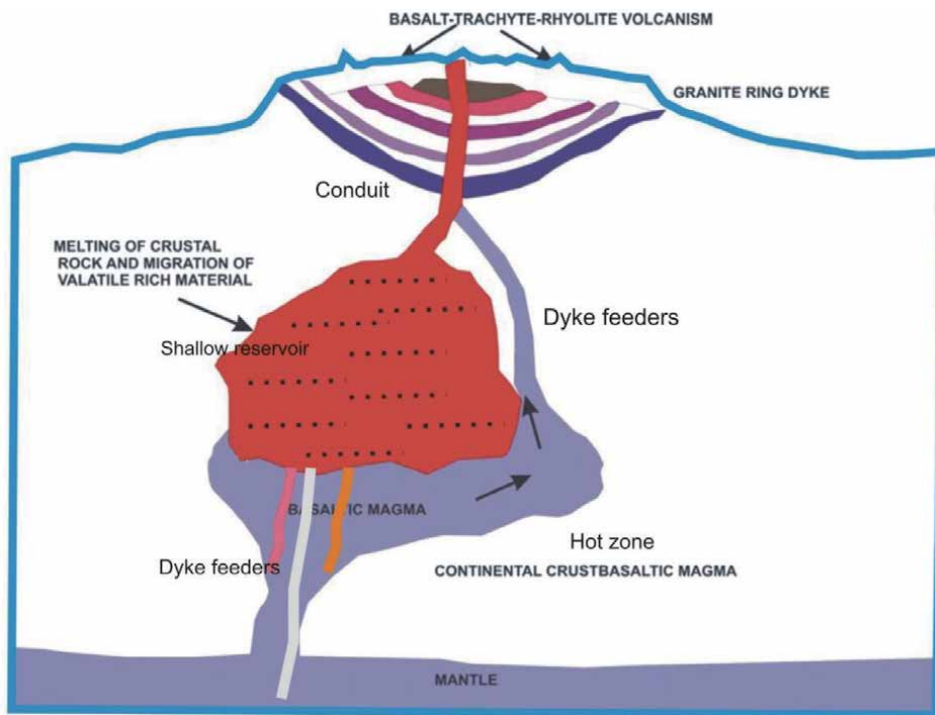

Figure 12.
Schematic presentation of Nakora area (after Annen et al. [39]), showing magma chamber and intrusion basaltic magma producing a zone of melting in the continental crust.

8. Conclusion

The rock types exposed in Nakora Ring Complex were classified into three major lithological divisions: basalt and rhyolite as first phase, second phase of granites of different colors and third and last phase magmatism of dykes of fine-grained granites and rhyolites. Based on petrographical observations, it is suggested that rhyolites show ophitic, sub-ophitic, porphyritic, granophyric, glomeroporphyritic, aphyritic, spherulitic, perlitic, hypidiomorphic, granophyric and microgranophyric textures. These textures have close similarities with A-type, anorogenic and within-plate granitoids as early reported by MIS rock-types behave. The volcano-plutonic rock associations and physio-chemical characteristics showed that during complex geological processes, the rock types of the Nakora Ring Complex were formed. Volcanic vent (approx. 40 m wide and semicircular to elongated shape) and sudden change pathways of Luni River advocates the relationship between tectonism and volcanism. Magmatic growth, phase petrology and geodynamic indicated that the studied areas in the NW Indian shield belonging to the MIS extension could be developed under the plume-related hot spot extension model.

Author details

Naresh Kumar* and Radhika Sharma
Department of Geology, Kurukshetra University, Kurukshetra, Haryana, India

*Address all correspondence to: sagwalnaresh@gmail.com

IntechOpen

References

[1] B. B. Decker and R. W. Decker, "Volcano". Encyclopedia Britannica, 1 Oct. 2020.

[2] J. A. Richardson, J. E. Bleacher, C. B. Connor and L. S. Glaze, "Small Volcanic Vents of the Tharsis Volcanic Province, Mars". Journal of geophysical research, 126 (2), 2021.

[3] J. W. Head and L. Wilson, "Basaltic pyroclastic eruptions: infuence of gas-release patterns and volume fuxes on fountain structure, and the formation of cinder cones, spatter cones, rootless fows, lava ponds and lava fows". Journal of volcanology Geothermal Research, 37, 261–271, 1989.

[4] J. M. Sumner, S. Blake, R. J. Matela and J. A. Wolf, "Spatter". Journal of Volcanology and Geothermal Research, 142, 49–65, 2005.

[5] F. Jodi M., M. Jocelyn, J.C. Rebecca, J. Fred and M. Daniel P.," The volcanic history of Heard Island". Bulletin of Volcanology,83, 27, 2021.

[6] G. Vallinayagam, "Geochemistry of rare metal and rare earth ore deposits: a study of the Malani Igneous Suite TransAravalli Block of NW Peninsular India". Indian Journal of Geochemistry, 21 (2), 439–446, 2006.

[7] R. Sharma, N. Kumar, N. Kumar and A.K. Singh, "Petrogenesis and tectonic impications of Anorogenic acid plutonic rocks of southwestern Haryana of Northwestern Peninsular India". Geochemical International, 58 (12), 1331–1356, 2020.

[8] N. Kumar, N. Kumar, R. Sharma and A.K. Singh, "Petrogenesis and tectonic Significance of the Neoproterozoic magmatism of the Tausham Ring Complex (NWIndian Shield): Insight into Tectonic Evolution of the Malani Igneous Suite and Rodinia

Supercontinent". Geotectonics, 54(3), 428–453, 2020.

[9] N. Kochhar, "Attributes and significance of the A-type Malani magmatism, Northwestern Peninsular Indian shield," in Crustal Evolution and Metallogeny in the Northwestern India, Ed. by M. Deb (Narosa Publishers, New Delhi, 2000b), pp. 158–188.

[10] H. S. Pareek, "Petrochemistry and petrogenesis of the Malani Igneous Suite, India". Geological Society of America Bulletin, 92, 206–273, 1981.

[11] N. Kumar, N. Kumar, A.K. Singh, "Petrology and Geochemistry of Acid Volcano-Plutonic Rocks from Riwasa and Nigana Areas of Neoproterozoic Malani Igneous Suite, Northwestern Peninsular India: An Understanding Approach to Magmatic Evolution". Geochemical International, 57, 645–667, 2019.

[12] R. Sharma, and N. Kumar, "Petrology and Geochemistry of A-type granites from Khanak and Devsar Areas of Bhiwani District, Southwestern Haryana". Journal of the geological Society of India, 90, 138–146, 2017.

[13] W. Wang, P.A. Cawood, M-F. Zhou, M.K. Pandit, X. Xiao-Ping and J-H. Zhao. "Low-$\delta 18O$ Rhyolites From the Malani Igneous Suite: A Positive Test for South China and NW India Linkage in Rodinia". Geophysical Research Letters, 44 (10), 298–305, 2017.

[14] N. Kumar, R. Sharma, N. Kumar and A.K. Singh, "A Review on Petrology and Geochemistry of the Neoproterozoic Malani Igneous Suite and Related Rocks (Northwestern Peninsular India)". Petrology, 28(6), 591–657, 2020.

[15] N. Kumar, and G. Vallinayagam, "Tectonic significance of

Neoproterozoic magmatism of Nakora area, Malani Igneous Suite, District Barmer, Western Rajasthan, India". Geotectonics by Springer-Verlag, Germany, 48, 239–253, 2014.

[16] S. K. Bhushan, "Malani rhyolites: a review". Gondwana Research, 3 (1), 65–77, 2000.

[17] N. Kochhar, "Malani Igneous Suite: hotspot magma tism and cratonization of the Northern part of the Indian shield". Journal of Geological Society of India, 25, 155–161, 1984.

[18] N. Kumar and N. Kumar, "Geochemistry of volcanic flows of Nakora area of Malani igneous suite, Northwestern India: Constraints on magmatic evolution and petrogenesis". International Journal of Engineering, Science and Technology, 12(1), 66–82, 2020.

[19] G. R. Narayan Das, A. K. Begchi, D. N. Chaube, C. V. Sharma and K. V. Naveneetham, "Rare metal content, geology and tectonic setting of the alkaline complexes across the TransAravalli region, Rajasthan". in Recent Researches in Geology, Ed. by P. K. Verma and V. K. Verma (Hindustan Publishing Corporation, Delhi, 1978), Vol. 7, pp. 201–217.

[20] D. K. Bailey, "Continental drifting and alkaline mag matism". in Alkaline Rocks, Ed. by T. S. Sorensan (John Wiley and Sons, 1974), pp. 148–159.

[21] G. N. Eby and N. Kochhar, "Geochemistry and petro genesis of the Malani Igneous Suite, North Peninsular India". Journal of Geological Society of India, 36, 109–130, 1990.

[22] W. S. Fyfe, "The evolution of earth' crust: modern plate tectonics to hot tectonics?," Chemical Geology, 23, 89–114,1978.

[23] M.J. Le Bas, R.W. Le Maitre, A. Streckeisen and B. Zanettin, 'A chemical classification of volcanic rocks based on the total alkali-silica diagram'. Journal of Petrology, 27, 747–750, 1986.

[24] R.A. Batchelor and P. Bowden, "Petrogenetic interpretation of granitoid rock series using multicationic parameters". Chemical Geology, 48, 43–55, 1985.

[25] R. Black and J.P. Liegeois, "Cratons, mobile belts, alkaline rocks and continental lithospheric mantle: the Pan-African testimony". Journal of Geological Society of London, 150, 89–98, 1993.

[26] A. Harker, A Natural History of Igneous Rocks. Mac Millan, 408 pages, 1990.

[27] J.A. Pearce, N.B.W. Harris and A.G Tindle, "Trace element description diagrams for the tectonic interpretation of granitic rocks". Journal of Petrology, 25, 956–983, 1984.

[28] S. S. Sun and W.F. McDonough, "Chemical and isotopic systematics of oceanic basalts: Implications for mantle composition and processes". In: Norry, M.J., Saunders, A.D. (Eds.), Magmatism in the ocean Basin. Special Publication, Geological Society, 42, 313–345, 1989.

[29] A.K. Singh, R.K.B. Singh and G. Vallinayagam, "Anorogenic acid volcanic rocks in the Kundal area of the Malani Igneous Suite, Northwestern India: geochemical and petrogenetic studies", Journal of Asian Earth Science, 27, 544–557, 2006.

[30] S. Dhar, R. Frel, R., S.J.D. Kramer, et al., "Sr, Pb and Nd isotope studies and their bearing on the petrogenesis of the Jalor and Siwana complexes, Rajasthan, India", Journal of Geological Society of India, 48(2), 151–160, 1996.

[31] R. Sharma, "Petrology and Geochemistry of the Granites and the Associated Acid Volcanic around

Jhunjhunu, District Jhunjhunu, Rajasthan, India". Ph.D. Thesis (unpubl.), Punjab University, 1992.

[32] N. Kochhar, "Geological evolution of the Trans Aravalli Block (TAB) of the NW Indian Shield: con straints from the Malani Igneous Suite (MIS) and its Seychelles Connection during Late Proterozoic," Geological Survey of India, Special Publication 84, 247–264, 2004.

[33] N. Kochhar, G. Vallinayagam and L. N. Gupta, " Zircon from the granitic rocks of the Malani Igneous Suite: Morphological and chemical studies". Journal of the Geological Society of India, 38(6), 556–576, 1991.

[34] P.T. Leat and R.S. Thorpe, "Geochemistry of an Ordovician basalt-trachybasalt-subalkaline/peralkaline rhyolite association from the Lieyn Peninsula, North Wales, U.K". Journal of Geology, 21, 29–43, 1986.

[35] G. Jarrar, H. Wachendorf and G. Saffarini, "A late Proterozoic bimodal volcanic/subvolcanic suite from Wadi Araba, Southwest Jorden". Precambrian Research, 56, 51–72, 1992.

[36] G. Vallinayagam, "Geology and geochemistry of alkali granites and the associated acid volcanics around Mokalsar, District Barmer, W. Rajasthan, India and their bearing on the rift tectonics". Unpublished Ph.D. Thesis, Punjab University, Chandigarh, 113 pages, 1988.

[37] R. Baskar, "Petrology and geochemistry of the alkali granites and the associated acid volcanics around Goliya Bhalyan, district Barmer, W. Rajasthan, India". Unpublished Ph.D. Thesis, Punjab University, Chandigarh, 153 pages, 1992.

[38] R. Chellasamy, "Petrology and geochemistry of the alkali granites and the associated acid volcanic around

Gura Nal area, district Barmer, Wesetern Rajasthan". Unpublished M. Phil. Thesis, Punjab University, Chandigargh, 536 pages, 1992.

[39] C. Annen, J. D. Blundy and R. S. J. Sparks, "The Genesis of Intermediate and Silicic Magmas in Deep Crustal Hot Zones". Journal of Petrology, 47(3), 505–539, 2006.

[40] N. Kochhar, "A type Malani magmatism: Signatures of the Pan-African event in the Northwest Indian shield assembly of the Late Proterozoic Malani Supercontinent". Special Publication of Geological Survey of India, 91, 112–126, 2008.

[41] M. Handke, R.D. Tucker and M.A. Hamillion, "Early Neoproterozoic (800–790) intrusive igneous rocks in central Medagascar, Geochemistry and petrogenesis". Geological Society, Abstract Program, 29, 468, 1997.

[42] J.J.W. Rogers, "Comparison of India and Nubian shield. In: Naqvi, S.M. (Ed.), Precambrian continental crust and its economic resources". Development in Precambrian Geology. Elsevier, New York, 6, 1990.

[43] C. Payette and R.F. Martin, "The Welsford Igneous Complex Southern New Brunswick: rift related Acadian magmaism". Geological Survey of Canada, 87(1A), 239–248, 1987.

A View to Anorthosites

Homayoon Mohammadiha

Abstract

It seems anorthosites are by far interested by geologists because they give us great information about Earth history and how it was evolved in planetary geology. Planetary geology is subject the geology of the celestial bodies such as the planets and their moons, asteroids, comets, and meteorites. It is nearly abundant in the moon. So, it seems studying of these rocks give us good information about planetary evolution and the own early time conditions. Anorthosites can be divided into few types on earth such as: Archean-age (*between 4,000 to 2,500 million years ago*) anorthosites, Proterozoic (*2.5 billion years ago*) anorthosite (also known as massif or massif-type anorthosite) – the most abundant type of anorthosite on Earth, Anorthosite xenoliths in other rocks (often granites, kimberlites, or basalts). Furthermore, Lunar anorthosites constitute the light-colored areas of the Moon's surface and have been the subject of much research. According to the Giant-impact hypothesis the moon and earth were both originated from ejecta of a collision between the proto-Earth and a Mars-sized planetesimal, approximately 4.5 billion years ago. The geology of the Moon (lunar science) is different from Earth. The Moon has a lower gravity and it got cooled faster due to its small size. Also, it has no plate tectonics and due to lack of a true atmosphere it has no erosion and weathering alike the earth. However, Eric A.K. Middlemost believed the astrogeology will help petrologist to make better petrogenic models to understand the magma changing process despite some terms geological differences among the Earth and other extraterrestrial bodies like the Moon. So, it seems that these future studies will clarify new facts about planet formation in planetary and earth, too.

Keywords: Anorthosites, Archean, Proterozoic, the Moon, plagioclase

1. Introduction

Anorthosites can give us great information about Earth history and how it was evolved. They can be divided into few types on earth such as: Archean-age (between 4,000 to 2,500 million years ago) anorthosites, Proterozoic (2.5 billion years ago) anorthosite (also known as massif or massif-type anorthosite) – the most abundant type of anorthosite on Earth, Anorthosite xenoliths in other rocks (often granites, kimberlites, or basalts). Furthermore, Lunar anorthosites constitute the light-colored areas of the Moon's surface and have been the subject of much research. So, these studies will clarify new facts about planet formation in planetary, too.

Magmatic rocks or Igneous rocks are the dominant rock type that the other two main type rocks (I, e sedimentary and metamorphic rocks) are originated them. These Igneous rocks are formed through the cooling and solidification of magma or lava.

Magma is a natural semi-molten material is existed inside the Earth and magmatism is a commonplace phenomenon in terrestrial planets like the Mars and the Venus and some natural satellites such as the Moon. The high internal heat of planets (more than 700°C) like the Earth causes the volcanism phenomenon in which solid rock are formed by cooling magma which are called lava. Definitely, lava is a viscous material but it can be flowed at great distances before cooling as igneous rocks. It should be reminded that melting is not caused by rising temperature, it can also be generated by pressure decreasing or changing in composition, too.

Magma solidification can occur either below or on the surface of the Earth (Planet surface) which are called as intrusive rocks and extrusive rocks, in turn. Moreover, these Igneous rocks can form via crystallization or without crystallization which are called natural glasses. Intrusive rocks which are formed within Earth's crust can be observed as diverse forms even such as dikes (Magmatic dikes are created by flowing magma into a pre-existing fracture of rock body) or even great Batholiths (Large mass of intrusive igneous rock more than 100 square km in area get formed through cooling magma in the depth of Earth.

Petrologists try to find good information about the conditions of igneous rock formation by study them, for example, Plagioclases are really important to identify the origin and evolution of igneous rocks. Fortunately, Anorthosites are dominantly contained Plagioclase minerals and it seems it would be possible to find the answers of suggested questions about how the earth was at own early history and how other extraterrestrial bodies like the Moon get formed, although, Phanerozoic (The eon from the Cambrian Period to the present) rocks are dominantly exposure in the earth as a more evolved planet and Anorthosites are not abundant in the Earth. In a simpler language, these studies will help scientists to make a good planetary formation model which will be vitally important at space exploration time within the solar system or beyond it through the galaxy, or even in astrobiology studies.

2. What are Anorthosites?

Anorthosites are a fascinating type of igneous rocks which are composed predominantly of calcium-rich plagioclase feldspar and mostly formed during Precambrian times. It has to be reminded that all found anorthosites on Earth are contained coarse crystals (See **Figures 1** and **2**) but moon anorthosite samples are finely crystalline which were collected from The Moon highlands (See **Figures 3–5**).

Lunar anorthosites within the light-colored areas of the Moon's surface are subject of investigations to understand the history of moon evolution. It seems the light coloured lunar highland crust was formed by the crystallization and floatation of plagioclase from a global magma ocean, although the actual generation mechanisms are still debated [5].

Additionally, Lunar anorthosites are known for displaying a limited range of plagioclase (∼94 to 98) and basis nearly recent studies at 2019 [6, 7], the plagioclase trace-element variations from Apollo ferroan anorthosites (FAN) samples (collected by the Apollo 15 and 16 missions) display more significant chemical heterogeneity and it can give us a better illustration about the timing and formation mechanisms of the Moon's crust. This study clarified a chemical heterogeneity within the LMO[1] as a global moon feature in the crustal formation. It seems that maybe during mantle overturn, the act of exhuming deep mafic-rich cumulates to the base of the lunar crust would have triggered decompression

---

[1] The lunar magma ocean (LMO).

Figure 1.
Large outcrop of anorthosite in the Helleren massif, Jibbeheia, Rogaland-Norway [1].
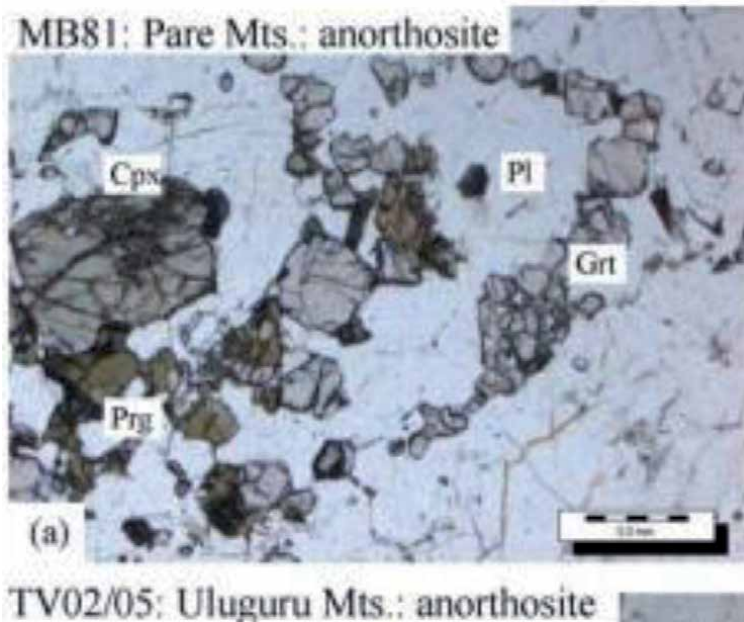

Figure 2.
Anorthosite from the Pare Mountains with mafic lense and Grt (spell out) corona [2].

melting. These are likely to be small degree (<10%) partial melts[2], which are typically enriched in incompatible elements[3]. It is not contradict with the idea of

---

[2] Partial melting is the transformation of some mass solid rock fraction into a liquid as a result of heat input, decompression or flux addition. This resulting liquid is nominated either magma or lava as if eruption from a volcano.

[3] Incompatible elements own difficulty in entering cation sites of the minerals, so they get concentrated in the melt phase of magma.
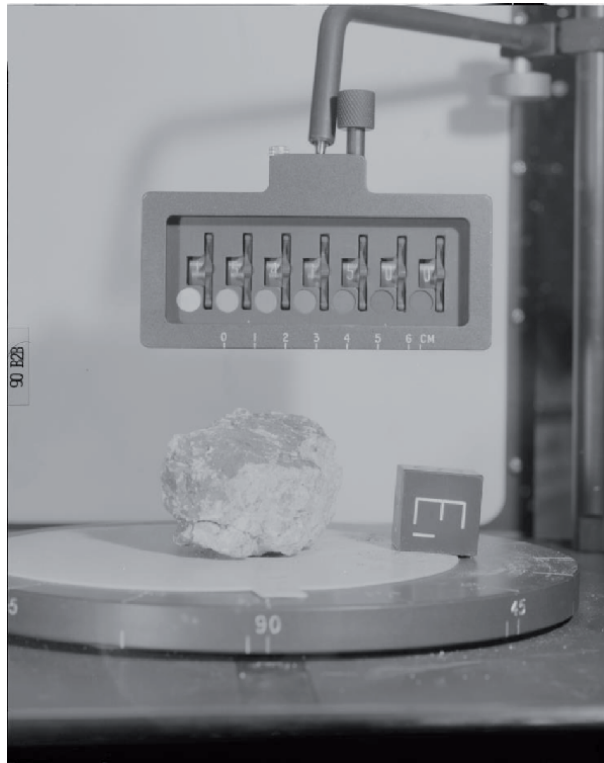
Figure 3.
Black and White Photograph of Apollo 15 Sample (s) 15415-Nasa - Lunar Samples [3].

Figure 4.
Ferroan Anorthosite (1836 grams)- 60025. NASA #S72–41586. Cube and scale are 1 cm. Note the thick black glass coating and numerous micrometeorite pits [4].
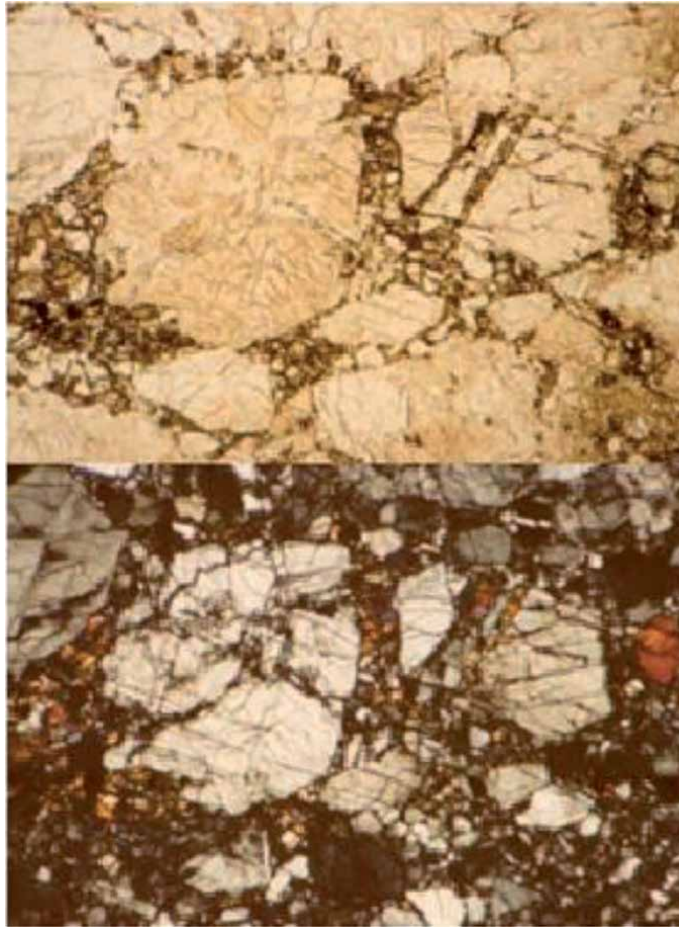
Figure 5.
Plane-polarized and cross-polarized photos of thin Section 60025,21. Field of view is 2.5 mm. S79–27300 and 301 [4].

local LMO magmas infiltration[4] by more evolved liquids through metasomatism[5] process, too.

The terrestrail anorthosites can be divided into five types: Archean-age anorthosites, Mid-ocean ridge and transform fault anorthosites, Anorthosite xenoliths in other rocks, Layers within Layered Intrusions and Proterozoic anorthosite as the most abundant anorthosite kind. Lunar geological studies also clarified that the light areas of the moon also consist of very old anorthosite. The dark areas of the moon, many of which are circular, consist of the black volcanic rock basalt. In fact, the primary pre-Nectarian lunar highlands are contained light-grey anorthosites which are caused at the early moon crust formation.

3. Anorthosites- geologic timescale

The geological history of Moon is categorized into six major epochs which is called the lunar geologic timescale. The boundaries of this time scale are subject to

---

[4] Infiltration is defined as the flow of liquid such as water from aboveground into the subsurface.

[5] Metasomatism is replacing one mineral with another that mineral dissolution and minerals deposition are occurred at the same time.

large impact events which affected the lunar surface through time as crater formation and their absolute ages got determined by radiometric dating of obtained lunar samples. The lunar surface is generally modified by impact cratering and volcanism, so, it is possible to define the lunar geological events in time basis on stratigraphic principles [8–10].

In the moon history, the Nectaris Basin and other major moon basins were formed by large impact events at the Nectarian Period (from 3920 million years ago to 3850 million years ago). Also, the pre-Nectarian period of the lunar geologic timescale is between 4.53 billion years ago to 3.92 billion years ago. It is extended between the initial Moon formation time to Nectaris Basin by a large impact. During this time, these light anorthosites came from the cooling of the surface lunar magma ocean (LMO). The impact event is subject the collision of astronomical objects like asteroids, comets or meteoroids on the surface of planets and moons, and they have a significant role in the evolution of the Solar System like the Earth and the Moon. For instance, approximately 4.5 billion years ago the Moon created from the ejecta of a collision between the proto-Earth and a Mars-sized planetesimal and it seems a giant hit causing from this hit at both parent bodies (I, e the earth and moon) [11].

The pre-Nectarian system was characterized by the formation of an anorthositic crust and its subsequent brecciation by large basin- forming impact events [12]. In fact, it contains the minerals that were emplaced at the lunar surface over the period extending from the moon formation to the excavation of the Nectaris impact- basin. According to studies, the lunar highlands being compose of anorthositic gabbros and gabbroic anorthosites, but the pre-Nectarian terrain are now probably breccias (rather than pristine igneous rocks) produced during the excavation of the basin cavities.

During the Nectarian Period (*from 3920 million to 3850 million years ago*), the Nectaris Basin and other major lunar mare or sea basins (Volcanic-basaltic lava as the dark spots of moon) were formed by large impact events that Ejecta from Nectaris forms the upper part of the densely cratered terrain found in lunar highlands. In the following of Nectarian Period, along with the Late Heavy Bombardment of the Inner Solar System, the huge Mare Imbrium basin was formed at 3850 to 3800 million years ago (The Early Imbrian epoch), then, this basin and other formed basins get filled with basalt mostly during the subsequent Late Imbrian epoch (3800 to about 3200 million years ago) (See **Figure 6**).

The lunar geological timescale went away on with *Eratosthenian* (from 3,200 million to 1,100 million years ago) and the massive basaltic volcanism of the Imbrian period tapered off and ceased during this long span of lunar time. In the following, impact craters lost their bright ray systems (thrown out radial streaks of fine ejecta at the formation of impact crater) due to space weathering processes[6] and It ends up to *The Copernican period* (From 1.1 billion years ago to the present day) in which light freshly excavated lunar surface has been growing to become darker over time due to space weathering processes.

This lunar geologic time scale is based on the recognition of few geomorphological markers, but it is practical to correlate the geological events at the solar system, in specific too much far distant early Earth time. The Hadean eon of Earth between 4.6 to 4 billion years ago which it begun with the Earth formation and ended up before the earliest-known rocks on Earth. According to the Lunar geologic timescale, this eon can be subdivided to *Pre-Nectarian* (the formation of the Moon's crust, 4533 to 3920 million years ago) and Nectarian (the Late Heavy Bombardment, from 3920 to 3850 million years ago). Some Hadean rocks as the oldest Earthen rocks

---

[6] Including, bombardment surface planetary bodies like the Moon or the Mercury by different sizes of meteorites, coalition of solar cosmic rays, solar wind and galactic cosmic rays.

Figure 6.
The location of lunar Mare Imbrium [13].

were found out at western Greenland, northwestern Canada, and Western Australia with the oldest dated zircon crystals in a metamorphosed sandstone conglomerate in the Jack Hills of Western Australia which these xenocryst zircons formed after 200 million years after Earth formation.

The Earth history can be subdivided to few Eons which are the Hadean, the Archean, the Proterozoic and the Phanerozoic (See **Figure 7**). Each eon can be divided into eras, which are in turn divided into periods, epochs and ages. The Phanerozoic (541 million years ago to the present) is the current geologic eon with abundant animal and plant life and it begun at the Cambrian Period when the first hard shells of animals developed and have been preserved as fossil record. The time before the Phanerozoic Eon which is the Hadean, Archaean and Proterozoic eons are called the Precambrian, too.

During the Archean eon (between 4,000 to 2,500 million years ago), the Earth's crust had cooled enough in forming continents and also the emergence of life. At the early Archean, the Earth's heat flow was nearly three times as high as it is today and also it was still twice the current level at the transition from the Archean to the Proterozoic (2.5 billion years ago) due to the heat remnant of planetary formation and the decay of radioactive elements.

Therefore, it can be assumed that these volcanic activities at the Precambrian had great role in The Cambrian explosion at 541 million years ago to rapid emergence life diversification at a short period time between 13 to 25 million years and this trend has being continued. It owns to say the life was mostly simple unicell organisms at the Precambrian, but it got suddenly was turned into colonies as multi-cellular life after the snow earth period.

There is a lot of exposed rocks relevant to this eon which can be observed around the globe such as Greenland, Siberia, the Canadian Shield, the Baltic Shield, India,
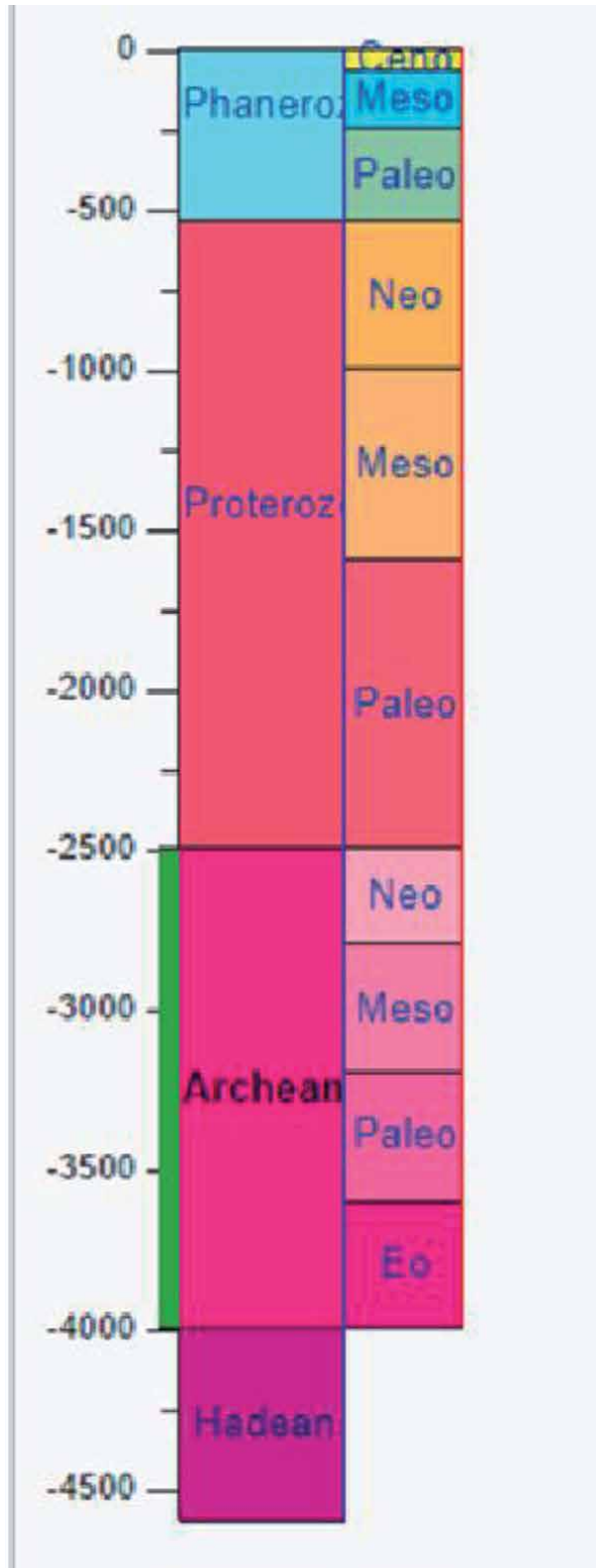
Figure 7.
Earth geologic time scale- Scale: millions of years [14].

Brazil, western Australia, and southern Africa. For example, granitic rocks have been significantly observed from the crystalline remnants of Archean crust, and also other rocks like monzonites (An igneous intrusive rock with equal amount of plagioclase and alkali feldspar and less than 5% quartz) anorthosites (*mostly plagioclase feldspar (90–100%)*) and, too.

4. Petrological specifications of Anorthosites

Plagioclase is a major constituent mineral which is really important to identify the composition, origin and evolution of igneous rocks and it is observed at different parts of the Earth and even other parts of world such as the highlands of the Moon or the Martian crust. Johann F. C. Hessel showed at 1826 that plagioclase feldspars are solid solutions of albite (the sodium (Na^+) endmember of the plagioclase solid solution series) and anorthite (the calcium (Ca^{2+}) endmember of the plagioclase feldspar mineral series) that the formula of pure albite and pure albite endmembers are $NaAlSi3O8$ and $CaAl2Si2O8$, in turn.

General speaking, Anorthosites are dominantly contained Plagioclase minerals that the first researchers such as Thomas Sterry Hunt at 19 centuries understood this fact. These pioneer geologists tried to explain the origin of Anorthosites like the granite. For instance, there is a lot of anorthosite lenses within Archean gneisses around diverse parts of world such as Africa, Greenland or even the Scotland. So, it is supposed that they get formed like Gneiss. Gneisses are metamorphic rock with foliated texture that they get made by heating and squeezing previous igneous and sedimentary rocks during mineral recrystallizations and The Lewisian complex with the Archean age at the north of Scotland is a typical example and these granitic gneisses form the basement of later deposited sediments. Therefore, these pioneers tried to illustrate the origin of huge massif anorthosites basis on this natural procedure.

A lot of Archean anorthosites are lenses within Archean gneisses. Moreover, it is clear that the ambient temperature of the Archaean mantle (1500–1600°C) was 200–300°C higher than today's mantle (1300–1400°C) [15, 16], so, the higher mantle temperatures under the Archaean oceanic spreading means more 7–10% partial melting than present-day and it was caused thicker oceanic crust was made in comparison to modern ocean ridges. In a simple language, there was more voluminous basaltic magma with generating large, shallow magma chambers. In fact, higher geothermal gradients in the Archaean oceanic crust let shallow magma chambers cool slowly and it was caused more differentiation and stratification to produce cumulates of dunite, peridotite, chromitite, pyroxenite, gabbro and anorthosite (See **Figure 8**).

As far as, lithological and geochemical characteristics are concerned, it seems that these Anorthosite-bearing layered intrusions in the southern West Greenland and Canada are subject Archaean subduction-related ophiolites. The changes of anorthosites can reflect the thermal evolution of the Earth. Furthermore, the presence of water at these magma zones had played great role in the formation of plagioclase mega crystals due to rising cooling time.

In one hand, the major difference between the Earth and Moon and their influence on the formation of anorthosite is the presence water, and in first glance it seems that anorthosite could not form on the Earth if the terrestrial magma ocean was saturated with the water. By considering lunar anorthosites, it can be interpreted that the early earth - terrestrial magma was not saturated with water as the moon [17], so, it is possible that these plagioclases crystallized from the dry terrestrial magma ocean, so the Earth and the Moon were maybe both dry just after the formation.
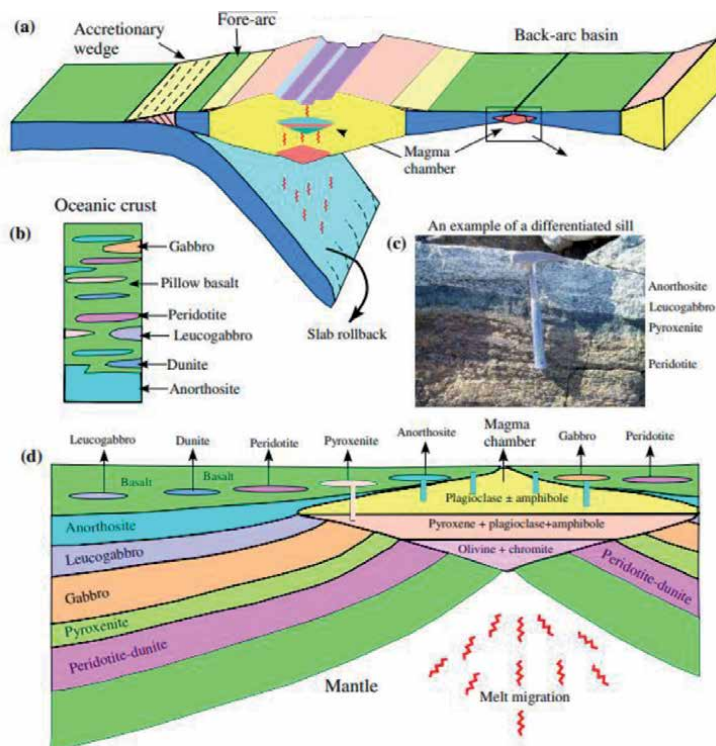
Figure 8.
Simplified geodynamic model for the origin of Archaean anorthosite-bearing layered intrusions. (c) shows an example of mineralogically stratified sill, representing a small version of Archaean magma chambers [16].

It should be mentioned that the origin of the water on the Earth is still debated, one of the scenarios is the "late-veneer" hypothesis[7] in which the Earth and the Moon were dry just after the formation of the Moon, and late-accretion of volatile-rich carbonaceous chondrites beyond the asteroid belt supplied water to the "dry" Earth. In this case, it is possible that plagioclase crystallized from the "dry" terrestrial magma ocean and anorthosite formed on the Hadean Earth [17].

Geological records of anorthosite crusts of the Hadean[8] have been erased by tectonic erosion on the Earth, or reprocessed by impacts. Once the anorthosite is subducted to a depth of 30 km, the plagioclase changes to garnet due to the phase transition, and the density of the garnet-composing "meta-anorthosite" becomes higher than the pyrolite. The result suggests that the meta-anorthosite could easily be transported into the mantle due to the density difference. Future works should be focusing on the detection of the geophysical evidences of meta-anorthosite buried in the deep interior of the Earth [17].

On the other hand, at the end of Hadean around 4 billion years ago, Earth changed from having a hot, molten surface and atmosphere full of carbon dioxide to being very much like it is today. Furthermore, the abundance of large anorthosite massifs in the Proterozoic[9] (2.5 billion years ago up to 500 million years ago) are good indicators of other the early Earth history and inherits and

---

[7] Basis on late-veneer hypothesis, it seems nearly all earth water were formed by impacts with icy comets, meteorites and other passing objects at the Late accretion (about 4.5 billion to 3.8 billion years ago).

[8] It began with the formation of the Earth about 4.6 billion years ago and ended at 4 billion years ago.

[9] It began from the appearance of oxygen in Earth's atmosphere (2.5 billion years ago) to just before the proliferation of complex life at 500 million years ago.

it point outs a specific condition of earth-crust evolution and the Proterozoic magmatism.

It seems the Archaean—Proterozoic boundary represents a transitional period during which the Archaean-thickened continental crust was uplifted and eroded to give rise to abundant clastic debris [18]. A Continental rift is a too much deformed continental lithosphere which can lead to form new ocean basins that the East African Rift System is a typical example of this type of tectonic valley. Even, it is possible that, some parts of this old crustal component may be derived either by direct erosion of Archean rocks. It is clear that the Earth's heat flow had been nearly three times as high as it is today in the beginning of the Archean and it was still twice the current level at the transition from the Archean to the Proterozoic (2,5 billion years ago).

It owns to say that, magmatic differentiation (Igneous differentiation) owns important role in making these old anorthosite rocks. It should be reminded that is an umbrella term to describe the natural processes such as partial melting process, cooling, emplacement, or even eruption in which magmas undergo bulk chemical changing. The composition of magma (Parental-primitive magma) can be different into diverse composition magma due to these factors. For example, basis on diverse cooling rate, the various crystallize minerals get created from the melt or liquid portion of the magma. Also, contamination is another cause of magma differentiation which made by mixing other wall rocks of magma chambers.

The anorthosites are even observed at younger the Phanerozoic rocks as xenolith or Layers within Layered Intrusions as in Africa and Nigeria. Finally, it seems anorthosites can be caused from each basaltic magma mass as if the opportunity of accumulation and sorting of plagioclase crystals get provided, as if it was occurred at the lunar surface or early earth crustal evolution time.

5. Conclusions

Anorthosites are very much interested by geologists because they give us great information about Earth history and how it was evolved. They are able to be classified as Archean-age anorthosites, Proterozoic anorthosite in the Earth and Lunar anorthosites which are constituted the light-colored areas of the Moon's surface.

Petrologists try to find good information about the conditions of igneous rock formation by study them and anorthosites (As an igneous rock which are dominantly contained Plagioclase minerals) are good rocks in this regard to find out more than about early history and how other extraterrestrial bodies like the Moon get formed.

It seems that the light-colored areas got formed by the crystallization and floatation of plagioclase from a global magma ocean with a significant chemical heterogeneity. Furthermore, the Earth was remarkably hotter than to day in the Archean (4 to 2.5 billion years ago) and the Proterozoic (2.5–0.5 billion years ago) nearly three and two times as today, respectively. The Archean anorthosites are more than as lenses within other Archean rocks due to high mantle temperature at this time and let more differentiation and stratification to produce cumulates. Furthermore, Proterozoic anorthosite are massif-type anorthosite which are the most abundant type of anorthosite on Earth. So, it can be assumed that these volcanic activities at the Precambrian probably had great role in The Cambrian explosion. Definitely, these studies will help scientists to make a better planetary formation model to study extraterrestrial bodies within the solar system or other star systems through the galaxy, or even in astrobiology studies.

Future works should be focusing on the detection of these ideas to confirm or on contrary suggesting new ideas. Definitely, by considering new astro -geological studies like the Moon, our knowledge about the earth early condition and developing planetary formation modeling will be remarkably developed as an important science to study in the space exploration era.

Acknowledgements

Author details

Homayoon Mohammadiha
Research Institute of Earth Sciences - Geological Survey of Iran, Tehran, Iran

*Address all correspondence to: homayoon532000@gmail.com

IntechOpen

References

[1] Available from: https://www.
britannica.com/science/anorthosite
[Accessed July 2020]

[2] V. Tenczer a, C.A. Hauzenberger a,
H. Fritz a, M.J. Whitehouse b, A.
Mogessie a, E. Wallbrecher a, S.
Muhongo c, G. Hoinkes: Anorthosites in
the Eastern Granulites of Tanzania—
New SIMS zircon U–Pb age data,
petrography and geochemistry. DOI:
i:10.1016/j.precamres.2006.03.004.

[3] Available from: Nasa- Lunar
Samples- https://curator.jsc.nasa.gov/ ,
[Accessed July 2020].

[4] Lunar Sample Compendium- C
Meyer 2011- https://www.researchgate.
net/publication/234491909_Lunar_
Sample_Compendium, [Accessed
July 2020].

[5] Makiko Ohtake, Tsuneo Matsunaga,
Junichi Haruyama, Yasuhiro Yokota,
Tomokatsu Morota, Chikatoshi Honda,
Yoshiko Ogawa, Masaya Torii, Hideaki
Miyamoto, Tomoko Arai, Naru Hirata,
Akira Iwasaki, Ryosuke Nakamura,
Takahiro Hiroi, Takamitsu Sugihara,
Hiroshi Takeda, Hisashi Otake, Carle M.
Pieters, Kazuto Saiki, Kohei Kitazato,
Masanao Abe, Noriaki Asada, Hirohide
Demura, Yasushi Yamaguchi, Sho
Sasaki, Shinsuke Kodama, Junya
Terazono, Motomaro Shirao, Atsushi
Yamaji, Shigeyuki Minami, Hiroaki
Akiyama & Jean-Luc Josset : The global
distribution of pure anorthosite on the
Moon.DOI: 10.1038/nature08317.

[6] Eric A.K. Middlemost, Magmas and
Magmatic Rocks: An Introduction to
Igneous Petrology-1985.

[7] John F.Pernet-Fisher,
EtienneDeloule, Katherine H.Joy:
Evidence of chemical heterogeneity
within lunar anorthosite parental
magmas- 22 April 2019- https://doi.
org/10.1016/j.gca.2019.03.033.

[8] R. F. Emslie: Proterozoic Anorthosite
Massifs. In: The Deep Proterozoic Crust
in the North Atlantic Provinces. 1985. pp
39-60. DOI: https://doi.org/10.1007/
978-94-009-5450-2

[9] SA Bowring, JP Grotzinger, CE
Isachsen, AH Knoll, SM Pelechaty, P
Kolosov: Calibrating rates of early
Cambrian evolution-1993- DOI:
10.1126/science.11539488

[10] Don Wilhelms : Geologic History of
the Moon, U.S. Geological Survey
Professional Paper 1348, −1987.

[11] Edward D. Young1 , Issaku E. Kohl1 ,
Paul H. Warren1 , David C. Rubie2 ,
Seth A. Jacobson2,3, and Alessandro
Morbidelli3- Affiliations: Oxygen isotopic
evidence for vigorous mixing during the
Moon-forming Giant Impact- 15 Mar
2016. DOI: 10.1126/science.aad0525.

[12] J.L.Whitford-stark : Lunar surface
morphology and stratigraphy, a remote
sensing synthesis-Department of
geological science, Brown university,
Providence Rhode Island 02912, USA-
This paper presented at the BAA(British
Astronomical Association) lunar
symposium held at Keel University on
1979 July 7-8.

[13] Avialable from: Mare Imbrium-
Wikipedia- https://en.wikipedia.org/
wiki/Mare_Imbrium, [Accessed
July 2020].

[14] Avialable from: Archean-
Wikipedia- https://en.wikipedia.org/
wiki/Archean, [Accessed July 2020]

[15] Keith A. Milam, Harry Y. Mc Sween
Jr. Jeffrey Moersch and Philip R.
Christensen: Distribution and variation
of plagioclase compositions on Mars-
2010. DOI: 10.1029/2009JE003495.

[16] Ali Polat, Fred J. Longstaffe &
Robert Frei: An overview of

anorthosite-bearing layered intrusions in the Archaean craton of southern West Greenland and the Superior Province of Canada: implications for Archaean tectonics and the origin of megacrystic plagioclase-2018. DOI: 10.1080/ 09853111.2018.1427408.

[17] Tatsuyuki Arai, ShigenoriMaruyama: Formation of anorthosite on the Moon through magma ocean fractional crystallization-2017. DOI: 10.1016/j. gsf.2016.11.007

[18] Brian F.Windley : Developments in Precambrian Geology- Volume 4, Chapter 1 Precambrian Rocks in the Light of the Plate-Tectonic Concept-1981, Available online 21 April 2008.

Edited by Angelo Paone and Sung-Hyo Yun

Progress in Volcanology includes nine chapters in three sections. The first section is the "Introduction" while the other two sections speak on "Applied Volcanology" and "Volcanic Sedimentology, Geochemistry and Petrology." The chapters address volcanology in several areas around the world, including Italy, Indonesia, Ethiopia, Argentina, India, and others.

IntechOpen